Universidade do Minho
Escola de Ciências

Diana Isabela Faria Meira

Development of nanoplasmonic thin film biosensors with enhanced sensitivity for detection of Ochratoxin-A

junho de 2024

Development of nanoplasmonic thin film biosensors with enhanced sensitivity for detection of Ochratoxin-A

Diana Isabela Faria Meira

UMinho | 2024

Universidade do Minho
Escola de Ciências

Diana Isabela Faria Meira

Development of nanoplasmonic thin film biosensors with enhanced sensitivity for detection of Ochratoxin-A

Tese de Doutoramento
Programa Doutoral em Física (MAP-Fis)

Trabalho efetuado sob a orientação de
Professor Doutor José Filipe Vilela Vaz
Doutor Joel Nuno Pinto Borges
Doutor Vitor Manuel Correlo da Silva

junho de 2024

COPYRIGHT AND TERMS OF USE OF THE WORK BY THIRD PARTIES

This is an academic work that can be used by third parties as long as they respect internationally accepted rules and good practices, with regard to copyright and related rights. Thus, this work can be used under the terms of the license indicated below.

If the user needs permission to use the work under conditions not provided by the indicated license, he/she must contact the author through the RepositóriUM of the University of Minho.



Atribuição-NãoComercial-SemDerivações

CC BY-NC-ND

https://creativecommons.org/licenses/by-nc-nd/4.0/

ACKNOWLEDGEMENTS

Firstly, I would like to acknowledge my supervisors, Professor Filipe Vaz, Doctor Joel Borges, and Doctor Vitor Correlo. Their guidance deeply shaped my scientific journey, instilling a strong commitment to hard work in pursuit of excellence. Words cannot fully express my gratitude for their wisdom, mentorship, and support, which have been pivotal in both my academic and personal growth.

During my PhD journey, I had the privilege of working with and learning from Doctor Ana Isabel Barbosa. I sincerely thank her for generously sharing vast scientific knowledge, providing insightful guidance, and maintaining a consistently supportive and friendly presence. I also want to thank all co-authors for their expertise and invaluable assistance, which have greatly enriched the scientific work presented in this thesis.

To my friends, Patrícia, Diogo, Manuela, and Marco, thank you for the countless shared moments and companionship over the last few years.

To my parents and sisters. Thank you so much for your boundless love, for believing in me unconditionally, and for encouraging me to pursue my dreams. I would never be able to thank you enough.

Last but not least, I want to thank Flávio, who has been by my side on this rollercoaster journey. Thank you for your infinite patience and constant support. Most importantly, thank you for your love.

FINANCIAL SUPPORT

I would also like to acknowledge the Portuguese Foundation for Science and Technology (FCT) for the PhD scholarship (SFRH/BD/143262/2019). This research was also supported by FCT under the Strategic Funding UIDB/04650/2020, by the research projects NANO4BIO, POCI-01-0145-FEDER-032299, with reference PTDC/FIS-MAC/32299/2017 and CO2Plasmon, with reference EXPL/CTM-REF/0750/2021.

Additionally, I extend my thanks to the "TERM RES Hub – Scientific Infrastructure for Tissue Engineering and Regenerative Medicine", reference PINFRA/22190/2016 (Norte-01-0145-FEDER-022190), funded by the FCT in cooperation with the Northern Portugal Regional Coordination and Development Commission (CCDR-N). Ultimately, I would like to thank the research project MyμMAT granted by FCT with the reference PTDC/CTM-CTM/2846/2020.

STATEMENT OF INTEGRITY

I hereby declare having conducted this academic work with integrity. I confirm that I have not used plagiarism or any form of undue use of information or falsification of results along the process leading to its elaboration.

I further declare that I have fully acknowledged the Code of Ethical Conduct of the University of Minho.

RESUMO: Desenvolvimento de Biossensores baseados em Filmes Finos Nanoplasmónicos com Sensibilidade Melhorada para Deteção de Ocratoxina-A

Ocratoxina-A (OTA), uma micotoxina potencialmente cancerígena, é uma das principais preocupações no âmbito da segurança alimentar, uma vez que pode contaminar vários produtos alimentícios de primeira necessidade (p.e., cereais e vinho). A deteção precoce da OTA evita perdas económicas significativas na indústria alimentar e permite salvaguardar a saúde humana contra os riscos associados à sua ingestão. Entre vários procedimentos de controlo e estratégias de deteção, o fenómeno da Ressonância de Plasmões de Superfície Localizados (LSPR) surge como uma estratégia de deteção inovadora e eficaz, ultrapassando limitações inerentes às abordagens convencionais. A espectroscopia LSPR permite uma solução em tempo real, rápida, sensível e económica na deteção e monitorização da presença da OTA. Na sua essência, o fenómeno ótico de LSPR resulta de uma oscilação coletiva dos eletrões da banda de condução em nanopartículas (NPs) de metais nobres quando excitadas por um campo eletromagnético incidente. O princípio de transdução baseia-se no desvio da banda LSPR resultante de alterações locais do índice de refração que ocorrem na vizinhança das NPs, provocadas pela presença de (bio)moléculas. Assim, esta tese de doutoramento centra-se no desenvolvimento de um biossensor LSPR para a deteção de OTA, utilizando NPs de metais nobres dispersas num filme fino de óxido dielétrico como plataforma de transdução.

Filmes finos nanoplasmónicos, constituídos por NPs metálicas (Au, Ag, Au-Ag) embebidas numa matriz dielétrica de TiO_2, foram produzidos utilizando pulverização catódica reativa em magnetrão. Os filmes finos foram depois submetidos a um tratamento térmico à pressão atmosférica, promovendo a alteração morfológica das NPs (tamanho e distribuição) no filme fino de TiO_2. Diferentes respostas LSPR foram obtidas através da combinação de diferentes composições metálicas e temperaturas de tratamento térmico.

Na primeira fase do trabalho, filmes finos de Au-TiO_2 foram testados como plataformas transdutoras LSPR na deteção da interação biotina-estreptavidina. Contudo, face à sua baixa sensibilidade, foram necessárias várias otimizações. A eficácia da interface biomolecular foi otimizada, considerando as estratégias de imobilização por adsorção física e por funcionalização química. Demonstrou-se que a funcionalização de uma camada de adesão, utilizando um ligante com grupo funcional -tiol (molécula de ditiobis(succinimidil propionato, DSP), melhora a eficácia da ligação biomolecular. Adicionalmente, a eficiência de extinção de luz e a resposta plasmónica foi melhorada através do ajuste da composição e da nano-estrutura dos filmes. Uma das principais conclusões deste trabalho é que a combinação de Au e Ag, numa proporção de 1:1, em NPs bimetálicas melhora significativamente a resposta do sensor LSPR, alcançando uma sensibilidade de 181 nm/RIU. Por fim, os biossensores LSPR, compostos por anticorpos anti-OTA imobilizados nos filmes AuAg-TiO_2, detetaram OTA em amostras padrão e reais (vinho), evidenciando um notável desempenho. Em resumo, os biossensores LSPR provaram ser uma estratégia promissora e eficiente na deteção ótica de (bio)moléculas, como a OTA.

Palavras-chave: Biossensor; Filme fino nanoplasmónico; LSPR; Nanopartículas Au-Ag; Ocratoxina-A.

ABSTRACT: Development of Nanoplasmonic Thin Film Biosensors with Enhanced Sensitivity for Detection of Ochratoxin-A

Ochratoxin-A (OTA), a potentially carcinogenic mycotoxin, is a major concern to food safety since it can contaminate various essential food products (i.e., cereals and wine). The early detection of OTA prevents significant economic losses in the food industry and, more importantly, safeguards human health against the risks associated to OTA ingestion. Among several control procedures and detection strategies, Localized Surface Plasmon Resonance (LSPR) phenomenon has emerged as an innovative and effective sensing strategy, overcoming inherent limitations of conventional approaches. In particular, LSPR biosensing allows a real-time, rapid, sensitive, and cost-effective solution for detecting and monitoring OTA contamination. At its core, LSPR is an optical phenomenon that results from a collective oscillation of conduction band electrons in noble metal nanoparticles (NPs) when excited from an incident electromagnetic field. The transduction principle is based on LSPR band shift resulting from local refractive index changes occurring in the vicinity of NPs, induced by the presence of (bio)molecules. This doctoral thesis focuses on the development of an LSPR-based biosensor for OTA detection, using noble metal NPs dispersed in a dielectric oxide thin film as a transduction platform.

Nanoplasmonic thin films composed of metallic (Au, Ag, Au-Ag) NPs embedded in a host TiO_2 dielectric matrix were produced using reactive DC magnetron sputtering. The thin films were then subjected to a thermal treatment process at atmospheric pressure to promote the change of the NPs morphology (size and distribution) within the TiO_2 thin film. Different LSPR responses were obtained by combining different metal compositions and thermal treatment temperatures.

In the first stage of the work, nanoplasmonic Au-TiO_2 thin films were evaluated as LSPR transducer platforms for detecting the biotin-streptavidin interaction. However, due to its relatively low sensing performance, various optimizations were necessary to enhance their efficacy. Among these, the effectiveness of the biomolecular interface was considered by studying both adsorption (physisorption) and cross-linker functionalization (chemisorption) immobilization strategies. The functionalization of an intermediate adhesion layer, using a -thiol based (Dithiobis(succinimidyl propionate) (DSP) molecule) cross-linker, improves biomolecular binding efficiency. Moreover, the extinction efficiency and plasmonic response were enhanced by adjusting the metallic composition and nanostructure of the thin films. A major finding in this work is that combining Au and Ag in a 1:1 ratio to create bimetallic NPs significantly enhances the LSPR sensor's response, achieving an outstanding refractive index sensitivity of 181 nm/RIU, which translates to an important sensitivity strategy. Ultimately, the LSPR-based biosensors, composed of immobilized anti-OTA antibodies on AuAg-TiO_2 films, successfully detected OTA analytes in both standard and real wine samples, evidencing a notable biosensing performance. In summary, LSPR-based biosensors proved to be a promising and efficient optical strategy for (bio)molecules detection, such as OTA.

Keywords: Au-Ag nanoparticles; Biosensor; LSPR; Nanoplasmonic thin film; Ochratoxin-A.

TABLE OF CONTENTS

Acknowledgements iii

Financial Support iii

Statement of Integrity iv

Resumo v

Abstract vi

List of Abbreviations and Acronyms xi

List of Figures xvi

List of Tables xxv

Short *Curriculum Vitae* xxvi

Scientific Outputs xxvii

Motivation and Main Objectives xxxi

Introduction to the Thesis Outline xxxiv

1. Recent Advances in Nanomaterial-based Optical Biosensors for Food Safety Applications: Ochratoxin-A Detection 36

1.1. Abstract 37

1.2. Mycotoxins Introduction 38

1.2.1. Mycotoxins Importance in Farming Industry 38

1.2.2. Influence of the Agricultural Environment on Mycotoxins Appearance 38

1.3. Ochratoxin-A Critical Issues: Food Safety, Standard Methods, and the Role of Biosensors 40

1.3.1. Food Regulation and Conventional Detection 42

1.3.2. An Overview of Biosensing Nanotechnology 44

1.3.3. Current Available On-Site Detection Approaches 47

1.4. Recent Advances in Optical Biosensors for Ochratoxin-A Detection 49

1.4.1. Single and Dual-Mode Optical Detection Method 56

1.4.2. Comparison Performance of the Different Optical Biosensors 88

1.4.3. Patents Survey on Localized Surface Plasmon Resonance Biosensors 90
1.5. Major Challenges and New Trends of Ochratoxin-A Optical Sensors 94
1.6. Conclusion 96
2. Immobilization of Streptavidin on a Plasmonic Au-TiO_2 Thin Film towards an LSPR Biosensing Platform 98
2.1. Abstract 99
2.2. Introduction 100
2.3. Materials and Methods 101
2.3.1. Preparation and Characterization of the LSPR Biosensor Platform 101
2.3.2. Protein Immobilization and Binding Assay 104
2.3.3. Optical Response of the LSPR Biosensing Platform 105
2.4. Results and Discussion 106
2.4.1. Characterization of Au-TiO_2 Thin Films 106
2.4.2. Streptavidin Immobilization and Binding Assay 109
2.4.3. LSPR Biosensing Platform Sensitivity 112
2.5. Conclusion 114
3. Immobilizing Antibody Biorecognition Layers on Au-TiO_2 Thin Films: Direct (Physisorption) vs. DSP-crosslinking (Chemisorption) Surface Functionalization 115
3.1. Abstract 116
3.2. Introduction 117
3.3. Materials and Methods 119
3.3.1. Preparation of Au-TiO_2 Thin Films 119
3.3.2. Functionalization and Characterization of Au-TiO_2 Thin Film with DSP cross-linker 120
3.3.3. Immunoassays Development 121
3.4. Results and Discussion 123
3.4.1. Surface Morphology Analysis 123
3.4.2. Surface Chemistry Analysis 126

3.4.3. Antibody Immobilization and Immunoassay in Functionalized Au-TiO_2 Thin Film 128
3.5. Conclusion 132
3.6. Supporting Information 133
4. Enhancing the Extinction Efficiency and Plasmonic Response of Bimetallic Nanoparticles of Au-Ag in Robust Thin Film Sensing Platforms 138
4.1. Abstract 139
4.2. Introduction 140
4.3. Materials and Methods 143
4.3.1. Reactive DC Magnetron Sputtering Deposition 143
4.3.2. Post-Deposition Annealing Treatment 144
4.3.3. Chemical Composition Analysis 144
4.3.4. Optical Response Measurements 145
4.3.5. Nanoparticles Distribution Analysis by SEM 145
4.3.6. Thin Film Surface Nano-Morphology by AFM 145
4.3.7. Refractive Index Sensitivity Tests 145
4.4. Results and Discussion 146
4.4.1. Chemical Composition Analysis 146
4.4.2. Optical Response Analysis 147
4.4.3. Refractive Index Sensitivity 150
4.4.4. Morphological Analysis of High-Sensitive AuAg-TiO_2 Thin Film 153
4.5. Conclusion 156
5. Novel Label-Free Localized Surface Plasmon Resonance (LSPR) Biosensor, based on Au-Ag NPs Embedded in TiO_2 Matrix, for On-site and Sensitive Detection of Ochratoxin-A (OTA) in Wine 157
5.1. Abstract 158
5.2. Introduction 159
5.3. Materials and Methods 161
5.3.1. Preparation and Characterization of Nanoplasmonic AuAg-TiO_2 Thin Film 161

5.3.2. Preparation of LSPR-based Biosensor for OTA Detection 162
5.3.3. OTA Detection: T-LSPR Spectroscopy vs. Microplate Standard ELISA 163
5.3.4. Experimental Setup and Data Analysis 163
5.4. Results and Discussion 165
5.4.1. Nanoplasmonic AuAg-TiO_2 Thin Films as LSPR-based Transducers 165
5.4.2. LSPR-based Biosensor Optimization 166
5.4.3. OTA Detection: T-LSPR Spectroscopy vs. Microplate Standard ELISA 168
5.4.4. OTA Detection: Spiked White Wine 171
5.5. Conclusion 172
5.6. Supporting Information 173
6. Final Remarks, Conclusions and Future Perspectives 175
6.1. Final Remarks and Conclusions 176
6.2. Future Perspectives 180
Bibliography 182

LIST OF ABBREVIATIONS AND ACRONYMS

2D	Two-Dimensional
3D	Three-Dimensional
4PL	4-Parameter Logistic Mathematical Model
A.R.	Aspect Ratio
Ab	Antibody
AFB1	Aflatoxin B1
AFM	Atomic Force Microscopy
Ag	Silver
AGOx	Aptamer-Conjugated Glucose Oxidase
Al_2O_3	Aluminum Oxide
AlN	Aluminum Nitride
AOAC	Association of Official Analytical Collaboration
Ar	Argon
at. %	Atomic percentage
ATR	Attenuated Total Reflectance
Au	Gold
BB	Berberine
BEN	Balkan Endemic Nephropathy
$BMDL_{10}$	Benchmark Dose
BPE	Gold-Plated Bipolar Electrode
BSA	Bovine Serum Albumin
bw	body weight
CDM	Color Difference Map
CDs	Carbon Dots
CEN	European Committee for Standardization
CIN	Chronic Interstitial Nephropathy
CI-ELASA	Chemiluminescence Based Enzyme Linked Apta-Sorbent Assay
CNPs	Carbon Nanoparticles
Co-ELASA	Colorimetric Based Enzyme Linked Apta-Sorbent Assay
CONTAM	Chemical Contaminants Panel of EFSA
COOH	Carboxyl group

CuO	Copper Oxide
CuS	Copper Monosulfide
CV	Coefficient of Variation
DAP	2,3-diaminophenazin
DC	Direct Current
DI water	Deionized water
DMSO	Dimethyl sulfoxide
DNA	Deoxyribonucleic Acid
DSP	Lomant's Reagent, Dithiobis(succinimidyl propionate)
ECL	Electrochemiluminescence
EFSA	European Food Safety Authority
ELISA	Enzyme-Linked Immunosorbent Assay
FAO	Food Agriculture Organization
FDA	Food And Drug Administration
FEG-SEM	Field Emission Gun - Scanning Electron Microscope
FITC	Fluorescein isothiocyanate
FM-ICTS	Fluorescent Microsphere in Immunochromatographic Test Strip
FoM	Figure of Merit
FPIA	Fluorescence Polarization Immunoassay
FRET	Förster Resonance Energy Transfer
FTIR	Fourier Transform Infrared Spectroscopy
FUM1	Fumonisin
FWHH	Full Width at Half Height
GC-MS	Gas Chromatography with Mass Spectroscopy
GO	Graphene Oxide
H_2O_2	Hydrogen Peroxide
H_3PO_4	Phosphoric Acid
HPLC-FLD	High-Performance Liquid Chromatography with Fluorescence Detection
HRP	Horseradish Peroxidase
IAC	Immunoaffinity Chromatography
IARC	International Agency for Research on Cancer
IF	Impact Factor

IgG	Immunoglobulin G
ISO	International Standard Organization
ITO	Indium Tin Oxide
IUPAC	International Union of Pure and Applied Chemistry
JECFA	Joint FAO/WHO Expert Committee on Food Additives
LC-MS	Liquid Chromatography with Mass Spectroscopy
LD_{50}	Lethal Dose
LFIA	Lateral Flow Immunoassay
LOB	Limit of Blank
LOD	Limit of Detection
LOQ	Limit of Quantification
LRD	Linear Dynamic Range
LRET	Luminescence Resonance Energy Transfer
LSPR	Localized Surface Plasmon Resonance
LSPs	Localized Surface Plasmons
mAb	Monoclonal antibody
MBs	Magnetic Beads
MGNHs	Magneto-Au Nanohybrids
MIPs	Molecularly Imprinted Polymers
MLs	Maximum Levels
MNPs	Magnetic Nanoparticles
MOE	Margin of Exposure
N.N.	Nearest Neighbor
NaOH	Sodium Hydroxide
Nb	Nanobody
NBPs	Nanobipyramids
NCs	Nanocones
NH_2	Amine group
NHS	N-hydroxysuccinimide group
NPs	Nanoparticles
NRs	Nanorods
NSs	Nanosheets

O_2	Oxygen
OD	Optical Density
OH	Hydroxyl group
OIV	International Organization of Vine and Wine
OPD	*o*-phenylenediamine
OTA	Ochratoxin-A
OTB	Ochratoxin-B
OTC	Ochratoxin-C
OVA	Ovalbumin
PB	Prussian Blue
PBS	Phosphate-Buffered Saline
PBS-T	Phosphate-Buffered Saline with Tween-20
PL	Persistent Luminescence
PW	Prussian White
QDs	Quantum Dots
R	Recovery
r-GO	Reduced GO
RBS	Rutherford Backscattering Spectrometry
RI	Refractive Index
RIS	Refractive Index Sensitivity
RIU	Refractive Index Unit
RSD	Relative Standard Deviation
SEM	Scanning Electron Microscopy
SERS	Surface-Enhanced Raman Scattering
SH	Thiol group
SNR	Signal-to-Noise ratio
SPCE	Surface Plasmon-Coupled Emission
SPE	Solid-Phase Extraction
SPPs	Surface Plasmon Polaritons
SPR	Surface Plasmon Resonance
SPs	Surface Plasmons
STEM	Scanning Transmission Electron Microscopy

SWC NHs	Single-Walled Carbon Nanohorns
TDI	Tolerable Daily Intake
TiO_2	Titanium Dioxide
TLC	Thin Layer Chromatography
TLD	Through-Lens Detector
TMB	3,3′,5,5′-Tetramethylbenzidine
UPLC	Ultrahigh Performance Liquid Chromatography
US	United States
WHO	World Health Organization
WoS	Web of Science
ZEN	Zearalenone

LIST OF FIGURES

Figure 1.1. *Scheme of the International Agency for Research on Cancer (IARC) monographs evaluation of carcinogenic hazard of mycotoxins, being highlighted the OTA evaluation.* 40

Figure 1.2. *Chemical structure of OTA, IUPAC name N-{[(3R)-5-chloro-8-hydroxy-3-methyl-1-oxo-7-isochromanyl]carbonyl}-3-phenyl-l-alanine. The yellow part represents the chlorine substituent, blue is the phenylalanine part, orange is the dihydro-isocoumaring ring, and green are the acidic hydrogens. Adapted and reprinted with permission from Kőszegi and Poór (2016) [8]. Copyright 2016 MDPI, Basel, Switzerland.*..... 41

Figure 1.3. *Schematic representation of the LFIA methodology at (a) and image of LFIA strip devices used for measuring OTA at different concentrations in spiked red wine in (b). Reprinted with permission from Anfossi et al. (2012) [118]. Copyright 2012 American Chemical Society.*..... 48

Figure 1.4. *General scheme of the main topics addressed in this review, regarding the recent advances in OTA optical biosensor nanotechnologies.*..... 50

Figure 1.5. *Schematic representation of the working mode of the competitive fluorescence assay based on free-complementary DNA at (a). The fluorescence intensity spectra at various concentrations of OTA at (b) and the linear relationship between the fluorescence intensity (520 nm) and OTA concentration among 10^{-5} and 1 μg mL^{-1} in (c). Reprinted with permission from Hitabatuma et al. [125]. Copyright 2021 Elsevier.*..... 57

Figure 1.6. *Schematic representation of the working mode of the label-free aptasensor for "turn-on" fluorescent detection at (a). The fluorescence intensity spectra at various concentrations of OTA at (b), and the fluorescence intensity (540 nm) plotted against OTA concentration; insert of the linear relationship between 0.5 and 3 ng mL^{-1} in (c). Reprinted with permission from Guo et al. [126]. Copyright 2021 Elsevier.* 58

Figure 1.7. *Schematic representation of the fabrication and working mode of fluorescent CuS NPs used in the detection assay at (a). The fluorescence intensity spectra at various concentrations of OTA; insert of the linear relationship between the fluorescence intensity (554 nm) and OTA concentration among 0.1 and 100 ng mL^{-1} at (b). Recovery rates of OTA in several samples (i.e., spiked corn, soybean, and coffee) in (c). Reprinted with permission from Chen et al. [128]. Copyright 2021 Elsevier.*..... 59

Figure 1.8. *Schematic representation of the working mode of the "turn off-on" fluorescent sensor for OTA detection in (a). The fluorescence intensity spectra of the ZnCdSe QDs, named as "on", at (b), and the nanocomplex composed by ZnCdSe QDs linked to SA-ZnTPyP, named as "off", in (c).

The fluorescence intensity spectra at various concentrations of OTA in (d). Reprinted with permission from Liu et al. [129]. Copyright 2020 Elsevier. 60

Figure 1.9. *Schematic representation of working mode of dual DNA tweezers nanomachine for OTA detection at (a). Fluorescence intensity spectra of the dual DNA tweezers nanomachine at various concentrations of OTA and another mycotoxin at (b), and the fluorescence intensity at a defined wavelength plotted against OTA concentration; insert of the linear relationship between 0.5 and 50 ppb in (c). Reprinted with permission from Xiong et al. [130]. Copyright 2021 Elsevier.* 61

Figure 1.10. *Schematic representation of working mode of FRET-based aptasensor for OTA detection at (a), and the linear relationship of the recovered fluorescence intensity (ΔF at 469 nm) plotted against OTA concentration between 0 and 160 nM; insert of fluorescence intensity spectra at the various concentrations of OTA at (b). Selectivity evaluation using mycotoxins or similar chemical molecules at (c) Reprinted with permission from Bi et al. [132]. Copyright 2020 Elsevier.* 63

Figure 1.11. *Schematic representation of working mode of FRET-based immunosensor using Nb and mAb immobilization for OTA detection at (a) and the energy transfer efficiency plotted against OTA concentration, between 0.005 and 10,000 pg mL^{-1}, being the Nb biodetection approach represented by the square symbol and the mAb symbolized by the circle, at (B). Reprinted with permission from Tang et al. [133]. Copyright 2020 Elsevier.* 64

Figure 1.12. *Schematic representation of fabrication and working mode of the FRET aptasensor for OTA detection in (a). Representative normalized fluorescence spectra of the mixture of CDs/apt1 and QDs/apt2 (b), CDs/apt1-MoS_2-QDs/apt2 bioconjugations before (c) and after (d) incubation with AFB1 and OTA. Reprinted with permission from Qian et al. [134]. Copyright 2020 Elsevier.* 65

Figure 1.13. *Schematic representation of fabrication and working mode of the LRET aptasensor for OTA detection in (a). Persistent luminescence (PL) intensity at different OTA concentrations in (b) and the linear relationship between the recovered PL (ΔP) and OTA concentration among 0.01 and 10 ng mL^{-1} in (c). Reprinted with permission from Jiang et al. [135]. Copyright 2020 Elsevier.* 66

Figure 1.14. *Schematic representation of working mode of the LSPR immunosensor detecting OTA and this optical response in (a). UV-vis absorption spectra of the colloidal Au NPs before and after adding OTA antibodies in (b). UV-vis absorption spectra at different OTA concentrations in (c) and the linear relationship between the absorbance intensity (528 nm) and OTA concentration in*

(d), using spiked wine samples. Reprinted with permission from Pereira et al. [137]. Copyright 2021 Elsevier. 68

Figure 1.15. *Schematic representation of fabrication and the working mode of Au Film– Au@Ag core–shell NP structured SERS aptasensor for OTA detection at (a). SERS spectra at different concentrations of OTA in (b) and the linear relationship between the Raman intensity ratio and the logarithmic OTA concentration in (c). Reprinted with permission from Jing et al. [138]. Copyright 2020 American Chemical Society.* 69

Figure 1.16. *Schematic representation of the working mode of the multiplex SERS-based lateral flow immunosensor for OTA detection in (a). Representative SEM images and Raman spectra from the test lines of negative sample in (b, d) and strong positive sample in (c, e). Reprinted with permission from Zhang et al. [140]. Copyright 2020 Elsevier.* 71

Figure 1.17. *Schematic representation of the working mode of the multi-colorimetric based on the structural switching of aptamer and the enzyme-induced deposition of AuNRs for OTA detection in (a). Photographs of the enzyme-induced aptasensor solutions (b) and UV-vis absorption spectra (c) at different OTA concentrations. The linear relationship between the blueshift of the longitudinal LSPR peak (Δλ) and OTA concentration among 12.5 to 20,000 nM at (d). Reprinted with permission from Tian et al. [142]. Copyright 2020 Elsevier.* 73

Figure 1.18. *Schematic representation of the working mode of a colorimetric immunosensor based on a paper-based analytical device for OTA detection in (a). Variation of normalized absorbance signal as a function of OTA concentration in (b) and normalized signal intensity was obtained from potential interferents in (c). Detection comparison between the reported biosensor and other sensing detection at several OTA concentrations in (d). Normalized signal intensity was obtained from different several real spiked samples (i.e., beer, urine, and serum) in (e). Reprinted with permission from Suea-Ngam et al. [145]. Copyright 2020 Elsevier.* 75

Figure 1.19. *Schematic representation of the working mode of the AuNPs-based multicolor immunochromatographic test strip biosensor in (a). Stereograms of the individual test at different OTA concentrations (marked with an arrow) in (b) and the linear relationship between the optical signal (B3/B03) and OTA concentration in (c). Reprinted with permission from Wu et al. [146]. Copyright 2020 Elsevier.* 76

Figure 1.20. *Schematic representation of the fabrication and working mode of the magneto-Au nanohybrid-enhanced LFIA biosensor for OTA detection in (a). Optical response at different OTA concentrations in (b) and the linear relationship between the optical signal (B/B0) and the*

logarithm of OTA concentration in (c). Reprinted with permission from Hao et al. [147]. Copyright 2021 Elsevier. 77

Figure 1.21. *Schematic representation of the hybrid fluorimetry and visual OTA detection in the absence and presence of Cu^{2+} and EDTA in (a). Fluorescence intensity spectra of a non-extracted blank sample (b – a), spiked samples with an increased linear concentration in (b from b – e), after the addition of Cu^{2+} to the spiked sample in (b – f) and their corresponding color difference map (CDM) images. The linear relationship between the fluorescence intensity and OTA concentration is plotted in (c). Reprinted with permission from Alizadeh, Hashemi, and Shahdost-Fard [148]. Copyright 2021 Elsevier.* 79

Figure 1.22. *Schematic representation of the working mode of the dual-modal immunosensor for OTA detection: multi-colorimetric and ratiometric fluorescence in (a). UV-vis absorption spectra (b) and fluorescence spectra (c) at different concentrations of OTA and their photographs in (d) and (e), respectively. The linear relationship between LSPR peak shift in (f) and fluorescence intensity ratio in (g) with OTA concentration. Reprinted with permission from Zhu et al. [151]. Copyright 2021 Elsevier.* 81

Figure 1.23. *Schematic representation of the working mode of the colorimetric ELASA (Co-ELASA) and chemiluminescence ELASA (CI-ELASA) assays for OTA detection in (a) and (b), respectively. Plots of the linear relationship between inhibition (%), in (c), and relative luminescence, in (d), with OTA concentration between 1 pg mL^{-1} and 1 µg mL^{-1}. Reprinted with permission from Mukherjee, Nandhini, and Bhatt [86]. Copyright 2021 Elsevier.* 83

Figure 1.24. *Schematic drawing of the dark box with the smartphone adapter in (a) and the photograph of the biosensor device in (b). Schematic representation of assay procedure: the analytical cartridge in (c), sample loading into the proper chamber (d), LFIA strip receiving the sample and the HRP-OTA conjugate solution in (e), the introduction of the HRP CL substrate in (f). Chemiluminescence images obtained by analyzing OTA-free wine and instant coffee samples spiked with known OTA concentrations in (g). Representative calibration curves obtained in spiked wine and instant coffee matrices in (h). Reprinted with permission from Zangheri et al. [152]. Copyright 2021 Elsevier.* 84

Figure 1.25. *Electrochemiluminescence (ECL) intensity response of the BPE-ECL biosensor with different OTA concentrations in (a). Variation of ECL signal as a function of OTA concentration; insert of the linear relationship between the ECL intensity signal and logarithm OTA concentration in (b). Reprinted with permission from Lu et al. [153]. Copyright 2021 Elsevier.* 85

Figure 1.26. *Schematic representation of the fabrication and working mode of the dual-modal electrochemical and optical biosensor for OTA detection in (a). Plots of linear relationship between electrochemical response with OTA concentration displayed in (b from a – h). Plots of linear relationship between colorimetric signal with OTA concentration displayed in (c from a – e). Reprinted with permission from Zhang et al. [154]. Copyright 2021 Elsevier.* 86

Figure 1.27. *Schematic representation of fabrication of the portable solar-driven ratiometric photo-electrochromic visualization biosensor in (a). The UV-visible absorption spectra at different concentrations of OTA in (b). Calibration curve of absorption intensity A2/A1 ratio and OTA concentration; insert of the linear relationship between absorption intensity A2/A1 ratio and logarithm OTA concentration in (c). Reprinted with permission from Hao et al. [155]. Copyright 2020 Elsevier.* 87

Figure 1.28. *Schematic representation of the bioanalytical performance parameters (i.e., the limit of detection (LOD) and linear dynamic range (LDR)), converted to ng mL^{-1}, of the conventional detection methods (i.e., HPLC-FD, ELISA, TLC, GC-MS, and LC-MS) and the biosensors described in the previous section (Table 1.3).* 88

Figure 1.29. *Schematic representation of the working mode of LSPR-based high sensitivity aptasensor for OTA detection in (a). Optical response (LSPR peak shift) of the patented biosensor to increasing OTA concentration, and also to another mycotoxin (i.e., AFB1) in (b). Reprinted from patent application publication no. US201715418100A (Kim, Jin-Ho, and Byun [173]).* 90

Figure 1.30. *Schematic representation of the reusable optical fiber LSPR-aptasensor for OTA detection in (a) and the detection assay in (b). The amplified view of the aptamer modified Au NRs chemically attached to the optical fiber core in (c). UV-vis absorption spectra at different concentrations of OTA in (d). The linear relationship between the relative LSPR peak shift (Δλ) and OTA concentration is plotted in (e). Reprinted with permission from Lee et al. [175]. Copyright 2018 Elsevier* 92

Figure 1.31. *Schematic representation of the dual modality immunosensor for OTA detection in (a). TEM images of the morphology and sizy evolution of the Au NCs during the detection assay in (b), and their corresponding UV-vis absorption spectra in (c). UV-vis absorption spectra at different OTA concentrations in (d), and the linear relationship between the blueshift of the longitudinal LSPR peak (Δλ) and OTA concentration in (e). Reprinted with permission from Wei et al. [177]. Copyright 2019 Elsevier.* 93

Figure 2.1. *Effect of Ar plasma treatment on the optical and morphological properties of the Au-TiO_2 thin films annealed at 400 °C: (a) optical transmittance spectra and (b) cross-section micrographs before and after Ar plasma.* 107

Figure 2.2. *Hydrophilic properties of the Au-TiO_2 thin films. (a) Photographs of a water droplet and the (b) contact angle (in degrees) measured as a function of O_2 plasma treatment time in seconds (s) on the surface of Au-TiO_2 thin films.* 108

Figure 2.3. *LSPR band evolution as a function of O_2 plasma treatment time (0, 10, 30, and 60 s) of the Au-TiO_2 thin film annealed at 400 °C: (a) transmittance spectra from 450 to 700 nm and (b) close-up of the highlighted area in graph a.* 109

Figure 2.4. *Streptavidin/biotin–HRP binding assay. (a) Absorbance values measured as a function of different streptavidin and biotin–HRP concentrations (µg/mL); (b) absorbance values measured as a function of streptavidin/biotin ratio, for streptavidin concentrations between 0.025 and 25 µg/mL; (c) absorbance values measured as a function of streptavidin concentration (µg/mL), for all combinations of streptavidin/biotin–HRP at the ratio of 0.33.* 110

Figure 2.5. *Influence of O_2 plasma treatment on the immobilization of streptavidin on the thin film's surface. Absorbance values measured as a function of streptavidin and biotin–HRP concentrations, without O_2 plasma treatment in (a) glass substrate and (b) Au-TiO_2 thin film and with O_2 plasma treatment in (c) glass substrate and (d) Au-TiO_2 thin film.* 111

Figure 2.6. *LSPR peak wavelength of the Au-TiO_2 thin films as a function of the refractive index of the different sucrose solutions (20, 30, 40, and 50% (w/w)). The solid line is a linear fit to the data.* 112

Figure 2.7. *Ten-minute LSPR peak wavelength monitoring of the produced Au-TiO_2 biosensor after incubation with PBS (control) and after the incubation with 13.5 µg/mL biotin–HRP (analyte detection). n1, n2, and n3 are the three independent samples tested.* 113

Figure 3.1. *Illustrative representation of functionalized Au-TiO_2 thin film with an adhesion layer composed by DSP cross-linker. Through the cleavage of DSP's disulfide linkage, the thiol (-SH) functional group can chemically interact with the partially exposed Au NPs. The adhesion layer acts as an intermediary, facilitating the specific binding of the bioreceptor to the thin film's surface, through the aminolysis reaction.* 119

Figure 3.2. *Illustrative representation of the envisaged immobilization of antibody surface coverage and the immunoassay analysis in plasma-activated (without DSP) and DSP-functionalized*

Au-TiO_2 thin films, depicting the physisorption strategy (represented in I. and II. by a) and the chemisorption strategy (represented in I. and II. by b). 122

Figure 3.3. *Influence of the DSP cross-linker concentration in the morphology of O_2 plasma-activated thin films (300 s). (a) Two-dimensional (2D) AFM height images and (b) morphological parameters (i.e., root mean square roughness (Sq), surface mean roughness (Sa), and mean height).* 123

Figure 3.4. *Influence of O_2 plasma treatment time in the morphology of plasma-activated (without DSP) and DSP-functionalized Au-TiO_2 thin films with the specific concentration of 4 mg mL^{-1}. (a) Two-dimensional (2D) and (b) morphological parameters (i.e., root mean square roughness (Sq), surface mean roughness (Sa), and mean height).* 125

Figure 3.5. *Infrared spectra of DSP (powder) and DSP-functionalized Au-TiO_2 thin films, with different concentrations.* 127

Figure 3.6. *Antibody surface coverage on O_2 plasma-activated (without DSP) and DSP-functionalized Au-TiO_2 thin film, using anti-IgG-FITC secondary antibody. (a) Processed confocal microscopy images and (b) fluorescent intensity per total thin film's area, considering the physisorption and chemisorption immobilization approaches, at different DSP concentrations.* 128

Figure 3.7. *Immunoassay on O_2 plasma-activated (without DSP) and DSP-functionalized Au-TiO_2 thin film, using bioreceptor (IgG) and its respective biological pair (Fab-specific anti-IgG-FITC secondary antibody). (a) Processed confocal microscopy images and (b) fluorescent intensity per total thin film's area, considering the physisorption and chemisorption immobilization approaches.* 131

Figure 4.1. *Calculated extinction, scattering, and absorption efficiencies of a spherical nanoparticle with variable size (D = 10, 20, 30 nm), composed of (a) Ag and (b) Au, surrounded by a dielectric medium with a constant refractive index of 2.3 (simulating a TiO_2 matrix). Calculations were performed using a software from Nanohub.org [316].* 141

Figure 4.2. *Simulated refractive index sensitivity (RIS) of a spherical nanoparticle (D = 10, 20, 30 nm) surrounded by a TiO_2 finite layer (d = 2, 4, 8 nm), immersed into two environments with different refractive index units, η_1 (RIU) = 1.333 and η_2 (RIU) = 1.381 ($\Delta\eta$ = 0.048) [316]. RIS was calculated by the difference in the wavelength of extinction maxima, divided by the difference in refractive index units, according to RIS = $(\lambda_2 - \lambda_1)/\Delta\eta$.* 142

Figure 4.3. *Optical transmittance spectra of the Au-TiO_2, AuAg-TiO_2, and Ag-TiO_2 films with different Au and/or Ag contents and subjected to different annealing temperatures.* 147

Figure 4.4. *LSPR band minimum wavelength shift of AuAg-TiO_2 thin films (Au/Ag atomic ratio of 1 and 2), annealed at 400 °C, during the RIS assessment, concerning each cycle. The surrounding media of the plasmonic nanocomposite thin film changed between DI water and sucrose solution of 30% (w/w) of sucrose.* 151

Figure 4.5. *LSPR band minimum wavelength shift of Au-TiO_2, and AuAg-TiO_2 thin films (Au/Ag atomic ratio of 1 and 2), annealed at 700 °C, during the RIS assessment, concerning each cycle. The surrounding media of the plasmonic nanocomposite thin film changed between DI water and sucrose solution of 30% (w/w) of sucrose.* 152

Figure 4.6. *SEM micrographs of the AuAg-TiO_2 thin film annealed at 700 °C, at increasing amplifications in (a), and the bimetallic NPs size distributions analysis in (b), considering the Feret diameter, nearest neighbor distance, and aspect ratio parameters.* 154

Figure 4.7. *Morphological analysis of the AuAg-TiO_2 thin films annealed at 700 °C: (a) two-dimensional (2D) AFM height images of 10 × 10 μm^2 and 5 × 5 μm^2, with roughness and height parameters. Considering the 2D AFM height image 5 × 5 μm^2, the topographic profile (delimited in the black dashed line in (a)), average height estimation (delimited by orange dotted line), and height distribution profile are represented in (b), and (c), respectively.* 155

Figure 5.1. *Schematic representation of OTA detection using the developed LSPR-based biosensor. (a) Anti-OTA antibody immobilized on the surface of AuAg-TiO_2 thin film; (b) In the presence of OTA, it binds to the immobilized anti-OTA Ab. This binding event alters the local refractive index near the NP surface, leading to a measurable LSPR sensing response, and (c) OTA is absent, the LSPR response remains unchanged.* 161

Figure 5.2. *Nanostructural and optical characteristics of the AuAg-TiO_2 thin film: (a) STEM micrographs, (b) analysis of bimetallic NPs size distributions, and (c) T-LSPR band.* 166

Figure 5.3. *Immobilization strategies on AuAg-TiO_2 thin films for OTA detection (a) Illustration of immobilization strategies: physisorption and chemisorption. (b) LSPR response (nm) as a function of immobilization strategy and anti-OTA Ab concentration.* 167

Figure 5.4. *Comparison between LSPR-based biosensor and competitive ELISA for OTA detection. (a) LSPR response in wavelength shift (nm) caused by different OTA concentrations (insert shows the linear relationship between the LSPR response and OTA concentration (in log scale), resulting in a dynamic range from 0.05 to 2 ng mL^{-1}). (b) Inhibition (%) caused by different OTA concentrations (insert presented in log scale).* 169

Figure 5.5. *(a) LSPR response (nm) caused by different OTA concentrations, using standard solutions (PBS buffer) and real sample solution (wine). (b) Recovery (%) of spiked wine samples with 3 different OTA concentrations, 0.5, 2 and 8 ng mL^{-1}*..... 172

LIST OF TABLES

Table 1.1. *Conventional detection methods for OTA.* 44

Table 1.2. *Description of bioanalytical performance parameters and bioanalytical requirements.* 46

Table 1.3. *Overview of optical biosensors for OTA detection, highlighting their bioanalytical performance.* 51

Table 3.1. *Comparison of physisorption and chemisorption immobilization strategies.* 118

Table 4.1. *Atomic concentration of Au and Ag in nanocomposite Au-TiO_2, AuAg-TiO_2, and Ag-TiO_2 thin film systems.* 146

Table 4.2. *LSPR band parameters of Au-TiO_2, AuAg-TiO_2 (Au/Ag atomic ratio of 1 and 2), and Ag-TiO_2 films subjected to different annealing temperatures.* 148

Table 4.3. *The optical response analysis of Au-TiO_2, AuAg-TiO_2 (Au/Ag atomic ratio of 1 and 2), and Ag-TiO_2 films, annealed at 400 °C and 700 °C, to the sensitivity assay, considering the LSPR band wavelength shift, SNR and RIS (nm/RIU) values.* 150

Table 5.1. *Overview of LSPR strategies for OTA detection, highlighting their biosensing strategy (i.e., biorecognition element, transducer) and bioanalytical performance.* 171

SHORT *CURRICULUM VITAE*

Diana Isabela Faria Meira was born on the 14th of June 1995, in Barcelos, Portugal.

In 2016, Diana graduated in Biology-Geology (BSc) from the Science School of the University of Minho, achieving a final grade of 15 out of 20.

In 2018, Diana concluded her Master's degree in Biophysics and Bionanosystems (MSc) with a final graduation mark of 17 of 20 at the Science School of the University of Minho. During this period, her MSc dissertation focused on the functionalization of plasmonic Au-TiO_2 thin films with biorecognition elements for biomolecules detection, under the NANO4BIO project.

In 2020, Diana began her PhD in the MAP-Fis programme at the University of Minho, supported by an individual doctoral scholarship from FCT (SFRH/BD/143262/2019). Her research primarily involved developing nanoplasmonic thin films for biosensing applications, particularly in detecting Ochratoxin-A.

During her PhD, Diana was also actively involved in other projects and supported the instruction and mentorship of several students and colleagues. As a result of her research work during the PhD, Diana improved her skills in materials science, plasmonics, and biosensing, leading to significant scientific achievements, including 9 peer-reviewed and submitted papers, with 5 as first author and co-first authorship in 2. Additionally, her work was presented in important international meetings in the field, 4 as first-author oral presentations, and she participated in various poster presentations, two of which received notable awards.

SCIENTIFIC OUTPUTS

The work performed during the PhD period resulted in the publications listed below:

PUBLICATIONS PRESENTED IN THIS THESIS

1. **D.I. Meira**, A.I. Barbosa, J. Borges, R.L. Reis, V.M. Correlo, F. Vaz, Recent Advances in Nanomaterial-based Optical Biosensors for Food Safety Applications: Ochratoxin-A Detection, as Case Study, Critical Reviews in Food Science and Nutrition (2023) 1–43. https://doi.org/10.1080/10408398.2023.2168248.
2. P. Pereira-Silva†, **D.I. Meira†**, A. Costa-Barbosa, D. Costa, M.S. Rodrigues, J. Borges, A. V. Machado, A. Cavaleiro, P. Sampaio, F. Vaz, Immobilization of Streptavidin on a Plasmonic Au-TiO_2 Thin Film towards an LSPR Biosensing Platform, Nanomaterials 12 (2022) 1526. https://doi.org/10.3390/nano12091526.
3. **D.I. Meira**, A.I. Barbosa, M. Proença, P. Pereira-Silva, J. Borges, V.M. Correlo, R.L. Reis, F. Vaz, Immobilizing Antibody Biorecognition Layers on Au-TiO_2 Thin Films: Direct (Physisorption) vs. DSP-crosslinking (Chemisorption) Surface Functionalization. *Submitted to Journal of Physics D: Applied Physics* (2024).
4. **D.I. Meira**, M.S. Rodrigues, J. Borges, F. Vaz, Enhancing the Extinction Efficiency and Plasmonic Response of Bimetallic Nanoparticles of Au-Ag in Robust Thin Film Sensing Platforms, Sensors 23 (2023) 9618. https://doi.org/10.3390/s23239618.
5. **D.I. Meira**, A.I. Barbosa, J. Borges, V.M. Correlo, R.L. Reis, F. Vaz, Novel Label-Free Localized Surface Plasmon Resonance (LSPR) Biosensor, based on Au-Ag NPs Embedded in TiO_2 Matrix, for On-Site and Sensitive Detection of Ochratoxin-A (OTA) in Wine. *Submitted to Sensors and Actuators B: Chemical* (2024).

OTHER PUBLISHED SCIENTIFIC PUBLICATIONS RELATED TO THE THESIS

6. **D.I. Meira**, R.P. Domingues, M.S. Rodrigues, E. Alves, N.P. Barradas, J. Borges, F. Vaz, Thin Films of Au-Al_2O_3 for Plasmonic Sensing, Applied Surface Science 500 (2020) 144035. https://doi.org/10.1016/j.apsusc.2019.144035.
7. M.S. Rodrigues, **D.I. Meira**, C. Lopes, J. Borges, F. Vaz, Preparation of Plasmonic Au-TiO_2 Thin Films on a Transparent Polymer Substrate, Coatings 10 (2020) 227. https://doi.org/10.3390/coatings10030227.

8. M. Proença, M.S. Rodrigues, **D.I. Meira**, M.C.R. Castro, P. V. Rodrigues, A. V. Machado, E. Alves, N.P. Barradas, J. Borges, F. Vaz, Optimization of Au:CuO Thin Films by Plasma Surface Modification for High-Resolution LSPR Gas Sensing at Room Temperature, Sensors 22 (2022) 7043. https://doi.org/10.3390/s22187043.
9. **D.I. Meira**†, M. Proença†, R. Rebelo, A.I. Barbosa, M.S. Rodrigues, J. Borges, F. Vaz, R.L. Reis, V.M. Correlo, Chitosan Micro-Membranes with Integrated Gold Nanoparticles as an LSPR-Based Sensing Platform, Biosensors 12 (2022) 951. https://doi.org/10.3390/bios12110951.

CONFERENCE ORAL PRESENTATIONS

- J. Borges, **D.I. Meira**, M. Proença, F. Vaz, Thin films manifesting Localized Surface Plasmon Resonances for applications in sensing and photosynthetic mechanisms. ICTF-JVC 2023 – 19th International Conference on Thin Films & Joint Vacuum Conference, Spain 2023
- J. Borges, M.S. Rodrigues, M. Proença, **D.I. Meira**, R.M.S. Pereira, M.I. Vasilevskiy, F. Vaz, Plasmonic gold nanoparticles embedded in oxide thin films deposited by reactive magnetron sputtering for LSPR sensing and Bio-Applications. 3-day International Conference on Materials Science, Italy 2022
- J. Borges, **D.I. Meira**, P. Pereira-Silva, M. Proença, M.S. Rodrigues, F. Vaz, Thin Films manifesting Localized Surface Plasmon Resonances for Sensing and Bio-Applications. Future Materials Conference, Italy 2022
- N.M. Figueiredo, R. Serra, **D.I. Meira**, M. Proença, J. Borges, F. Vaz, A. Cavaleiro, Robust label-free LSPR sensing using thermally embedded Au nanoparticles in glass substrates. 95th IUVSTA Plasmonic Thin Films: Theory, Synthesis and Applications Workshop – International Union for Vacuum Science, Technique and Applications, Portugal 2022
- **D.I. Meira**, J. Borges, F. Vaz, Plasmonic behaviour of Au-AlN thin films deposited by glancing angle deposition. BraMat 2022 – 12th International Conference Materials Science & Engineering, Romania 2022
- **D.I. Meira**, J. Borges, V. Correlo, F. Vaz, Nanoplasmonic Thin Film Biosensors with Enhanced Sensitivity for Ochratoxin-A detection. 3B's Seminars, Portugal 2021
- **D.I. Meira**, J. Borges, V. M. Correlo, F. Vaz, Development of Nanoplasmonic Thin Film Biosensors with Enhanced Sensitivity for Detection of Ochratoxin-A, MAP-Fis Annual Conference, Portugal 2021

- M. Proença, **D.I. Meira**, M.S. Rodrigues, J. Borges, F. Vaz, Nanocomposite Thin Films for Gas Sensing with High Resolution Localized Surface Plasmon Resonance Spectroscopy. ICTF-JVC 2020 – 18th International Conference on Thin Films & Joint Vacuum Conference, Hungary 2020
- J. Borges, **D.I. Meira**, M.S. Rodrigues, F. Vaz, Development of plasmonic sensors based on thin films composed by Au(-Ag) nanoparticles embedded in dielectric matrixes. E-MRS 2019 Spring Meeting Conference – European Materials Research Society, France 2019
- **D.I. Meira**, R.P. Domingues, M.S. Rodrigues, J. Borges, F. Vaz, Thin films of Au-Al_2O_3 for plasmonic sensing. BraMat 2019 – 11th International Conference Materials Science & Engineering, Romania 2019

CONFERENCE POSTERS

- **D.I. Meira**, J. Borges, F. Vaz, Design of Localized Surface Plasmon Resonance (LSPR) Biosensors using Gold Nanoparticles Embedded in Dielectric Thin Films. INL Global – Local Photonic Meetup, Portugal 2023
- **D.I. Meira**, J. Borges, F. Vaz, Nanomaterial-Based Biosensor Development: Application of Plasmonic Thin Film for Optical Detection Purposes. Materiais 2023 – Sustainability for a Future, Portugal 2023
- **D.I. Meira**, J. Borges, F. Vaz, Development of nanoplasmonic thin films composed by Au nanoparticles embedded in dielectric matrixes for biosensing application. Encontro da Ciência – FCT, Portugal 2023
- **D.I. Meira**, P. Pereira-Silva, D. Costa, M. Proença, M.S. Rodrigues, J. Borges, F. Vaz, Plasmonic thin films for LSPR-based applications. Encontro da Ciência – FCT, Portugal 2023
- **D.I. Meira**, P. Pereira-Silva, D. Costa, M. Proença, M.S. Rodrigues, J. Borges, F. Vaz, Thin Films for LSPR-based sensors. Steering Committee (SC) Meeting CF-UM-UP University of Minho, Portugal 2022
- **D.I. Meira**, P. Pereira-Silva, J. Borges, F. Vaz, Plasmonic thin films for biosensing. 95th IUVSTA Plasmonic Thin Films: Theory, Synthesis and Applications Workshop – International Union for Vacuum Science, Technique and Applications, Portugal 2022
- T. Lednický, M. Proença, M.S. Rodrigues, **D.I. Meira**, J. Borges, A. Bonyár, Gold nanoparticle arrays for gas sensing. 95th IUVSTA Plasmonic Thin Films: Theory, Synthesis

and Applications workshop – International Union for Vacuum Science, Technique and Applications, Portugal 2022

- J. Borges, **D.I. Meira**, D. Costa, M. Proença, M.S. Rodrigues, F. Vaz, Thin Films for LSPR-based sensors. RIVA 2022 – XII Iberian Vacuum and Applications Conference, Portugal 2022
- **D.I. Meira**, P. Pereira-Silva, J. Borges, F. Vaz, Development of plasmonic thin films for new biodetection approaches. 5th International Conference on Applications in Optics and Photonics, Portugal 2022
- R. Rebelo, A.I. Barbosa, **D.I. Meira**, J. Borges, R.L. Reis, F. Vaz, V.M. Correlo, Development of plasmonic polymeric based membranes for Localized Surface Plasmon Resonance biosensing. 3rd ForeCast Workshop, Portugal 2021
- **D.I. Meira**, M.S. Rodrigues, J. Borges, F. Vaz, Plasmonic Response of Au-Al_2O_3 Thin Films, EuroNanoForum Conference. Portugal 2021
- **D.I. Meira**, M.S. Rodrigues, J. Borges, F. Vaz, Influence of a plasma treatment on the microstructure and plasmonic behaviour of Au-Al_2O_3 thin films. Jornadas CF-UM-UP 2019, Portugal 2019

AWARDS

- **D.I. Meira**, P. Pereira-Silva, J. Borges, F. Vaz, Development of plasmonic thin films for new biodetection approaches. **Awarded as EOS' Best Student Poster Presentation** in AOP – 5th International Conference on Applications in Optics and Photonics, Portugal 2022.
- **D.I. Meira**, M.S. Rodrigues, J. Borges, F. Vaz, Influence of a plasma treatment on the microstructure and plasmonic behaviour of Au-Al_2O_3 thin films. **2nd Best Student Poster Presentation** in Jornadas CF-UM-UP 2019, Portugal 2019.

MOTIVATION AND MAIN OBJECTIVES

Global population is projected to reach 9.7 thousand million by 2050, an increase of 1.65 thousand million from 2023 [1]. The challenge of meeting the consequent rise in food demand is significant, requiring a food production raise of 70% (between 2005 and 2050), according to the Food and Agricultural Organization (FAO) of the United Nations [1]. This expansion in food supply must not only meet the growing quantity demanded by a larger global population, but also address the food safety and quality requirements.

Ochratoxin-A (OTA), a specific type of mycotoxin produced by certain molds, is increasingly recognized as a relevant food safety concern [2,3]. The widespread occurrence of OTA in both feed and food products [4,5], along with its potential carcinogenic and neurological effects [6–12], highlights its critical role in human health and food safety issues. OTA contamination has a ripple effect across the agricultural, food, and healthcare sectors, leading to substantial economic burdens and requiring comprehensive strategies for effective management and mitigation. OTA stands out as the sole mycotoxin known to contaminate wine [13], and its global contamination levels can reach as high as 43% [14]. This fact is particularly alarming, considering that the viticulture industry achieved a record global market value of €37.6 thousand million in 2022 [15]. Monitoring and controlling OTA levels in agricultural and food products, in accordance with international regulatory standards and screening methods [2,16,17], is paramount to ensure consumer safety and mitigate economic impacts.

To address the widespread issue of OTA contamination, it is essential to develop and implement highly sensitive technologies for early detection [18]. These advanced biosensing technologies must be capable of accurately quantifying extremely low levels of OTA throughout the entire food production and processing stages, from the initial agricultural phase to the final product reaching consumers. In this context, the integration of user-friendly, portable devices into the food supply chain represents a strategic approach to ensure real-time, fast, and continuous monitoring. The immediate detection of OTA can significantly enhance the effectiveness of control measures [19–21], allowing for quick decision-making and potentially preventing contaminated products from reaching consumers and entering the market. Consequently, there is an urgent need to devise cost-effective and efficient detection strategies that can effectively manage OTA contamination.

In this context, the Localized Surface Plasmon Resonance (LSPR) phenomenon is emerging as an advanced optical sensing strategy, enabling highly sensitive detection with outstanding limits of detection and dynamic ranges [22]. LSPR is an optical phenomenon resulting from a Surface Plasmon (SP) excitation, i.e., associated to coherent oscillations of free electrons excited by electromagnetic radiation

at the boundaries between a metal and a dielectric. SP excitation can be categorized into two classes: Surface Plasmon Polaritons (SPPs) and Localized Surface Plasmons (LSPs) [23,24]. SPPs are propagating surface electromagnetic waves coupled to the electron plasma of a metal at the dielectric interface [23–25]. In turn, LSPs are non-propagating excitations of the conduction band electrons, in subwavelength metallic nanostructures, coupled to the electromagnetic field [26–28]. In this case, the LSPs excitation occurs when the frequency of collective oscillation of the conduction band electrons of noble metal Nanoparticles (NPs) surface matches the frequency of incident light, generating a Localized Surface Plasmon Resonance (LSPR) band [25]. The LSPR band can be detected by a minimum on the optical transmittance spectrum, where the LSPR frequency corresponds to the maximum of light extinction (i.e., absorption + scattering) [29], also referred to as resonance wavelength. It depends on different factors, including the morphological features of the NPs (size, shape, distribution) and the surrounding dielectric environment where the NPs might be dispersed [26].

In biosensing applications, the LSPR phenomenon has been receiving more attention once it can provide label-free, portable, low-cost, and real-time monitoring of diverse analytes with high sensing ability [22]. The LSPR sensitivity is attributed to the evanescent nature of the LSP electric field, extending from the surface of the metallic NPs into the surrounding environment. The Plasmon field decays exponentially with the distance from the NPs, and its effective volume is typically limited to a length range from 10 to 30 nm [30,31]. For instance, a biological interaction on the NPs surface will induce refractive index (RI) variations in a sensing volume contained within the Plasmon decay length, resulting in an LSPR band shift [32].

In addition, the LSPR sensitivity, or LSPR response, [26,33] can be quantified by the well-known relation $\Delta\lambda = RIS\ (\Delta\eta)\ \left[1 - e^{\left(\frac{-d}{l_d}\right)}\right]$, where $\Delta\lambda$ is the LSPR response (usually resonance wavelength shift), RIS is the RI sensitivity to bulk changes, $\Delta\eta$ is the RI difference of the surrounding media when it changes from η_1 to η_2, d is the effective analyte layer thickness and l_d is the Plasmon decay length. However, when the change in RI surrounding the NPs is homogeneous ($d = \infty$), for instance, immersed in liquid and gas that do not adsorb at the surface, e.g., with specified RI value, the mathematical expression can simplified to $\Delta\lambda = RIS\ (\Delta\eta)$ [26]. As a result, the sensing performance is typically compared using RIS (nm/RIU) values.

To confer stability and robustness of an LSPR-based biosensor, metallic NPs (i.e., gold (Au) and silver (Ag)) can be dispersed in host matrices (namely titanium dioxide (TiO_2)), creating nanoplasmonic thin films [34]. These matrices enable tuning of the LSPR band by altering the surrounding RI and NPs

size distribution [35]. Nevertheless, a capping layer can potentially affect the sensitivity of the NPs, yet it can be eliminated by an erosion of the superficial oxide layers, diminishing the distance between the NPs and the analyte targets, as reported in [34,36]. For instance, nanoplasmonic Au-TiO_2 films were subjected to plasma etching processes and successfully immobilized an antibody (Ab) layer for molecule detection using label-free LSPR technique [34]. Therefore, LSPR-based biosensors, based on nanoplasmonic thin films, might be tailored to accommodate bioreceptor elements (antibodies, Ab) able to provide biochemical reactions with the analyte, leading to a variation of the RI surrounding dielectric environment.

LSPR-based biosensors represent a cutting-edge advancement in OTA detection, providing numerous advantages and differentiating factors over conventional methods (i.e., ELISA and HPLC). These biosensors excel in providing label-free detection, alongside their capacity for both qualitative and quantitative assessments with exceptional sensitivity. Among their notable attributes, the differentiating factors rely on rapid response times, the potential for miniaturization into user-friendly setups, and the requirement for only minimal sample and reagent volumes.

In line with this context, this thesis explores the development of LSPR-based biosensors specifically designed for OTA detection, using nanoplasmonic thin films as transduction platforms. This approach combines the innovative biosensing application of plasmonic phenomena with the pertinence of OTA detection.

To achieve the main goal, different objectives were outlined:

- Preparation of nanocomposite thin films manifesting plasmonic behaviour, composed of noble metal NPs (Au, Ag) dispersed in a dielectric host (TiO_2) matrix, using reactive DC magnetron sputtering deposition, followed by post-deposition treatments;
- Comprehensive and detailed analysis of the nanocomposite thin films, focusing on the influence of the structural and morphological features in the optical properties evolution;
- Evaluation of the developed nanoplasmonic thin films as LSPR transducers in biosensing applications, using a bioreceptor-analyte model;
- Optimization of immobilization design strategy: physisorption (adsorption) *versus* chemisorption (intermediate adhesion layer) in the development of an effective biorecognition interface;
- Optimization of the nanoplasmonic thin film sensitivity: influence of noble metal content (Au, Ag) and nanostructure on the plasmonic responses;
- Evaluation of LSPR-based biosensor for OTA detection, focusing on its sensitivity and efficiency in detecting OTA in both standard and spiked real food product (wine) samples.

INTRODUCTION TO THE THESIS OUTLINE

This thesis is divided into five main chapters that are independently published or submitted as full-length papers in international peer-reviewed journals. Additionally, this thesis also contains the introductory parts that include the main motivation, objectives, and thesis outline, as well as a final chapter of conclusions and future work.

Chapter 1 results from a Review Article, which was published in the journal "Critical Reviews in Food Science and Nutrition" (a Q1 journal in Web of Science (WoS), with an impact factor, IF = 10.2). This first chapter presents a comprehensive overview of the literature, outlining both the challenges in current OTA detection methods and the potential of cutting-edge biosensing nanotechnologies. Among the optical detection strategies described, the LSPR-based biosensing approach was distinguished as the most promising nanotechnology for OTA monitorization applications. Therefore, this chapter also explores new promising patented LSPR-based biosensing strategies specifically developed for OTA detection. The PhD candidate was responsible for conducting the literature review, analyzing, and synthesizing the research findings, which culminated in this chapter.

Chapter 2, resulting from a full-length publication in the journal "Nanomaterials" (a Q1 journal in WoS, IF = 5.3), explores a proof-of-concept for an LSPR-based biosensor, employing a nanoplasmonic Au-TiO_2 thin film as a robust and effective transducer platform. In this context, streptavidin and biotin were chosen as the model receptor–analyte. Streptavidin was immobilized on the plasma-activated of the Au-TiO_2 film's surface, targeting biotin as the analyte. The biochemical interaction was translated by measurable optical (LSPR) response and validated by a secondary detection approach, horseradish peroxidase (HRP) activity measurement, employing an enzyme-linked immunosorbent assay (ELISA). The PhD candidate contributed to the methodology, investigation, and writing process of the co-authored paper. Specifically, the candidate was mainly responsible for preparing the nanoplasmonic thin films and, also, for evaluating the LSPR's sensitivity response. This chapter plays a crucial role in establishing the foundation for the subsequent chapters, which further develop and optimize these LSPR biosensing platforms for OTA detection.

Chapter 3 corresponds to a full-length paper submitted to the journal "Journal of Physics D: Applied Physics" (a Q1 journal in WoS, IF = 3.4). This third chapter focuses on the optimization of the immobilization design strategy, a critical component in the development and performance of biosensors. Two predominant immobilization approaches were studied in order to achieve a functional and robust bioreceptor layer: i) adsorption (physisorption) and ii) cross-linker functionalization (chemisorption). Considering the chemisorption strategy, a DSP cross-linker (Lomant's reagent) was added to the Au-TiO_2

film's surface, assessing the influence of various factors (concentration and plasma activation) on adhesion layer development. Additionally, this chapter presents immunoassay experiments, designed to assess the functionality and adhesion strength of immobilized bioreceptors, specifically using anti-IgG-FITC and mouse IgG Ab interactions. This chapter is the result of the PhD candidate's comprehensive work including its conceptualization, methodology, formal analysis and writing.

Chapter 4 is the result of a full-length paper published in the journal "Sensors" (a Q2 journal in WoS, IF = 3.9). This fourth chapter focuses on the sensitivity enhancement of the LSPR-based biosensing transducer. Taking into account the main conclusions of previous chapters, this chapter became of paramount importance to find a thin film design with improved sensitivity to be able to deal with small expectable LSPR band shifts, which result from biochemical interactions occurring on immobilized molecules within the Plasmon decay length of the NPs. Hence, this fourth chapter emphasizes that the LSPR response can be tuned by the noble metal content, particularly by adding silver (Ag) to the initially tested Au-TiO_2 film to form bimetallic NPs with enhanced extinction efficiency and plasmonic response. Consequently, the sensitivity of nanoplasmonic thin films is shown to be improved through the optimization of the preparation conditions. Responsible for conceptualization and methodology, this PhD candidate conducted an in-depth investigation and formal analysis, resulting in the writing and publication of this scientific article with her authorship.

Chapter 5, submitted as full-length article to the journal "Sensors and Actuators B: Chemical" (a Q1 journal in WoS, IF = 8.4), represents the achievement of the main aim of this research, emphasizing a novel LSPR-based biosensor designed specifically for OTA detection. This LSPR-based biosensor incorporates a highly sensitive nanoplasmonic AuAg-TiO_2 thin film functionalized with anti-OTA Ab. When exposed to the target mycotoxin, the developed LSPR-based biosensor transduces the chemical interaction between the analyte (OTA) and the bioreceptor (anti-OTA Ab) into a measurable optical LSPR response, facilitating the detection of OTA over a wide range of concentrations, from ultra-low to the higher levels specified by food safety regulations. Chapter 5 further demonstrates the biosensor's applicability in real-world scenarios by analyzing deliberately contaminated real wine samples with OTA. This final chapter results from the PhD candidate's conceptual vision, rigorous methodology, comprehensive investigation, formal analysis, and writing composition.

Finally, in Chapter 6, the PhD candidate summarizes the Final Remarks and Conclusions, highlighting the main achievements, and describes future perspectives.

Chapter 1

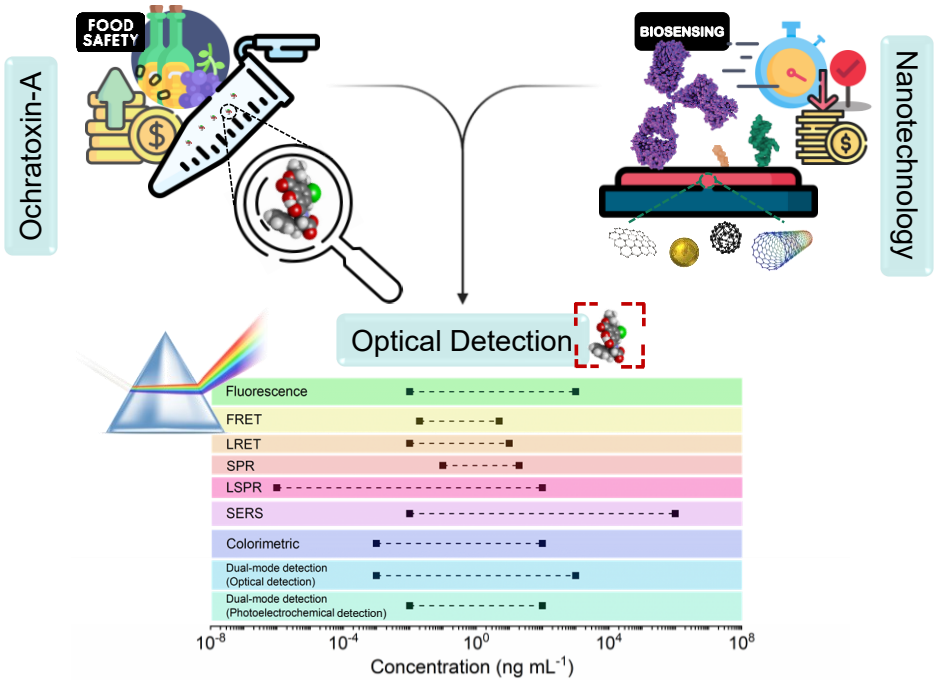
Recent Advances in Nanomaterial-based Optical Biosensors for Food Safety Applications: Ochratoxin-A Detection

D.I. Meira, A.I. Barbosa, J. Borges, R.L. Reis, V.M. Correlo, F. Vaz, Recent Advances in Nanomaterial-based Optical Biosensors for Food Safety Applications: Ochratoxin-A Detection, as Case Study, Critical Reviews in Food Science and Nutrition (2023) 1–43. https://doi.org/10.1080/10408398.2023.2168248.

1.1. Abstract

Global population growth tremendously impacts the global food industry, endangering food safety and quality. Mycotoxins, particularly Ochratoxin-A (OTA), emerge as a food chain production threat, since it is produced by fungus that contaminates different food species and products. Beyond this, OTA exhibits a possible human toxicological risk that can lead to carcinogenic and neurological diseases. A selective, sensitive, and reliable OTA biodetection approach is essential to ensure food safety. Current detection approaches rely on accurate and time-consuming laboratory techniques performed at the end of the food production process, or lateral-flow technologies that are rapid and on-site, but do not provide quantitative and precise OTA concentration measurements. Nanoengineered optical biosensors arise as an avant-garde solution, providing high sensing performance, and a fast and accurate OTA biodetection screening, which is attractive for the industrial market. This review core presents and discusses the recent advancements in optical OTA biosensing, considering engineered nanomaterials, optical transduction principle and biorecognition methodologies. Finally, the major challenges and future trends are discussed, and current patented OTA optical biosensors are emphasized for a particular promising detection method.

Keywords: Biosensing; Food industry; Food safety; Nanotechnology; Ochratoxin-A (OTA); Optical biosensors



1.2. Mycotoxins Introduction

1.2.1. Mycotoxins Importance in Farming Industry

The farming industry and agriculture products are an integral part of the primary sector, playing a significant role in the economy. However, its importance goes beyond mere economic aspects, being transversal to other sectors, such as socio-cultural and environmental. Furthermore, the exponential growth of the population worldwide and its consequent needs can positively impact the farming industry. The food's quality and conservation emerge as a current requirement since several natural factors (i.e., climate change and soil composition) and biological or chemical processes (i.e., pests, plants invasion, and chemical contamination) severely influence agriculture performance. Despite the introduction of good agricultural practices and innovation of production methods, fungi contamination persists as an agricultural challenge [37,38]. The illness risk in farm animals compromises their productivity, and any contamination in the food chain production causes an increase in product cost, consequently, the decrease in food market value. Therefore, food safety/quality control and monitoring costs may increase significantly [39–42]. A large-scale global survey in farming products identifies mycotoxins contamination as a possible cause of significant economic loss in the food industry [43,44].

Mycotoxins are secondary metabolites produced by several types of fungi genera, such as *Aspergillus*, *Penicillium*, *Fusarium*, and, with a minor scope, *Alternaria* and *Claviceps*. Numerous fungi species can produce more than one type of mycotoxin, and a specific mycotoxin can be produced by more than one fungus species. Mycotoxins present a low molecular weight (about 500 g mol^{-1}) and can cause biochemical, physiologic, and pathologic alterations in several species of animals, plants, and other microorganisms [41]. Although only 20 of more than 400 identified mycotoxins present a toxic trait, their molecular stability and the capability to survive food processing raise security concerns [45]. Mycotoxins are biologically dangerous; consequently, extended regulatory restrictions for each mycotoxin were established by several institutions: i) European Food Safety Authority (EFSA), ii) United States (US) Food and Drug Administration (FDA), iii) World Health Organization (WHO) and iv) Food Agriculture Organization (FAO). The acuteness of the toxic effect can be classified as chronic effect or acute toxicity with a severe illness, adequately described as mycotoxicosis (e.g., ergotism, aflatoxicosis, and alimentary toxic aleukia) [42,44].

1.2.2. Influence of the Agricultural Environment on Mycotoxins Appearance

The agricultural growing environments influence fungus development and the production of mycotoxins (i.e., temperature, relative humidity, rainfall, water activity, pH, soil composition, and texture),

atmospheric composition, and the presence of a competitive microflora, but also the cultivation technique and foodstuff conservation [46,47]. The plants are more susceptible to fungal invasion in periods of stress caused by the amount of water available, the presence of pests, and the absence of pesticide exposure. Therefore, it is expected that Climate Change will lead to new modified forms of mycotoxins, increasing the mycotoxins levels in farming products. The susceptibility of each flora species and their response to climate change define the mycological growth and the rate of mycotoxin production. Consequently, the contamination risk can increase toxic threats to the consumers [43].

Environmental and social-economic interactions play a major role in the dynamics between the fungi presence and mycotoxins contamination in food production and their delivery. The mycotoxigenic fungi can develop in the food product during the plant growth (i.e., crops, cereals, dried fruits, nuts, and spices), both before and/or after harvest, during poor and/or prolonged storage, under the optimal conditions for pathogenic development according to the fungus species [47]. Already in 1999, FAO reported that the plant pathogenic fungi contamination and, consequently, the presence of mycotoxins was the cause of 25% of the crop's contamination worldwide. However, Eskola et al. [38] reported that the occurrence of mycotoxins could be much more prominent in food samples, reaching 60 to 80%, depending on the mycotoxin type.

A large-scale global survey of mycotoxins contamination identifies regional differences in the occurrence of each toxic metabolite [5]. From 2008 to 2017, feed samples (e.g., maize, wheat, soybean, barley, and rice) were collected in 15 different geographic regions worldwide, and the prevalence and the results showed that 88% of the samples were at least contaminated with one mycotoxin and the co-occurrence of multi-mycotoxins achieved a total of 64% [5]. However, Global Warming is constantly affecting food security through climate variations, such as the increase of temperatures, alteration of precipitation patterns, and the regular occurrence of extreme meteorological events. Therefore, the relationship between plant growth and mycotoxin development can change from suppressive to beneficial conditions leading to their appearance in new regions worldwide. The climatic conditions of each geographic area influence the presence and type of mycotoxin developed during crop growth and storage. Considering the regional trends and climate, the Mediterranean countries present favorable environmental conditions for developing mycotoxins fungus in the agriculture field. The viniculture in the Mediterranean area presents an important role since more than 53% of the world wine production is concentrated in Southern Europe, according to the International Organization of Vine and Wine (OIV) [48]. Furthermore, considering the increased risk of mycological contamination and human consumption, Ochratoxin-A (OTA) is the only mycotoxin with established regulatory limits in wine [13]. Vitali Čepo et al.

[49] reported that 63% of commercial wines conventionally produced in the Balkan area tested positive for OTA presence. OTA presence can be frequent at lower concentrations, and their food consumption causes health harm. For instance, through a risk assessment study, Mousavi Khaneghah et al. [50] reported that OTA prevalence in cereal-based products (i.e., bread, cornflakes, breakfast cereals, and pasta) was significantly higher than in other mycotoxins. Beyond coffee and coffee-based products, the global prevalence of OTA was estimated to be 53%, but Southern Europe achieved higher values (Portugal 83%, e.g.) [51].

1.3. Ochratoxin-A Critical Issues: Food Safety, Standard Methods, and the Role of Biosensors

OTA is the most prevalent and toxic member of ochratoxins due to the chemical structure (i.e., chlorine atom in the substituent group of the molecule), exhibiting a Lethal Dose (LD_{50}) of about 1 mg kg^{-1} of body weight (bw) in pigs (no LD_{50} value was defined for humans yet) [2]. This mycotoxin is identified as potentially carcinogenic in humans (Figure 1.1) [6].

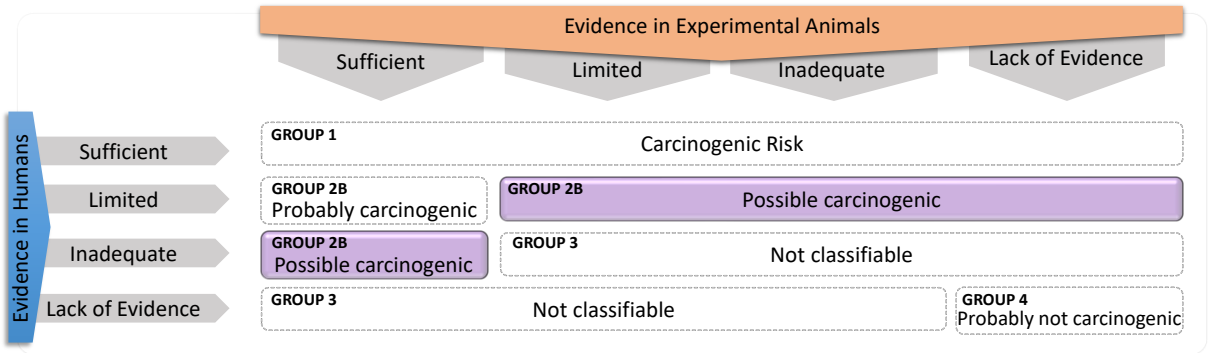


Figure 1.1. Scheme of the International Agency for Research on Cancer (IARC) monographs evaluation of carcinogenic hazard of mycotoxins, being highlighted the OTA evaluation.

OTA has a molecular weight of 403.8 g mol^{-1} [52]. This mycotoxin is a white compound, odorless, chemical, and thermally stable, presenting poor solubility in water and moderate solubility in polar organic solvents [53,54]. The physicochemical properties are defined by the amide bond between L-phenylalanine and the 7-carboxylic group of the dihydroisocoumarin moiety (Figure 1.2). However, due to its carboxylic group and phenolic hydroxyl group, the chemical structure can change to monoanionic (OTA^{-}) and dianionic (OTA^{2-}) forms, depending on the pH of the microenvironment [8,55]. Therefore, OTA is a weak organic acid, exhibiting a pK_a value of 4.3–4.4 (carboxyl group) and 7.0–7.3 (phenolic hydroxyl group)

[7]. After absorption of UV light, OTA exhibits green or blue fluorescence in acid and basic environments, respectively [52].

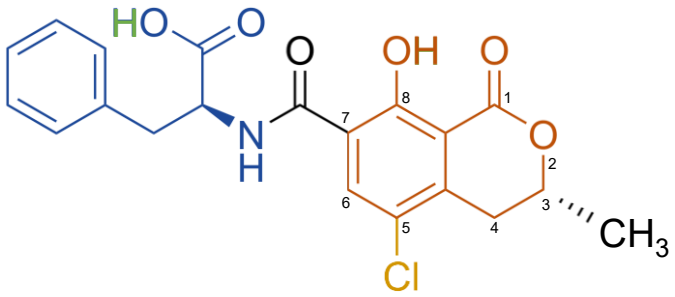


Figure 1.2. Chemical structure of OTA, IUPAC name N-{[(3R)-5-chloro-8-hydroxy-3-methyl-1-oxo-7-isochromanyl]carbonyl}-3-phenyl-l-alanine. The yellow part represents the chlorine substituent, blue is the phenylalanine part, orange is the dihydro-isocoumaring ring, and green are the acidic hydrogens. Adapted and reprinted with permission from Kőszegi and Poór (2016) [8]. Copyright 2016 MDPI, Basel, Switzerland.

First described in 1965, OTA is a secondary metabolite secreted by several genera of fungi. These fungal species can colonize several food groups and secondary food products, such as cereals [50], coffee [51] and cocoa beans [56], grapes [57], nuts [58], spices [59], animal-based foods [60], wine [61], beer [62], and juice [63]. OTA is a highly stable molecule capable of surviving the eradication of its host fungi. During food production, the mycotoxin tends to resist the numerous steps of the long process in secondary food elaboration or long-time storage under ambient conditions (e.g., prolonged storage, high temperature, and humidity) [55,64–66].

The ingestion of food contaminated by OTA can significantly affect human health, increasing the risk of cancer development. The toxicokinetic studies reveal that OTA intoxication occurs not only through a single intake with a high OTA concentration in the contaminated food product (i.e., acute ingestion dose) but also by the combination of several contaminated foodstuffs with lower OTA concentration during an extended period of time (i.e., chronic ingestion dose) [67]. In 2020, the Chemical Contaminants (CONTAM) panel of EFSA did not recognize that OTA is acutely toxic [2]. However, the synergistic effect caused by chronic dietary can potentiate the toxic effect [68]. There are also reported episodes of food poisoning through physical contact and inhalation [69,70]. The intoxication occurs through the gastrointestinal tract (i.e., stomach, and proximal portion of the jejunum), where the mycotoxin is rapidly absorbed and reaches the highest peak level in blood within a few hours.

The high affinity of nonionized OTA for plasma and serum proteins, particularly to the albumin protein (up to 99.98% in humans) [66], is one of its most specific pharmacokinetic properties [71]. After

5 days of ingestion, OTA is metabolized in two organs (i.e., liver and spleen), potentiating OTA bioaccumulation in the enterohepatic circulation [8]. This pharmacokinetic characteristic provides the persistent presence of OTA on the vascular circulation, inhibiting its elimination process, thus, increasing its half-life up to 35 days in humans after a single exposure [65,66]. Moreover, OTA can persist at the renal level up to 16 days, leading to a severe nephrotoxicity effect [72]. Beyond kidneys and liver, OTA can be present also in the intestine, brain, skeletal muscle, and fat tissue in less substantial concentrations [73].

In repeated exposure, the induced DNA lesions become irreversible, leading to persistent mutations, cell apoptosis, necrosis, and malignant tumors [7,8]. Even though OTA does not have a direct genotoxic effect, it can deeply induce oxidative stress potentiating the carcinogenic impact [9]. Moreover, reduction of the immune response, alterations in cellular proliferation response and cell signaling, genomic mutation, and inhibition of protein synthesis might cause carcinogenic characteristics [9]. Balkan Endemic Nephropathy (BEN) and Chronic Interstitial Nephropathy (CIN) diseases, characterized by tumors on renal and kidney organs, can be caused by OTA chronic exposure. Both renal chronic progressive diseases can lead to irreversible organ failure and potentially fatal outcome [74]. Furthermore, the genotoxicity and the epigenetic modulations caused by the activation of several biological mechanisms can lead to the progression of neurodegenerative diseases (i.e., Alzheimer's disease) [10].

1.3.1. Food Regulation and Conventional Detection

In order to ensure food safety, several worldwide food safety entities defined food control protocols for agriculture production, food processing, and the food market regarding OTA contamination [2,75–77]. In the European Union, the regulatory limits for OTA levels are extremely well defined based on the Scientific Panel on Contaminants in Food of EFSA. In 2020, the CONTAM panel of EFSA considered that chronic dietary exposure has carcinogenic consequences. However, the genotoxicity effect remains unclear [2]. Considering the neoplastic effect, both genotoxic and carcinogenic, the Benchmark Dose ($BMDL_{10}$) was established at 14.5 μg kg^{-1} bw per day, with a Margin of Exposure (MOE) below 10.000 times. The non-neoplastic effect only considers the carcinogenic risk. In this case, the limit established is a $BMDL_{10}$ of 4.73 μg kg^{-1} bw per day for MOE below 200 [2].

A highly sensitive analysis of mycotoxins, in particular OTA, requires an appropriate and certified detection ability, with accurate quantification, since its toxicity can be revealed at low-dose levels [78]. For OTA detection, several recommended analysis methods are defined by the Association of Official Analytical Collaboration (AOAC) International or standard practices described by the International

Standard Organization (ISO), and the European Committee for Standardization (CEN) [79]. Official procedures for sampling for analytical methods performance consider three important steps: 1) sampling, 2) extraction, and 3) clean-up [79,80]. In the chosen representative sample, previously homogenized, an extraction protocol is implemented to release the mycotoxin from the sample matrix, using a specific type of extraction solvent (e.g., organic solvents) and extraction methods (e.g., centrifugation and filtration) [79,80]. Following the extraction, a clean-up procedure is responsible for reducing the matrix effects and removing impurities in the sample extract, which can interfere with mycotoxin detection and thus affecting the detection performance (e.g., specificity, sensitivity, accuracy, and precision). The most used methods for mycotoxins clean-up are Solid-Phase Extraction (SPE) and Immunoaffinity Chromatography (IAC) [79,80].

Currently, the food analysis is performed at the final production process, being predominant the use of conventional techniques, such as different types of chromatography combined with various detectors: diode array, fluorescence, and UV, either as a single process or in dual-combination with other techniques [81–83]. The bioanalytical performance parameters of the standard detection methods are presented in Table 1.1, namely the respective optimal limit of detection (LOD) and limit of quantification (LOQ) (these analytical parameters are described in Table 1.2). The recommended protocol (AOAC 2001.01) for instrumental analysis and quantification is Immunoaffinity Columns (IAC) clean-up, followed by High-Performance Liquid Chromatography (HPLC) coupled with fluorescent detection for wine and beer [84]. These combined bioanalytical protocols appear reasonably accurate and reproducible in OTA detection, exhibiting a LOD value of 0.006 ng mL^{-1} for white wine and 0.010 ng mL^{-1} for rosé and red wines.

Table 1.1. Conventional detection methods for OTA.

Conventional detection methods	Limit of Detection (LOD)	Limit of Quantification (LOQ)	Dynamic Range	Tested Sample	Reference, Year
High-Performance Liquid Chromatography (HPLC) coupled with fluorescent detection	0.006 ng mL^{-1} 0.010 ng mL^{-1}	0.02 ng mL^{-1} 0.03 ng mL^{-1}	0.1 to 1 ng mL^{-1}	White Wine Red and rosé Wine	Var et al. 2007 [85]
Enzyme-Linked Immunosorbent Assay (ELISA)	0.00113 ng mL^{-1}	0.00341 ng mL^{-1}	0.01 to 100 ng mL^{-1}	Standard OTA buffer	Mukherjee et al. 2021 [86]
Thin Layer Chromatography (TLC)	0.2 ng mL^{-1}	0.8ng mL^{-1}	1 to 12 ng mL^{-1}	Wine	Teixeira et al. 2011 [87]
Gas Chromatography with Mass Spectroscopy (GC-MS)	0.1 ng mL^{-1}	1 ng mL^{-1}	0.2 to 10 ng mL^{-1}	Wine	Soleas et al. 2001 [88]
Liquid Chromatography with Mass Spectroscopy (LC-MS)	0.02 ng mL^{-1}	0.05 ng mL^{-1}	0.2 to 3.8 ng mL^{-1}	Wine	Andrade et al. 2017 [89]

Standard detection methods can be applied in several real samples, achieving interesting sensitivities. However, these traditional detection approaches reveal some limitations, such as i) pretreatment of sample, ii) time-consuming, iii) laborious sample cleaning and extraction processes, and iv) expensive laboratory equipment requiring well-trained technicians, which are not appropriate for on-site monitoring [90–92]. Additional challenges in identifying mycotoxins using analytical techniques fall into the presence of mycotoxins at ultra-low concentrations, the coexistence of numerous mycotoxins in the same food matrix, and their various chemical structures [78].

1.3.2. An Overview of Biosensing Nanotechnology

The high incidence of food contamination and the significant amount of analytical challenges conducted a research effort in the nanotechnology area to develop more advanced and efficient solutions [93–95]. Thus, advanced nanotechnologies can deliver a great effort to understand customer needs and application scenarios and benchmarking with the existing solution [96].

Nanomaterial-based biosensor can reveals as a detection alternative for food sample analysis offering outstanding bioanalytical capabilities and overcoming various limitations in conventional approaches [97,98]. Biosensors applied in the food industry are mostly used for two distinct categories,

i.e. food safety and food quality control [99]. The development of portable label-free devices, with real-time detection, has been creating interest in the food industry, since it opens the capability of on-site monitoring. For instance, optimal detection methods allow for recognizing contaminants (e.g., mycotoxins and pathogenic microorganisms) at all phases of food production [97]. A faster detection speed in a miniaturized lab-on-chip device for a cost-effective sample analysis is the main drive for developing a proper alternative nanotechnology for food safety monitoring.

The combination of novel nanomaterials enables the development of advanced biosensing approaches [100]. The small size of a nanomaterial (<100 nm) compels the atoms to be present or near the surface, providing exceptional intrinsic properties (e.g., optical, chemical, thermal, magnetic, and electronic), that contrast with their bulk counterparts. Thus, nanomaterials' inherent features and their biosensing application enhance the desired analytical parameters (i.e., specificity, selectivity, stability, and portability) [101]. Hence, the nanomaterial integration in biosensing technology has gradually become more relevant, with the most common nanomaterials used being gold nanoparticles (Au NPs), carbon NPs (CNPs), graphene, graphene-metal, metal oxide NP nanocomposites, and quantum dots (QDs) [102,103].

OTA biosensors aim to perform on-site analysis and provide rapid response time, cost-effective manufacturing, and reliability (i.e., accuracy and precision) [104]. OTA analysis techniques can be divided into two main approaches, namely i) rapid screening tests, and ii) confirmatory tests [105,106]. The first group focuses on qualitative detection (typically responding with a positive or negative result), and the second group provides a more accurate quantitative result.

The potential of an efficient biosensor is defined by several dynamic and static analytic characteristics of the sensing performance, as summarized in Table 1.2. Such analytical sensing parameters can be severely influenced by the detection method, the biosensor's composition, and its characteristics [107–109]. In addition, AOAC International defines the guidelines for standard method performance requirements for food sensing (see Table 1.2).

Table 1.2. Description of bioanalytical performance parameters and bioanalytical requirements.

Bioanalytical Performance Parameters	**Simplest description**
Limit of Blank (LOB)	Highest measurement result that is expected to be observed with a stated probability (typically at 95% certainty) for a blank sample [107]
Limit of detection (LOD)	Lowest analyte concentration that can be consistently detected with a stated probability (typically at 95% certainty) and distinguished from the limit of the blank [107]
Limit of quantification (LOQ) / Sensitivity	Lowest analyte concentration that can be quantitatively detected with stated accuracy and precision [107]
Linear dynamic range (LRD)	Interval between the upper and lower analyte concentrations that the detection signal is proportional to the analyte concentration [107]
Bioanalytical Requirements	**Simplest description**
Specificity	Ability to differentiate and quantify the desired analyte in an intended biological sample composed by potentially interfering substances [107]
Selectivity	Ability to differentiate and quantify all the desired analytes in an intended biological sample composed by potentially interfering substances [107]
Response Time	The duration between the exposure of the spiked sample or variation of the analyte concentration and the detection signal output at 90% of its final value
Accuracy	Closeness of analytical measurement with the actual target concentration of the analyte. This requirement is defined by the performance of at least five measurements per analyte concentration and three different analyte concentrations [107]
Precision	Closeness of analytical measurements series. This requirement can be divided into repeatability (i.e., closeness of agreement between 5 independent test results obtained under stipulated condition) and reproducibility (i.e., closeness of agreement between independent test results obtained under different conditions) [107,110]. The precision is determined through the relative standard deviation value (RSD).
Robustness	Ability to reproduce the analytical procedure, besides different circumstances or small deviations in the method parameters, with the reliable analytical measurements [110]
Recovery	Analyte extraction efficiency. Detection signal obtained from the amount of the analyte added to the biological matrix in comparison with the detection signal obtained for the actual concentration of the analyte in a solvent [107].
Storage Stability	Evaluation of biosensor's performance and properties after stored under defined conditions during a long period at time (at least 30 days) [107,109]

Biosensors can be classified according to their detection mode or immobilized biorecognition element [111]. Firstly, the detection mode of a biosensor can be defined by its transducer type: optical, electrochemical, thermal, and mass-based [112,113]. Regarding the biorecognition element approach, the mycotoxin sensing strategies focus on immunosensors or aptasensors, which rely on antibodies (Ab) or aptamers as biorecognition components; however, innovative molecularly imprinted polymers (MIPs) have also been applied as synthetic biorecognition elements. Regardless of the bioreceptor molecular structure, the biorecognition element is responsible for recognizing and associating a specific analyte [83,114]. The biological recognition event (transduction), considered by the biorecognition element and analyte interaction (and possible binding), generates a proportional signal, converted through the transducer and amplified to determine the analyte concentration [109].

1.3.3. Current Available On-Site Detection Approaches

The importance of mycotoxins detection in the food industry is unquestionable. The economic value of mycotoxin testing was evaluated at USD 1.23 billion in 2021. It is expected to reach USD 1.65 billion by 2026, with an expected annual growth rate of 6.1% [115]. Commercial detection kits emerge as a new alternative to mycotoxin detection, providing critical information about food safety products. Most sensitive and selective commercial tests are developed in an immunoassay format, that is, a specific bio-interaction between the immobilized biorecognition element (i.e., Ab) and the biological analyte aimed to detect [90]. Commonly, the commercial biochemical methods are the direct competitive ELISA and membrane-based immunoassays (i.e., Lateral Flow Immunoassay (LFIA) and Fluorescence Polarization Immunoassay (FPIA)). Commercial tests for mycotoxins detection are available through several industrial companies (e.g., BioSystems, Charm Sciences Inc., Cusabio Technology LLC, EnviroLogix, EuroProxima, Pribolab Pte.Ltd., Romer Labs, R-Biopharm, Vicam, Veratox, among others).

Currently, the most commercialized sensing approach relies on the LFIA biosensor, which provides optical (i.e., colorimetric) detection. Generally, the biodetection strategy occurs on a paper-based portable analytical device, with the most straightforward assay procedure, that can provide a fast qualitative detection and intuitive result (i.e., through visible variations of color in the biosensor's surface).

The LFIA detection approach is a unidirectional assay used to detect the presence (or absence) of the biological analyte in a potentially contaminated sample in an immunochromatographic strip available on a microfluidic paper-based analytical device. The immunoassay can appear in two formats, i) sandwich assay (two types of Ab are required) or ii) competitive assay (only one type of Ab is required). Mycotoxins cannot be labeled by two types of biorecognition Ab, because they do not possess multiple epitopes, so

competitive LFIA is the ideal approach [116]. Therefore, the development of a single detectable color (in C line) should be considered favorable for OTA's presence [117], assuming that chromogenic detection occurs when the concentration exceeds the determined threshold (i.e., LOD). The labels responsible for the color in the C and T lines are chosen accordingly with the test components' compatibility.

In qualitative immunoassays, the analysis occurs in a specific portable diagnostic device (i.e., dipstick or cassette format). For example, the LFIA device comprises a sample pad, a conjugate pad (including the T and C line), and an absorbent pad, as represented in Figure 1.3.

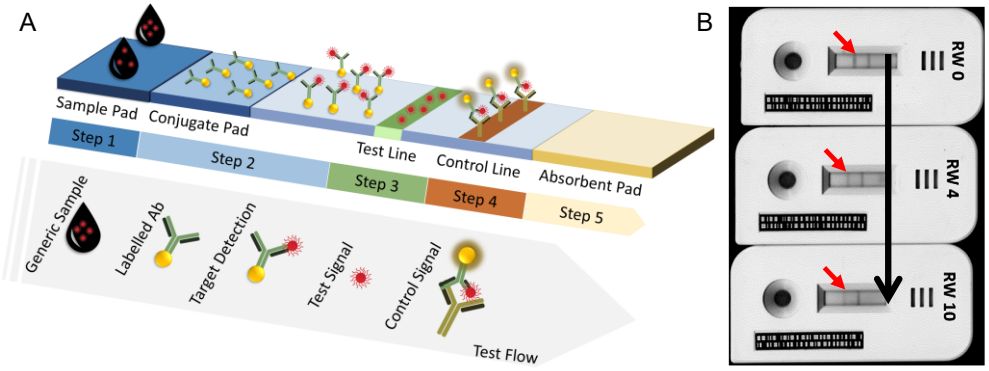


Figure 1.3. Schematic representation of the LFIA methodology at (a) and image of LFIA strip devices used for measuring OTA at different concentrations in spiked red wine in (b). Reprinted with permission from Anfossi et al. (2012) [118]. Copyright 2012 American Chemical Society.

The biochemical analysis begins with dropping a minimal amount of the test sample (liquid state) in the sample pad. After receiving the sample containing OTA, the sample travels in the conjugate pad through the capillary action at the nitrocellulose membrane (Figure 1.3a, Step 1). As an example, the conjugate pad area is characterized by the presence of Au NPs labeled with specific Ab for the targeting OTA. On the conjugate pad, the target antigen interacts with its corresponding specific labeled Au Ab, creating a bio-complex (i.e., OTA-Au-Ab_1 complex) (Figure 1.3a, Step 2). The OTA present in the sample will occupy the available Ab preventing the bio-interaction between the immobilized OTA and the specific labeled Au-Ab (Figure 1.3a, Step 3). The control signal is produced by matching a commonly labeled Ab with its partner (Ab_3 – Au-Ab_1 complex) (Figure 1.3a, Step 4). The T and C lines contain capture reagents to display the result [119]. In this case, the visual C line indicates the optimal performance of the sensing test and a positive test. In contrast, the presence of a visual signal from both T line and C line represents a negative result. The absorbent pad helps the sample flow and collects the excess at the end (Figure 1.3a, Step 5) [119]. After finishing the assay, all the contaminated material is destroyed or decontaminated by adding sodium hypochlorite solution (5 to 10% v/v). This sensing approach was

applied by Anfossi et al. [118] with different samples (i.e., white and red wine), and the presence of the T line disappeared as the OTA concentration increased, as demonstrated in Figure 1.3b.

However, this method presents several limitations: i) the inaccurate interpretation of the results caused by the membrane saturation, ii) the characteristics of the tested sample (e.g., reduced concentration of the analyte, viscosity, pretreatment/enrichment process, and matrix interference), iii) limits of shelf-life of the label material, iv) the high cutoff values, and v) naked eye discrimination, among others [90,120–122]. As mentioned previously, OTA has defined thresholds in food safety policy. Therefore, current food safety market necessity leads to the development of miniaturized cost-effective lab-on-chip devices for mycotoxin detection, providing highly sensitivity and selectivity (e.g., qualitative and/or quantitative analyses at an appropriate dynamic range), with faster detection modes.

1.4. Recent Advances in Optical Biosensors for Ochratoxin-A Detection

Optical biosensors are considered the most common nanotechnological alternative to conventional detection methods, providing high detection sensing' performance (i.e., fast detection analysis with high sensitivity and specificity), with low noise background and low detection limit, and potential for multiplexing. Beyond, label-free optical biosensors require a low volume of the sample for an on-site and real-time monitoring analysis [108,123,124]. This type of biosensors requires a transducer component to convert the interaction between the biorecognition elements and the biological analyte into a precise measurable optical signal (i.e., absorption, transmission, reflection, refraction, phase, amplitude, frequency, or light polarization) [113].

This review intends to analyze the recent advances in OTA optical biosensors, fabricated using different nanotechnologies, reported in the past two years (from 2020 to 2022), as illustrated in Figure 1.4. Beyond, the review aims to understand and discuss sensing nanotechnology strategies, that can overcome the existing gap in on-site food monitoring, contributing to a more efficient and cost-effective food safety guarantee. Also, it will analyze the currently published patents of a particular promising detection technology and will discuss the challenges and future directions of OTA optical biosensors.

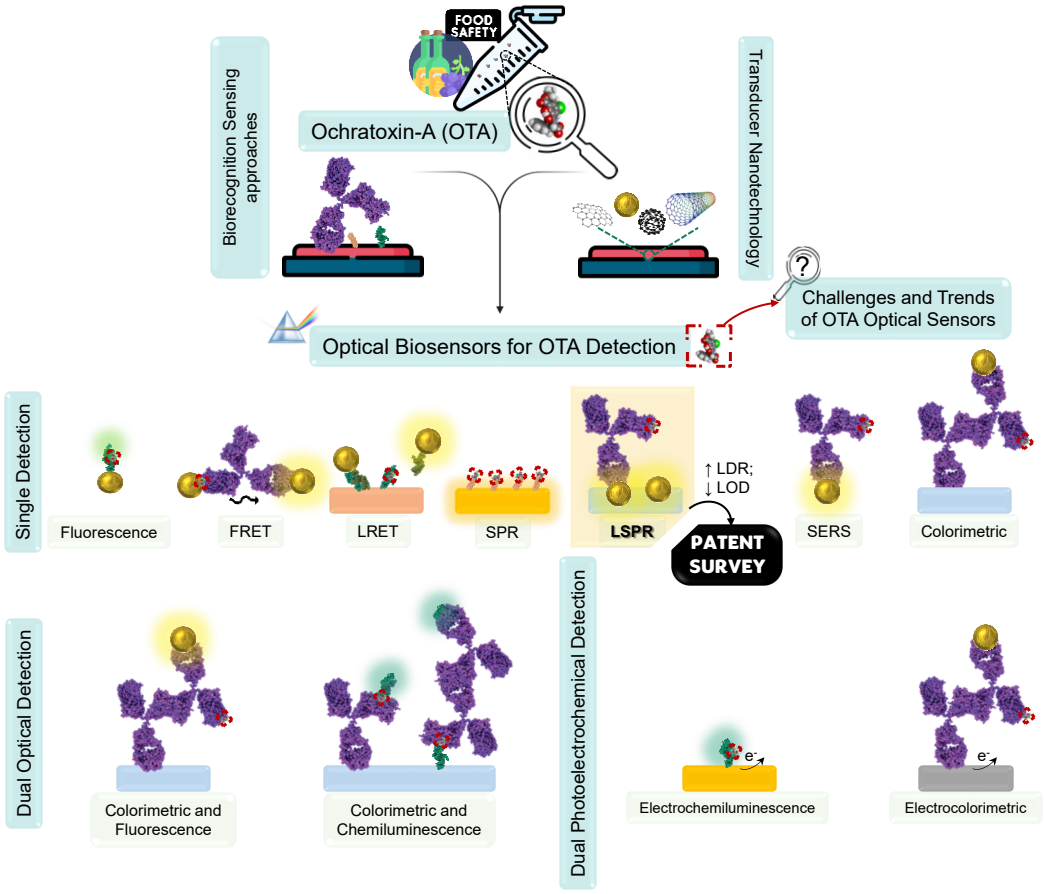


Figure 1.4. General scheme of the main topics addressed in this review, regarding the recent advances in OTA optical biosensor nanotechnologies.

As can be observed in Table 1.3, a diverse variety of biodetection strategies, engineered nanomaterials, optical sensing phenomenon, and biorecognition methods can be employed for OTA detection in real spiked food samples. The final performance of the biosensor can be evaluated through several bioanalytical parameters: limit of detection (LOD), limit of quantification (LOQ), linear dynamic range (LDR), accuracy (i.e., recovery range), and reproducibility (i.e., RSD). The affinity and selectivity of the various biosensors were tested through exposure to other interfering substances (e.g., mycotoxins, or similar chemical molecules). Moreover, the presented detection methods were compared with other conventional methods using real spiked food samples to prove their practicability and reliability.

Table 1.3. Overview of optical biosensors for OTA detection, highlighting their bioanalytical performance.

Optical Detection Method	Biorecognition Method	Transducer Matrix	Limit of Detection (LOD)	Limit of Quantification (LOQ)	Linear Dynamic Range (LDR)	Tested food sample	Recovery Range	Assay Precision	Reference, Year
Fluorescence	Anti-OTA-aptamer functionalization		0.247 pg mL^{-1}	N/R	10 pg mL^{-1} to 1 µg mL^{-1}	Wheat	88.02 to 104.03%		Hitabatuma et al. 2021 [125]
	Anti-OTA-aptamer functionalization	SWC NHs	2.3 ng mL^{-1}	N/R	5 to 500 ng mL^{-1}	Red wine	91.5 to 108.3%	3.3 to 5.6% (RSD)	Guo et al. 2021 [126]
	Anti-OTA Ab functionalization	MNPs	0.1 ng mL^{-1} (OTA Ab) 0.08 ng mL^{-1} ($F(ab')_2$ fragment)	N/R	0.1 to 2.5 ng mL^{-1} (OTA Ab) 0.1 to 7.5 ng mL^{-1} ($F(ab')_2$ fragment)	Milk	99.4 to 118.0% ($F(ab')_2$ fragment)	6.5 to 7.7% ($F(ab')_2$ fragment) (RSD)	Becheva et al. 2020 [127]
	Anti-OTA Ab functionalization	CuS NPs	0.01 ng mL^{-1}	N/R	0.1 to 100 ng mL^{-1}	Corn Soybean Coffee	93.89 to 109.96%	2.37 to 5.12%	Chen et al. 2021 [128]
	Self-assembled Zinc Porphyrin (SA-ZnTPyP)	ZnCdSe QDs	0.33 ng mL^{-1}	N/R	0.5 to 80 ng mL^{-1}	Coffee Milk	98.62 to 103.70%	1.44 to 4.99% (RSD)	Liu et al. 2020 [129]
	Anti-OTA-aptamer functionalization		0.1 ppb	N/R	0.5 to 50 ppb	Corn Olive oil Peanut Peanut oil Sesame Soybean oil	90 to 110%	5.9 to 9.2% (RSD)	Xiong et al. 2021 [130]

	Anti-OTA-aptamer functionalization	GO	1.48 ng mL^{-1}	N/R	1 to 500 ng mL^{-1}	Wine	91.75 to 103.56%		Wang et al. 2020 [131]
FRET	Anti-OTA-aptamer functionalization	CoOOH NSs	0.5 nM	N/R	1 to 140 nM	Corn Barley flour	95.4 to 101.0%	0.53 to 2.24% (RSD)	Bi et al. 2020 [132]
	Anti-OTA-Nb and Ab functionalization	ZnCdSe/ZnS QDs	5 pg mL^{-1} (Nb) 50 pg mL^{-1} (Ab)	N/R	0.005 to 1 ng mL^{-1} (Nb) 0.05 to 10 ng mL^{-1} (Ab)	Extract of Rice Barley Wheat Oats	80 to 109% (Nb)	4.5 to 9.0% (Nb) (RSD)	Tang et al. 2020 [133]
	Anti-OTA-aptamer functionalization	MoS_2 NSs bound to CDs and CdZnTe QDs	7.1 pg mL^{-1}	N/R	0.02 to 5 ng mL^{-1}	Peanut	96.7 to 107.0%	6.5 to 7.9% (RSD)	Qian et al. 2020 [134]
LRET	Anti-OTA-aptamer functionalization	$Zn_2GeO_4:Mn^{2+}$ NRs	3 pg mL^{-1}	N/R	0.01 to 10 ng mL^{-1}	Degassed beer	92.3% to 104.0%	2.7% (RSD)	Jiang et al. 2020 [135]
SPR	MIPs	Au coating	0.028 ng mL^{-1}	0.093 ng mL^{-1}	0.1 to 20 ng mL^{-1}	Dried fig	98 to 100%	1.75 to 2.46% (RSD)	Akgönüllü et al. 2021 [136]
LSPR	Anti-OTA Ab functionalization	Au NPs	0.001 pg mL^{-1}	N/R	10^{-9} to 10^{-1} µg mL^{-1}	Water White wine			Pereira et al. 2021 [137]
SERS	Anti-OTA-aptamer functionalization	Au@Ag NPs	5 pM	N/R	0.005 to 5 nM	Red wine	96.12 to 97.41%	0.94% (RSD)	Jing et al. 2020 [138]
	Anti-OTA Ab functionalization	MBs	0.61 pg mL^{-1}	N/R	1 to 1000 pg mL^{-1}	Red wine	90.6 to 103.0%	2.47 to 2.97% (RSD)	Ding et al. 2020 [139]

	Anti-OTA Ab functionalization	LFIA[a] device of AuNPs and Au@Ag NPs	15.7 pg mL^{-1}	N/R	0.027 to 6.7 ng mL^{-1}	Maize	78.9 to 106.2%	9.3 to 13.7% (CV)	Zhang et al. 2020 [140]
		Ag NPs	2.63 pg mL^{-1}	N/R	10^{-5} to 10^{3} µg mL^{-1}	Cocoa beans	98.58 to 108.44%	1.15 to 5.51% (CV)	Kutsanedzie et al. 2020 [141]
	Anti-OTA-aptamer functionalization	Au NRs@Ag	9.0 nM	N/R	50 to 20 000 nM	Grape juice	97.14 to 106.20%	8.3% (RSD)	Tian et al. 2020 [142]
	Anti-OTA Ab functionalization	Au NBPs	0.47 ng L^{-1}	N/R	1 ng L^{-1} to 5 µg L^{-1}	Millet	98.6 to 111.4%		Zhu et al. 2021 [143]
	Anti-OTA Ab functionalization	Hydrogel microsphere	0.77 ng L^{-1}	N/R	0.001 to 100 ng mL^{-1}	Corn	80.83 to 115.67%	6.02 to 6.52% (RSD)	Zhang et al. 2021 [144]
Colorimetric	Anti-OTA Ab functionalization	LFIA[a] device	20 pg mL^{-1}	320 pg mL^{-1}	10^{-1} to 10^{5} ng mL^{-1}	Beer Artificial urine Artificial Human serum	95 to 117%	<5% (RSD)	Suea-Ngam et al. 2020 [145]
	Anti-OTA- Ab functionalization	LFIA[a] device with Au nanospheres, nanocacti, nanoflowers, and hyperbranched Au plasmonic blackbodies	0.096 ng mL^{-1}	N/R	0.2 to 2 ng mL^{-1}	Corn	82.36 to 116.23%	10.39 to 12.98% (CV)	Wu et al. 2020 [146]
	Anti-OTA Ab functionalization	MGNH enhanced LFIA[a] device	0.094 ng mL^{-1}	N/R	0.098 to 12.50 ng mL^{-1}	Grape Juice	92.31 to 108.97 %	3.80 to 8.93 (CV)	L. Hao et al. 2021 [147]

Dual-mode detection (Optical)			Metal cations (Cu^{2+})	0.4 ng g^{-1}	1.2 ng g^{-1}	5 to 20 ng g^{-1}				Alizadeh et al. 2021 [148]
		Anti-OTA Ab functionalization	LFIA[a] device	1.27 ng mL^{-1}	N/R	0.5 to 16 ng mL^{-1}	Rice flour			Cheng et al. 2020 [149]
	Colorimetric Fluorescence	Anti-OTA Ab functionalization	CdSe/ZnS QDs in LFIA[a] device	2.5 ng mL^{-1} (Qualitative detection) 0.07 ng mL^{-1} (Quantitative detection)	N/R	0.05 to 10 ng mL^{-1}	Corn	94.29 to 104.62%	4.70 to 9.15% (CV)	Zhou et al. 2021 [150]
		Anti-OTA Ab functionalization	Cu_2O@$Fe(OH)_3$ NPs Au NRs CDs	0.83 ng L^{-1} (Colorimetric method) 0.56 ng L^{-1} (Ratiometric fluorescence method)	N/R	0.1 ng L^{-1} to 10 µg L^{-1} (Ratiometric fluorescence method)	Millet Lake water	94.7 to 107.8% (Colorimetric method) 94.5% to 112.3% (Ratiometric fluorescent method)		Zhu et al. 2021 [151]
	Colorimetric Chemiluminescence	Anti-OTA-aptamer functionalization in Co-ELASA[b] Anti-OTA Ab functionalization in CI-ELASA[c]	96 well plate	0.84 pg mL^{-1} (Co-ELASA) 1.29 pg mL^{-1} (CI-ELASA)	2.54 pg mL^{-1} (Co-ELASA) 3.94 pg mL^{-1} (CI-ELASA)	1 pg mL^{-1} to 1 µg mL^{-1}	Groundnut Coffee bean	50.21 to 113.37% (Co-ELASA) 90.47 to 107.72% (CI-ELASA)	———	Mukherjee et al. 2021 [86]
		Anti-OTA Ab functionalization	LFIA[a] device	0.3 µg L^{-1} (Wine)	N/R	≤ 25 µg L^{-1}	Wine Grape must		12% (Wine)	Zangheri et al. 2021 [152]

				0.1 μg L^{-1} (Instant coffee)			Instant coffee		7% (Instant coffee) (RSD)	
Dual-mode detection (Photoelectrochemical)	Chemiluminescence	Anti-OTA-aptamer functionalization	BPE	3 pg mL^{-1}	N/R	0.01 to 100 ng mL^{-1}	Rice Wheat seed Corn seed Sorghum seed Barley seed Buckwheat seed	75 to118%		Lu et al. 2021 [153]
	Colorimetric	Anti-OTA-aptamer functionalization	Paper-based analytical device Graphene-supported cobalt and nitrogen co-doped titanium dioxide (Co,N-TiO_2/3DGH) nanocomposite in ITO electrode	100 pg mL^{-1}	N/R	0.1 to 200 ng mL^{-1}	Corn	94.8 to 105.0%	2.96 to 4.1% (RSD)	Zhang et al. 2021 [154]
		Anti-OTA-aptamer functionalization		0.29 ng mL^{-1}	N/R	1 to 500 ng mL^{-1}	Corn juice	98.0 to 101.2%	2.33 to 3.36 % (RSD)	Hao et al. 2020 [155]

Table Legend: MIPs – Molecularly Imprinted Polymers; SWC NHs – Single-Walled Carbon Nanohorns; MNPs – Magnetic Nanoparticles; NPs – Nanoparticles; QDs – Quantum Dots; GO – Graphene Oxide; NSs – Nanosheets; CDs – Carbon Dots; NRs – Nanorods; MBs – Magnetic Beads; LFIA – Lateral Flow Immunoassay; NBPs – Nanobipyramids; MGNHs – Magneto-Gold Nanohybrids; Co-ELASA – Colorimetric based enzyme linked apta-sorbent assay; Cl-ELASA – Chemiluminescence based enzyme linked apta-sorbent assay; BPE – Gold-plated Bipolar Electrode; ITO – Indium Tin Oxide; Ab – Antibody; Nb – Nanobody; RSD – Relative Standard Deviation Value; CV – Coefficient of Variation; N/R – Not reported.

1.4.1. Single and Dual-Mode Optical Detection Method

1.4.1.1. Fluorescence

Fluorescence phenomenon is a photophysical radiative process that results from the transition of electrons from the lowest vibrational level of the first singlet excited state to the different vibrational levels of the ground state emitting photons [156]. The fluorescence phenomenon occurs in specific molecules named fluorochromes or dyes, and the conjugation of larger macromolecules with a fluorochrome is called fluorophore [156]. This optical sensing approach is one of the most developed in OTA detection, because it provides high sensitivity, stable signal, and fast detection response [116].

A fluorescence biosensor with a proper biorecognition layer to accurately detect OTA presence was developed by Hitabatuma et al. [125]. The authors developed a competitive fluorescence assay based on free-complementary DNA, and its working mode is represented in Figure 1.5a. The biosensor was composed by a molecular beacon (i.e., functionalized hairpin) labeled with a fluorophore (i.e., fluorescein) and a quencher (i.e., Dabcyl), and a specific DNA aptamer and its partial complementary strand (cDNA). The quencher had the ability to suppress the fluorescence effect on the biosensor (Figure 1.5a (1)). In the absence of the OTA, the biosensor did not exhibit fluorescence (Figure 1.5a (2)). However, in this presence, the DNA aptamer bounds preferentially to OTA, creating a DNA aptamer-OTA complex, leading to the release of cDNA. The presence of free cDNA forced the dissociation of a stem hybrid structure, triggering the emission of fluorescence (Figure 1.5a (3)). The fluorescence intensity was directly proportional to OTA concentration (Figure 1.5b,c). The LOD value was calculated as 0.247 pg mL^{-1} and the detection range as 10 pg mL^{-1} to 1 μg mL^{-1}. In the specificity assay, the biosensor was exposed to several mycotoxins, and only OTA induced a significant fluorescence signal. The fluorescent method was tested in real wheat spiked samples and achieved recovery values established between 88.02 and 104.03%, demonstrating the potential biosensing application.

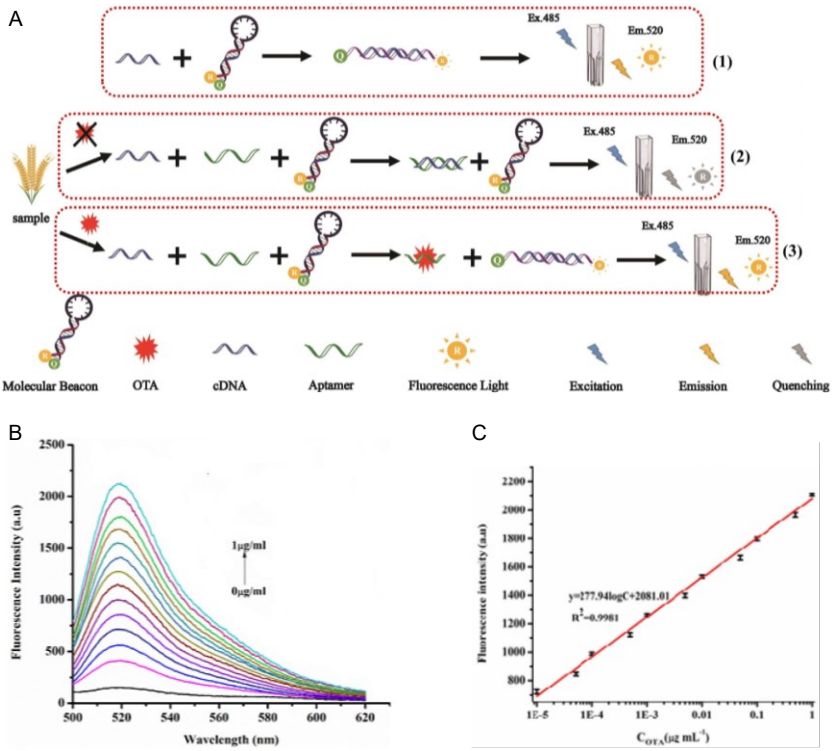


Figure 1.5. Schematic representation of the working mode of the competitive fluorescence assay based on free-complementary DNA at (a). The fluorescence intensity spectra at various concentrations of OTA at (b) and the linear relationship between the fluorescence intensity (520 nm) and OTA concentration among 10^{-5} and 1 μg mL^{-1} in (c). Reprinted with permission from Hitabatuma et al. [125]. Copyright 2021 Elsevier.

Guo et al. [126] reported a distinct fluorescence aptasensor for OTA detection. The biosensor is composed by aptamer linked to SYBR gold dye (i.e., DNA bounded to a fluorophore) and adsorbed onto single-walled carbon nanohorns (SWC NHs) used as a quencher, as demonstrated in Figure 1.6a. In the absence of OTA, the nanocomplex was adsorbed onto SWC NHs, exhibiting a weak fluorescence emission. However, in the presence of OTA, the aptamer changed its conformation and, consequently, was associated with SYBR gold dye, leading to a strong fluorescence emission. The fluorescence intensity was proportional to the OTA content until the saturation occurred at an established concentration, 1 μg mL^{-1} (Figure 1.6b,c). The LOD value was established at 2.3 ng mL^{-1}, and the sensing system covered a range of 5 to 500 ng mL^{-1}. The selectivity of the biosensor was tested through exposure to various OTA analogues (i.e., OTB, NAP, and Warfarin) and other mycotoxins (i.e., AFB1 and ZEN). The selectivity assay results showed that the sensing platform did not respond in the presence of other molecules, proving the biosensor's affinity and specificity. Spiked red wine samples allowed the evaluation of the recovery and the RSD of the aptasensor with a complex sample matrix. The recovery and RSD ranges were established from 91.5% to 108.3% and 3.3% to 5.6%, respectively.

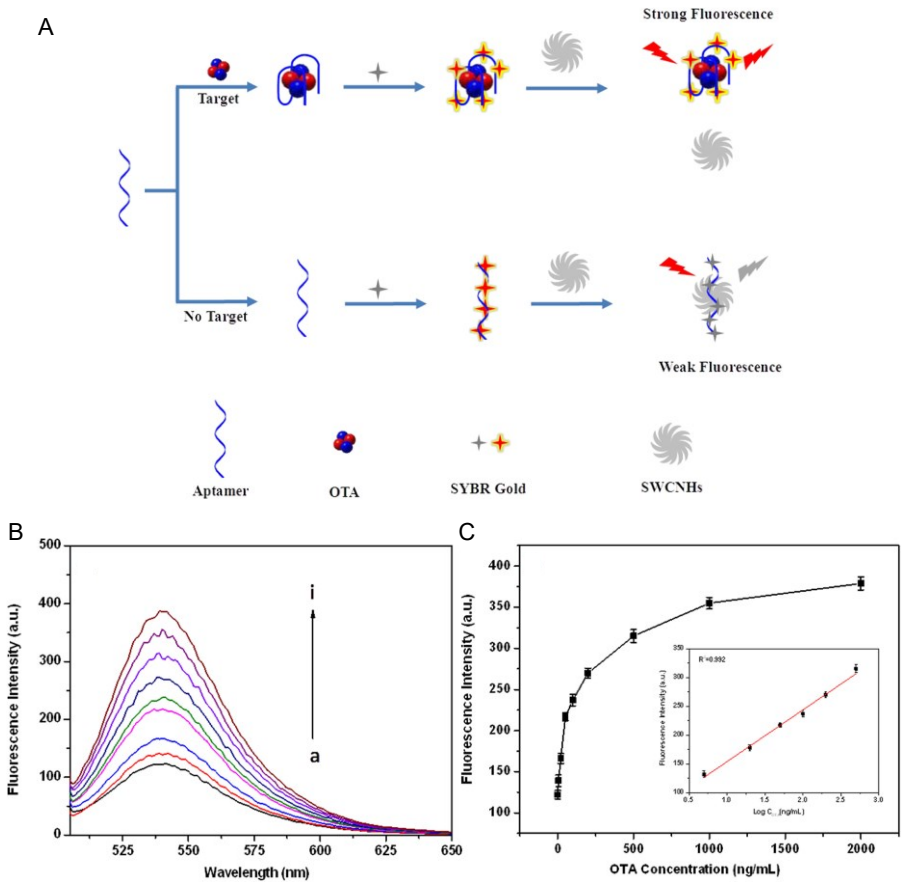


Figure 1.6. Schematic representation of the working mode of the label-free aptasensor for "turn-on" fluorescent detection at (a). The fluorescence intensity spectra at various concentrations of OTA at (b), and the fluorescence intensity (540 nm) plotted against OTA concentration; insert of the linear relationship between 0.5 and 3 ng mL^{-1} in (c). Reprinted with permission from Guo et al. [126]. Copyright 2021 Elsevier.

The development of a fluorescent immunosensor based on magnetic NPs (MNPs) for OTA detection was also developed by Becheva et al. [127]. A competitive immunosensor based on polyclonal Ab or F(ab')$_2$ fragment immobilization into MNPs was reported. Furthermore, a conjugate of OTA-OVA-FITC (OTA coupled to ovalbumin (OVA), and then conjugated FITC fluorochrome) was assembled. The competition between the aim OTA presented in the test sample and the OTA-OVA-FITC conjugate for binding in the antigen sites, previous immobilized on the surface of the MNPs, led to the release of a certain amount of OTA-OVA-FITC conjugate. In the supernatant, the OTA-OVA-FITC conjugate exhibited fluorescence. In the case of polyclonal Ab, the LOD value was established at 0.1 ng mL^{-1} and a linear detection range between 0.1 to 2.5 ng mL^{-1}. In turn, when F(ab')$_2$ fragment was used as the biorecognition element, the established LOD value was 0.08 ng mL^{-1}, and the linear detection range was 0.1 to 7.5 ng mL^{-1}.

Chen et al. [128] also developed a fluorescent immunoassay using metallic NPs (i.e., copper monosulfide (CuS NPs)), as demonstrated in Figure 1.7a. The biosensor was composed by an OTA's

antigen platform. The aim OTA was associated to the Ab-conjugated CuS NPs and added to the biosensor platform. The biosensor approach was based on the interaction of OTA-Ab-conjugated CuS NPs with the OTA's antigen presented on the biosensor's surface. From this interaction, a fluorescence emission peak was recorded. The intensity of the fluorescent emission peak was inversely proportional to the OTA concentration, as shown in Figure 1.7b. Through the linear relationship between the fluorescence intensity and OTA concentration, the LOD value was calculated as 0.01 ng mL^{-1}, and the detection range was limited between 0.1 and 100 ng mL^{-1}. The ultrasensitive platform was able to detect the presence of three concentrations of OTA (0.5, 5, and 50 ng mL^{-1}) in corn, soybean, and coffee samples with a recovery range between 93.89 to 109.96%, as demonstrated in Figure 1.7c.

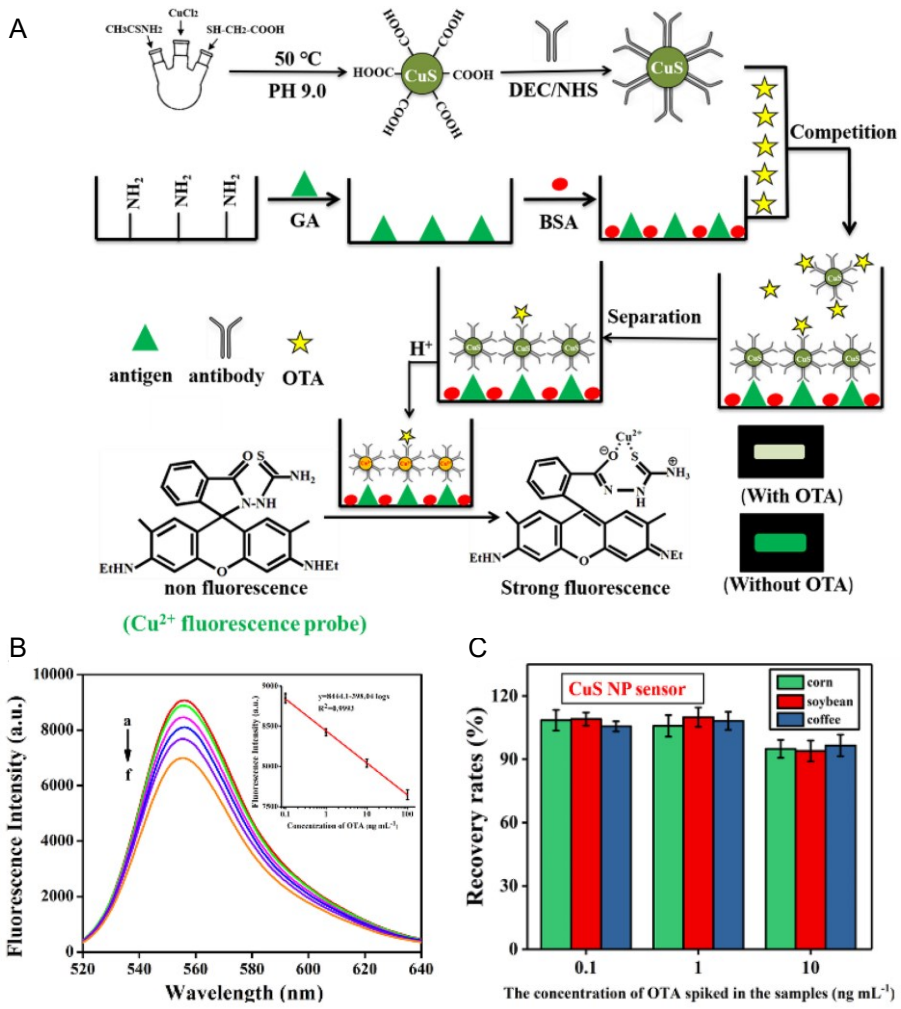


Figure 1.7. Schematic representation of the fabrication and working mode of fluorescent CuS NPs used in the detection assay at (a). The fluorescence intensity spectra at various concentrations of OTA; insert of the linear relationship between the fluorescence intensity (554 nm) and OTA concentration among 0.1 and 100 ng mL^{-1} at (b). Recovery rates of OTA in several samples (i.e., spiked corn, soybean, and coffee) in (c). Reprinted with permission from Chen et al. [128]. Copyright 2021 Elsevier.

QDs can be applied to develop new approaches in fluorescent biosensing detection. QDs are semiconductor nanocrystals with favorable fluorescent characteristics: i) high photostability, ii) size-adjustable spectrum, iii) wide excitation spectrum, iv) easy modification, and v) significant surface area-to-volume ratio. For example, the "turn off-on" fluorescent sensor based on the ZnCdSe QDs was developed by Liu et al. [129]. The performance of the fluorescent sensor is based on the interaction between the biological analyte and the self-assembled zinc porphyrin (SA-ZnTPyP), leading to the emission of fluorescence by ZnCdSe QDs, as represented in Figure 1.8a. The fluorescence spectra of the ZnCdSe QDs, named as "on", and the nanocomplex composed by ZnCdSe QDs linked to SA-ZnTPyP, named as "off", are represented in Figure 1.8b,c, respectively. The SA-ZnTPyP worked as a quencher molecule in the biosensing detection method. The interaction between the OTA and the SA-ZnTPyP molecule led to a significant fluorescence signal change of distanced ZnCdSe QDs, becoming more evident as the OTA concentration increases, as represented in Figure 1.8d. In 5 minutes, the biosensor detected OTA in real spiked samples (i.e., milk and coffee), reaching a LOD value of 0.33 ng mL^{-1} in a wide detection range of 0.5 to 80 ng mL^{-1}.

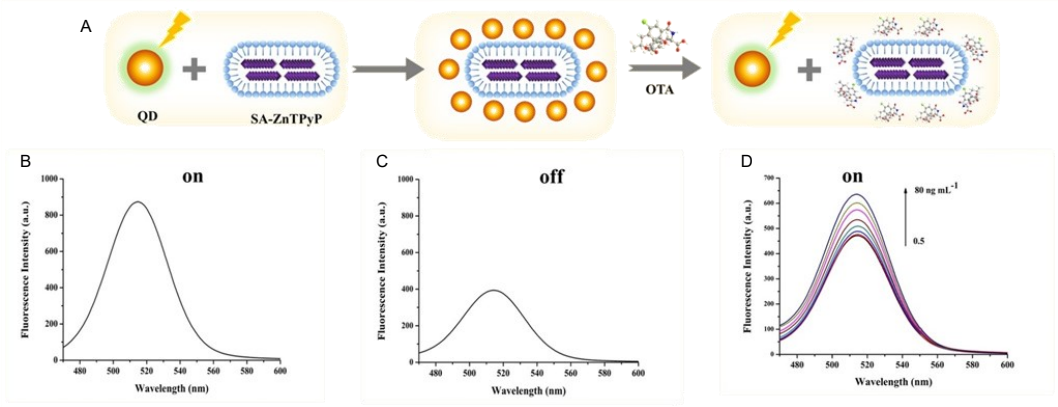


Figure 1.8. Schematic representation of the working mode of the "turn off-on" fluorescent sensor for OTA detection in (a). The fluorescence intensity spectra of the ZnCdSe QDs, named as "on", at (b), and the nanocomplex composed by ZnCdSe QDs linked to SA-ZnTPyP, named as "off", in (c). The fluorescence intensity spectra at various concentrations of OTA in (d). Reprinted with permission from Liu et al. [129]. Copyright 2020 Elsevier.

The "turn off-on" fluorescent sensor can be applied as a multi-mycotoxin detection, as reported by Xiong et al. [130]. Dual tweezers nanomachine was developed to detect OTA and another mycotoxin (i.e., AFB1) simultaneously. The turn "off" of the stable sensing platform presented a DNA tweezers configuration linked to fluorophores (i.e., FAM and Cy5) and quenchers. In OTA presence, the bio-interaction between the aimed target and its specific aptamer, DNA tweezers configuration changes. This

phenomenon causes an increasing distance of the specific fluorophore-quencher complex and, consequently, the fluorescence emission, as demonstrated in Figure 1.9a. The sensitivity of the fluorescence aptasensor was tested at different concentrations for both targets, and the fluorescence intensity increased according to the target concentration (Figure 1.9b). The linear relationship was established between the fluorescence intensity for OTA concentration (Figure 1.9c), allowing the LOD value determination of 0.1 ppb. The specificity of the aptasensor was tested by exposing it to other OTA analogues and, also, to OTA mixture with various mycotoxins, achieving promising results. Finally, the accuracy and precision of the biosensor were evaluated through exposure to several spiked samples (i.e., corn, olive oil, peanut, peanut oil, sesame, and soybean oil), achieving recovery values between 90 to 110% and an RSD of 5.9 to 9.2%.

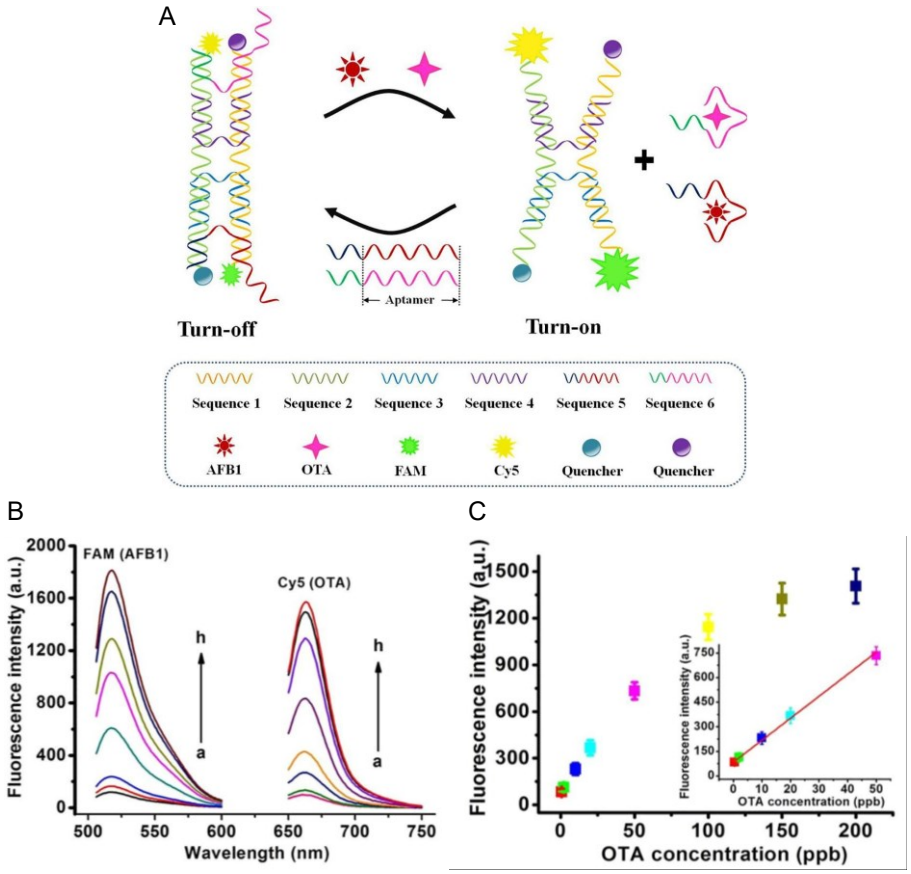


Figure 1.9. Schematic representation of working mode of dual DNA tweezers nanomachine for OTA detection at (a). Fluorescence intensity spectra of the dual DNA tweezers nanomachine at various concentrations of OTA and another mycotoxin at (b), and the fluorescence intensity at a defined wavelength plotted against OTA concentration; insert of the linear relationship between 0.5 and 50 ppb in (c). Reprinted with permission from Xiong et al. [130]. Copyright 2021 Elsevier.

The application of graphene, a material with a single-layer atomic surface, is a susceptible technology for biosensing since the surface plasmon polariton properties provide higher sensitivity to variations in the refractive index (RI) surroundings. Wang, Yang, and Wu [131] used graphene oxide (GO) to develop a steganographic aptasensor to detect OTA and another mycotoxin (i.e., ZEN) simultaneously. The biosensing method was based on the biosensor's selective absorption and fluorescence quenching capabilities. Wine samples were spiked, and the sensor detected the presence of OTA with a LOD value of 1.48 ng mL^{-1} and established recovery values ranging between 91.75 to 103.56%.

1.4.1.2. Förster Resonance Energy Transfer (FRET)

Another promising tool for developing optical biosensing methods is the Förster Resonance Energy Transfer (FRET) phenomenon. This non-radiative process is based on the transmission of photoexcitation energy from an excited fluorophore (the "donor") to a nearby quencher molecule (the "acceptor"). FRET can also be named by Fluorescence Resonance Energy Transfer when both "donor" and "acceptor" are fluorescent. For instance, one of the main requirements for the FRET phenomenon to occur is the proximity between the "donor" and the "acceptor", allowing the transference of energy between them, instead of being dissipated in the surrounding medium. Another essential requirement is the overlap of the acceptor excitation and the donor emission spectra [157].

FRET-based aptasensor for OTA detection was reported by Bi et al. [132], as depicted in Figure 1.10a. The detection method of the fluorescence aptasensor was based on the quenching phenomenon of cobalt oxyhydroxide nanosheets (CoOOH NSs). The biosensor was composed of "donor-acceptor" pair of graphitic carbon nitride QDs (g-CN QDs) linked to the aptamer and CoOOH NSs. The presence of OTA influenced the FRET process between the "donor-acceptor" pair. The fluorescence emission intensity of g-CNQDs-apt increased according to OTA concentration, as shown in Figure 1.10b. The LOD value of the biosensor was measured as being 0.5 nM. The exposure of spiked corn and barley flour samples achieved RSD values under 2.24%, with recovery values from 95.4% to 101%. The specificity of the biosensor was tested with other compounds (i.e., OTA analogues and other mycotoxins) and their mixture containing OTA (Figure 1.10c). In the presence of OTA, the results showed that the fluorescence recovery of the g-CNQDs-apt was reliable, with the results obtained when the OTA content was pure, indicating excellent selectivity.

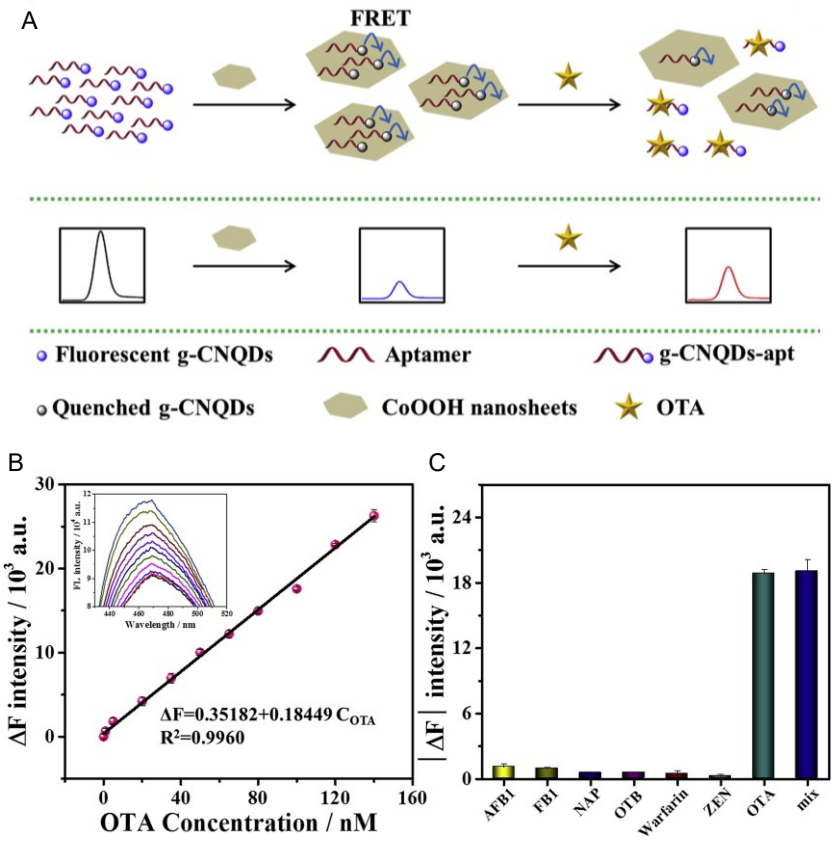


Figure 1.10. Schematic representation of working mode of FRET-based aptasensor for OTA detection at (a), and the linear relationship of the recovered fluorescence intensity (ΔF at 469 nm) plotted against OTA concentration between 0 and 160 nM; insert of fluorescence intensity spectra at the various concentrations of OTA at (b). Selectivity evaluation using mycotoxins or similar chemical molecules at (c) Reprinted with permission from Bi et al. [132]. Copyright 2020 Elsevier.

In another study, Tang et al. [133] proposed the development of a FRET immunosensor based on modified ZnCdSe/ZnS QDs. The biorecognition strategy varied from the nanobody (Nb) and monoclonal Ab (mAb) immobilization. However, the most promising results were achieved in Nb immobilization, due to the extremely small size that provides a more suitable sensitive FRET-based immunoassay. The effective distance between the "donor" (OTA-GQDs-10) and the "acceptor" (Nb-RQDs-5) was a crucial parameter to enhance the energy transfer efficiency and improve the detection limit of the biosensor, as demonstrated in Figure 1.11a. The competitive binding between both elements reduced the FRET efficiency and, consequently, the fluorescence intensity decreased, as shown in Figure 1.11b. Regarding the Nb immobilization approach, the LOD value achieved was 5 pg mL^{-1} with a detection range established between 0.005 to 1 ng mL^{-1}, as shown in Figure 1.11b (square). Under the same experimental conditions, the mAb-FRET immunosensor exhibited a LOD value of 50 pg mL^{-1} with a detection range established between 0.05 to 10 ng mL^{-1}, as shown in Figure 1.11b (circle).

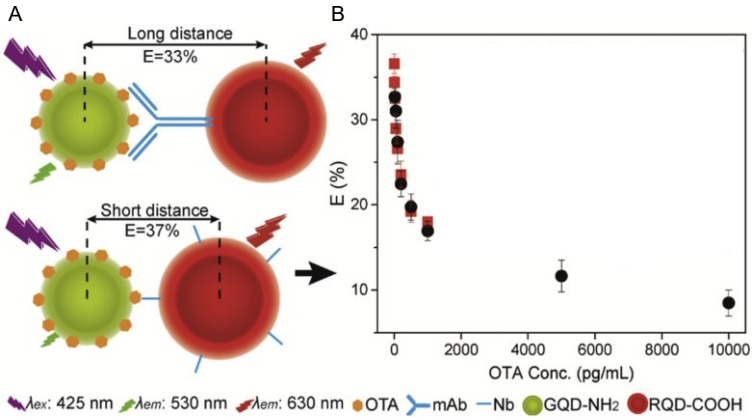


Figure 1.11. Schematic representation of working mode of FRET-based immunosensor using Nb and mAb immobilization for OTA detection at (a) and the energy transfer efficiency plotted against OTA concentration, between 0.005 and 10,000 pg mL^{-1}, being the Nb biodetection approach represented by the square symbol and the mAb symbolized by the circle, at (B). Reprinted with permission from Tang et al. [133]. Copyright 2020 Elsevier.

A bi-color FRET effect between a single nano-acceptor (MoS_2 NS), and two different nano-donors (carbon dots (CDs) and CdZnTe QDs) was developed by Qian et al. [134], as demonstrated in Figure 1.12a. The CDs and CdZnTe QDs were functionalized with two specific aptamers for AFB1 and OTA detection, respectively, and their representative fluorescence spectra are exhibited in Figure 1.12b. The spectra overlap between the absorption spectrum of MoS_2 NSs and the "donors" emission spectra allowed the simultaneous mycotoxin detection, as shown in Figure 1.12c. The bio-interaction of both mycotoxins and their respective aptamer led to the release of the complex CDs-ap1t-AFB1 and CdZnTe QDs-apt2-OTA from the surface of the MoS_2 NS and, consequently, signal variations in the Fourier Transform Infrared (FTIR) spectra were detected. The increasing mycotoxin concentrations also caused an increase in the normalized fluorescence intensity of the biosensor, as shown in Figure 1.12d. Regarding OTA mycotoxin, the detection range was established between 0.02 to 5 ng mL^{-1}, and the LOD value was calculated as 7.1 pg mL^{-1}. Spiked peanut samples were tested, and the recovery of the biosensor was obtained between a range of 96.7 to 107.0%, with an RSD value below 7.8%.

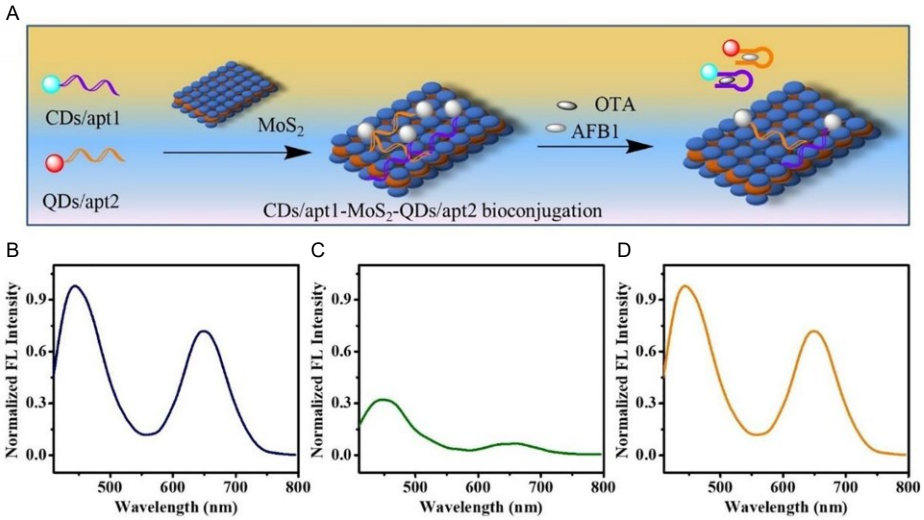


Figure 1.12. Schematic representation of fabrication and working mode of the FRET aptasensor for OTA detection in (a). Representative normalized fluorescence spectra of the mixture of CDs/apt1 and QDs/apt2 (b), CDs/apt1-MoS_2-QDs/apt2 bioconjugations before (c) and after (d) incubation with AFB1 and OTA. Reprinted with permission from Qian et al. [134]. Copyright 2020 Elsevier.

1.4.1.3. Luminescence Resonance Energy Transfer (LRET)

The OTA detection based on persistent Luminescence Resonance Energy Transfer (LRET) phenomenon was reported by Jiang et al. [135]. This photophysical radiative process is a derivative of the FRET technique. This phenomenon relies on the transference of energy between two nearby fluorophores when the emission spectrum of the "donor" luminophore overlaps the absorption spectrum of the "acceptor" fluorophore [158]. Thus, the optical biosensing detection is based on the persistent luminescence NPs (PLNPs) that store excitation energy and emit long-lasting luminescence.

An LRET-aptasensor for OTA detection was developed, using a "donor" complex, OTA aptamer immobilized in a persistent luminescence nanorod (Zn_2GeO_4:Mn^{2+} PLNR-Apt), and an "acceptor" complex, a cDNA linked to Au NPs. In the presence of OTA content, the aim target competed with the Au NPs-cDNA to bound at the PLNR-Apt. The Au NPs were released from the complex, causing the persistent emission of the luminescence by PLNR-Apt, as shown in Figure 1.13a. The aptasensor presented a dynamic performance of luminescence signal when exposed to OTA, as demonstrated in Figure 1.13b. Through the linear relationship between the recovered PLNR and the OTA concentration, the LOD value was calculated to be 3 pg mL^{-1} with an RSD value of 2.7% (Figure 1.13c). The feasibility of the biosensor was tested with real spiked beer samples achieving recovery values between 92.3 to 104%.

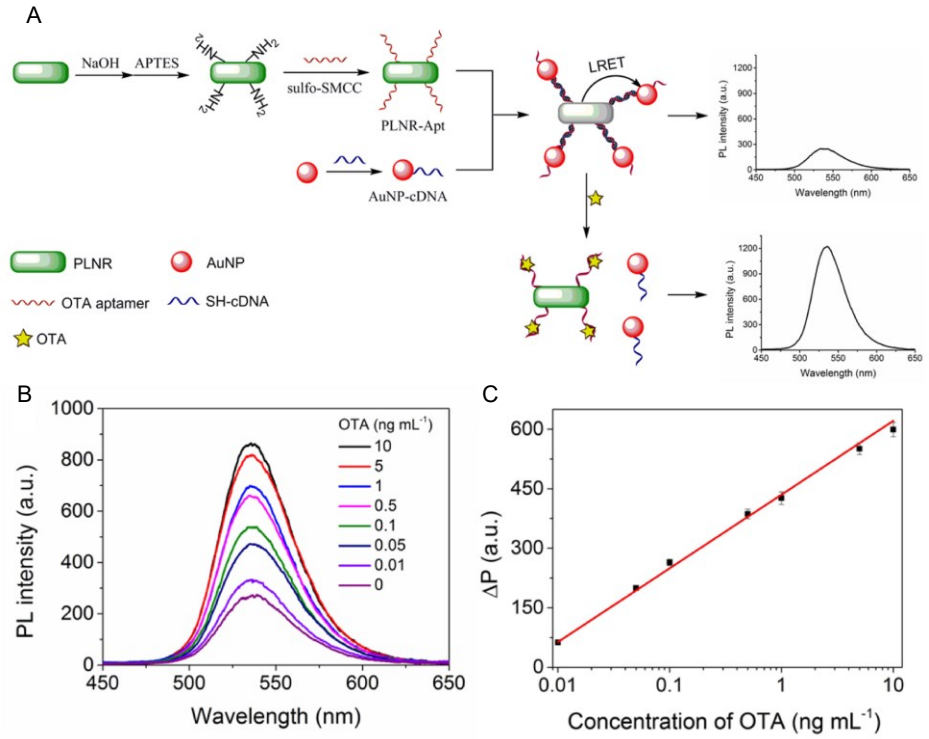


Figure 1.13. Schematic representation of fabrication and working mode of the LRET aptasensor for OTA detection in (a). Persistent luminescence (PL) intensity at different OTA concentrations in (b) and the linear relationship between the recovered PL (ΔP) and OTA concentration among 0.01 and 10 ng mL⁻¹ in (c). Reprinted with permission from Jiang et al. [135]. Copyright 2020 Elsevier.

1.4.1.4. Surface Plasmon Resonance (SPR) and Localized Surface Plasmon Resonance (LSPR)

Optical biosensors based on Surface Plasmons (SPs) appear as an emerging detection method among traditional signal-transduction mechanisms, since they present several interesting sensing characteristics. The resonance between collective oscillations of the surface conduction electrons in a metal and an incident electromagnetic field is defined as a plasmonic effect. The plasmonic effect can occur on a continuous metallic surface. In this case, the light-matter interaction propagates along the metal-dielectric interface, leading to the well-known Surface Plasmon Resonance (SPR) phenomenon [159]. Besides the SPR effect, Localized Surface Plasmon Resonance (LSPR) is characterized by the occurrence of the plasmonic effect in confined metallic nanostructures or NPs. SPR and LSPR-based sensors detect RI changes in the dielectric surroundings at different plasmon decay lengths, generating a detectable wavelength shift or signal intensity of the plasmonic band [159]. Therefore, changes in the excitation of plasmons can suggest molecular adsorption of small molecules, ligand-receptor binding, protein adsorption, and nucleic acid hybridization, among others [160].

The application of the SPR phenomenon can be a new biotechnology sensing approach [161]. A label-free and selective SPR-based sensor was developed by Akgönüllü, Armutcu, and Denizli [136] to detect OTA. The SPR (Au) biosensor chip was immobilized with a specific MIPs capable of interacting with target OTA molecules. The biosensor performance was divided into several steps: 1) incubation of equilibration buffer, 2) addition of OTA solutions, and 3) desorption of OTA through the addition of cleaning solutions. The interaction between OTA and the polymer surface changed the RI of their surroundings, and, consequently, the resonance angle drifted in refractivity spectra. Several samples (i.e., aqueous solutions, and dried fig) were used for real-time detection. The relationship between the OTA concentration and the reflectivity is proportional. The LOD and LOQ values were calculated at 0.028 and 0.093 ng mL^{-1} in a linear dynamic range established between 0.1 ng mL^{-1} and 20 ng mL^{-1}. Real samples (i.e., dried fig) were spiked with several concentrations, and the results confirmed the SPR sensor accuracy with a recovery range between 98 and 100% and an RSD of 1.75 to 2.46%.

An immunosensor, taking advantage of the LSPR phenomenon, for OTA detection was developed by Pereira et al. [137]. The OTA immunosensor was based on the physical adsorption of the OTA Ab on the surface of colloidal Au NPs. The detection approach was based on detectable variations in the absorption intensity of the LSPR band. The colloidal suspension showed an intense extinction of light at 520 nm. However, the addition of the OTA mAb led to variations of the RI of the surrounding media, causing a maximum extinction shift to 528 nm, as demonstrated in Figure 1.14a,b. In the presence of OTA content in white wine, the bio-reaction between the OTA and the immobilized Ab caused a linear decrease in the absorption intensity of the LSPR band at 528 nm, as shown in Figure 1.14c. The bioanalytical performance parameters were tested in real spiked samples (i.e., water, and wine), and the LSPR nanosensor revealed a final optical response within a minute. Through the linear relationship between the absorption intensity at 528 nm and the OTA concentration (Figure 1.14d), the LOD value was calculated at 0.001 pg mL^{-1} with correlation coefficients of 0.99. The linear dynamic range was established between 10^{-9} to 10^{-1} µg mL^{-1}.

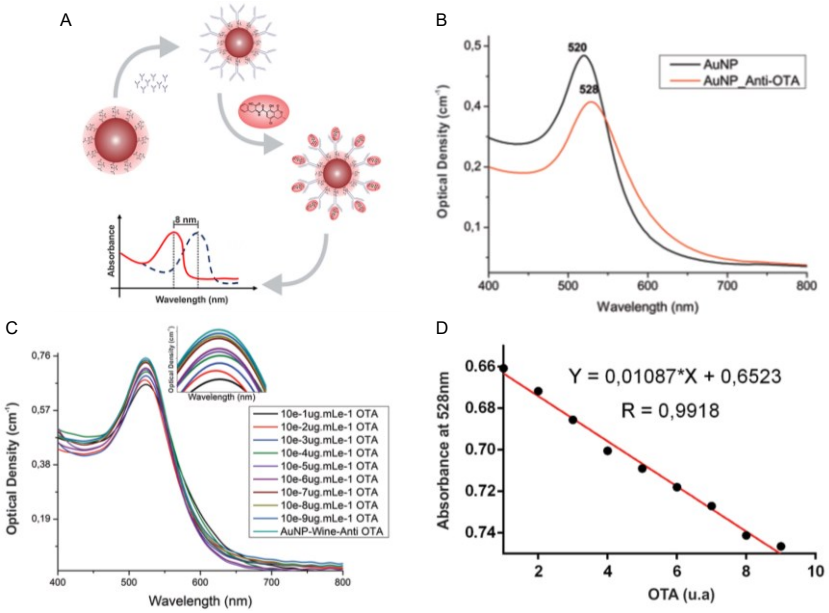


Figure 1.14. Schematic representation of working mode of the LSPR immunosensor detecting OTA and this optical response in (a). UV-vis absorption spectra of the colloidal Au NPs before and after adding OTA antibodies in (b). UV-vis absorption spectra at different OTA concentrations in (c) and the linear relationship between the absorbance intensity (528 nm) and OTA concentration in (d), using spiked wine samples. Reprinted with permission from Pereira et al. [137]. Copyright 2021 Elsevier.

1.4.1.5. Surface-Enhanced Raman Scattering (SERS)

Surface-enhanced Raman Scattering (SERS) phenomenon is a well-established method for sensitive detection of biological analytes [162]. This non-radiative phenomenon amplifies the common weak Raman signals at many orders of magnitude. The fundament of SERS lies in the surface plasmon resonance (SPR) phenomenon between the noble metallic NP and the incident light. The SERS effect falls in electromagnetic (i.e., LSP excitation) and chemical enhancement (i.e., charge-transference); however, the significant enhancement is played by the electromagnetic effect [162]. When the incident light reaches the nanometallic material, the excitation of the surface plasmon occurs on the metal surface. The strong scattering and absorption of light leads to an enhancement of the electromagnetic field at specific sites of the metallic NP [163]. The scattering frequency is different from the incident light frequency, and the Raman scattering is instigated due to the stronger electromagnetic field next to the metal surface [164]. Afterwards, the bio-interaction leads to a change of the surface plasmon energy and, consequently, the detection based on the SERS phenomenon delivers a structural analysis through the complete vibrational information of the aimed analyte molecule [164]. Biosensors based on the SERS phenomenon are commonly used for mycotoxin detection, namely OTA, with an amplification strategy [165–167].

Jing et al. [138] developed an accurate aptasensor based on the SERS effect in Au Film - Au@Ag core-shell NPs for OTA detection, as demonstrated in Figure 1.15a. Two standard molecules were used as Raman reporters, one linked to the Au@Ag NPs (i.e., 4-ATP) and the other linked to the Au NPs film (i.e., 4-NTP). The application of Raman reporters is commonly used to deliver information and confirm biological interaction. The Raman reporters' molecules present a strong enhanced SERS signal, exhibiting a well-known intensity peak of easy detection [162]. The Au Film - Au@Ag core-shell NPs complex was associated by aptamer hybridization (i.e., aptamer and probe linkage). The interaction between the OTA and their specific aptamer caused the release of Au@Ag core-shell NPs from the Au NPs film. Consequently, the intensity of the specific reporter Raman signal (i.e., 4-ATP) at 1078 cm^{-1} was reduced, and the intensity of another reporter Raman signal (i.e., 4-NTP) at 1335 cm^{-1} remained stable, as shown in Figure 1.15b. Through the ratio between the intensity of both Raman signals, the LOD value was established at 5 pM and an RSD value of 0.94% (Figure 1.15c). The aptasensor was exposed to spiked red wine samples, achieving recovery values from 96.12 to 97.24%.

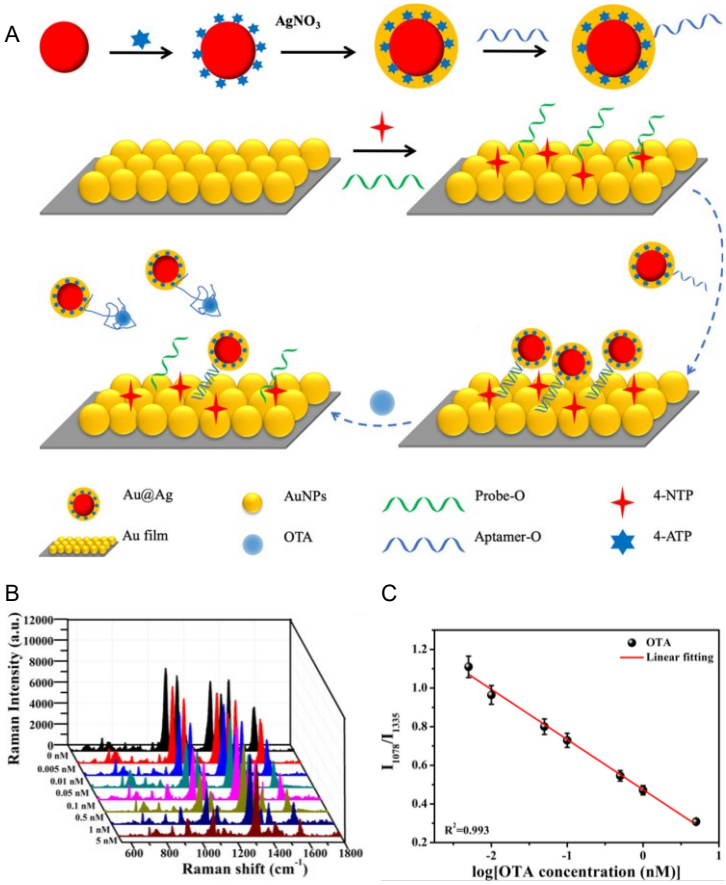


Figure 1.15. Schematic representation of fabrication and the working mode of Au Film– Au@Ag core–shell NP structured SERS aptasensor for OTA detection at (a). SERS spectra at different concentrations of OTA in (b) and the linear relationship between the Raman intensity ratio and the logarithmic OTA concentration in (c). Reprinted with permission from Jing et al. [138]. Copyright 2020 American Chemical Society.

A SERS-based competitive immunosensor for OTA detection was reported by Ding et al. [139]. The assay consists of two parts: OTA-BSA-immobilized SERS nanotags and anti-OTA Ab-functionalized magnetic beads (MBs). In the presence of the target OTA, a competitive reaction occurred among the target OTA and the OTA-BSA-immobilized SERS nanotags complex towards the anti-OTA Ab-functionalized MBs. Therefore, the immunosensor responded with the decrease of the intensity of Raman peak in the SERS signal since the amount of SERS nanotags linked to the anti-OTA-Ab decreased. A linear correlation was found in a range of concentrations between 1 pg mL^{-1} to 1000 pg mL^{-1}, and the LOD value was calculated as 0.61 pg mL^{-1}. The recovery rates obtained in a spiked red wine samples analysis were established between 90.6% to 103.3%, and an RSD value between 2.47% to 2.97%.

New dual-mode optical detection approaches using an immunochromatographic strip, based on a microfluidic paper-based analytical device, have been successfully developed for OTA sensing. Zhang et al. [140] developed a LFIA based on the combination between the SERS and fluorescence phenomena for the detection of several mycotoxins. SERS-based Au@Ag core-shell NPs were labeled with two Raman reporters' molecules (i.e., DTNB and MBA), and six specific hapten-protein conjugates were distributed in the three T-line of nitrocellulose membrane, as demonstrated in Figure 1.16a. The interaction between the mycotoxin and the nanometallic structure led to variations in the SERS signal intensity. In the absence of OTA content, several SERS nanoprobes were linked to the nanostructure, and the spectral features were detected, as shown in Figure 1.16b,d. However, the increase of the specific mycotoxin concentration led to the decrease of SERS signal intensities of each T-line, as shown in Figure 1.16c,e. Regarding the OTA detection, spiked maize samples were exposed to the biosensor, and the LOD value was established at 15.7 pg mL^{-1} with a detection range between 0.027 to 6.7 ng mL^{-1}. Thus, the immunosensor revealed satisfactory sensing performance (i.e., accuracy and precision).

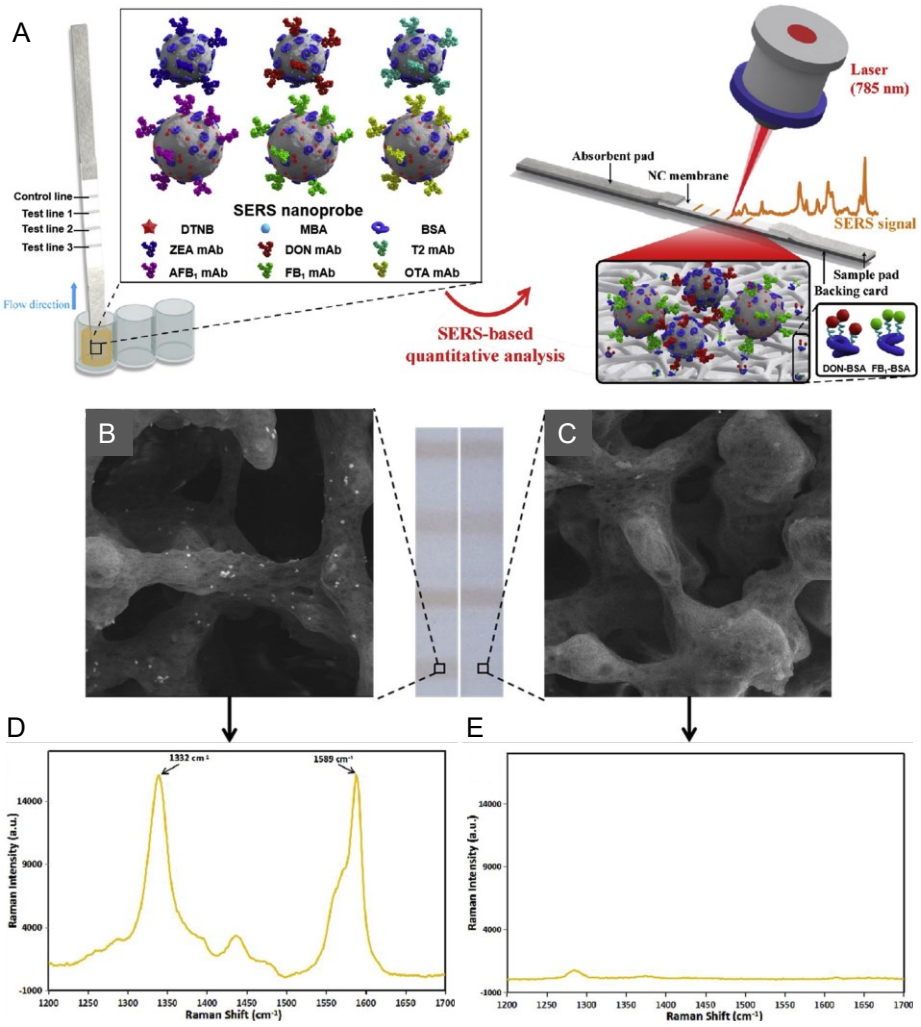


Figure 1.16. Schematic representation of the working mode of the multiplex SERS-based lateral flow immunosensor for OTA detection in (a). Representative SEM images and Raman spectra from the test lines of negative sample in (b, d) and strong positive sample in (c, e). Reprinted with permission from Zhang et al. [140]. Copyright 2020 Elsevier.

The multi-detection of OTA and another mycotoxin (i.e., AFB1) was achieved through a signal-enhanced SERS biosensor, as Kutsanedzie et al. [141] reported. This biosensor was based on Ag NPs, with a high analytical enhancement factor, coupled with variable chemometric algorithms. The established LOD value for OTA detection was 2.63 pg mL^{-1} in spiked cocoa bean samples, with recovery rates between 98.58 and 108.44%.

1.4.1.6. Colorimetry

Colorimetry have become a promising intuitive detection strategy since the signal outcome can be realized by naked-eye visual recognition. Colorimetric sensing takes advantage of the LSPR phenomenon in metallic NPs (e.g., Ag or Au). Typically, the colorimetric-based biosensor presents an immobilized biorecognition element in a metallic NP. The bio-interaction between the biorecognition element and the aimed target leads to both LSPR spectra shift and color variations due to the surface plasmon coupling induced by aggregation or dispersion of NPs [168]. This optical biosensing method provides several interesting advantages: i) a fast detection speed, ii) cost-effective biodetection device, iii) well-established chemistry assay with a simple result understanding, since the biosensing performance is based on visible variations of the color intensity in the test solution [169]. However, this method is not appropriate for quantitative detection [169]. The detection of biological analyte at low concentrations will cause a negligible visual color intensity variation, leading to a short dynamic range for biodetection, besides being extremely sensitive to external conditions (i.e., temperature and pH) [170]. Therefore, this biosensing method is usually combined with other sensing approaches, allowing their independent response but mutual confirmation. The independent dual-readout immunoassay can be a relevant alternative to improve the accuracy and precision of this biosensing approach.

Tian et al. [142] reported a multi-colorimetric detection method against OTA by developing an enzyme-induced aptasensor in a silver nanoshell on the surface of Au nanorods (Au NRs@Ag), as demonstrated in Figure 1.17a. Streptavidin MBs (SA-MBs) were immobilized by a biotinylated OTA aptamer (OTA aptamer - SA-MBs), and this aptamer was linked to a biotinylated DNA-alkaline phosphatase enzyme (cDNA- SA-ALP). In the presence of OTA, the bio-interaction between the mycotoxin and its aptamer led to G-quadruplex (GQx) molecular structure creation and, consequently, the release of the DNA-ALP complex. After magnetic separation, the catalysation of ALP created a product that caused the reduction of Ag^{+} allowing the development of Au NRs@Ag. The biological interaction between the target and the complex generated a longitudinal LSPR peak shift of Au NRs. The increase of OTA concentration caused a visible naked eye change of the solution to darker colors (Figure 1.17b) and a blueshift of the LSPR peak (Figure 1.17c). In spiked grape juice samples, the quantification method determined the LOD value at 9 nM with a linear detection range of 12.5 to 20,000 nM (Figure 1.17d) and an RSD value below 8.3%.

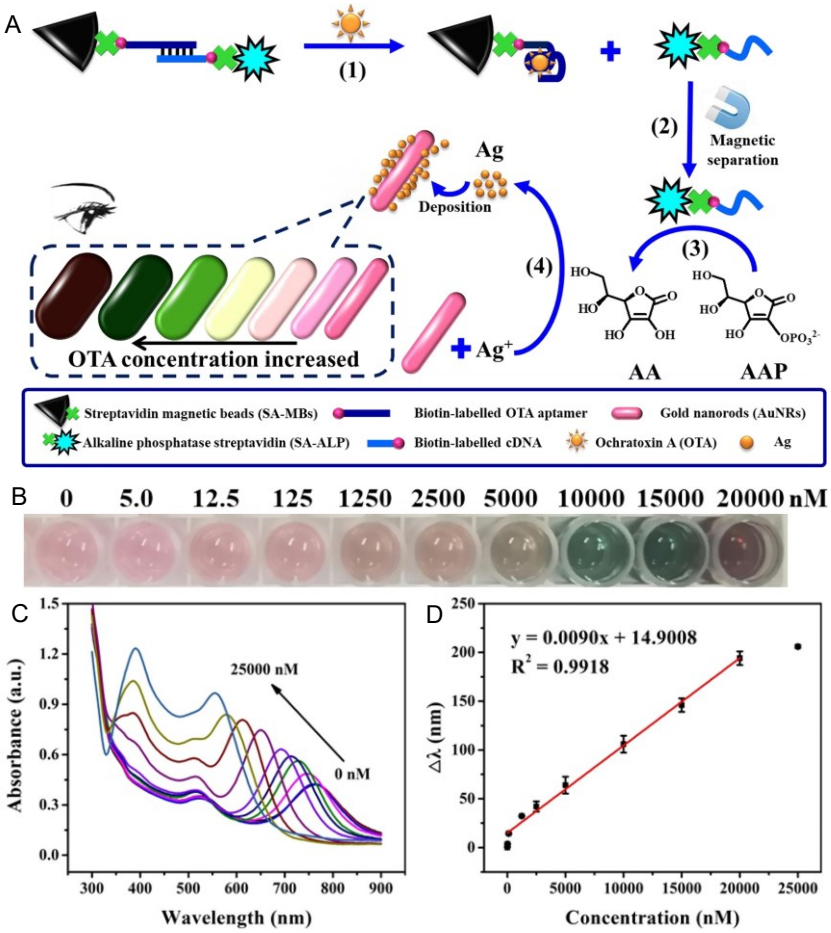


Figure 1.17. Schematic representation of the working mode of the multi-colorimetric based on the structural switching of aptamer and the enzyme-induced deposition of AuNRs for OTA detection in (a). Photographs of the enzyme-induced aptasensor solutions (b) and UV-vis absorption spectra (c) at different OTA concentrations. The linear relationship between the blueshift of the longitudinal LSPR peak (Δλ) and OTA concentration among 12.5 to 20,000 nM at (d). Reprinted with permission from Tian et al. [142]. Copyright 2020 Elsevier.

Zhu et al. [143] developed a multi-colorimetric immunosensor through the mimetic enzyme etching of Au nanobipyramids (Au NBPs). In an antigen-coated 96-well plate, a mixture of different concentrations of aimed OTA and fixed concentrations of OTA Ab (Ab_1) were added. The immobilized antigen and the free OTA competed for the combination to Ab_1. As higher OTA concentration, less of the immobilized Ab_1. A Cu_2O-labeled with a secondary Ab (Ab_2) linked to the remaining free OTA, and TMB was added to the solution to promote the TMB^{2+} appearance. The TMB^{2+} content was inversely proportional to $Cu_2O@Ab_2$ and, consequently, to OTA concentration. The interaction between TMB^{2+} and Au NBPs spontaneously changed the solution's colors identified through naked eye. The LSPR peak of the Au NBPs changed according to the logarithm of OTA concentration. The detection range of this biosensor was established between 1 ng L^{-1} to 5 μg L^{-1}, and the LOD value was calculated at 0.47 ng L^{-1}. In millet spiked samples,

the qualitative detection was well performed through color variations to vivid color in the detection area of the immunosensor, and the quantification method determined a wide recovery rate established between 98.6 and 111.4%.

A direct competitive enzyme immunoassay system for OTA detection compatible with smartphone image processing was developed by Zhang et al. [144]. The competitive enzyme colorimetric immunoassay based on hydrogel microspheres could detect multi-mycotoxins (i.e., OTA and ZEN). This biosensing method is divided into 3 steps: 1) competitive response between the aimed target and artificial antigen to bound at the immobilized mAb in the solid-phase carrier hydrogel particles, 2) signal amplification through the addiction of urea, previously linked to the artificial antigen, leading to a colorimetric ELISA and 3) smartphone analysis program through average brightness value of the particles delivered the final test result. In 30 minutes, the detection process was entirely performed, and within 10 seconds, the results were evaluated through the smartphone analysis program. The LOD value of this biosensor was calculated as 0.77 ng L^{-1} for the OTA molecule, and the linear dynamic range was established between 0.001 to 100 ng mL^{-1}. Real spiked samples (i.e., dry corn) were tested in this biosensing platform, and the detection results revealed a recovery range between 80.83 to 115.67% and an RSD of 6.02 to 6.52%.

New colorimetric detection approaches have been created using an LFIA paper-based (bio)analytical technique. Typically, the LFIA sensing approach requires the use of metallic NPs (e.g., Ag or Au) to detect OTA, possibly increasing the production cost of the biosensor. Thus, Suea-Ngam et al. [145] developed an ultrasensitive detection method against OTA based on a non-noble metal colorimetric assay in a paper-based analytical device. The immobilization of OTA Ab in a cellulose surface allowed the OTA capture. In the sandwich mechanism, OTA was labeled with an aptamer-conjugated glucose oxidase (AGOx). With the addition of other chemical compounds, the AGOx released the hydrogen peroxide (H_2O_2), leading to a distinct color change to blue in a positive test, as demonstrated in Figure 1.18a. In the absence of the aimed mycotoxin, the solution remained colorless. The color intensity and the OTA concentration quantification were analyzed through a smartphone-captured image process. The linear detection range was established between 10^{-1} and 10^{5} ng mL^{-1} (Figure 1.18b) with a LOD and LOQ values of 20 and 320 pg mL^{-1}, respectively. The selectivity evaluation of the biosensor noted negligible responses to other interferents (Figure 1.18c). To evaluate the assay accuracy, the biosensor system was compared to other detection methods (i.e., Ultrahigh Performance Liquid Chromatography (UPLC) and an electrochemical aptasensor), and the results showed a good agreement with a 95% confidence level, as demonstrated in Figure 1.18d. The biosensor was tested in several real spiked samples (Figure 1.18e),

performing a recovery range between 95 and 117% and an RSD value lower than 5%. However, artificial serum and urine samples showed a higher signal variance, possibly due to the high concentration of proteins in the samples, which severely influences the sandwich complex formation. Finally, after 30 days of storage, the sensor's performance was affected by a 20% reduction in signal intensity, possibly due to the denaturation of Ab in the biosensor.

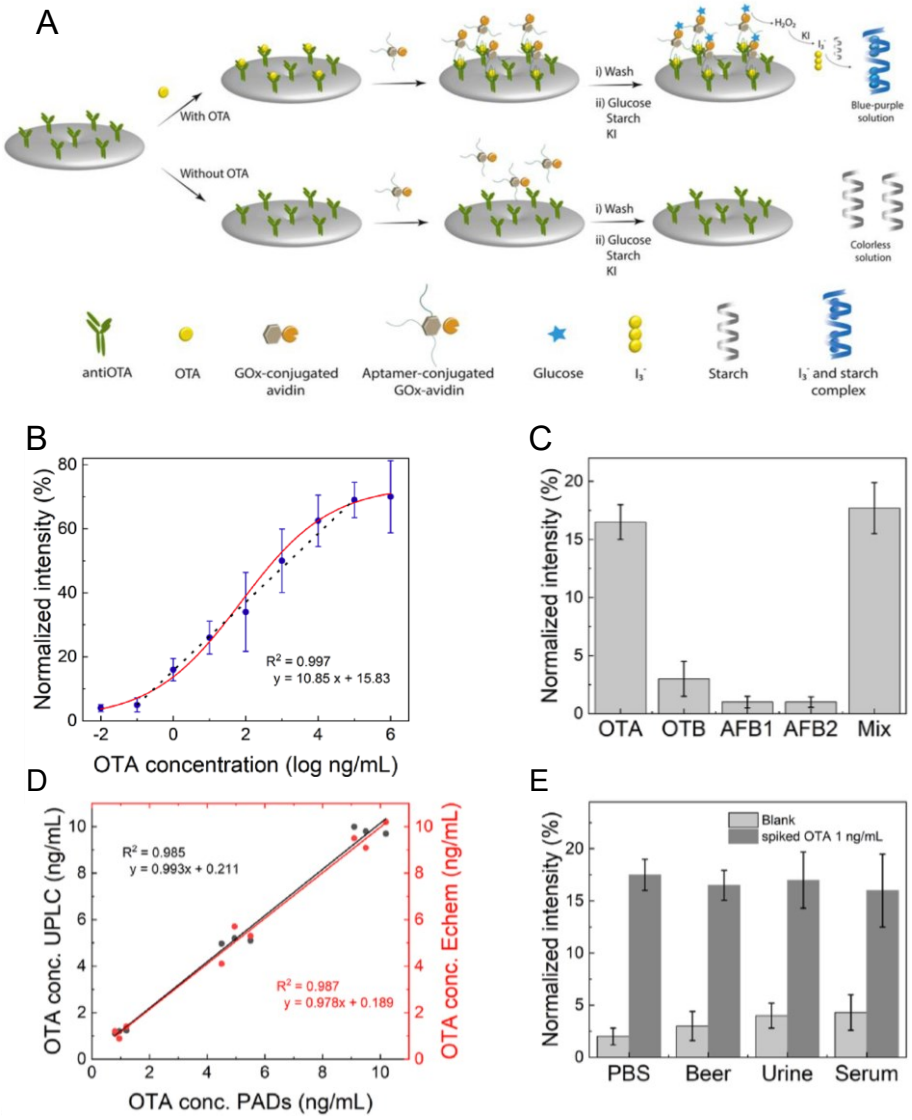


Figure 1.18. Schematic representation of the working mode of a colorimetric immunosensor based on a paper-based analytical device for OTA detection in (a). Variation of normalized absorbance signal as a function of OTA concentration in (b) and normalized signal intensity was obtained from potential interferents in (c). Detection comparison between the reported biosensor and other sensing detection at several OTA concentrations in (d). Normalized signal intensity was obtained from different several real spiked samples (i.e., beer, urine, and serum) in (e). Reprinted with permission from Suea-Ngam et al. [145]. Copyright 2020 Elsevier.

LFIA biosensing can be also developed for simultaneous multi-target detection in a single immunochromatographic test strip, improving the sensing assay to all the possible toxic components present in a representative sample of the food product. The development of a multicolor immunochromatographic test strip nanosensor capable of detecting several mycotoxins was developed by Wu et al. [146]. The sensing device for the simultaneous detection of OTA and other mycotoxins (i.e., FUM1, ZEN, and AFB1) was composed of four T lines and an independent C line, as demonstrated in Figure 1.19a. The T lines were differentiated by four different structures of Au NPs (i.e., nanospheres, nanocacti, nanoflowers, and hyperbranched blackbodies), with distinct absorption peaks linked to the corresponding Ab. The correspondence between a specific signal from the T line and the target presence allowed the naked eye visual detection, as represented in Figure 1.19b. The biosensing system presented a LOD value of 0.096 ng mL^{-1} calculated through the linear relationship between the optical signal and OTA concentration, as shown in Figure 1.19c. The feasibility was tested with spiked corn samples at different concentrations, achieving high-level sensitivity for the simultaneous mycotoxins' detection.

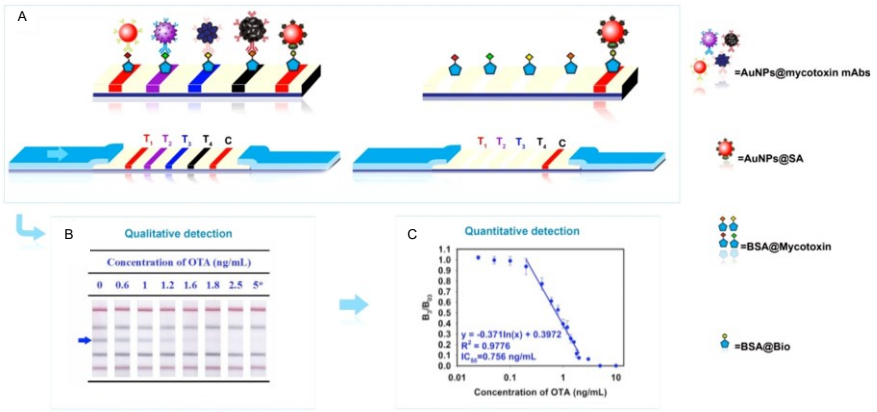


Figure 1.19. Schematic representation of the working mode of the AuNPs-based multicolor immunochromatographic test strip biosensor in (a). Stereograms of the individual test at different OTA concentrations (marked with an arrow) in (b) and the linear relationship between the optical signal (B3/B03) and OTA concentration in (c). Reprinted with permission from Wu et al. [146]. Copyright 2020 Elsevier.

As previous shown, this sensing approach has significant limitations on real sample foodstuff. First, the grape juice was prepared by crushing and blending grapes into purple liquid juice. The Au NPs-LFIA sensing technique cannot be used as an OTA detection method in juice grapes since it has inadequate resistance to background matrix and color interference. To overcome this limitation, Hao et al. [147] created an alternative using bifunctional magneto-Au nanohybrids (MGNHs) by encapsulating oleylamine-coated AuNPs (OA-AuNPs) with oleic acid-coated iron oxide NPs (OC-IONPs) into polymer nanobeads. The

MGNHs were conjugated with an mAb and exposed to a grape juice deliberately contaminated with several concentrations of OTA (between a range of 0.39 to 3.12 ng mL^{-1}). After the immunoreaction, the MGNH-Ab-OTA complex and the MGNH-mAb free were collected to run the competitive LFIA test strip, as demonstrated in Figure 1.20a. In the presence of target OTA, the MGNH-mAb-OTA complex could not generate the signal from the T line in the LFIA device. Thus, the concentration of OTA in the sample had the opposite effect on the optical density value of the T line (Figure 1.20b). The LOD value was calculated as 0.094 ng mL^{-1}, through the determination of the competitive inhibition curve for OTA concentration ranging from 0.098 ng mL^{-1} to 12.5 ng mL^{-1} (Figure 1.20c). The selectivity of the developed biosensor was successfully tested against other mycotoxins; moreover, the detection results from this MGNH-LFIA approach corresponded nicely with the current LC-MS detection method.

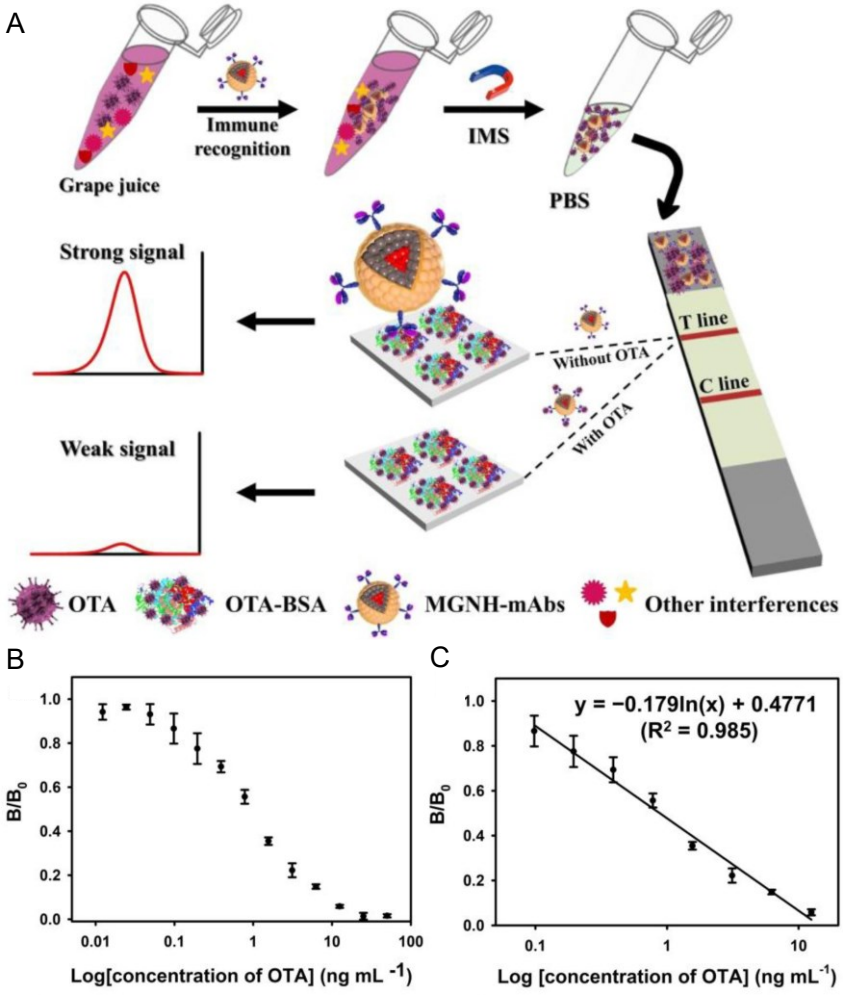


Figure 1.20. Schematic representation of the fabrication and working mode of the magneto-Au nanohybrid-enhanced LFIA biosensor for OTA detection in (a). Optical response at different OTA concentrations in (b) and the linear relationship between the optical signal (B/B0) and the logarithm of OTA concentration in (c). Reprinted with permission from Hao et al. [147]. Copyright 2021 Elsevier.

1.4.1.7. Dual-Mode Optical Detection – Colorimetry and Fluorescence

The nanotechnology vanguard outstands the combination of several optical phenomena highlighting its advantages in biosensing detection: i) higher sensitivity, ii) a wider range of detection, iii) a faster detection speed, and iv) a reciprocated validation. An intrinsic characteristic of the biological analyte can be the key to its optical detection since OTA individually exhibits a good fluorescence emission signal at 448 nm. Knowing this particular feature, Alizadeh, Hashemi, and Shahdost-Fard [148] focused on the spectrofluorimetric study of the OTA-metal cations (i.e., Cu^{2+}) complexation, since the complex formation altered OTA fluorescence intensity. The introduction of Cu^{2+} enabled the formation of a non-fluorescent complex with OTA. However, the complex formation was reversible, by adding a masking agent (i.e., EDTA) that formed a stronger complex with Cu^{2+} than OTA. This chemical reaction eliminated the Cu^{2+}-OTA complex, and the fluorescence response recovered its initial signal (Figure 1.21a). The developed biosensor was based on hybrid fluorimetric and visual detection, exhibiting LOD and LOQ values of 0.4 and 1.2 ng g^{-1}, respectively. The efficiency of the proposed strategy was tested in four different types of non-extracted samples and a moldy sample of wheat flour. The fluorescence spectrum of a non-extracted sample is shown in Figure 1.21b – a. However, the extracted samples were spiked with different OTA concentrations. The fluorescence intensity increased linearly (Figure 1.21b from b – e), allowing the determination of a linear relationship between the fluorescence intensity and OTA concentration (Figure 1.21c). The hybrid fluorimetric and visual OTA color detection was provided by a color difference map (CDM) extracted from the fluorimetric studies, as shown in Figure 1.21b. The addition of Cu^{2+} led to a decrease in fluorescence intensity. Nevertheless, it did not achieve the initial blank sample signal indicating the possibility of OTA contamination in the non-extracted blank samples (Figure 1.21b – f).

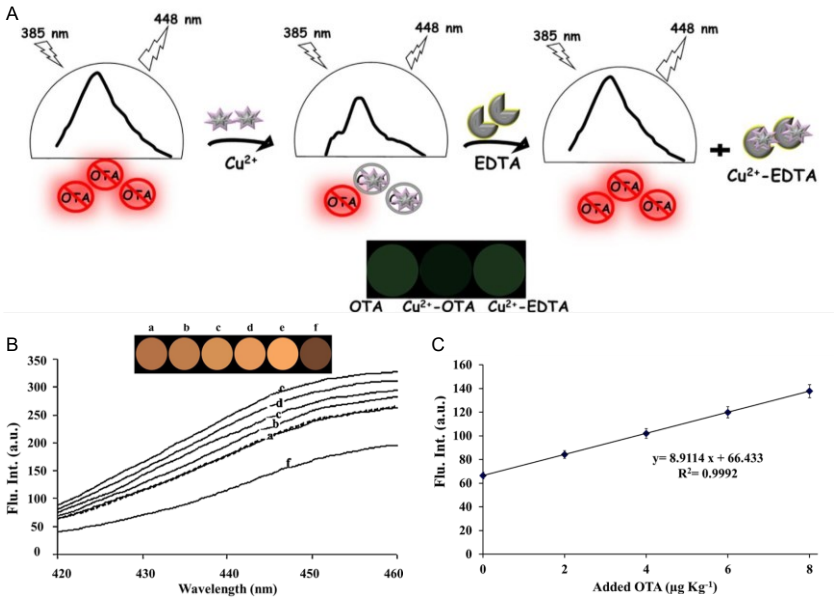


Figure 1.21. Schematic representation of the hybrid fluorimetry and visual OTA detection in the absence and presence of Cu^{2+} and EDTA in (a). Fluorescence intensity spectra of a non-extracted blank sample (b – a), spiked samples with an increased linear concentration in (b from b – e), after the addition of Cu^{2+} to the spiked sample in (b – f) and their corresponding color difference map (CDM) images. The linear relationship between the fluorescence intensity and OTA concentration is plotted in (c). Reprinted with permission from Alizadeh, Hashemi, and Shahdost-Fard [148]. Copyright 2021 Elsevier.

The development of a fluorescent microsphere in an immunochromatographic test strip (FM-ICTS) allowed OTA dual-optical detection in a single device. Cheng et al. [149] reported a specific optical sensor based on a similar LFIA technique; however, it provides an improved visible fluorescent signal in a portable device. As the concentration of the OTA increased, the fluorescence intensity decreased. The fluorescence intensity was quantified in a strip reader by establishing the fitting curve. The assay's sensitivity was tested in rice flour samples achieving a LOD value of 1.27 ng mL^{-1}. In turn, Zhou et al. [150] developed an improved OTA immunochromatographic test strip based on a fluorescence signal probe of CdSe/ZnS QDs. In 15 minutes, the immunoreaction occurs, and the sensing device provides a qualitative signal characterized by the disappearance of the T line. For the quantification detection, the fluorescence intensity of T and C lines was measured, and its ratio was recorded through an immunochromatographic test strip analyzer. The biosensor was able for qualitative and quantitative detection, achieving LOD values of 2.5 and 0.07 ng mL^{-1}, respectively. The sensing device was tested using several spiked corn samples and responded at a recovery rate ranging from 94.29 to 104.62%.

Zhu et al. [151] developed a dual-modal multi-colorimetric and ratiometric fluorescence immunosensor, as demonstrated in Figure 1.22a. In an antigen-coated 96-well plate, a mixture of different

concentrations of free aimed OTA and fixed concentrations of OTA Ab (Ab_1) was added. Consequently, the antigen, previously fixed at a 96-well plate, and free aimed OTA competes for the OTA Ab (Ab_1) linkage. As the higher the OTA concentration, the less Ab_1 was immobilized. Cu_2O@$Fe(OH)_3$ NPs, previously bound to a second OTA Ab (Ab_2), were added, culminating in an immunoreaction. After the immunoreaction step, an antigen-Ab_1-Ab_2 complex structure was developed, and the unconjugated solution was collected for both detection assays. A fixed volume of the unconjugated mixture (OTA-Ab_2-Cu_2O@$Fe(OH)_3$ NPs) was exposed to Au NRs, allowing colorimetric detection. The increasing concentration of the mycotoxin caused a blueshift in the LSPR peak, as demonstrated in Figure 1.22b. Consequently, it was perceptible alterations in the color of the solution sample, as shown in Figure 1.22d. The LOD value was calculated as 0.83 ng L^{-1}, through the linear relationship between the LSPR peak shift and OTA concentration, as exhibited in Figure 1.22f. However, the quantitative method was based on ratiometric fluorescence detection. The unconjugated solution with Cu_2O@$Fe(OH)_3$ NPs oxidized the *o*-phenylenediamine (OPD), colorless, to 2,3-diaminophenazin (DAP), exhibiting yellow color, in the presence of H_2O_2. Due to the inner filter effect between DAP and CDs, this reaction caused variations in the fluorescence spectra. The fluorescence spectra evolved to the decrease of CDs intensity peak at 424 nm and increase of DAP intensity peak at 563 nm (Figure 1.22c), and the color of the solution turned from blue to yellow, as shown in Figure 1.22e. The relation between the fluorescence intensity of both DAP and CDs allowed the LOD value calculation to be 0.56 ng L^{-1} between a range of 0.1 ng L^{-1} to 10 µg L^{-1} through the linear calibration curve, as exhibited in Figure 1.22g. The potential of the dual-modal strategy was tested in three concentrations of real spiked samples, and the results were promising.

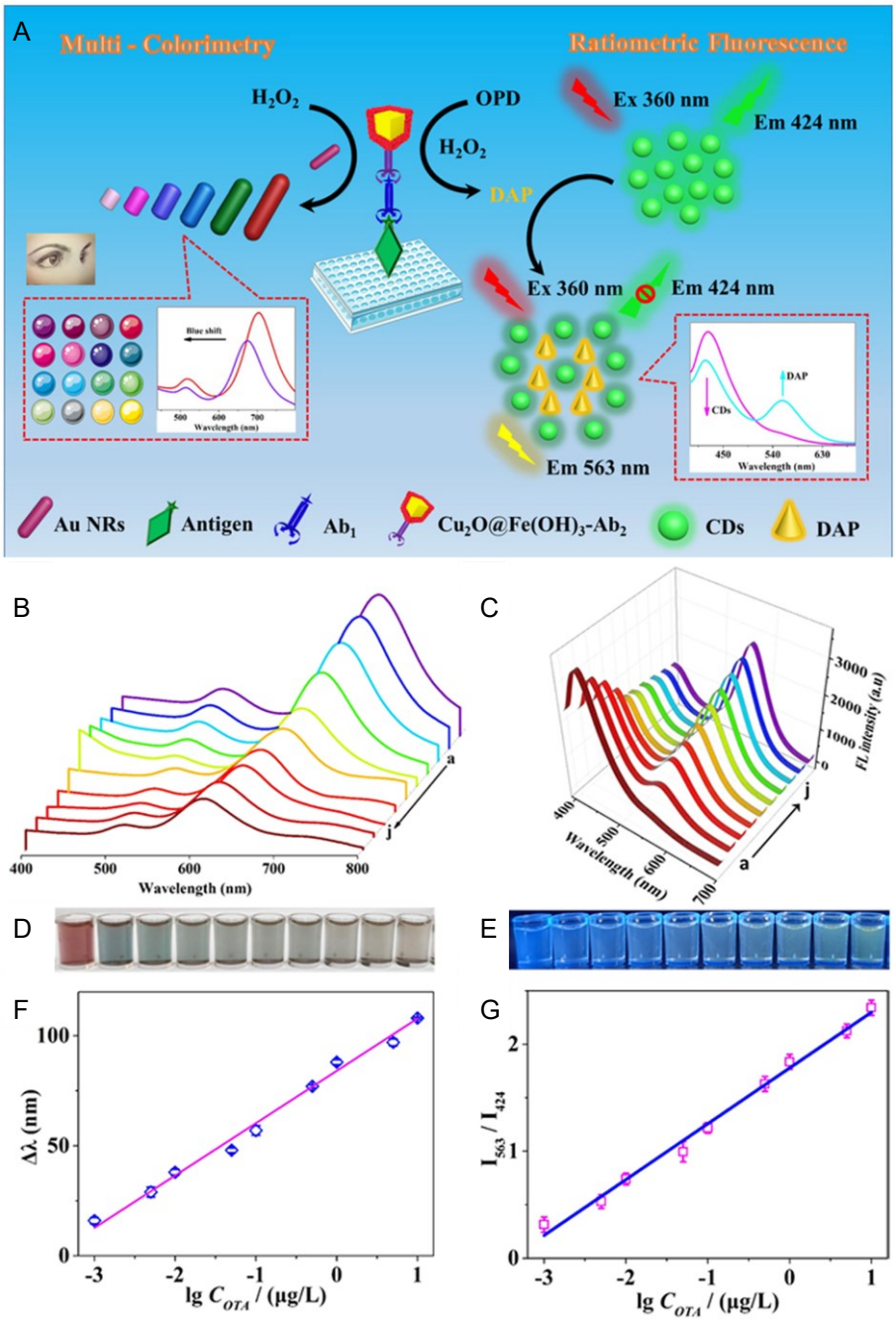


Figure 1.22. Schematic representation of the working mode of the dual-modal immunosensor for OTA detection: multi-colorimetric and ratiometric fluorescence in (a). UV-vis absorption spectra (b) and fluorescence spectra (c) at different concentrations of OTA and their photographs in (d) and (e), respectively. The linear relationship between LSPR peak shift in (f) and fluorescence intensity ratio in (g) with OTA concentration. Reprinted with permission from Zhu et al. [151]. Copyright 2021 Elsevier.

1.4.1.8. Dual-Mode Optical Detection – Colorimetry and Chemiluminescence

Chemiluminescence phenomenon relies on the occurrence of luminescence, caused by releasing energy from a chemical reaction. The transition between the electronically excited state of a particular molecule to the ground state leads to light emission with a proper wavelength [171]. The combination of both colorimetric and chemiluminescence methods for OTA detection was reported by Mukherjee, Nandhini, and Bhatt [86]. The sensing detection was developed through an enzyme-linked apta-sorbent (ELASA) assay coupled with colorimetric and chemiluminescent enzymes. Compared to ELISA, the ELASA assay enhances the sensitivity and specificity of the sensing system due to the dual biorecognition elements. In the presence of OTA, the aptamer was linked to the mycotoxin. The OTA was exposed to an anti-OTA IgG primary Ab followed by anti-rabbit ALP tagged secondary Ab. The colorimetric detection (Co-ELASA) occurred when the anti-rabbit ALP tagged reacted with the substrate (i.e., p-NPP), resulting in a color variation and measurement of absorbance, as demonstrated in Figure 1.23a. Regarding the chemiluminescent assay (Cl-ELASA), the interaction between the mycotoxin and the anti-OTA IgG complex can be identified by adding a biotinylated OTA aptamer and streptavidin-HRP (streptavidin linked to horseradish peroxidase). The addition of substrate (i.e., luminol and urea-H_2O_2) permitted the chemiluminescence effect, as represented in Figure 1.23b. Both sensing performances revealed a wide range of detection between 1 pg mL^{-1} to 1 µg mL^{-1}. However, the LOD and LOQ values, for both phenomena effect, were distinct. The linear relationship between inhibition (%) and the relative luminescence with OTA concentration allowed the determination of the LOD values at 0.84 pg mL^{-1} and 1.29 pg mL^{-1} for Co-ELASA and Cl-ELASA, respectively (Figure 1.23c,d). Regarding the LOQ value, Co-ELASA presented a value of 2.54 pg mL^{-1} and Cl-ELASA of 3.94 pg mL^{-1}. The feasibility of the biosensor was evaluated in real spiked samples (i.e., groundnut, and coffee bean), achieving reliable results. The cross-reactivity assay focused on the aptamer's affinity to other mycotoxins reached less than 40%.

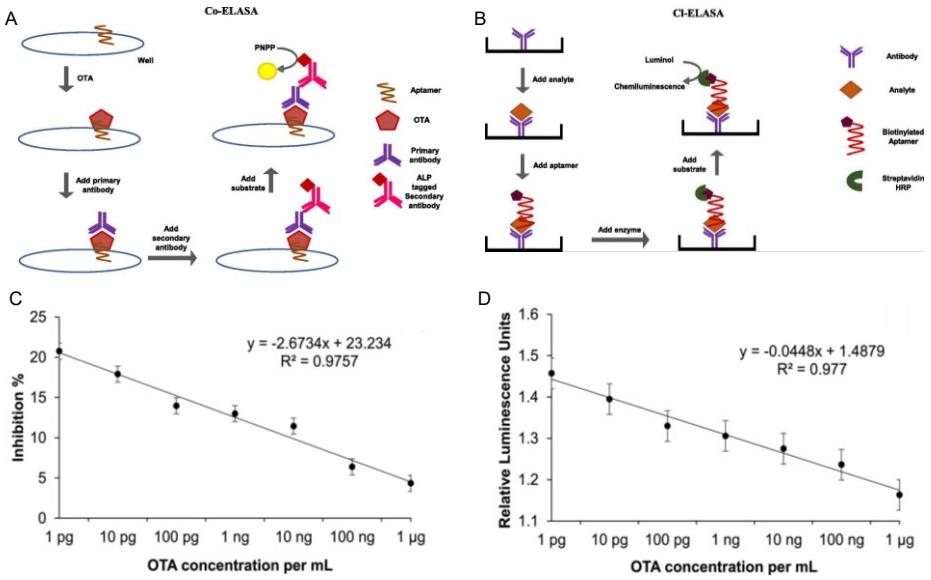


Figure 1.23. Schematic representation of the working mode of the colorimetric ELASA (Co-ELASA) and chemiluminescence ELASA (CI-ELASA) assays for OTA detection in (a) and (b), respectively. Plots of the linear relationship between inhibition (%), in (c), and relative luminescence, in (d), with OTA concentration between 1 pg mL^{-1} and 1 µg mL^{-1}. Reprinted with permission from Mukherjee, Nandhini, and Bhatt [86]. Copyright 2021 Elsevier.

A smartphone-based biosensor composed of LFIA technique coupled with chemiluminescence detection (CL-LFIA) for quantification of OTA in wine, grape must, and coffee samples were reported by Zangheri et al. [152]. The chemiluminescence detection performance occurred through the inclusion of a smartphone camera that worked as both light detector and proper disposable sensing platform (i.e., analytical cartridge), including all the reagents required, represented in Figure 1.24a,b. Non-specialized operators could perform the OTA detection using a simple manual operation. The structure of the analytical cartridge, where the immunoassay occurred, is represented in Figure 1.24c. The immunoassay protocol was divided into 3 steps: 1) injection of the sample in the metering chamber (Figure 1.24d), 2) loading of the sample and the HRP-OTA conjugate solution to the sample pad of the LFIA strip (Figure 1.24e) and 3) introduction of HRP CL (i.e., luminol/H_2O_2 and enhancers) substrate (Figure 1.24f). After finishing the immunoassay, the analytical cartridge was incorporated into the mini dark box connected to the smartphone, and the chemiluminescence signal was detected. The calibration curves were obtained using real spiked samples (i.e., wine, and instant coffee). Being a competitive assay, the intensity of T line is inversely proportional to OTA concentration (Figure 1.24g). The LOD values were calculated through T line/C line signal ratio corresponding to 0.3 µg L^{-1} and 0.1 µg L^{-1} of wine and instant coffee samples, respectively (Figure 1.24h). Regarding the reproducibility, the RSD value associated with calibration curve was consistently below 12% and 7% for wine and instant coffee, respectively.

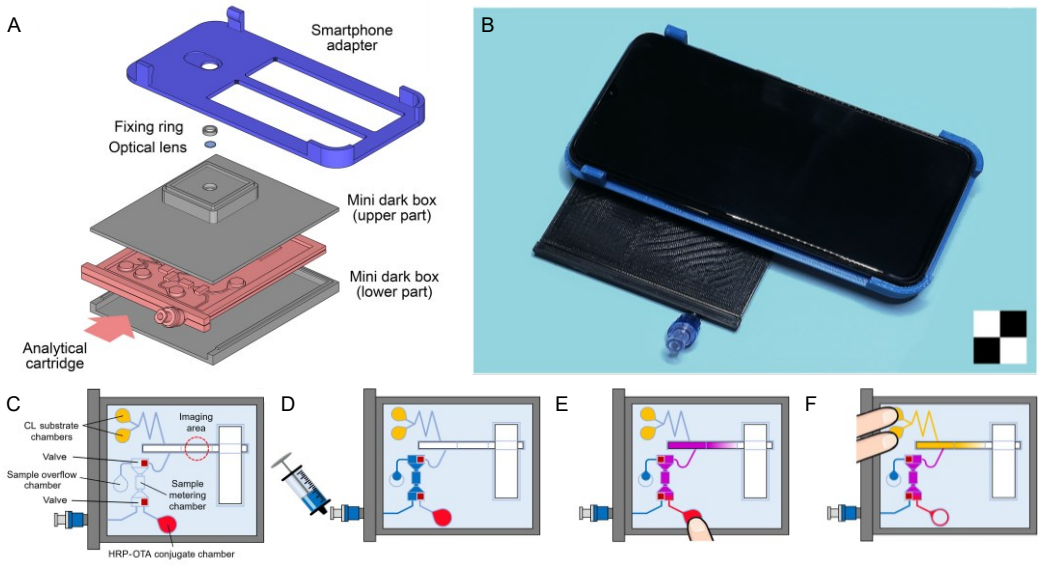


Figure 1.24. Schematic drawing of the dark box with the smartphone adapter in (a) and the photograph of the biosensor device in (b). Schematic representation of assay procedure: the analytical cartridge in (c), sample loading into the proper chamber (d), LFIA strip receiving the sample and the HRP-OTA conjugate solution in (e), the introduction of the HRP CL substrate in (f). Chemiluminescence images obtained by analyzing OTA-free wine and instant coffee samples spiked with known OTA concentrations in (g). Representative calibration curves obtained in spiked wine and instant coffee matrices in (h). Reprinted with permission from Zangheri et al. [152]. Copyright 2021 Elsevier.

1.4.1.9. Dual-Mode Photoelectrochemical Detection – Chemiluminescence

The development of biosensors with both electrical and optical detection methods is at the forefront of nanotechnology. The introduction of dual detection approaches became relevant, since it confers the ability to detect the aimed target, merging the advantages of electrochemical with optical transducer techniques, achieving high sensitivity and reliability combined with a fast and straightforward visualization detection. Electrochemiluminescence is the combination of electrochemistry and visual luminescence. The application of an electrical current into the surface of an electrode causes the excitation of the luminophore, and, consequently, the return to its fundamental state energy leading to the light-emitting reaction [172].

A novel bipolar Au-plated electrode-electrochemiluminescence (BPE-ECL) sensing platform was reported by Lu et al. [153] for OTA detection. The device was composed of a cathode of closed BPE in the functional sensing interface and an anode as a signal collection interface. The ECL signal intensity of the biosensor increased monotonically with OTA concentration, as shown Figure 1.25a,b. In this detection approach, the optimization of the pretreatment method of real samples was an essential concern, since

the sampling treatment severely influences the aptasensor's performance (i.e., sensitivity, accuracy, and stability parameters). The analytical performance of the sensor with the simplest pretreatment method presented a LOD value of 3 pg mL^{-1} with a dynamic range established between 0.01 and 5 ng mL^{-1} and 5 to 100 ng mL^{-1}. The biosensor was exposed to real spiked grain samples, and the average recovery was calculated at 94.2%.

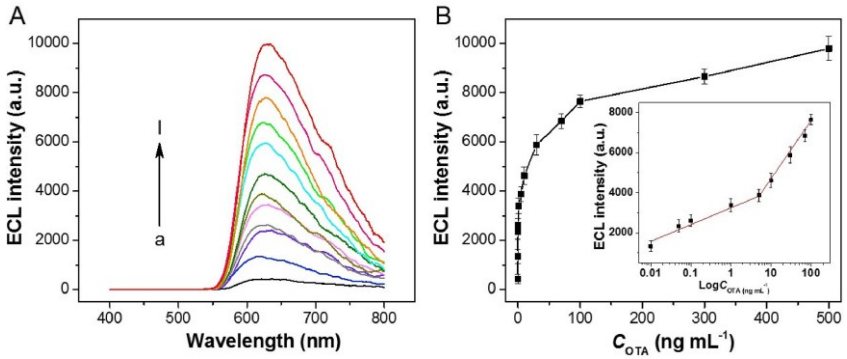


Figure 1.25. Electrochemiluminescence (ECL) intensity response of the BPE-ECL biosensor with different OTA concentrations in (a). Variation of ECL signal as a function of OTA concentration; insert of the linear relationship between the ECL intensity signal and logarithm OTA concentration in (b). Reprinted with permission from Lu et al. [153]. Copyright 2021 Elsevier.

1.4.1.10. Dual-Mode Photoelectrochemical Detection – Colorimetry

A dual-modal electrochemical and optical detection method, based on a paper-based analytical device, was advanced by Zhang et al. [154] and demonstrated in Figure 1.26a. On the surface of the transducer, a specific aptamer (apta1) allowed the modification of MnO_2-Au on the carbon working electrode. After blocking the nonspecific binding site, several concentrations of OTA were included and linked to apta1. The aptasensor was composed by conjugation of apta1-OTA and the second aptamer (apta2) linked to Ch–MoS_2-Au@Pt nanocomposite, creating an apta1-OTA-apta2 sandwich-type complex. When the complex was formed, the electrochemical signal increased, as shown in Figure 1.26b. Using such a detection method, the LOD value was calculated to be 25.2 fg mL^{-1} with a detection range of 0.0001 to 200 ng mL^{-1}. For the colorimetric detection, the chromogenic reaction led to darker colors with the increase of OTA concentration from 0.1 to 200 ng mL^{-1}, as shown in Figure 1.26c. The reliability of this method was tested in spiked corn samples achieving an RSD value below 4.10% and an average recovery ratio from 94.8 to 105.0%.

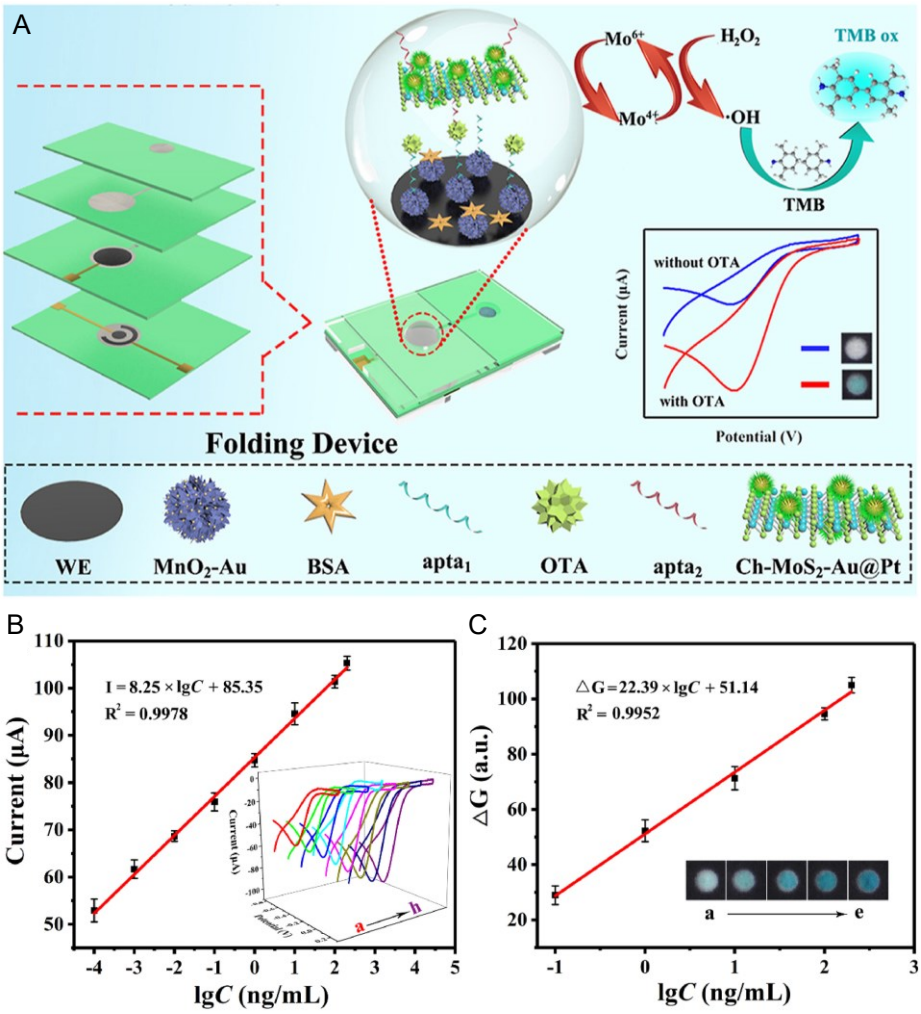


Figure 1.26. Schematic representation of the fabrication and working mode of the dual-modal electrochemical and optical biosensor for OTA detection in (a). Plots of linear relationship between electrochemical response with OTA concentration displayed in (b from a – h). Plots of linear relationship between colorimetric signal with OTA concentration displayed in (c from a – e). Reprinted with permission from Zhang et al. [154]. Copyright 2021 Elsevier.

Another dual-modal electrochemical and optical detection system was developed by Hao et al. [155]. The portable solar-driven visualization biosensor was divided into the detection (A) and the reference (B) module, and both modules were also divided into regions (i.e., visual and photoelectric area) in a small graphene-supported cobalt and nitrogen co-doped titanium dioxide (Co,N-TiO_2/3DGH) nanocomposite in an indium tin oxide (ITO) electrode, as represented in Figure 1.27a. The visual area was modified by electrochromic Prussian Blue (PB), present in region 1, and the photoelectric sensing area was composed of Co, N-TiO_2/3DGH nanocomposite, at region 2. PB changes from blue to colorless Prussian white (PW) when irradiated with UV light. The interaction between the OTA and the aptamer immobilized in the detection module (A) resulted in a steric hindrance leading to the decrease of the

number of electrons injected into the visual area and a slower transformation speed from PB to PW. The reference, module B, remained stable, and it was essential to guarantee feasible detection results. The quantification was based on the absorption intensity ratio of the detection module and the reference module (A2/A1). The UV-visible absorption spectra varied according to OTA concentration, as demonstrated in Figure 1.27b. Therefore, the absorption intensity ratio increased as the OTA concentration also increased, Figure 1.27c. The LOD value of the biosensor was determined at 0.29 ng ml^{-1} with a detection range established between 1 and 500 ng mL^{-1}. In spiked real samples, the RSD value was defined between 2.33% and 3.36%, with a recovery rate calculated to range between 98.0 and 101.2%. The stability of the biosensor was maintained until 20 days in storage. However, this detection platform is sensitive to the intensity of sunlight, weather, and time.

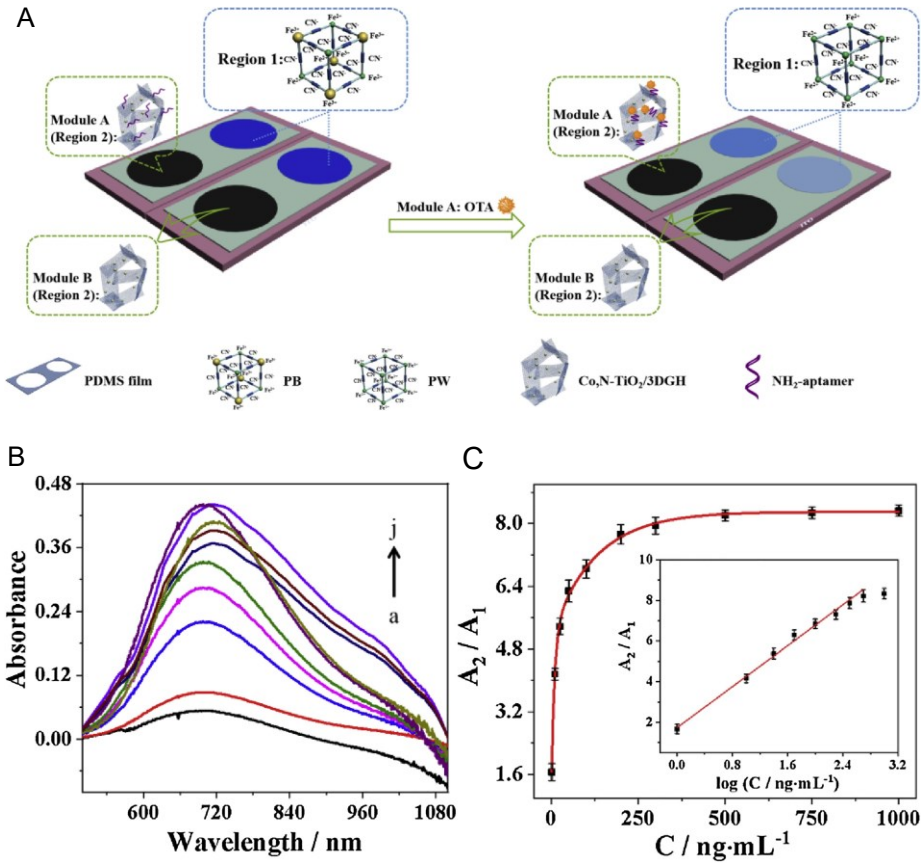


Figure 1.27. Schematic representation of fabrication of the portable solar-driven ratiometric photo-electrochromic visualization biosensor in (a). The UV-visible absorption spectra at different concentrations of OTA in (b). Calibration curve of absorption intensity A2/A1 ratio and OTA concentration; insert of the linear relationship between absorption intensity A2/A1 ratio and logarithm OTA concentration in (c). Reprinted with permission from Hao et al. [155]. Copyright 2020 Elsevier.

1.4.2. Comparison Performance of the Different Optical Biosensors

Innovative nanotechnology-associated detection approaches, with high sensitivity and specificity, have been devised, and should be compared with the standard detection methods, in order to understand the biosensing relevance of the previously described advanced optical detection methods. Therefore, a general scheme identifying the bioanalytical performance parameters (i.e., LOD and LDR) of both conventional detection methods and previously described optical biosensors is shown in Figure 1.28.

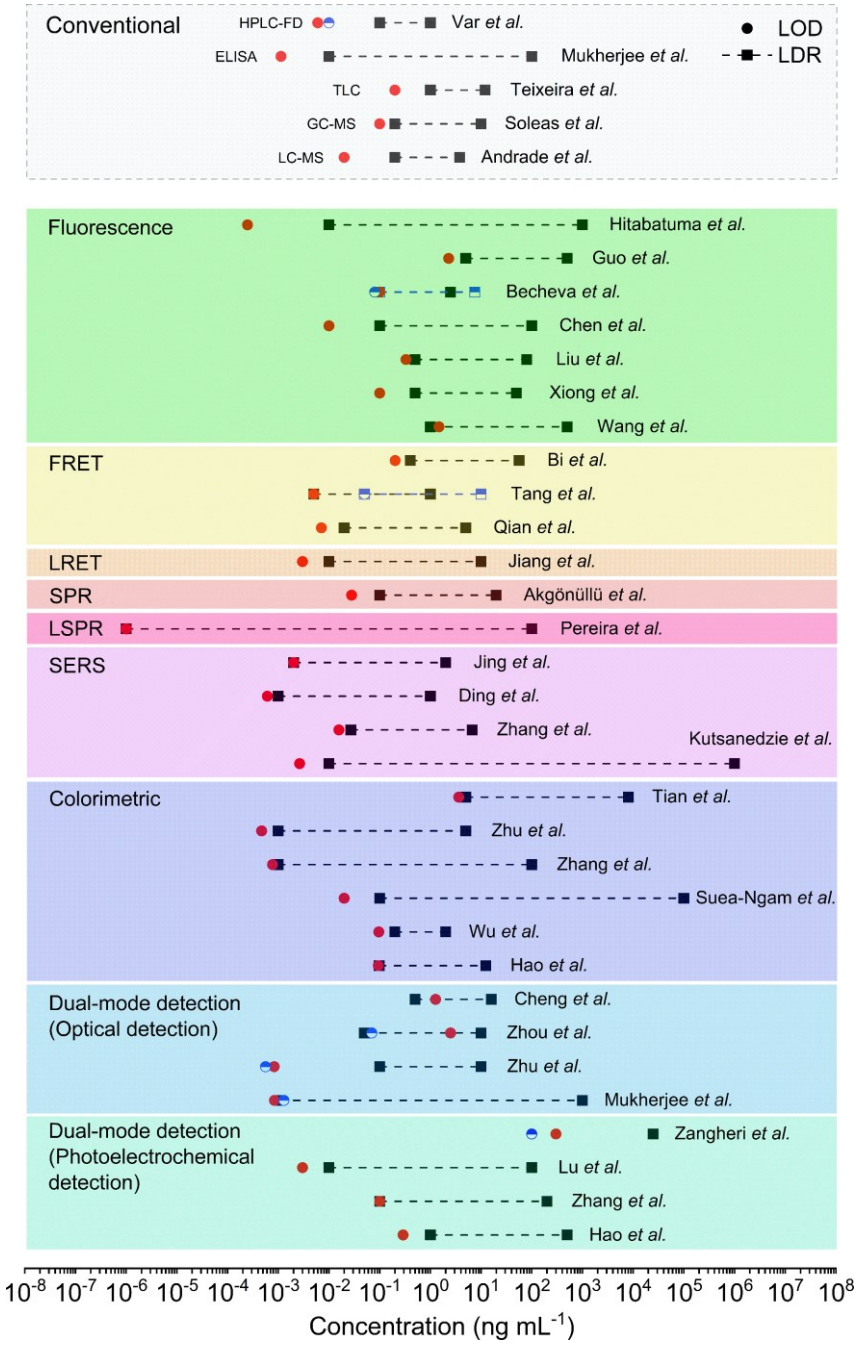


Figure 1.28. Schematic representation of the bioanalytical performance parameters (i.e., the limit of detection (LOD) and linear dynamic range (LDR)), converted to ng mL^{-1}, of the conventional detection methods (i.e., HPLC-FD, ELISA, TLC, GC-MS, and LC-MS) and the biosensors described in the previous section (Table 1.3).

From Figure 1.28, it is possible to confirm that the conventional detection methods presented LOD and LDR values limited to a specific concentration range. However, several alternatives of optical detection methods, reported in the previous section, can overlap and widen the detection range to much lower concentrations, confirming the development of high-quality biosensors for OTA detection. The constant advancement of nanotechnology has driven the development of several nanomaterials' (e.g., NPs, QDs, CDs, GO, and MBs), with distinct features and properties, promising to be employed for a wide variety of biosensing purposes. Thus, the application of nanomaterials in enhanced optical-based detection, taking advantage of optical phenomena (e.g., fluorescence, FRET, LRET, SPR, LSPR, SERS, colorimetry, chemiluminescence, among others) has been revealed as a remarkable biosensing asset for the industrial market.

The most popular nanomaterial-based optical biosensors were found to be fluorescence and colorimetric approaches. These detection methods are described as having high sensitivity, specificity, and accuracy, being relevant alternatives compared to other optical sensing techniques. Considering the advantages of these optical methods, a proper multi-sensing approach based on colorimetry and fluorescence combination strategy emerges as an innovative biosensing resource, towards an absolutely reliable detection signal with dual reciprocal validation, beyond the numerous advantages reported. Nevertheless, the biosensing approach based on the LSPR effects of AuNPs conjugated with OTA mAb revealed to be the most suitable biosensor for OTA detection, when dealing with ultra-low concentrations. This optical sensing method provides real-time, highly sensitive monitoring, with an ultra-lower detection limit, than the counterparts, and a broad dynamic range convenient for a reliable report of OTA contamination. Therefore, new promising commercial strategies for OTA detection based on the LSPR-biosensing approach encouraged the development of several patents in the past decade, as discussed in the following section.

1.4.3. Patents Survey on Localized Surface Plasmon Resonance Biosensors

Label-free optical transducers using the LSPR phenomenon revealed to be a suitable OTA detection approach. However, from hundreds of patents published involving optical biosensors for OTA detection, only 3 patents focused on the LSPR-biosensing approach have been granted until this moment. These patents were based on several recently published articles and are described below.

An LSPR-based high sensitivity aptamer sensor using an intercalation agent was patented (US201715418100A) by the Gwangju Institute of Science and Technology in Korea on April 23, 2019 [173]. The detection strategy of this patented LSPR aptasensor, with enhanced sensitivity, is based on the absorption spectrum changes of the LSPR band of metal NPs (i.e., Au, Pt, Ag NRs). The metallic NPs are fixed to a glass substrate, and, posteriorly, the biorecognition elements (i.e., OTA aptamer) are fixed on the surface of the metallic NPs. The binding event between the aptamer and the mycotoxin creates a GQx molecular structure and, consequently, the RI of the surrounding medium changes, as represented in Figure 1.29a. After the binding event, the LSPR absorption spectrum of the biosensor suffers a redshift. However, the inclusion of an intercalating agent (i.e., berberine, referred to as BB) amplifies the binding effect enabling the detection between a range of 1 pM to 10 μM with an increased sensitivity about 1000 times, as demonstrated in the plots of Figure 1.29b annotated with (w/ BB).

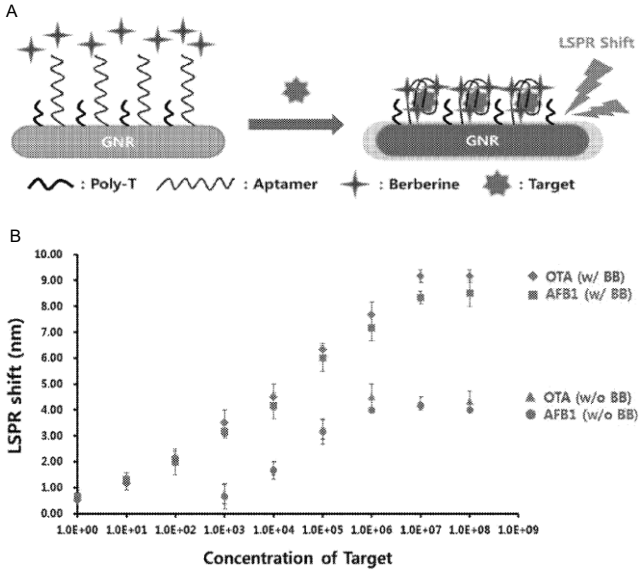


Figure 1.29. Schematic representation of the working mode of LSPR-based high sensitivity aptasensor for OTA detection in (a). Optical response (LSPR peak shift) of the patented biosensor to increasing OTA concentration, and also to another mycotoxin (i.e., AFB1) in (b). Reprinted from patent application publication no. US201715418100A (Kim, Jin-Ho, and Byun [173]).

A reusable optical fiber aptasensor based on photo-thermal effect was patented (US201715814312A) on April 20, 2021, by the Gwangju Institute of Science and Technology [174]. This patent was based on a published article in Biosensors and Bioelectronics Journal in 2018 [175]. The schematic representation of this biosensor is exhibited in Figure 1.30a. The sensing system is composed of a light output unit, sensor unit, detector, and optical fibers. The light output unit, composed of white light or/and a laser with a specific wavelength (i.e., 786 nm), is transmitted to the biosensor, through the optical fiber, and the refraction of the incident light back to the spectrometer allows the monitoring of LSPR band. The sensor unit is fixed inside a proper optical fiber. The biosensing test consists of the immersion of an optical fiber sensor into a solution containing the target for 30 minutes. The biosensor unit is based on highly sensitive Au NRs (601.05 nm/RIU) functionalized with a specific aptamer for OTA detection on the tip of the optical fiber, as showed in Figure 1.30b. The interaction between the biosensor and the contaminated liquid sample generates the binding event between the specific aptamer and OTA, leading to the creation of a GQx molecular structure. Consequently, the RI increases at the surrounding medium of the Au NRs. The irradiated light is directed to the optical detector, and the biological response is identified through redshift of the LSPR absorption spectrum of the Au NRs. LSPR band shift is deeply influenced by the number of binding events that occurred and, consequently, the mycotoxin concentration in the contaminated sample. Therefore, a gradual spectral redshift was observed as OTA concentration increased, as confirmed in Figure 1.30c. The LSPR peak shift displays a linear response to OTA concentrations established between 10 pM to 100 nM, as revealed in Figure 1.30d,e. The LOD value of this biosensor was calculated at 12.0 pM [175]. The photo-heating of the Au NRs allows the release of OTA from the GQx molecular structure and the restoration of the LSPR absorption spectrum to its original state. The photo-thermal effect is induced through the absorption of the laser beam. After the sensor's regeneration (with photo-heating), the detection repeatability achieves good results but is not accurate. Furthermore, the sensor's temperature can increase, causing the denaturation or destruction of the aim target and, consequently, damage to the sensing system. The selectivity of the biosensor was tested through the exposure of the other two mycotoxins, and the optical response was consistent with the expected. The feasibility of the biosensor was tested in spiked grape juice at different concentrations, and the optical response delivery a good agreement with the standard OTA solutions. The recovery values were established between 85.5 and 116.9%. The present invention is based on the portability of the biosensor with a possible quantitative analysis by the simple procedure of immersing the sensor unit in the contaminated liquid sample with good detection performance.

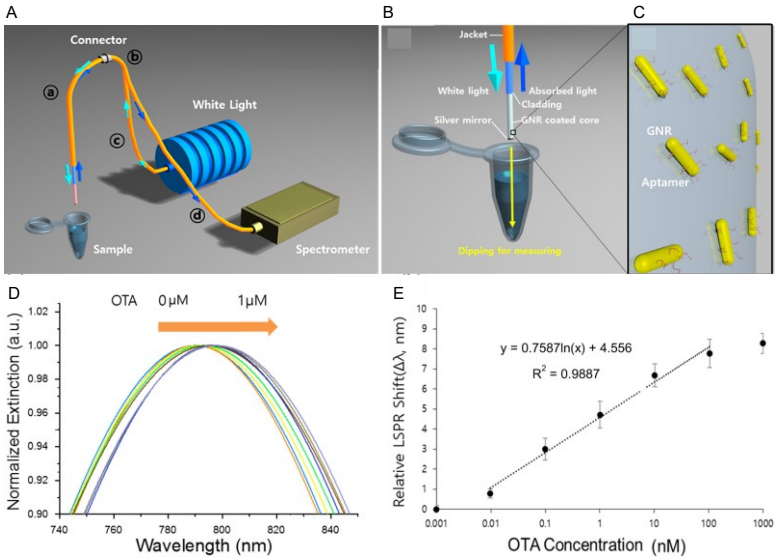


Figure 1.30. Schematic representation of the reusable optical fiber LSPR-aptasensor for OTA detection in (a) and the detection assay in (b). The amplified view of the aptamer modified Au NRs chemically attached to the optical fiber core in (c). UV-vis absorption spectra at different concentrations of OTA in (d). The linear relationship between the relative LSPR peak shift (Δλ) and OTA concentration is plotted in (e). Reprinted with permission from Lee et al. [175]. Copyright 2018 Elsevier

A dual-mode separation immunosensor for a multi-signal sensitive detection was patented (CN201910183819A) on September 21, 2021, by the South China Agricultural University [176]. This patent was based on scientific work available at ACS Applied Materials and Interfaces Journal in 2019 [177]. Photoelectrochemical detection method combined with a colorimetric approach was applied in this biosensor, and its schematic representation is exhibited in Figure 1.31a. This biosensor was developed for OTA, OTB and OTC detection. However, the focus is OTA detection. In a 96-well plate, OTA antigen and a blocking molecule (i.e., dopamine) are previously immobilized. A mixture of different concentrations of OTA and a fixed concentration of OTA Ab (Ab1) is added. At this stage, the immobilized OTA antigen, and the free OTA, available in the solution, compete to chemically bind to the OTA Ab (Ab1). The second moment of the biosensing test consists on the addiction of a nanocomplex composed by HRP encapsulated in a liposome and linked to a second Ab (Ab2). The dissolution of the HRP-liposome-Ab2 complex by a surfactant (i.e., Triton X-100) provides a higher amount of secondary Ab and the release of HRP. The free HRP potentiates the oxidation reaction between the H_2O_2 and the CdS component of the nanocomplex composed by CdS/ZnO NRs on reduced GO (r-GO). The hydroxyl radicals generated by catalytic oxidation can provide alterations in the size and morphology of Au nanocones (Au NCs). The standard Au NCs exhibits a double cone morphology (Figure 1.31b – a), becoming more smoothed along with the experiment (Figure 1.31b – b to c) until accomplishing a spheroidal structure (Figure 1.31b –d).

The change of the Au NCs' morphology and size lead to the blueshift of LSPR peak position and, consequently, color variations, from brown to pink, in the test solution, as shown in Figure 1.31c. The multicolor change and the blueshift of the LSPR peak position correspond to a decrease in OTA content. The colorimetric approach has a total duration of 10 minutes and exhibits a dynamic range established between 1 ng L^{-1} and 5 μ L^{-1} with a LOD value was 1.46 ng L^{-1}, as demonstrated in Figure 1.31d,e. Regarding the photoelectrochemical detection, the OTA content influences the amount of HRP-Liposome-Ab2 complex immobilized. At higher OTA concentrations, a smaller amount of the HRP-Liposome-Ab2 complex is immobilized, and the HRP release is also lower for the catalytic oxidation resulting in higher photoelectricity. This detection method also shows a good linear relationship between 1 ng L^{-1} and 5 μ L^{-1}, and the LOD value was 0.79 ng L^{-1}.

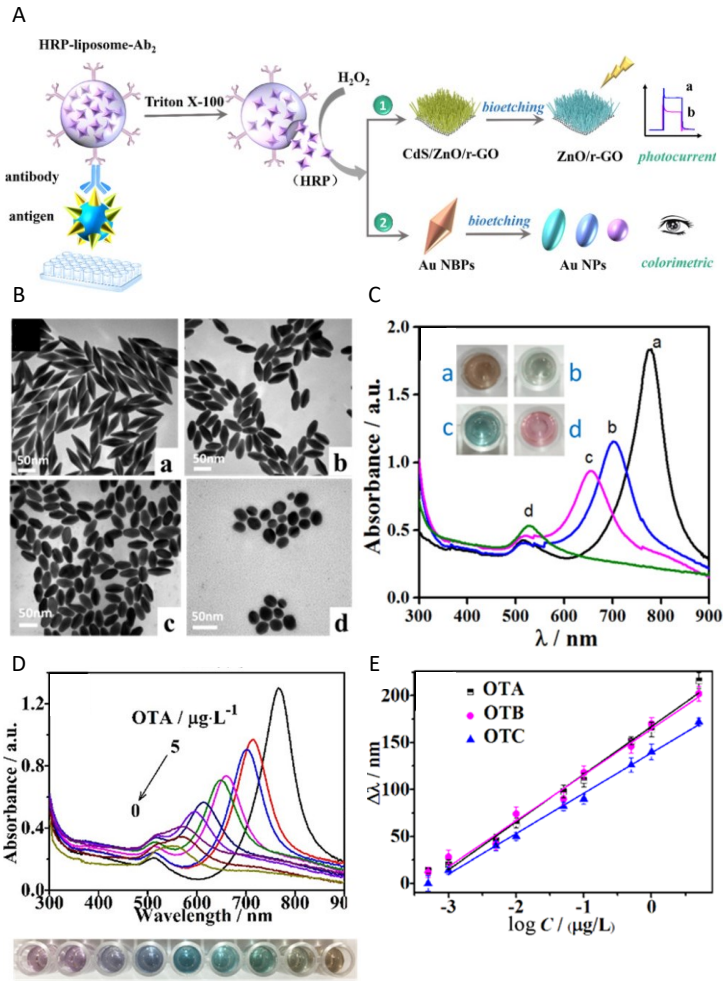


Figure 1.31. Schematic representation of the dual modality immunosensor for OTA detection in (a). TEM images of the morphology and sizy evolution of the Au NCs during the detection assay in (b), and their corresponding UV-vis absorption spectra in (c). UV-vis absorption spectra at different OTA concentrations in (d), and the linear relationship between the blueshift of the longitudinal LSPR peak (Δλ) and OTA concentration in (e). Reprinted with permission from Wei et al. [177]. Copyright 2019 Elsevier.

1.5. Major Challenges and New Trends of Ochratoxin-A Optical Sensors

The food industry focuses on preventing fungus development and mycotoxin presence in agricultural fields. However, the application of sensing detection approaches to verify and confirm food products' safety is mandatory. Typically, the chemical detection of possible contaminants occurs at the final stages of food production. The delayed OTA detection in the food product can cause high economic losses (e.g., decontamination costs and food waste). Therefore, the performance of biochemical analysis in real-time or in several food production steps can be highly advantageous. The use of new biosensing devices arises from the strategic combination of advanced nanofabrication methods and novel nanomaterials, allowing to overcome the current challenges. The development of an OTA biosensor, with faster detection speed combined with an extended range of biosensing performance, enables an early OTA identification in contaminated food. Consecutively, the primary application of decontamination approaches, according to the food safety entities' specifications, prevents food waste and ensures food safety.

One of the most critical aspects of OTA detection is the assumption that the mycotoxin present in the specific foodkind maintains its chemical structure. However, from fungus production to food processing, OTA is exposed to several factors (i.e., biological and environmental agents). These possible interactions can develop a "modified mycotoxin" with a new chemical structure naturally developed to restore biochemical stability between the OTA and the surrounding environment [178,179]. This modified OTA might provide broad exposure and potential toxicity, without being detected in a reasonable time with the existing routine analytic techniques. Consequently, the early detection of this modified OTA through the combination of several biorecognition approaches on a suitable biosensor is essential to ensure food safety.

Optical sensing technology emerges as a powerful resource for biosensing applications, allowing the detection and distinguishing of the target analyte in a variety of contaminated samples. The sensing performance of an optical biosensing detection strategy is variable accordingly to the immobilized biorecognition element or detection mode (i.e., optical-based phenomenon) and defined by several analytical sensing parameters: sensitivity, reproducibility, specificity, precision, and accuracy. Therefore, these analytical sensing parameters for OTA optical detection depend on the specific biorecognition layer (i.e., aptamer or Ab). For example, Ab denaturation, cross-reaction interaction, loss of bioactivity, and poor chemical stability are possible limitations in the feasibility of the biosensor. In addition, accuracy is also a vulnerable point in the development of a biosensor, whereby the adsorption of biomolecules of the test sample in the biosensor surface may interfere with the detection process [180]. Therefore, a

drawback is the sample pretreatment, which is required to remove undesirable components of food samples through an application of effective cleaning (and concentrating) techniques [181,182].

The biodetection market exhibits undeniable economic impacts on nanotechnology development and, thus, enables biosensing improvement toward the biosensor's potential commercialization. The development of novel optical-based biosensors reveals several economic drawbacks: high investment (i.e., stable and continuous financial investment) and slow economic return [96]. The development of patented commercialized biosensing is laborious and cumbersome, including minor and gradual time-consuming phases. The prolonged process for both regulatory approval and patent licensing, and the delayed transition from laboratory prototyping to industrial scale-up production (i.e., scalability constraints and cost-effectiveness factor) are explicit time-consuming disadvantages, that lead to unattractive financial investment misconceptions [96]. The inclusion of novel nanomaterials, an efficient nanocomposites' modification, and the immobilization strategy creates a new broad range of possibilities in the detection sensing biosystem, with optimal analytical performance in small devices and high-level cost-effectiveness. However, nanomaterials may not be suitable for real world applications and mass manufacturing, since they require complex and challenging production conditions, very often difficult to up-scale. Consequently, it is essential to develop an optimized fabrication process of nanomaterials that can guarantee their reproducibility and stability through inexpensive, easy to prepare, and based on environmentally friendly production techniques [183,184]. Moreover, most studies of new biosensing approaches are manufactured by prototyping techniques, and do not refer to the importance of large-scale sample testing, limiting, from one point of view, the development of biosensors and their commercialization. Therefore, it is essential to develop a cost-effective method with standardized bioanalytical protocols for the synthesis and treatment of the sensing platform, including a reliable immobilization efficiency and a long shelf-life [185,186].

Currently, these major challenges are being addressed by academic and industry communities, which led to new trends in optical biosensors that aim to enhance biosensors' analytical performance. Microfluidic devices, which allow analytical assays miniaturization, have emerged as an essential tool for biosensors, due to their numerous advantages: i) precise control of flow, ii) reagents volume, iii) reaction kinetics, iv) high surface area-to-volume and v) compatibility with standard analytical technologies [187,188]. The miniaturization combined with microfluidics integration potentializes the sensing performance and speed of analyte detection [189], promoting the development of multiplexing technologies, that can simultaneously detect several analytes of interest [190].

The sensing improvement, through nanofabrication, and the development of point-of-care platforms, are fundamental for several detection applications (i.e., identification and quantification), especially in food safety and quality. Beyond, other strategies have been applied to enhance the analytical performance of optical biosensors, e.g., fluid mixing and analyte concentrating (i.e., evaporating, thermo- and electrophoresis, and microbubble-based solute accumulation), as physical approaches to increase analyte–biosensor interaction during the incubation (detection step) [191]. However, one of the most common enhancing sensing approaches relies on label-based optical detection, using the specific properties of labels (i.e., enzymes, fluorophores, colloidal Au, or Ag-enhanced particles) for chemical signal amplification (i.e., polymerization and nanocatalysts signal-amplification strategies) [191,192]. In contrast, a label-free optical detection strategy translates the biological recognition event into a measurable optical signal without using molecular auxiliary structures, facilitating the entire detection process [192]. This optical detection strategy relies on physical signal amplification provided by transducer substrate modification (e.g., including plasmonic metal NPs) [191,193]. In particular, LSPR optical-based biosensors reveal remarkable advantages such as label-free monitoring with real-time analysis that delivers a high sensing performance with the potential to be combined on a cost-effective portable lab-on-chip simple to handle [124]. As disclosed in the review, LSPR-based biosensors have been revealed as an outstanding label-free sensing strategy, particularly for OTA detection. In the biosensing scope, the combination of several enhancing sensitivity approaches concerning sampling, target recognition, and signal transduction can overcome the current limitations and improved biosensor's performance [191].

1.6. Conclusion

In the food industry, the safety of food products is crucial for preventing foodborne illness and injury. OTA is a possible carcinogenic mycotoxin that suddenly and inevitably occurs in several feed types and foodstuff, leading to harmful health effects and significant economic losses in the agriculture sector. The ingestion of OTA causes progressive tissue damage in some organs of the human body (e.g., liver and kidneys), inducing potentially fatal diseases (i.e., BEN, CIN, and Alzheimer's). Therefore, several regulatory food safety institutions established the limit of concentration of this mycotoxin on any potentially contaminated foods. Conventional detection techniques (e.g., HPLC-FD and LFIA) are commonly applied; however, they do not meet current needs (e.g., direct, real-time, and quantitative analysis). Considering the worldwide concern in OTA detection, advances in nanotechnology provided suitable alternatives to conventional analytical techniques. Scientific efforts led to the development of portable label-free optical

biosensors with real-time monitoring, with outstanding biosensing performances (i.e., LOD below the defined threshold), beyond small-scale devices with high cost-effectiveness. In this review, several reported biosensors overcome the LOD of standard techniques (e.g., HPLC-FD and LFIA), confirming the potential of novel optical phenomena nanotechnologies for a reliable and efficient detection. Despite the most common optical sensing approaches being fluorescence and colorimetric methods, the LSPR-based biosensing approach was revealed to be the most promising nanotechnology for OTA monitorization application, regarding its biosensing parameters. This optical biosensing approach was demonstrated to be the most sensitive, associated with lower detection limits and a significantly broad dynamic range capable of detecting OTA at considerable limits of concentration. Finally, several patents for commercial methods have been reported, validating the LSPR-based biosensing potential as a simplified low-cost selective nanodevice capable of a real-time monitoring of this mycotoxin in diverse types of foodstuffs.

Chapter 2

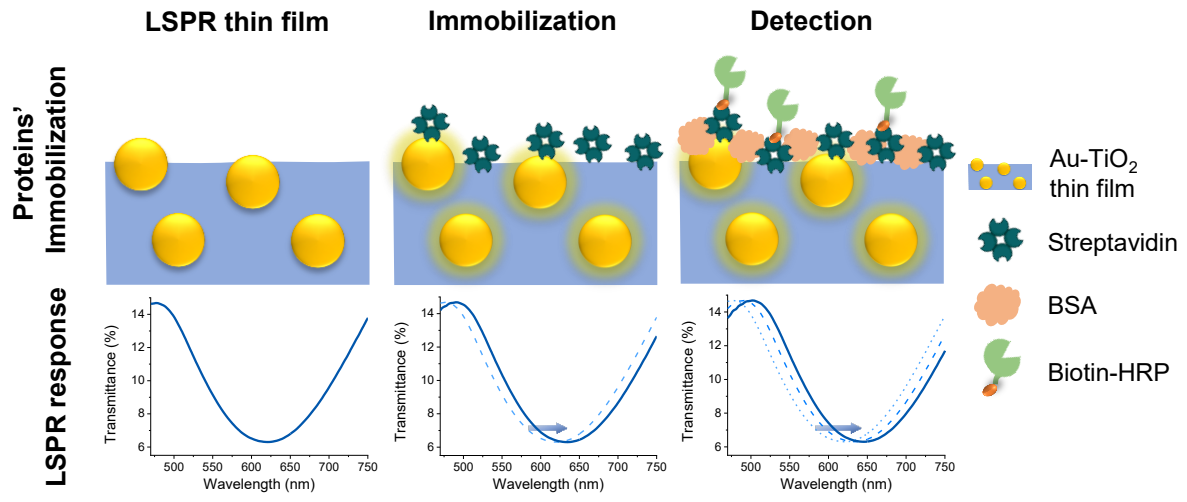
Immobilization of Streptavidin on a Plasmonic Au-TiO_2 Thin Film towards an LSPR Biosensing Platform

P. Pereira-Silva†, **D.I. Meira†**, A. Costa-Barbosa, D. Costa, M.S. Rodrigues, J. Borges, A. V. Machado, A. Cavaleiro, P. Sampaio, F. Vaz, Immobilization of Streptavidin on a Plasmonic Au-TiO_2 Thin Film towards an LSPR Biosensing Platform, Nanomaterials. 12 (2022) 1526. https://doi.org/10.3390/nano12091526.

2.1. Abstract

Optical biosensors based on localized surface plasmon resonance (LSPR) are the future of label-free detection methods. This work reports the development of plasmonic thin films, containing Au nanoparticles dispersed in a TiO_2 matrix, as platforms for LSPR biosensors. Post-deposition treatments were employed, namely annealing at 400 °C, to develop an LSPR band, and Ar plasma, to improve the sensitivity of the Au-TiO_2 thin film. Streptavidin and biotin conjugated with horseradish peroxidase (HRP) were chosen as the model receptor–analyte, to prove the efficiency of the immobilization method and to demonstrate the potential of the LSPR-based biosensor. The Au-TiO_2 thin films were activated with O_2 plasma, to promote the streptavidin immobilization as a biorecognition element, by increasing the surface hydrophilicity (contact angle drop to 7°). The interaction between biotin and the immobilized streptavidin was confirmed by the detection of HRP activity (average absorbance 1.9 ± 0.6), following a protocol based on enzyme-linked immunosorbent assay (ELISA). Furthermore, an LSPR wavelength shift was detectable (0.8 ± 0.1 nm), resulting from a plasmonic thin-film platform with a refractive index sensitivity estimated to be 33 nm/RIU. The detection of the analyte using these two different methods proves that the functionalization protocol was successful and the Au-TiO_2 thin films have the potential to be used as an LSPR platform for label-free biosensors.

Keywords: Au-TiO_2 thin film; Plasmonic biosensor; Streptavidin–Biotin; LSPR detection



2.2. Introduction

Biosensors have been widely developed as a tool for the environmental, food, and medical areas [97,194,195]. Due to their easy, rapid, low-cost, highly sensitive, and selective analysis, biosensors have a huge impact on the evolution of detection and diagnosis methods [196]. Usually, biosensor devices are composed of biorecognition elements (e.g., DNA, enzymes, and antibodies), for selective/specific binding with target analytes, and a transducer component converting the binding event into a readable signal. Based on the type of transducer, biosensors can be classified as electrical, thermal, and optical, among others [197].

Optical biosensors based on localized surface plasmon resonance (LSPR) are mentioned as one of the next generation of plasmonic label-free detection methods [198]. The optical phenomenon of LSPR occurs when an incident electromagnetic field interacts with noble metal nanoparticles (e.g., silver or gold), which can be dispersed in a dielectric matrix as a thin film [23,199,200]. As a result, the conduction band electrons of the nanoparticles oscillate in resonance with the incident electromagnetic wave, and this interaction enhances the local electromagnetic field and leads to a strong absorption band [201–203]. The LSPR properties are influenced by several factors, such as the surrounding dielectric matrix, the nanoparticles' features (concentration, size, shape, and distribution), and the refractive index of the environment [204–206]. Therefore, it is possible to tune the LSPR response of nanocomposite thin films to be sensitive to subtle refractive index changes [207–209], such as those induced by the molecular interactions near the nanoparticles' surface, providing effective transduction of the binding events into an LSPR band shift [210,211]. So, no conjugating reporter molecules are required, making LSPR-based sensing label-free, portable, and low-cost and allowing real-time analysis [212]. Moreover, the optical hardware is smaller, more affordable, and simpler compared to other optical sensors [213].

Many efforts have been made to develop LSPR-based sensors using different approaches such as (1) solution phase-based colloidal nanoparticles, (2) nanoparticle-coated optical fiber platforms, and (3) flat substrate-based platforms [22]. Concerning the last approach, plasmonic thin films are promising for sensing platforms, namely magnetron-sputtered nanocomposite thin films containing noble metal nanoparticles (Au and/or Ag) dispersed in dielectric or semiconducting matrices [34,36,214]. As solid supports, the nanoparticles are immobile in an inert solid matrix, preventing nanoparticle aggregation, a highly observed nuisance in colloidal solutions [27]. Moreover, flat substrate-based LSPR sensors show higher reproducibility, signal-to-noise ratio, and sensitivity compared to sensing approaches based on isolated nanoparticles [215–218]. Through adjustments in the deposition parameters and post-deposition treatments, it is possible to modify the plasmonic thin films' nanostructure to be used as both platforms

and transducers, detecting and converting the molecular interactions into an LSPR band shift [193,219–221].

Biotin (or vitamin B7/vitamin H) is a small molecule that binds with high affinity, specificity, and stability to streptavidin, a tetrameric protein with four identical binding sites for biotin [222,223]. The femtomolar affinity of biotin to streptavidin is one of the highest reported for a non-covalent interaction [224], and therefore it is commonly used as a model system for evaluating the performance of a biosensor [225–227]. Sensors can be coated with streptavidin protein, and biotin can be functionalized with any molecule, including enzymes such as horseradish peroxidase (HRP). The strong, specific, and stable bond between streptavidin and biotin can be easily confirmed by HRP activity [228].

Considering the demand for sensitive and fast biosensors, the development of plasmonic thin films as sensing platforms is beneficial. Therefore, in this work, the biosensing ability of the nanoplasmonic thin films, composed of gold nanoparticles dispersed in a titanium dioxide matrix (Au-TiO_2), was tested through the attachment of molecular biorecognition layers. These thin films were produced by reactive direct current (DC) magnetron sputtering and subjected to post-deposition treatments to promote the growth of the Au nanoparticles throughout the TiO_2 matrix [36]. Streptavidin protein was immobilized on the surface of the thin films, as a biorecognition layer, followed by binding with biotin conjugated with HRP, in a procedure similar to enzyme-linked immunosorbent assay (ELISA) [229]. Then, the plasmonic platform's ability to detect the analyte (biotin molecule) was evaluated through two different methods: the detection of HRP activity and the LSPR band shift. This work aimed to develop an LSPR biosensor based on plasmonic Au-TiO_2 thin films, as well as to demonstrate the efficiency of the immobilization protocol, using the streptavidin and biotin–HRP interactions.

2.3. Materials and Methods

2.3.1. Preparation and Characterization of the LSPR Biosensor Platform

2.3.1.1. Deposition of Au-TiO_2 by Reactive DC Magnetron Sputtering

Thin films, composed of gold (Au) dispersed in a titanium dioxide (TiO_2) matrix, were deposited by one-step reactive DC magnetron sputtering in a custom-made high-vacuum chamber. Two different types of substrates were used for the depositions, namely glass lamellae (ISO8037) and monocrystalline silicon (Si) wafers with (100) orientation. Before the depositions, these substrates were cleaned with oxygen (O_2) plasma, at a partial pressure of 60 Pa for 5 min, to remove impurities from the substrate's surface. Then, to activate the substrate's surface and improve the thin film's adhesion, argon (Ar) plasma was applied at a partial pressure of 60 Pa for 15 min. Those plasma treatments were performed at a base pressure

of 20 Pa in a Diener (Zepto Type Model) instrument, operating at a power of 50 W, using a 13.56 MHz RF generator.

A high purity (99.99%) and rectangular (200 mm × 100 mm × 6 mm) titanium target was used as a cathode for the production of thin films. Gold pellets with a total surface area of 16 mm^2 and a thickness of 0.5 mm were placed symmetrically in the preferential erosion zone of the target for the homogeneous incorporation of the noble metal in the TiO_2 matrix. The substrates were placed on a grounded rotating substrate holder, with a constant rotation speed of 12 rpm.

Before the depositions, the sputtering chamber was pumped down to 3.2×10^{-4} Pa. The deposition of the thin films occurred at a working pressure of 4.0×10^{-1} Pa, using a plasma of Ar (working gas) and O_2 (reactive gas). The Ar and O_2 flows were kept constant during the deposition at partial pressures of 3.6×10^{-1} Pa and 4.0×10^{-2} Pa, respectively. The deposition time was 30 min, based on previous work [36]. The applied direct current density was set to 100 A m^{-2}, resulting in a (negative) target potential of (400 ± 4) V.

2.3.1.2. Post-Deposition Annealing Treatment to Promote the Growth of the Au Nanoparticles

Au-TiO_2 thin films were subjected to an in-air annealing treatment to promote the diffusion of Au atoms and hence the growth of Au nanoparticles throughout the matrix, enhancing the LSPR response, as reported in other works [205,230,231]. The thermal treatments were performed in a programmable furnace (Termolab FP21) at 400 °C. The chosen annealing temperature was reached by raising the temperature at a rate of 5 °C/min until the desired temperature was attained, fixing this temperature for 5 h [36]. The samples were allowed to cool freely inside the furnace before reaching room temperature.

2.3.1.3. Surface Modification through Plasma Etching

The surface of the nanoplasmonic thin films was modified by plasma etching, using an Ar atmosphere at a partial pressure of 60 Pa for 60 min. The etching exposes the Au nanoparticles at the thin film's surface, increasing the nanoparticles' surface area available to the targeted biological analytes. This surface modification also increases the thin film's sensitivity, as reported in previous work [36]. A Diener (Zepto Type Model) instrument, using a 13.56 MHz RF generator, was used for plasma etching, operating at a base pressure of 20 Pa and 50 W of power. Four independent samples were used to estimate (mean ± standard deviation) the effect of plasma treatment on the LSPR band.

2.3.1.4. Characterization of Au-TiO_2 Thin Films

The in-depth chemical composition profile in thin films deposited on silicon wafers was evaluated by Rutherford backscattering spectrometry (RBS) with a Van de Graff accelerator. The measurements were made in a small chamber, where three detectors were installed: a standard detector at 140° and two pin-diode detectors located symmetrically to each other, both at 165°. Spectra were collected for 2 MeV $^4He^+$ beams at normal incidence (0°). The obtained RBS data were analyzed with IBA DataFurnace NDF v10.0b [232], and the double scattering and pileup were calculated with the algorithms given in N.P. Barradas et al. (2005) [233] and N.P. Barradas et al. (2006) [234], respectively.

The thickness of the thin films, before and after Ar plasma treatment, was evaluated in cross-sections of thin films deposited on silicon wafers. A scanning electron microscope, NanoSEM—FEI Nova 200 (FEG/SEM), operating at 10 keV was used.

2.3.1.5. Modification and Measurement of the Thin Films' Hydrophilic Property

The O_2 plasma treatment has been reported as a protein immobilization promoter [235]. Therefore, the surface hydrophilic property of the Au-TiO_2 nanoplasmonic thin film was modified by applying an O_2 plasma at a partial pressure of 60 Pa and 37.5 W power. The exposure times were 10, 30, 60, 120, 150, 180, 210, and 300 s to evaluate the influence of a reactive plasma on thin films' surface properties. The base pressure was 20 Pa in the Diener (Zepto Type Model) instrument, using a 13.56 MHz RF generator. Three independent samples were used to estimate (mean ± standard deviation) the effect of plasma treatment on optical properties.

The thin films' wettability was characterized by contact angle measurements, as a function of the time of exposure to O_2 plasma. The contact angle measurements were performed using the sessile drop in static mode, at room temperature and humidity in an OCA 20 instrument with a CCD video camera (resolution of 752 × 582 pixels) from Dataphysics Instruments GmbH (Filderstadt, Germany). Deionized water (3 µL drop) was used as the test liquid. The contact angle was calculated according to the Young–Laplace method [236], using the software SCA 20. At least 5 measurements were performed for each condition, using 3 samples, and the average contact angle was calculated. The contact angle values were plotted and analyzed using one phase decay in GraphPad Prism 9 software.

2.3.2. Protein Immobilization and Binding Assay

An in-house protocol built on standard HRP-based colorimetric ELISA protocol [229] was used for the detection of proteins' immobilization on thin-film surfaces. The streptavidin–biotin pair was used as molecules for receptor–ligand binding, in which biotin is conjugated with HRP.

2.3.2.1. Concentration Optimization

First, the ideal concentrations of streptavidin–biotin to be used were determined. So, a matrix of different concentrations of streptavidin (Millipore, Burlington, MA, USA) and biotin–HRP (Thermo Scientific, Waltham, MA, USA) ranging from 0.0025 to 25 µg/mL and from 0.0075 to 75 µg/mL, respectively, were used in the assay, carried out in 96-well plates (Thermo Scientific, Waltham, MA, USA).

Streptavidin was incubated for 1 h in each well, followed by washing steps with phosphate-buffered saline (PBS, pH 7.4), with 0.05% Tween-20 (PBS-T, from Sigma, St. Louis, MO, USA). To block unspecific binding sites, 2% bovine serum albumin (BSA, from Sigma-Aldrich, St. Louis, MO, USA) in PBS-T was added for another hour and then washed with PBS-T. The conjugated ligand, biotin–HRP, was incubated for 30 min and then washed with PBS-T. The substrate 3,3′,5,5′-tetramethylbenzidine (TMB, from Sigma-Aldrich, St. Louis, MO, USA) was added to the wells, to be converted into a colored product by the enzyme HRP. The enzymatic reaction lasted for 12 min and was stopped by adding phosphoric acid (H_3PO_4 1 M, from PanReac AppliChem, Darmstadt, Germany). The absorbance of the reaction product was measured at 450 nm, using a SPECTRAmax Plus 384 (Molecular Devices, San Jose, CA, USA). Samples with no streptavidin or biotin–HRP (blank) and samples with no specific binding (containing either only streptavidin or biotin–HRP) were used as controls. The optimal streptavidin–biotin ratio was calculated from the absorbance results.

2.3.2.2. Influence of O_2 Plasma on Streptavidin Immobilization

Kim et al. reported the enhancement of proteins' immobilization on surfaces after O_2 plasma treatment [235]. Therefore, an O_2 plasma was applied for 60 s to Au-TiO_2 thin films, at a partial pressure of 60 Pa and 37.5 W power.

Then, a matrix of different concentrations of streptavidin and biotin–HRP, ranging from 1.25 to 25 µg/mL and from 0.375 to 1.5 µg/mL, respectively, were used in the assay. The Au-TiO_2 thin films were incubated for 1 h with streptavidin, and the procedure followed was the same as the experimental protocol described in Section 2.3.2.1. Glass substrates previously treated with O_2 plasma were used as immobilization control, and Au-TiO_2 thin films and glass substrates without previous O_2 plasma treatment

were used to assess the effect of O_2 plasma on streptavidin immobilization. Blank sample and non-specific binding (containing either only streptavidin or biotin–HRP) samples were also used as binding controls.

2.3.2.3. Streptavidin Immobilization on Thin Film's Surface

Based on the ideal ligand–receptor ratio and surface binding area, an extrapolation was made for protein immobilization on the thin film's surface. To enhance protein immobilization, the Au-TiO_2 thin film's surface was previously activated with O_2 plasma treatment (60 s and 37.5 W). Then, streptavidin was immobilized for 1 h, and the procedure followed was the same as the one mentioned above in Section 2.3.2.1. Nine independent thin films and 9 glass substrates (as immobilization control) were used to assess the repeatability. Blank sample and non-specific binding (containing either only streptavidin or biotin–HRP) samples were also used as binding controls.

2.3.3. Optical Response of the LSPR Biosensing Platform

The optical analysis of the Au-TiO_2 thin films, namely the measurement of the LSPR band in transmittance mode, was performed in a custom-made optical system, with a light source (tungsten lamp), a custom sample holder, and an Ocean Optics HR4000 spectrometer, connected by optical fibers [237].

2.3.3.1. Refractive Index Sensitivity of Au-TiO_2 Thin Films

The refractive index sensitivity (RIS) of the produced Au-TiO_2 thin films was determined by monitoring their optical transmittance while immersed in solutions with different refractive indexes. Sucrose solutions of 20% (*w/w*) (η = 1.3639 RIU), 30% (*w/w*) (η = 1.3812 RIU), 40% (*w/w*) (η = 1.3999 RIU), and 50% (*w/w*) (η = 1.4201 RIU) were used in the experiments. The transmittance spectra were monitored for 1 min (for each half-cycle), and each spectrum was acquired using an integration time of 4 ms and an average of 500 scans. Data were processed by the NANOPTICS software to identify changes in the T-LSPR wavelength peak [238]. RIS was calculated using the equation RIS = $\Delta\lambda/\Delta\eta$ (nm/RIU), assuming a semi-infinite layer of the aimed solution, where $\Delta\lambda$ represents the peak wavelength shift and $\Delta\eta$ the difference of the refractive index of surrounding media [27].

2.3.3.2. LSPR Response of the Streptavidin-Immobilized Thin Films to Biotin–HRP

The LSPR response of the streptavidin-immobilized Au-TiO_2 thin films in the presence of the analyte was evaluated. This experimental step was crucial for assessing their potential as a biosensing platform.

Therefore, the surface of the thin films (the LSPR platform) was immobilized with streptavidin and blocked with BSA as described above, followed by a 30 min incubation with PBS, to build the biosensor. The optical spectra were recorded, corresponding to the basal spectra of the biosensor. Finally, the LSPR biosensor was incubated for 30 min with the ideal concentration of biotin–HRP, and the optical response was measured. In each measurement, the LSPR biosensors were immersed in 1 mL of PBS and the optical spectra were monitored for 10 min in transmittance mode. An integration time of 4 ms and an average of 500 scans were used to acquire each spectrum. The repeatability parameter was determined in 3 independent measurements. Data were processed by the NANOPTICS software to assess the LSPR response of the biosensor, identifying changes in the T-LSPR band peak [238].

Finally, TMB was added to confirm the binding of biotin–HRP to streptavidin-immobilized thin films and for correlation with LSPR response. After 12 min incubation, a colored product was detected.

2.4. Results and Discussion

2.4.1. Characterization of Au-TiO_2 Thin Films

2.4.1.1. Chemical, Optical, and Morphological Properties of Au-TiO_2 Thin Films

Materials' properties affect biosensor development, so different characterization techniques were applied to analyze the microstructural characteristics and optical response of the plasmonic thin films. The atomic concentration (at. %) of each chemical element present in the thin film, after thermal treatment at 400 °C, was determined by RBS analysis. The annealed Au-TiO_2 thin films are composed of 20.2 ± 0.5 at. % of gold. The O atomic concentration was found to be 50 ± 5 at. %, and the amount of Ti was found to be 30.4 ± 0.5 at. %. Nevertheless, given the uncertainties of the measurements, the matrix can be considered nearly stoichiometric.

Regarding the optical responses, Au-TiO_2 thin films were evaluated by spectrophotometry in transmittance mode. The as-deposited film is transparent to the visible light and lacks an LSPR band, as the non-crystallized nanoparticles formed during the sputtering process are too small (typically below 10 nm) [239]. The LSPR band appears after annealing treatment at 400 °C due to the growth and coalescence of the Au nanoparticles dispersed throughout the TiO_2 matrix, which typically crystallizes in the anatase phase, as previously observed [34,35,240,241]. The transmittance band minimum is positioned at a wavelength of 618 nm, corresponding to T = 6.7% (Figure 2.1a).

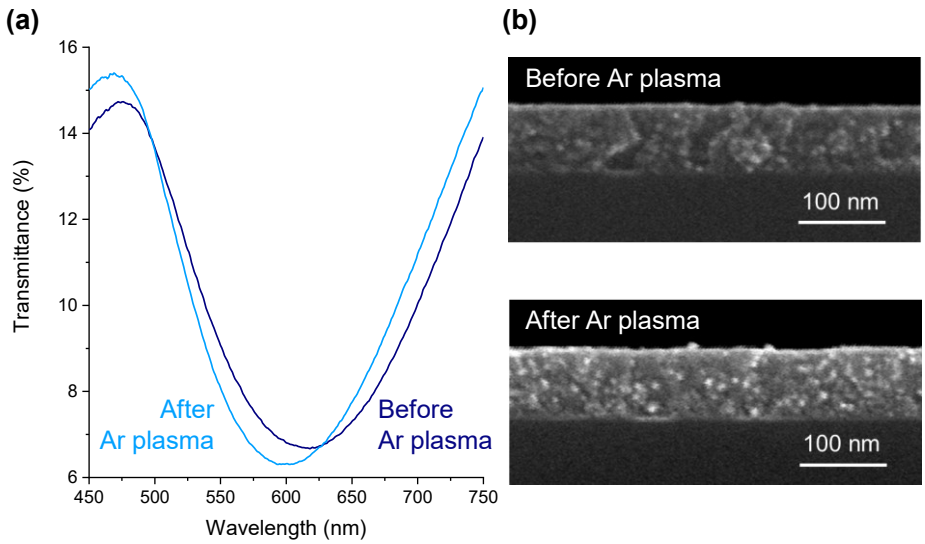


Figure 2.1. Effect of Ar plasma treatment on the optical and morphological properties of the Au-TiO_2 thin films annealed at 400 °C: (a) optical transmittance spectra and (b) cross-section micrographs before and after Ar plasma.

To develop nanoplasmonic thin films as a sensing platform, biorecognition elements must be immobilized on their surfaces to detect the analyte. Nevertheless, since the plasmon decay length of the nanoparticles is typically below a few tens of nanometers, and as demonstrated by discrete dipole approximation simulation models [29], the matrix where the nanoparticles are embedded might hinder the platform's sensitivity. On the other hand, proteins can be immobilized as biorecognition elements by adsorption on the Au nanoparticles [242]. Due to these reasons, the Au nanoparticles embedded in the TiO_2 matrix need to be partially exposed to the environment [27], allowing the immobilization of the molecular recognition elements. As shown in previous works [34,36], to enhance the density of gold nanoparticles at the film's surface, an Ar plasma treatment was applied, giving rise to an LSPR band blueshift of about 16.3 nm ± 3.7 nm (Figure 2.1a). This shift is due to an increase in the number of nanoparticles exposed to air, which become partially embedded in the TiO_2 matrix, thus decreasing the average refractive index surrounding them. However, as can be observed in Figure 2.1b, the plasma treatment did not cause a considerable etching of the matrix. In fact, in SEM micrographs, the annealed Au-TiO_2 thin films presented an average thickness of 93 ± 1 nm, and after the Ar plasma treatment, they exhibited an average thickness of 94.8 ± 0.8 nm. This implies that the plasma etching probably removed only some weakly adhered layers and some chemical contaminants on the thin film's surface (such as hydrocarbon layers) [36].

2.4.1.2. Au-TiO_2 Thin Films' Hydrophilic Properties

The biosensor development is determined by the adhesion of the biorecognition layer to the platform's surface. The presence of hydroxyl groups on the biosensor's surface promotes the adsorption of biomolecules [235,243]. Therefore, the Au-TiO_2 thin films were subjected to an activation plasma (O_2 plasma) at different exposure times, and the effect was evaluated through wettability measurements, based on the contact angle of deionized water droplets. The contact angle is defined as the tangent of the liquid–vapor interface and the solid surface at the three-phase contact line [244]. Surfaces with contact angles lower than 65° are considered hydrophilic due to the presence of polar functional groups [245].

Without O_2 plasma treatment (0 s), the Au-TiO_2 thin film's surface is already considered hydrophilic since it produced a contact angle of 29 ± 4° (Figure 2.2). After 10 s of O_2 plasma treatment, the contact angle value significantly dropped to 8 ± 1°. Increasing the time of O_2 plasma treatment did not induce major changes in contact angle value, and the plateau was reached after 60 s at 7°. From here, the thin films were treated with O_2 plasma for 60 s before immobilization with the biorecognition layer.

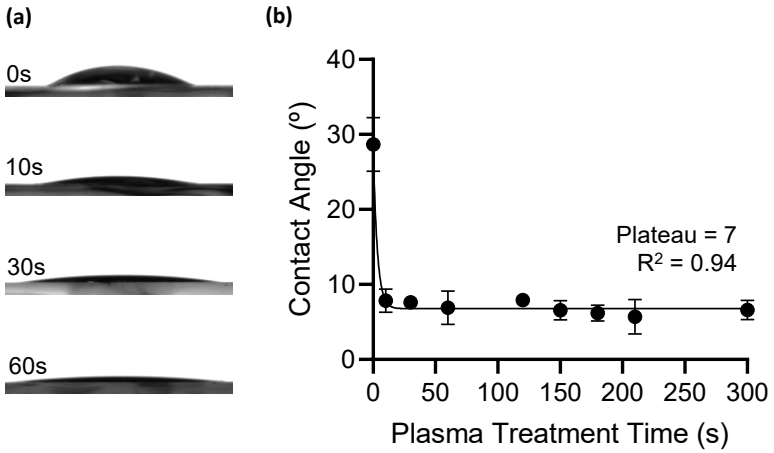


Figure 2.2. Hydrophilic properties of the Au-TiO_2 thin films. (a) Photographs of a water droplet and the (b) contact angle (in degrees) measured as a function of O_2 plasma treatment time in seconds (s) on the surface of Au-TiO_2 thin films.

The effect of O_2 plasma on the LSPR band was also evaluated, and it was observed that the exposure time of 60 s caused an LSPR band shift, to the right (redshift), of 4 ± 1 nm (Figure 2.3). Therefore, the O_2 plasma changed the thin film surface wettability, increasing the hydrophilicity through the formation of hydroxyl groups, and induced minor changes in the LSPR band.

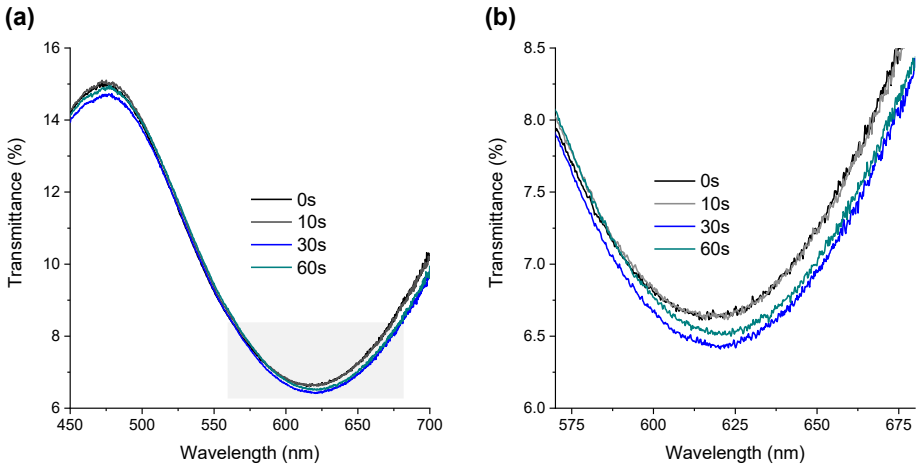


Figure 2.3. LSPR band evolution as a function of O_2 plasma treatment time (0, 10, 30, and 60 s) of the Au-TiO_2 thin film annealed at 400 °C: (a) transmittance spectra from 450 to 700 nm and (b) close-up of the highlighted area in graph a.

2.4.2. Streptavidin Immobilization and Binding Assay

The model receptor–analyte system, streptavidin–biotin, was chosen since it presents a high binding affinity between the molecules, and it is widely studied and used in biological fields [246]. Therefore, streptavidin was used as a biorecognition element to be immobilized on the surface of the Au-TiO_2 thin films, and the analyte was biotin–HRP. The efficiency of the streptavidin–biotin binding at the biosensor's surface is studied in this section.

In a first approach, the concentrations of streptavidin and biotin–HRP were optimized. The streptavidin–biotin binding was determined by the absorbance of TMB oxidation by HRP, following a protocol based on ELISA in a 96-well plate. To evaluate the optimal streptavidin concentration on the well's surface, different amounts were tested (from 0.0025 to 25 µg/mL) and conjugated with different amounts of biotin–HRP (from 0.0075 to 75 µg/mL). Absorbance data obtained were plotted as a function of streptavidin and biotin–HRP concentrations (Figure 2.4a). The results indicate that the increase in the amount of streptavidin had a greater impact on the absorbance values. The maximum absorbance (3.6) was achieved at 2.5 µg/mL of streptavidin, and raising its concentration leads to a reduction in the conjugate formation (Figure 2.4a).

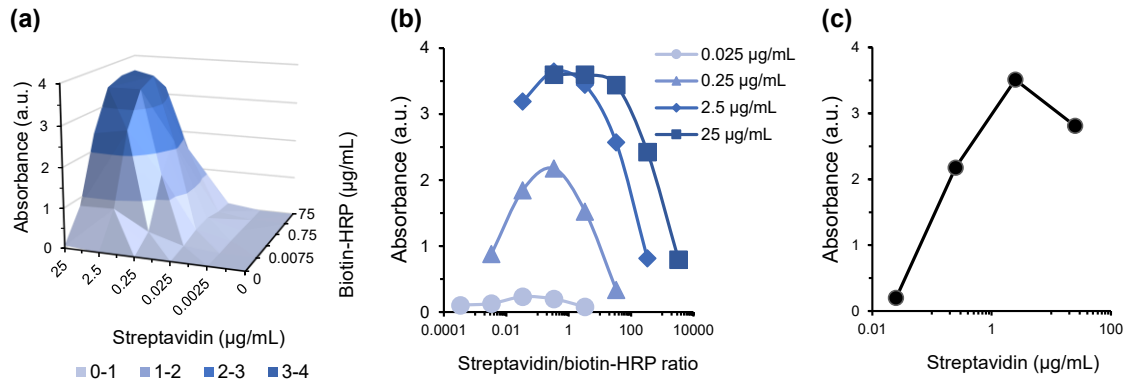


Figure 2.4. Streptavidin/biotin–HRP binding assay. (a) Absorbance values measured as a function of different streptavidin and biotin–HRP concentrations (µg/mL); (b) absorbance values measured as a function of streptavidin/biotin ratio, for streptavidin concentrations between 0.025 and 25 µg/mL; (c) absorbance values measured as a function of streptavidin concentration (µg/mL), for all combinations of streptavidin/biotin–HRP at the ratio of 0.33.

The streptavidin/biotin–HRP ratios as a function of absorbance, for the tested streptavidin concentrations, were plotted to determine the optimal ratio, which was found to be 0.33 for every condition (Figure 2.4b). Plotting the absorbance values of 0.33 ratios as a function of streptavidin concentration, it was concluded that the ideal condition was 2.5 µg/mL of streptavidin with 7.5 µg/mL of biotin–HRP (Figure 2.4c). This value is very close to the expected 1:4 streptavidin/biotin known ratio; the difference could be related to streptavidin adsorption to the well's surface, which prevents the binding of biotin to all the binding sites. Moreover, this could also be due to the conjugation of biotin with HRP, a large enzyme, which hinders the binding of other biotin molecules to the same streptavidin protein.

As previously shown, the O_2 plasma treatment increased the hydrophilicity of the thin film's surface. To evaluate the influence of O_2 plasma treatment on protein immobilization and validate its importance in the adhesion of the biorecognition layers, O_2 plasma treatment was applied on the glass substrates and Au-TiO_2 thin films, followed by the incubation with streptavidin, ranging from 1.25 to 25 µg/mL, according to the described experimental protocol. Results show that the thin films without plasma treatment (Figure 2.5b) behave similar to glass substrates either with (Figure 2.5c) or without plasma treatment (Figure 2.5a). This demonstrates that streptavidin binds to the thin film's surface, but only if treated with O_2 plasma (Figure 2.5d). Furthermore, no signal was detected in the non-specific binding controls. Thus, all thin films must be subjected to O_2 plasma treatment before the immobilization protocol.

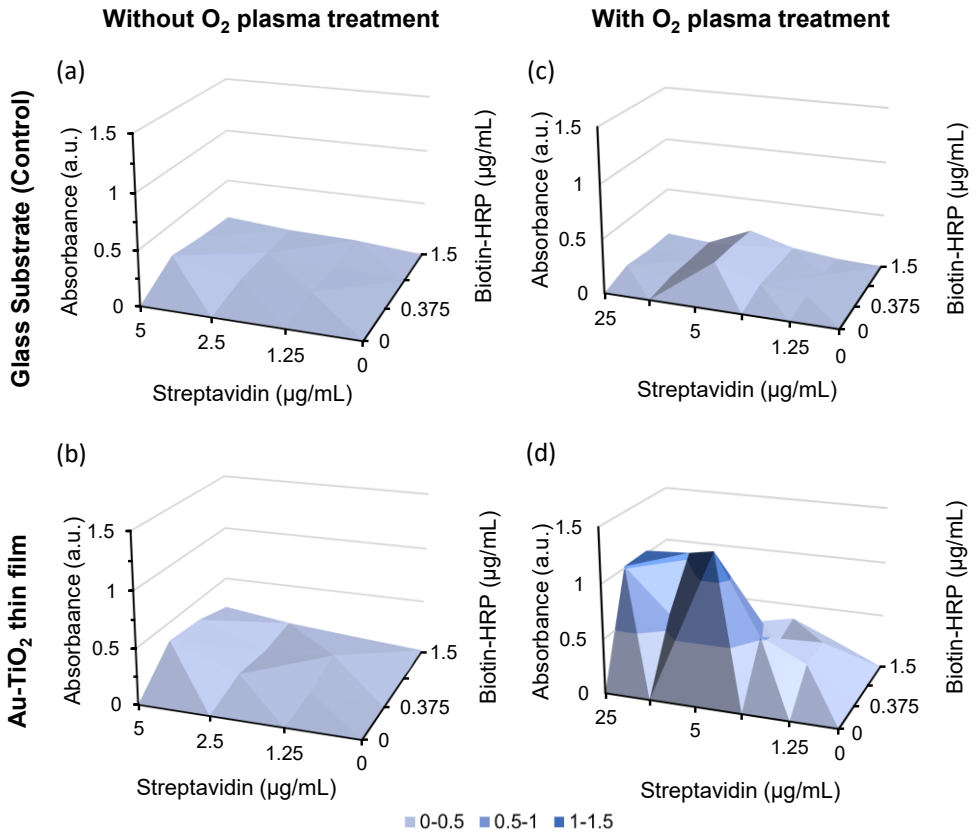


Figure 2.5. Influence of O_2 plasma treatment on the immobilization of streptavidin on the thin film's surface. Absorbance values measured as a function of streptavidin and biotin–HRP concentrations, without O_2 plasma treatment in (a) glass substrate and (b) Au-TiO_2 thin film and with O_2 plasma treatment in (c) glass substrate and (d) Au-TiO_2 thin film.

Therefore, the immobilization protocol of the Au-TiO_2 thin film's surface was designed based on the aforementioned findings. Comparing the wells' area (0.63 cm^2) with the thin films' surface area (1.125 cm^2) and the optimal streptavidin/biotin–HRP ratio, an extrapolation of the protein concentration was made to achieve maximum binding. Hence, the determined ideal concentration of streptavidin to be immobilized on the Au-TiO_2 surfaces was 4.5 µg/mL, and that of biotin–HRP was 13.5 µg/mL. After TMB oxidation by HRP, the average absorbance value in the immobilized Au-TiO_2 thin films was 1.9 ± 0.6. As expected, no binding was observed with the glass substrate controls or with the non-specific binding control samples.

The results reveal the success of the streptavidin immobilization on the surface of the thin films and the efficient streptavidin–biotin binding. The described ELISA-based protocol resulted as being a proper method for immobilizing biorecognition elements in plasmonic thin-film surfaces towards the development of sensing platforms integrating LSPR transducers.

2.4.3. LSPR Biosensing Platform Sensitivity

2.4.3.1. Refractive Index Sensitivity of the Au-TiO_2 Thin Films

The sensing performance of the LSPR thin-film platforms is dependent on the ability to distinguish between different refractive indexes (η) of the surrounding media. Therefore, the transmittance spectra of the Au-TiO_2 thin films were measured in the presence of sucrose solutions of four different concentrations with increasing refractive index values. Figure 2.6 plots the LSPR peak wavelength of the Au-TiO_2 thin films as a function of the refractive index of the different sucrose solutions. As evidenced, increasing the refractive index of the surrounding medium resulted in an LSPR band redshift. The linear fit yielded a correlation coefficient R^2 of 0.96 and a slope of 33 ± 5 nm/RIU, corresponding to the RIS, defined as the shift in LSPR wavelength per refractive index unit (RIU). However, the sensitivity of the film is still low when compared to the solution-based nanoplasmonic systems (≈200 nm/RIU) [247]. This might be related to the thickness of the film, which is about 95 nm, well above the plasmon decay length of the nanoparticles. Hence, the nanoparticles that effectively contribute to the detection signal are the ones closer to the surface of the film. Most of the nanoparticles are embedded in the matrix, so their signal contribution is defined by the dielectric matrix refractive index, and they do not "sense" the refractive index variations on the surface of the film [207,248]. Therefore, decreasing the film's thickness towards a value comparable to the plasmon decay length should be considered to improve the sensitivity. Another possible way to optimize the sensitivity is to tune the nanoparticles' features, such as the aspect ratio, concentration, and size distribution [249].

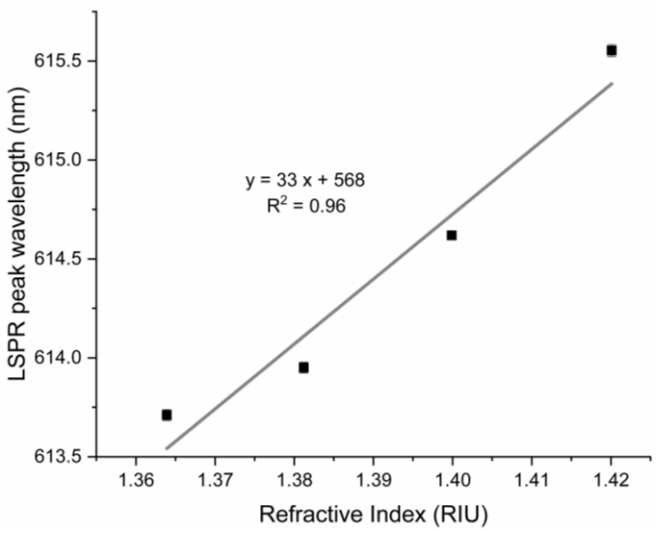


Figure 2.6. LSPR peak wavelength of the Au-TiO_2 thin films as a function of the refractive index of the different sucrose solutions (20, 30, 40, and 50% (w/w)). The solid line is a linear fit to the data.

2.4.3.2. LSPR Response of the Streptavidin-Immobilized Thin Films to Biotin–HRP

The performance of streptavidin-immobilized Au-TiO_2 thin films as sensing platforms was tested. The addition of the analyte (biotin–HRP) to the biosensor's surface caused an LSPR band shift of 0.8 ± 0.1 nm towards a longer wavelength, as seen in Figure 2.7. This LSPR shift is related to an increase in the refractive index of the region surrounding the nanoparticles, induced by biotin molecules that were bound to the immobilized streptavidin. This relatively low LSPR band shift, compared to other reports [250], might be related to the poor sensing ability of the LSPR platform (RIS = 33 nm/RIU). In addition, different concentrations of biotin–HRP were added to the biosensor's surface, but the low signal-to-noise ratio did not allow any measurable LSPR sensing response. Thus, the biosensor only presented an optical response in the presence of the ideal concentration of the analyte.

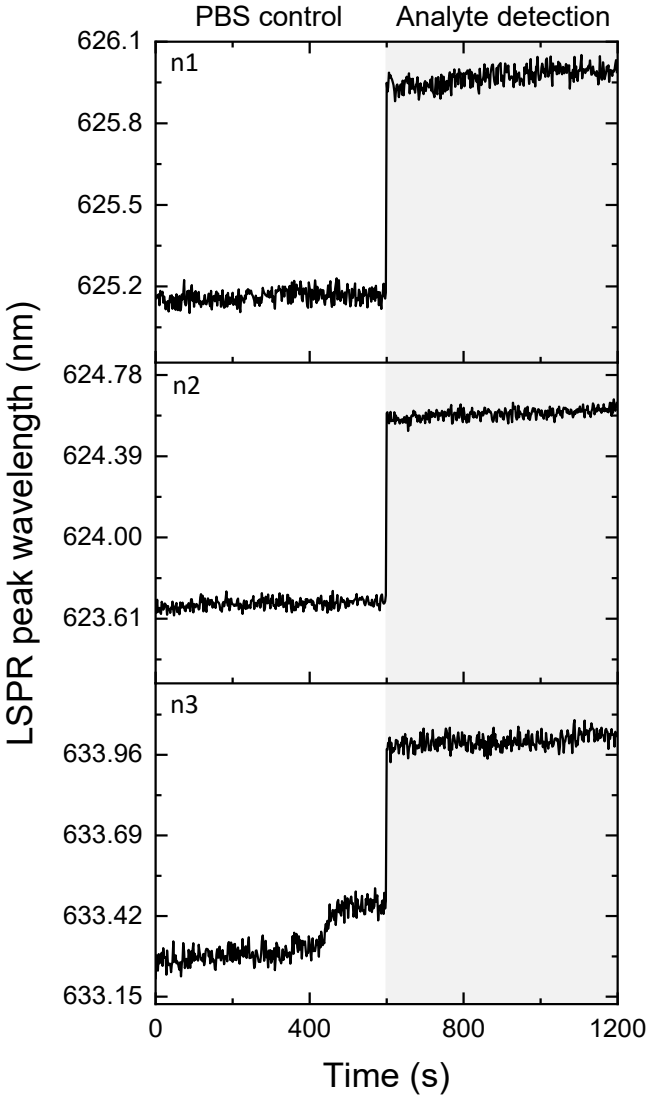


Figure 2.7. Ten-minute LSPR peak wavelength monitoring of the produced Au-TiO_2 biosensor after incubation with PBS (control) and after the incubation with 13.5 µg/mL biotin–HRP (analyte detection). n1, n2, and n3 are the three independent samples tested.

Additionally, to prove that this binding was specific, TMB was added to start the enzymatic reaction. The observed colored product proved the presence of biotin linked to streptavidin immobilized on the thin film's surface. This detection method confirms that the functionalization protocol was successful and Au-TiO_2 thin films immobilized with streptavidin can be used as LSPR biosensors. Despite this, additional optimization of the LSPR thin-film platform's sensitivity should be envisaged.

2.5. Conclusion

In this work, an LSPR sensing platform based on streptavidin-immobilized Au-TiO_2 thin films was developed. Nanoplasmonic thin films consisting of Au nanoparticles embedded in a TiO_2 dielectric matrix were deposited by reactive DC magnetron sputtering, an environmentally sound technology. Post-deposition treatments, such as annealing and Ar plasma, allowed the development of the sensing platform based on Au-TiO_2 thin films. The annealing at 400 °C promoted the growth and coalescence of the Au nanoparticles dispersed throughout the TiO_2 matrix, leading to the appearance of the LSPR band. An Ar plasma treatment was used to remove weakly bound contamination layers. Furthermore, the O_2 plasma increased the hydrophilic surface properties, enhancing the immobilization of streptavidin on the thin film. The specific binding of biotin–HRP to streptavidin was detected by the activity of the HRP, using a protocol based on ELISA. The performance of the biosensor, consisting of immobilized-streptavidin on Au-TiO_2 thin films, was corroborated by an LSPR wavelength peak shift of 0.8 ± 0.1 nm in the presence of the analyte.

The obtained results are promising; however, more improvements are needed before this biosensor can be employed in real-life applications. Future improvements include (1) optimization of the sensitivity (RIS) of the Au-TiO_2 thin films, by adjusting both deposition and post-deposition treatment parameters, and (2) evaluation of concentration dependency, selectivity, specificity, and reversibility of the sensing platform.

From the detection of HRP activity and LSPR sensing, it can be concluded that the functionalization protocol was successful and streptavidin-immobilized Au-TiO_2 thin films can be further exploited as LSPR biosensors.

Chapter 3

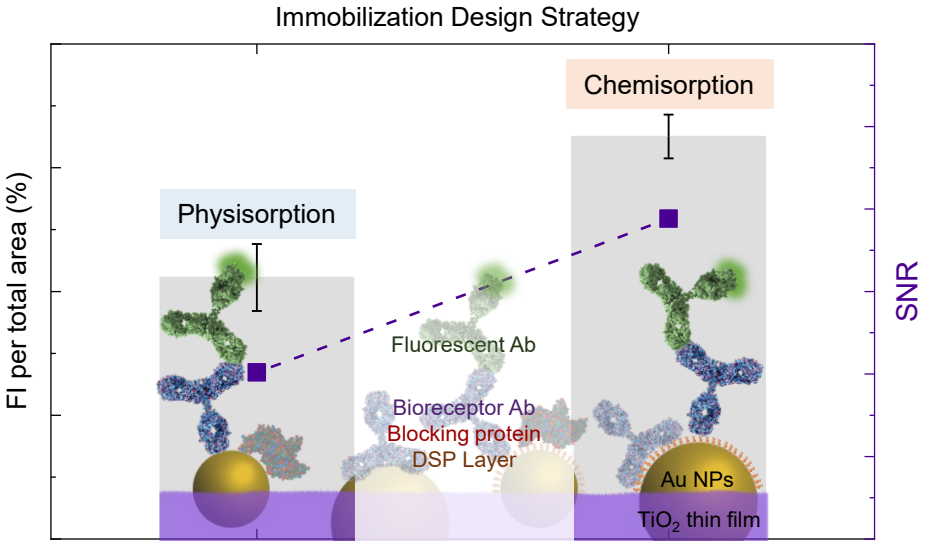
Immobilizing Antibody Biorecognition Layers on Au-TiO_2 Thin Films: Direct (Physisorption) vs. DSP-crosslinking (Chemisorption) Surface Functionalization

D.I. Meira, A.I. Barbosa, M. Proença, P. Pereira-Silva, J. Borges, V.M. Correlo, R.L. Reis, F. Vaz, Immobilizing Antibody Biorecognition Layers on Au-TiO_2 Thin Films: Direct (Physisorption) vs. DSP-crosslinking (Chemisorption) Surface Functionalization. *Submitted to Journal of Physics D: Applied Physics* (2024).

3.1. Abstract

The immobilization design strategy plays an important role in biosensor development and its sensing performance. Both adsorption (physisorption) and cross-linker functionalization (chemisorption) are common approaches for immobilizing a bioreceptor layer. In this work, these two approaches were studied and compared, envisaging a functional and strongly attached bioreceptor layer onto sputtered Au-TiO_2 thin films. DSP cross-linker (Lomant's reagent) was used in the thin film's functionalization, and the effect of different concentrations on the development of an adhesion layer was investigated. Surface morphology analysis of functionalized thin films suggested the development of uniformly coated self-assembled layers. However, DSP islands with a fractal structure were found for a concentration of 4 mg mL^{-1}. Infrared spectroscopy confirmed the cross-linker functionalization at the thin film's surface. Confocal microscopy of immobilized fluorescent antibodies revealed that DSP islands improve the chemical surface area available for bioreceptor immobilization. Moreover, an immunoassay using mouse IgG interaction with fluorescent anti-mouse IgG (Fab specific), working as capture and detection antibody, respectively, showed that DSP functionalization favors antibodies orientation and adhesion strength to the surface, when compared to physisorption.

Keywords: Nanocomposite Au-TiO_2 thin films; Surface functionalization; Antibody immobilization; Biochemical cross-linking; DSP islands



3.2. Introduction

The functionalization of a biosensing transducer platform involves the preparation or/and chemical modification of its surface for the specific bioreceptor attachment while minimizing non-specific adsorptions [180,251,252]. The analytical sensing performance of biosensors highly depends on the biorecognition element characteristics attached to the transducer's surface [253,254]. Hence, the immobilization strategy imposes critical requirements for high performance: i) biorecognition element orientation, uniform coverage and packaging density, ii) the activity and stability during the detection analysis time, and iii) antifouling capabilities, minimizing the possible interferences or non-specific adsorption of contaminants present in the sample matrix [255,256]. Biosensor functionalization can be divided into physisorption (direct physical adsorption) and chemisorption (covalent bonding to a self-assembled monolayer, e.g.) [252,256,257].

Physisorption is the most common and simplest biofunctionalization strategy, promoting the immobilization of the bioreceptor layer in the transducer's surface through intermolecular forces (e.g., electrostatic, hydrophobic, and/or polar interactions) [258,259]. However, poor orientation and incorrect secondary structural conformation can severely affect biochemical interaction and, consequently, the sensing ability [259]. Furthermore, the physisorption strategy unveils various drawbacks: i) desorption, ii) denaturation, iii) decrease of analyte affinity, iv) reproducibility, and v) stability [255,260,261]. Nonetheless, physisorption can be a suitable approach in sensing mechanisms, depending on the sensor's final purpose and characteristics. For instance, in gas sensors, it allows the detection of primary gas molecules that easily desorb with changes in temperature, pressure, or gas atmosphere, facilitating sensor reusability [262–265].

In turn, chemisorption may improve the immobilization process by functionalizing the transducer's surface with a specific cross-linker. This short vertical spacer (less than 2 nm thick, typically) serves as an intermediary between the transducer surface and the bioreceptor, guaranteeing a highly stable covalent (i.e., amine (-NH_2), carboxyl (-COOH) or hydroxyl (-OH) terminus) bonding or high-affinity molecular attachment [256,266,267]. A major function of a cross-linker is to certify a uniformly distributed bioreceptor layer with the ideal unidirectional configuration, ensuring higher recognition efficiency by allowing the active site to be oriented and accessible for biochemical interaction and detection [268–271]. Despite the slightly increased distance from the transducer's surface to the analyte, the improvements in bioanalytical requirements (i.e., robustness, versatility, reproducibility and sensitivity) are considered significantly advantageous [256,272].

To simplify the comparison between both immobilization strategies, Table 3.1 provides a detailed side-by-side analysis based on key criteria, highlighting the strengths and limitations of each approach.

Table 3.1. Comparison of physisorption and chemisorption immobilization strategies.

Criteria	Physisorption	Chemisorption
Bond Strength	Weak (e.g., Van der Waals, electrostatic, and hydrophobic interactions) [258,259]	Strong and irreversible (e.g., covalent, or ionic bonds) [256,266,267]
Chemical interactions	Nonspecific, reversible, and reusable interactions [258,259]	Specific, strong, and irreversible chemical bonding interactions [256,266,267]
Sensitivity	Moderate sensitivity, as weaker binding may lead to desorption, reducing detection levels [256,272]	High sensitivity [256,266,267,272]
Stability	Less stable [255,260,261]	More stable [256,266,267]
Energy Requirement	Low energy requirement for adsorption and desorption [255,260–263,273]	High energy requirement for both adsorption (activation energy) and desorption [273]
Complexity	Simpler and easier to implement due to the lack of specific surface preparation or treatment [258,259]	More complex as it often requires surface functionalization (activation or chemical modification) [256,266,267]

Nanocomposite thin films composed of gold nanoparticles (Au NPs) dispersed in a titanium dioxide matrix (Au-TiO_2) have been highlighted as potential plasmonic biosensing platforms [34,274]. This study aimed to functionalize Au-TiO_2 thin films' surface with a suitable adhesion layer capable of developing a highly functional, oriented, and attached bioreceptor layer. The Au-TiO_2 films were plasma-activated with O_2 to create hydroxyl (-OH) functional groups [275–277], that are known to be beneficial for protein's physisorption [235,243,274,278,279]. A chemisorbed layer composed of a short-chain organic alkanethiol cross-linker was then functionalized, as a coupling agent, in the plasma-activated thin films' surface. Dithiobis(succinimidyl propionate) (DSP), also named Lomant's reagent [280], is a homobifunctional cross-linker that can develop a proper self-assembled monolayer, as illustrated in Figure 3.1 [281–284]. DSP has a thiol group (-SH) at one end that interacts strongly with Au NPs, due to its disulphide linkage [285]. It also has a functional group (N-hydroxysuccinimide (-NHS) ester terminus) at the other end that can be replaced by amine-containing bioreceptors (e.g., antibodies), through covalent coupling via amide linkage, also known as aminolysis [282,286,287]. The morphological evolution of the Au-TiO_2 thin films' surface was studied, considering the different functionalization conditions: O_2 plasma treatment time and DSP functionalization with increasing concentrations. Additionally, the efficiency of the biorecognition process was evaluated by scrutinizing the influence of the immobilization strategy. For that, the surface coverage area available for bioreceptor immobilization, using both immobilization approaches, was evaluated using fluorescent anti-IgG-FITC (FITC = fluorescein isothiocyanate) antibody.

Moreover, the bioreceptor layer functionality and activity were studied through an immunoassay, using IgG antibody and Fab-specific anti-IgG-FITC as bioreceptor and biological pair, respectively.

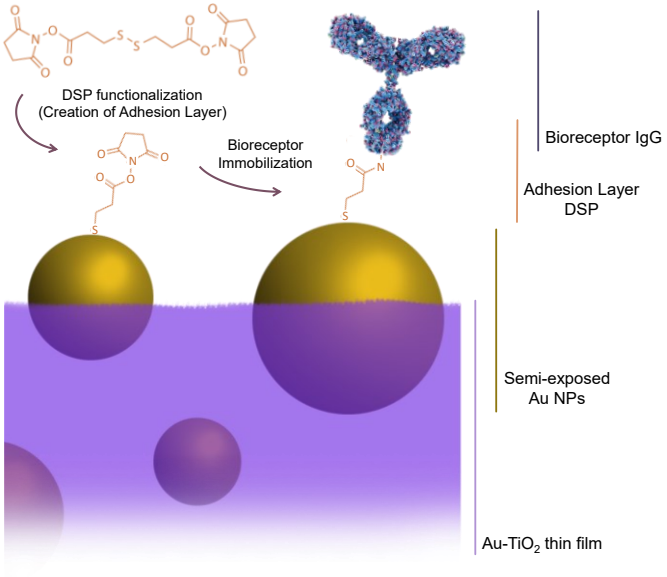


Figure 3.1. Illustrative representation of functionalized Au-TiO_2 thin film with an adhesion layer composed by DSP cross-linker. Through the cleavage of DSP's disulfide linkage, the thiol (-SH) functional group can chemically interact with the partially exposed Au NPs. The adhesion layer acts as an intermediary, facilitating the specific binding of the bioreceptor to the thin film's surface, through the aminolysis reaction.

3.3. Materials and Methods

3.3.1. Preparation of Au-TiO_2 Thin Films

3.3.1.1. Thin films Deposition by Reactive DC Magnetron Sputtering

Thin films composed of Au dispersed in a TiO_2 matrix were deposited on glass lamellae (ISO8037) by a one-step reactive Direct Current magnetron sputtering in a custom-made high-vacuum chamber (base pressure below 6.0×10^{-4} Pa). The cathode is a composite titanium target ($200 \times 100 \times 6$ mm^3, 99.99 % purity) symmetrically covered with 2 halves of a gold pellet (16 mm^2). The sputtering deposition was carried out with a plasma of argon (partial pressure, 3.6×10^{-1} Pa) and oxygen (partial pressure, 4.0×10^{-2} Pa), mixed using independent mass flow controllers. A current density of 100 A m^{-2} was applied, resulting in a (negative) target potential of 370 ± 4 V for 25 min deposition. The thin film's thickness was 100 nm, with Au concentration of about 20 at.% [274].

3.3.1.2. Post-Deposition Annealing Treatment

A post-deposition annealing in-air treatment at 400 °C was performed on Au-TiO_2 thin films to promote the diffusion of Au atoms, leading to the growth and coalescence of Au NPs throughout the matrix. Based on previous work [36], it is expected that the annealing process performed at this temperature will lead to the formation of Au NPs embedded with a TiO_2 matrix, crystallized in the anatase phase. These NPs are characterized by an average size of 15 nm and exhibit a relatively wide size distribution, ranging from about 10 to 40 nm [239].

3.3.1.3. Surface Activation by Plasma Treatment

An activation plasma treatment was applied using O_2 as a working gas, at a pressure of 10 Pa and 15 W power, starting at a base pressure of 2 Pa, for various times (0, 30, and 300 seconds). The O_2 plasma enables alterations of chemical properties, namely the formation of hydroxyl (-OH) groups on the thin film's surface [235,274].

3.3.2. Functionalization and Characterization of Au-TiO_2 Thin Film with DSP cross-linker

3.3.2.1 Surface Functionalization with DSP molecules

Plasma-activated Au-TiO_2 thin films were functionalized with DSP (dithiobis(succinimidyl propionate)) solutions, using various concentrations (0.4, 1, 4, and 10 mg mL^{-1}) dissolved in DMSO solvent (dimethyl sulfoxide, anhydrous, ≥ 99.9%). The immobilization time was 30 min, followed by cleaning steps, including DMSO, PBS (phosphate-buffered saline, pH 7.4, 10 mM), and ethanol 96 % solutions to remove any unbounded cross-linker molecules.

3.3.2.2. Surface Morphology Characterization by Atomic Force Microscopy (AFM)

A high-resolution Nano-Observer AFM microscope was used in resonant mode with a 5 × 5 μm^2 and 10 × 10 μm^2 scan sizes on DSP-functionalized thin films, with a resolution of 1024 × 1024 px, and 1 line s^{-1} scan speed. A platinum-coated silicon probe, with a resonance frequency of 60 kHz, a spring constant of 3 N m^{-1}, and a tip radius below 30 nm, was coupled to the modular probe holder. The topography AFM data was analyzed using the MountainsSPIP®.

3.3.2.3. Surface Chemistry Analysis by Fourier-Transform Infrared (FTIR) Spectroscopy

FTIR validated the DSP functionalization on the surface of the thin film in Attenuated Total Reflectance (ATR) mode, using a Jasco FT-IR4100 equipped with a Specac MkII Golden Gate single reflection ZnSe ATR crystal. ATR-FTIR spectra were recorded between 800 cm^{-1} and 2300 cm^{-1}, with a scan resolution of 8 cm^{-1} and 64 scans.

3.3.3. Immunoassays Development

3.3.3.1. Antibody Immobilization: Antibody Surface Coverage Capacity

The development of a high-performance biosensor can be influenced by the biorecognition layer immobilization design approach. Therefore, two separate experiments were conducted using different immobilization strategies: physisorption and chemisorption approaches [34].

For clarity, the physisorption strategy is associated to the plasma-activated film (without DSP), whereas the chemisorption strategy pertains to the thin film that has been both previously activated with O_2 plasma and functionalized with DSP (Figure 3.2).

Initially, an anti-IgG conjugated with FITC solution (20 μL of 100 μg mL^{-1}) [34] was incubated in both plasma-activated and DSP-functionalized thin film surfaces (Figure 3.2– I. a, b). For 2 hours, the immobilization experiment was reserved in the dark. Afterwards, the cleaning step was performed with PBS-T (0.05% Tween-20 in PBS) and PBS. The fluorescent signal of the thin films' surface was acquired using a confocal laser scanning microscope. The control experiment was considered the thin films auto-fluorescence.

3.3.3.2. Immunoassay: Bioreceptor Activity

The bioreceptor layer of mouse IgG solution (20 μL of 100 μg mL^{-1}) [34] was incubated overnight on the plasma-treated (without DSP) and, also, in DSP-functionalized thin film surfaces (Figure 3.2– II. a, b). Then, the thin films were incubated with 5% BSA (Bovine Serum Albumin, protease-free) for 2 hours to guarantee the blocking of non-specific sites on the biosensors' surface, followed by washing steps (PBS-T and PBS). Afterwards, the anti-IgG conjugated with FITC solution (20 μL of 10 μg mL^{-1}) was incubated in the dark for 30 min, followed by a final cleaning step (PBS-T and PBS). The fluorescent signal of the thin films' surface was observed using confocal laser scanning. In the control, the protocol was performed without the previous bioreceptor (mouse IgG) immobilization.

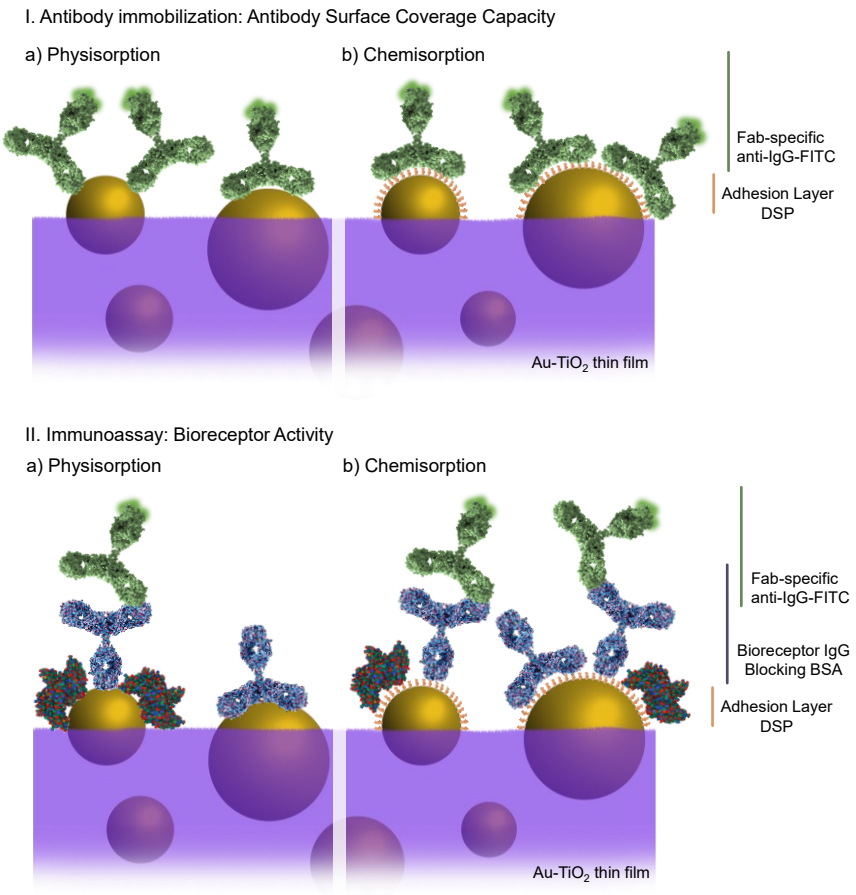


Figure 3.2. Illustrative representation of the envisaged immobilization of antibody surface coverage and the immunoassay analysis in plasma-activated (without DSP) and DSP-functionalized Au-TiO_2 thin films, depicting the physisorption strategy (represented in I. and II. by a) and the chemisorption strategy (represented in I. and II. by b).

3.3.3.3. Fluorescence Analysis

The functionalized Au-TiO_2 thin films were analyzed using the confocal laser scanning microscope with a constant 35% argon laser intensity and 1.0 pinhole. Each thin film sample was analyzed in at least three distinct surface areas, with a resolution of 1024 × 1024 px, and a minimum of three independent replicates was examined to consider the repeatability parameter. Considering the uniformity parameter, a representative image was divided into nine identical areas (82 × 82 μm^2) and the fluorescent signal was compared between these areas, for each immobilization condition. In MATLAB software, the "imbinarize" function was used to binarize the images with the same threshold value allowing quantification of the fluorescent signal and signal-to-noise (SNR) ratio. The calculation of the SNR involves a quantitative comparison of the fluorescence intensity from the experimental tested condition with that of the baseline control sample. An SNR exceeding 3 signifies a notably clearer and more distinct test signal compared to the control's background noise.

3.4. Results and Discussion

3.4.1. Surface Morphology Analysis

The morphology of Au-TiO_2 thin films was studied after different surface modifications: functionalization using different DSP concentrations (Figure 3.3) and O_2 plasma activation time (Figure 3.4). Overall, there is a clear evidence of adhesion layers' formation (DSP islands) on the film's surface, depending on the concentration (Figures 3.3 and S3.1) and plasma treatment time (Figures 3.4 and S3.2).

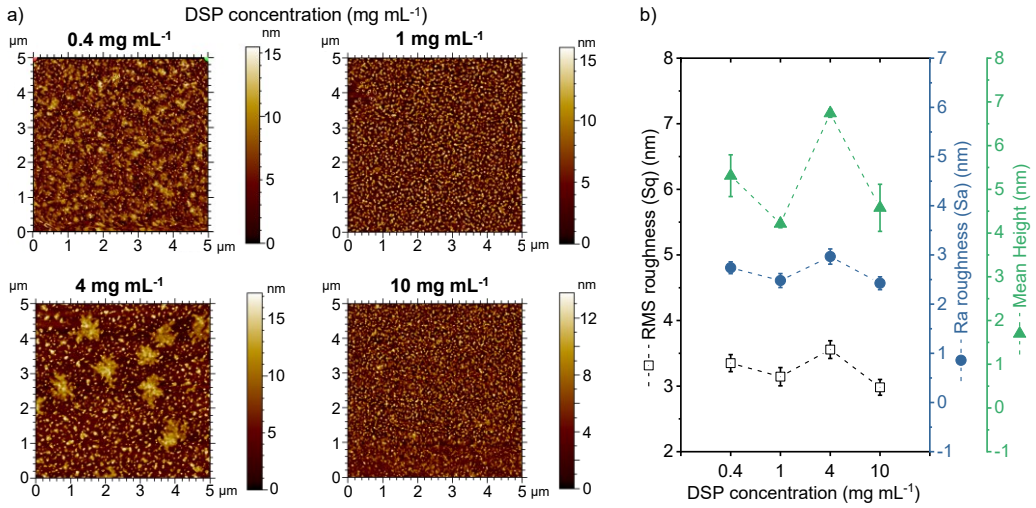


Figure 3.3. Influence of the DSP cross-linker concentration in the morphology of O_2 plasma-activated thin films (300 s). (a) Two-dimensional (2D) AFM height images and (b) morphological parameters (i.e., root mean square roughness (Sq), surface mean roughness (Sa), and mean height).

In the absence of an O_2 plasma activation, the Au-TiO_2 thin film exhibits a smooth surface, with a mean square roughness (Sq) value estimated at 2.84 ± 0.02 nm (Figure 3.4b). There are small hills observable, with a maximum height of 13.5 ± 0.3 nm and an average estimated size of 3.4 ± 0.1 nm ("0 s", Figures 3.4a and S3.2b). However, when the thin film was activated by O_2 plasma for 30 seconds, the morphological structure evolved, revealing the presence of higher hills with a maximum height of 34.5 ± 0.3 nm separated by smooth areas with around 10.1 ± 0.3 nm ("30 s", Figures 3.4a and S3.2b). Consequently, the morphological parameters have changed, achieving an average height of 8.5 ± 0.9 nm, and a Sq value of 3.78 ± 0.57 (Figure 3.4b). When the Au-TiO_2 thin film was subjected to the longer activation treatment (300 seconds), vast valleys separated by high hills emerged, with a maximum height of 41.8 ± 0.3 nm over a 0.5 µm width ("300 s", Figures 3.4a and S3.2b). This gave rise to a broader bimodal height distribution at higher sizes ranging from 0.1 to 41.8 nm (i.e., 0.1 to 16.8 nm (< 70 %) and 16.8 to 41.8 nm (< 30 %)), with the average height estimated to be 17 ± 1 nm (Figures 3.4b and

S3.2a). Consequently, the roughness of the thin film increased, reaching Sq value of 4.79 ± 0.09 nm (Figure 3.4b).

The DSP functionalization, with different concentrations, was performed in Au-TiO_2 thin film previously activated with an O_2 plasma for 300 s. The morphological evolution of the functionalized thin films exhibited erratic behavior as the DSP concentration increased (Figure 3.3). In the two lowest DSP concentrations (0.4 and 1 mg mL^{-1}), the heterogenous morphology of the thin film's surface tended to disappear, giving rise to a granular microstructure with relatively flat topography, and with a maximum height of about 15.5 ± 0.5 nm (Figures 3.3a and S3.1b). The uniform height distribution of both DSP conditions ranged from around 0 to 16 nm, and the mean height was estimated to be approximately 5.3 ± 0.5 to 4.2 ± 0.1 nm (Figure 3.3b). Beyond that, the estimated roughness parameters slightly decreased, with Sq value reducing from 3.35 ± 0.13 to 3.14 ± 0.14 nm (Figure 3.3b). This morphological evolution can suggest the formation of a uniform self-assembled cross-linked layer effectively covering the underlying thin film [288].

As the concentration of DSP further increases, a thicker semi-planar adhesion layer is expected to be developed. However, at a DSP concentration of 4 mg mL^{-1}, large aggregates, or "islands", with a fractal microstructure were observed, exhibiting a maximum height of 13 nm over a 1 μm width (Figures 3.3a and S3.1b). The morphological paraments tended to slightly increase compared to lower DSP concentrations, exhibiting an average mean height of 6.7 ± 0.1 nm, and a Sq value of 3.56 ± 0.13 nm (Figure 3.3b).

The morphological tendency shifts again at the maximum concentration of 10 mg mL^{-1} (Figure 3.3). Under this condition, the DSP islands tended to disappear and gave rise to a regular surface, significantly composed of low hills, suggesting the development of a continuous adhesion layer covering the entire film's surface with a Sq value estimated at 2.98 ± 0.12 nm (Figures 3.3a, b and S3.1b). Hence, the height distribution became more uniform, and narrow, at lower ranging values, from 0 to 14 nm, where the mean height decreased to 4.6 ± 0.5 nm (Figure 3.3b).

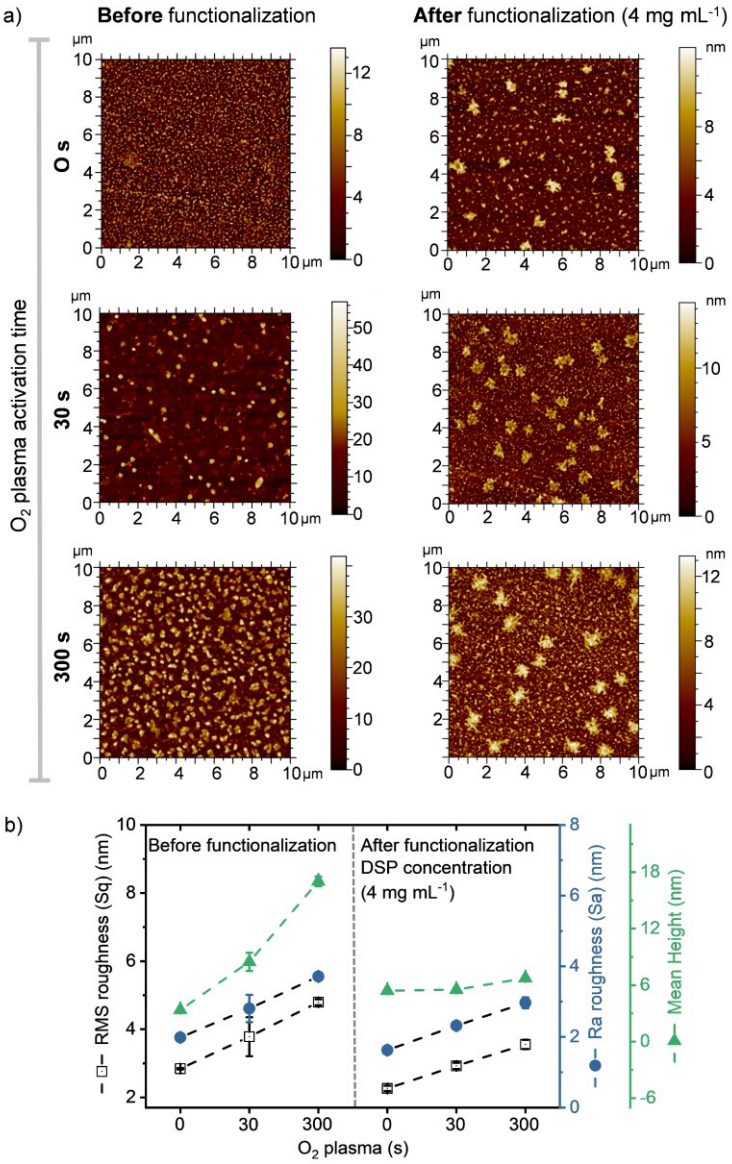


Figure 3.4. Influence of O_2 plasma treatment time in the morphology of plasma-activated (without DSP) and DSP-functionalized Au-TiO_2 thin films with the specific concentration of 4 mg mL^{-1}. (a) Two-dimensional (2D) and (b) morphological parameters (i.e., root mean square roughness (Sq), surface mean roughness (Sa), and mean height).

The impact of prior O_2 plasma activation on the formation of DSP islands in functionalized thin films, with a specific DSP concentration of 4 mg mL^{-1}, was also investigated using different activation times (0, 30 and 300 s) (Figure 3.4). The density of islands increased from (0.16 to 0.41) ± 0.01 per μm^2 as the activation time increased from 0 to 30 s, decreasing again, to 0.26 ± 0.01 per μm^2 at 300 s (Figures 3.4a and S3.2a). From the AFM images, it is evident that this trend is certainly related to the formation of fewer, but larger islands, likely attributable to the merging of smaller islands into a more prominent chemical structure (Figures 3.4a and S3.2a, b). The emergence of these densely packed

islands presumably influences the height distribution pattern. Notably, with the increase of the O_2 activation time on the DSP-functionalized film, it is possible to notice an evolution of a bimodal height distribution, established approximately between 0 to 4.5 nm (< 70 %) and 7.5 to 13.3 nm (< 30 %) (Figure S3.2a). In comparison, a bimodal distribution pattern with higher maximum height distributions (< 40 nm) was also observed in a plasma-activated thin film for 300 s, and not in the remaining activation times (Figure S3.2a). The notable decrease of the maximum limits of the bimodal distribution after cross-linker functionalization may imply that the adhesion layer covers the surrounding area of the hills, leading to a "uniformly" coated thin film's surface (Figure S3.2a, b). In agreement, the morphological parameters progressed to higher values with increasing O_2 activation time (Figures 3.4b and S3.2c). Correspondingly, as the plasma time extended to 30 s and then to 300 s, the average height of the functionalized thin films evolved from 5.4 ± 0.1 nm (0 s), to 5.5 ± 0.2 nm (30 s), and to 6.7 ± 0.1 nm (300 s). Further underlining this trend, the Sq values evolved from 2.26 ± 0.08 nm (0 s) to 2.92 ± 0.09 nm (30 s) and settled at 3.55 ± 0.13 nm (300 s).

Therefore, the O_2 plasma activation seems to facilitate the thin film's functionalization with DSP molecules, allowing the development of islands with increasing size and perhaps separated by a uniform adhesion monolayer across the entire thin film's surface.

As described above, the O_2 plasma treatment affects the thin film's surface by altering the morphological appearance, but also enabling the formation of hydroxyl groups (-OH) in the TiO_2 matrix [274–277]. Moreover, the activation plasma can affect the chemical stability of the semi-exposed Au NPs, leading to the formation of a metastable surface of oxidized Au on the thin film's surface [289,290]. Focusing on DSP functionalization, the DSP cross-linker chemisorbs in the Au NPs, through the high affinity of the -SH group to Au (Figure 3.1). In addition, DSP cross-linker can also be chemically bounded through the created hydroxyl (-OH) functional groups by plasma activation [275–277], freeing the NHS-terminated group of DSP molecule [287]. The DSP cross-linker can be functionalized on Au NPs (by -SH interactions), and on their surrounding area (by -OH interactions), creating a uniformly coated adhesion layer.

3.4.2. Surface Chemistry Analysis

The surface chemistry of DSP-functionalized thin films, with different DSP concentrations, was investigated using ATR-FTIR analysis. The FTIR spectra exhibit the band assignments of the NHS-terminated group of the DSP cross-linker, ranging between 800 and 2300 cm^{-1} (Figure 3.5).

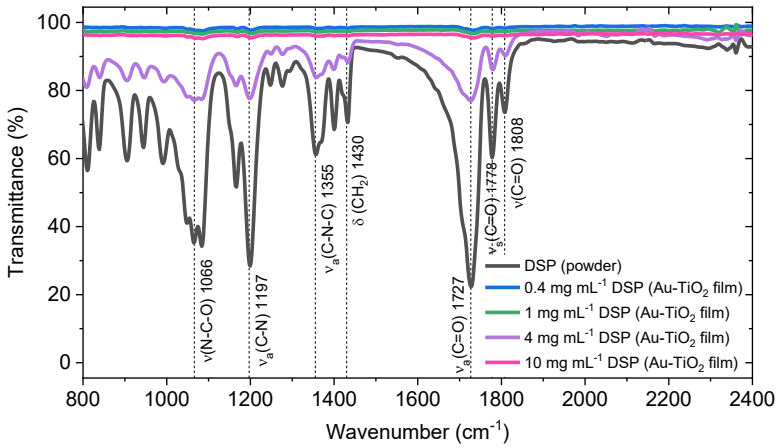


Figure 3.5. Infrared spectra of DSP (powder) and DSP-functionalized Au-TiO_2 thin films, with different concentrations.

The spectral features most characteristic of the NHS functional group in the DSP cross-linker are displayed at 1808 cm^{-1}, 1778 cm^{-1}, and 1727 cm^{-1}, corresponding to ν (C=O), symmetric ν_s (C=O) and asymmetric ν_a (C=O) carbonyl stretches vibrations, respectively [291,292]. Other characteristic bands are derived from bonds with nitrogen (N), presented by transmittance peaks at 1197 cm^{-1} and 1066 cm^{-1}, confirming the presence of the asymmetric ν_a (C-N) stretch and the succinimide ν (N-C-O) stretch, respectively [293,294]. Beyond that, the symmetric stretching of C–N–C was recognized by the 1355 cm^{-1} peak [295], while the vibrations of methylene scissors deformation (δCH_2) were identified at 1430 cm^{-1} [293]. The FTIR spectrum of the DSP (powder) was used as reference, identifying its fingerprint peaks to compare with the functionalized thin films. Overall, the DSP-functionalized thin films were able to mimic the most important band assignments of DSP (powder), confirming the cross-linker functionalization and, consequently, the development of the self-assembled DSP layers across the thin film's surface. Nevertheless, the relevant DSP signature transmittance peaks were very faint at the majority of the DSP concentrations (a zoom image can be found in Figure S3.3), with the exception being at 4 mg ml^{-1} concentration. At this DSP concentration, the functionalized thin film exhibited the formation of islands in a fractal morphology, as discussed above. Therefore, the highly dense DSP island structures reproduce the specific NHS-terminated group peaks of the DSP cross-linker with higher intensities, standing out from the other DSP concentrations, as demonstrated in Figure 3.5.

3.4.3. Antibody Immobilization and Immunoassay in Functionalized Au-TiO_2 Thin Film

3.4.3.1. Antibody Immobilization: Antibody Surface Coverage Capacity

In the fluorescent antibody immobilization experiment, both immobilization strategies were evaluated to comprehend which one reveals a higher antibody surface coverage (Figure 3.2– I).

Anti-IgG conjugated with FITC (fluorescent antibody) was immobilized directly onto the plasma-activated (without DSP) and DSP-functionalized thin films, as exhibited in Figure 3.6. The fluorescence intensity per total surface area (%) is directly proportional to the density of immobilized fluorescent antibodies on the Au-TiO_2 thin films' surface. The auto-fluorescence of the thin film is not represented in Figure 3.6, since the fluorescence intensity per total area is significantly low $(25.4 \pm 1.7) \times 10^{-5}$ %, with a coefficient of variation (CV) of 20.5%. Yet, this value was used to calculate SNR values in this experiment.

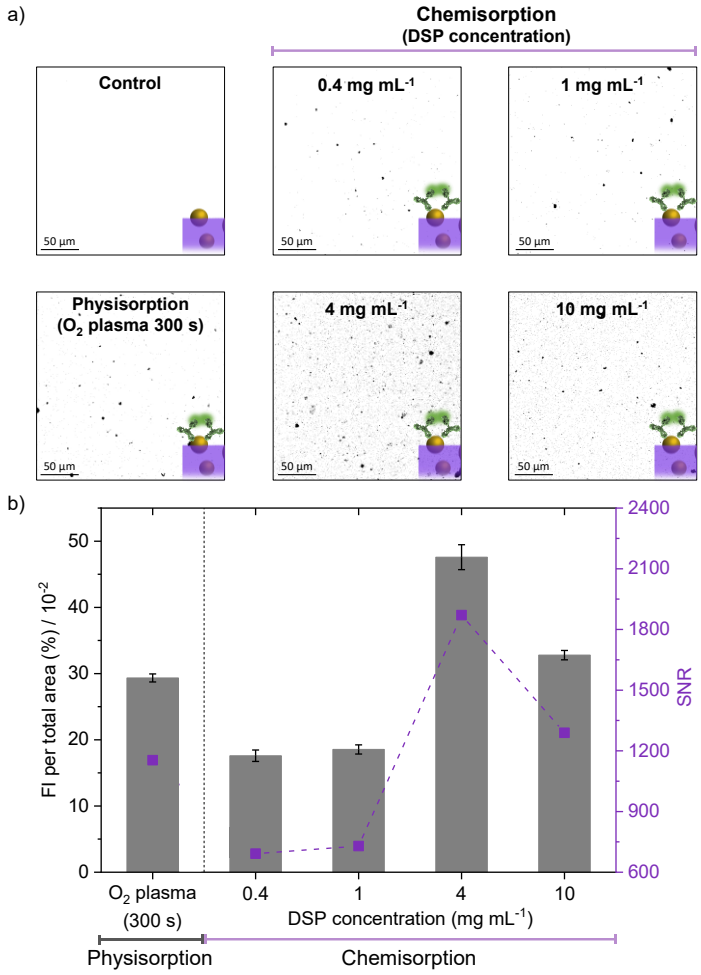


Figure 3.6. Antibody surface coverage on O_2 plasma-activated (without DSP) and DSP-functionalized Au-TiO_2 thin film, using anti-IgG-FITC secondary antibody. (a) Processed confocal microscopy images and (b) fluorescent intensity per total thin film's area, considering the physisorption and chemisorption immobilization approaches, at different DSP concentrations.

Regarding the physisorption strategy, fluorescent signal distribution can be associated with nearly dispersed immobilized antibodies into the plasma-activated Au-TiO_2 thin films (without DSP) (Figure 3.6a). These samples exhibited a fluorescence intensity per total area of (29.3 ± 0.6) × 10^{-2} %, establishing an SNR of 1153 with a CV value of 6.2 % (Figure 3.6b). In a previous work [34], a fluorescent antibody layer was immobilized on non-activated thin films (i.e., without O_2 plasma treatment). For a similar anti-IgG conjugated with FITC concentration (i.e., 117 mg mL^{-1}), the fluorescence intensity per analyzed area was lower compared to the exhibited results. Hence, the pre-activation with O_2 plasma, as described in the present work, already benefits antibody immobilization across the thin film's surface [274].

Regarding the chemisorption strategy, the fluorescence intensity per total area slightly increased from (17.6 ± 0.9) × 10^{-2} % to (18.5 ± 0.7) × 10^{-2} % for the lowest DSP concentrations (0.4 and 1 mg mL^{-1}), corresponding to an SNR increase of 692 to 729, respectively (Figure 3.6a, b). The CV values were estimated to be below 14.6%. However, within this range of DSP concentrations, the fluorescence intensity per total area was still lower than that achieved by the physisorption strategy. Although a uniformly distributed adhesion layer of DSP is expected to be present on the thin film's surface, as previously discussed (Figure 3.3), probably it is not chemically accessible to interact with the antibody, hindering the development of a uniform fluorescent antibody layer (Figure S3.4). This limitation might result from the state of the functionalization step (i.e., formation of the lying phase) or due to poor orientation of the antibody (e.g., inverted) caused by the polymerization of the self-assembled layers [288,296].

In contrast, at a DSP concentration of 4 mg mL^{-1}, the fluorescence intensity per total area increased significantly to (47.5 ± 1.8) × 10^{-2} %, leading to an SNR of 1870, indicating a higher amount of fluorescent antibody bound to the functionalized thin film's surface (Figures 3.6a, b and S3.2). The fluorescent signal remains consistently intense across the film's surface (Figure S3.4), and among multiple replicates (CV of 11.8%), emphasizing samples' reproducibility. The presence of multiple DSP island-like structures and their evenly coated surrounding area, including the activated TiO_2 matrix, appears to facilitate the immobilization of a uniform and densely covered fluorescent antibody layer.

Once again, following the trends discussed in AFM analysis, the fluorescence intensity per total area shifts again, being reduced at the highest DSP concentration (10 mg mL^{-1}) to (32.8 ± 0.7) × 10^{-2} % (Figure 3.6a, b). Consequently, the SNR decreased to 1289, and the CV value was estimated at 6.4%.

According to these findings, more fluorescence signal is recorded in functionalized thin films with higher DSP concentrations (4 and 10 mg mL^{-1}) compared to lower concentrations (0.4 and 1 mg mL^{-1}). A homogeneous adhesion layer cannot be translated into a dense and uniform fluorescent antibody layer

(Figure S3.4). Instead, these results suggest that the DSP multi-island layer, uniformly distributed through the film, is chemically more reactive and, hence, more prone to chemically bond with bioreceptors.

3.4.3.2. Immunoassay: Bioreceptor Activity

Once the optimal conditions for maximum antibody coverage were found, the next step was to determine the functionality of the biorecognition layer in both studied immobilization strategies (Figure 3.2– II).

For this purpose, an immunoassay procedure was developed with a bioreceptor (i.e., mouse IgG, first antibody) immobilized on the plasma-treated (without DSP) and DSP-functionalized thin film's surface, using an optimized concentration of 4 mg mL^{-1}. After blocking the non-specific sites, Fab-specific anti-IgG-FITC (second antibody) was incubated. Noteworthy, this anti-IgG (second antibody) only binds to the Fab region of the immobilized mouse IgG (first antibody), indicating the orientation, conformation, and activity of the immobilized bioreceptors. In this case, the fluorescence intensity per total area (%) is directly proportional to the density of fluorescent (second) antibodies chemically bonded to the immobilized bioreceptors (first antibody) at the thin film's surface. The immunoassay control was performed without the previous bioreceptor (first antibody) immobilization. The physisorption and chemisorption control approaches exhibited fluorescent intensities per total area of $(19.2 \pm 1.1) \times 10^{-3}$ % and $(25.3 \pm 3.0) \times 10^{-3}$ %, with CV values of 17.0% and 36.1%, respectively (Figure 3.7b). These two controls were not exhibited in Figures 3.7a and S3.5, since fluorescence intensity per total area was found to be extremely low, confirming the effective blocking of the Au-TiO_2 thin films.

In both immobilization strategies, the thin films exhibited a uniform fluorescent signal across their entire surface. This suggests that the immobilized bioreceptor (first antibody) layer is consistently dense, functional, active, and probably correctly ("end-on") oriented (Figures 3.7a and S3.5) [297].

Considering the physisorption strategy, the fluorescence intensity per total area was estimated at 2.1 ± 0.3 %, with an SNR of 110, and a CV value of 38.4% (Figure 3.7b). Compared to the preliminary studies [34,274], the fluorescent signal was higher and, also, uniform across the thin films' surface (Figures 3.7a and S3.5). This indicates the formation of a functional and active bioreceptor (first antibody) layer, able to effectively interact with its fluorescent (second antibody) pair. This improvement suggests that the nanotechnology involved in preparing these plasmonic thin films for biosensing applications has evolved due to the combination and advancement of various experimental factors, including the change of the sputtering deposition conditions, the post-deposition treatments, the plasma activation, and the antibody concentration.

Regarding the chemisorption approach, the results showed a slightly higher fluorescent signal per area, reaching 3.3 ± 0.2 % and an SNR of 129 (Figure 3.7b). The fluorescence coverage was uniformly distributed not only across the thin film's surface, but also among multiple replicates (CV of 16.3%), emphasizing reproducibility (Figures 3.7a and S3.5). The adhesion (DSP) layer improves the immobilization and orientation of the first antibody, creating a denser and more functional bioreceptor layer. This allows the fluorescent (second) antibody to interact more effectively with the bioreceptor elements, enhancing biosensing performance through stronger fluorescent detection.

Chemisorption, involving covalent bonding, offers stronger attachment of the bioreceptors to the thin film's surface compared to the non-covalent (electrostatic or hydrophobic) interactions. Firmly anchored bioreceptors (first antibodies) maintain favorable coverage and orientation, enabling consistent detection of fluorescent (second antibody) pairs and ensuring reliable detection performance across samples, which is critical for high-standard biosensors. As a result, this approach provides lower variability (lower CV) and higher reproducibility.

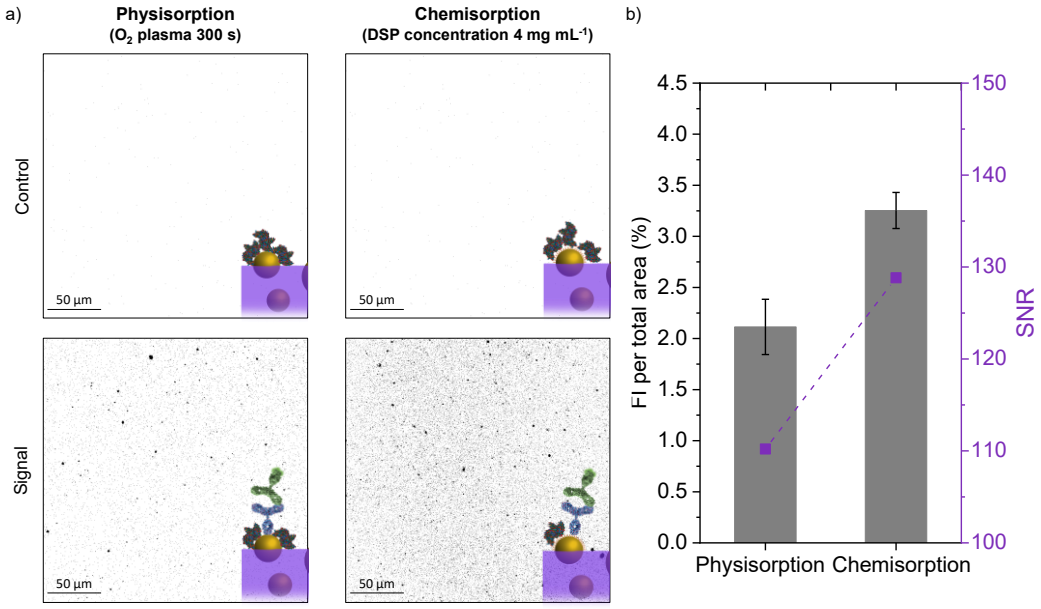


Figure 3.7. Immunoassay on O_2 plasma-activated (without DSP) and DSP-functionalized Au-TiO_2 thin film, using bioreceptor (IgG) and its respective biological pair (Fab-specific anti-IgG-FITC secondary antibody). (a) Processed confocal microscopy images and (b) fluorescent intensity per total thin film's area, considering the physisorption and chemisorption immobilization approaches.

3.5. Conclusion

This work aimed to study two different bioreceptor immobilization approaches by comparing both physisorption and chemisorption strategies. For the physisorption strategy, a prior O_2 plasma activation was applied to Au-TiO_2 thin films to improve the adsorption effectiveness of bioreceptors. Regarding the chemisorption strategy, plasma-activated thin films were functionalized with different DSP cross-linker concentrations.

For the DSP concentrations investigated, the cross-linker layer exhibited uniform coverage over the thin film's surface. Yet, at a specific concentration of 4 mg ml^{-1}, isolated islands arranged in a fractal structure emerged, reproducing the chemical footprint of DSP molecule.

According to the objective of this work, bioreceptor immobilization coverage and activity were assessed using both immobilization strategies. Both methods demonstrated uniformly fluorescent surfaces with high SNR, indicating consistent bioreceptor attachment and effective target binding. Nevertheless, chemisorption strategy, using the DSP concentration of 4 mg mL^{-1}, was considered the most attractive approach for creating a denser, oriented, and active bioreceptor layer.

To conclude, the DSP layer acts as an effective cross-linker, forming a stable and oriented bioreceptor layer. This ensures a high density of active sites for specific interactions with the target molecules, increasing the detection performance, uniformity, and reproducibility.

3.6. Supporting Information

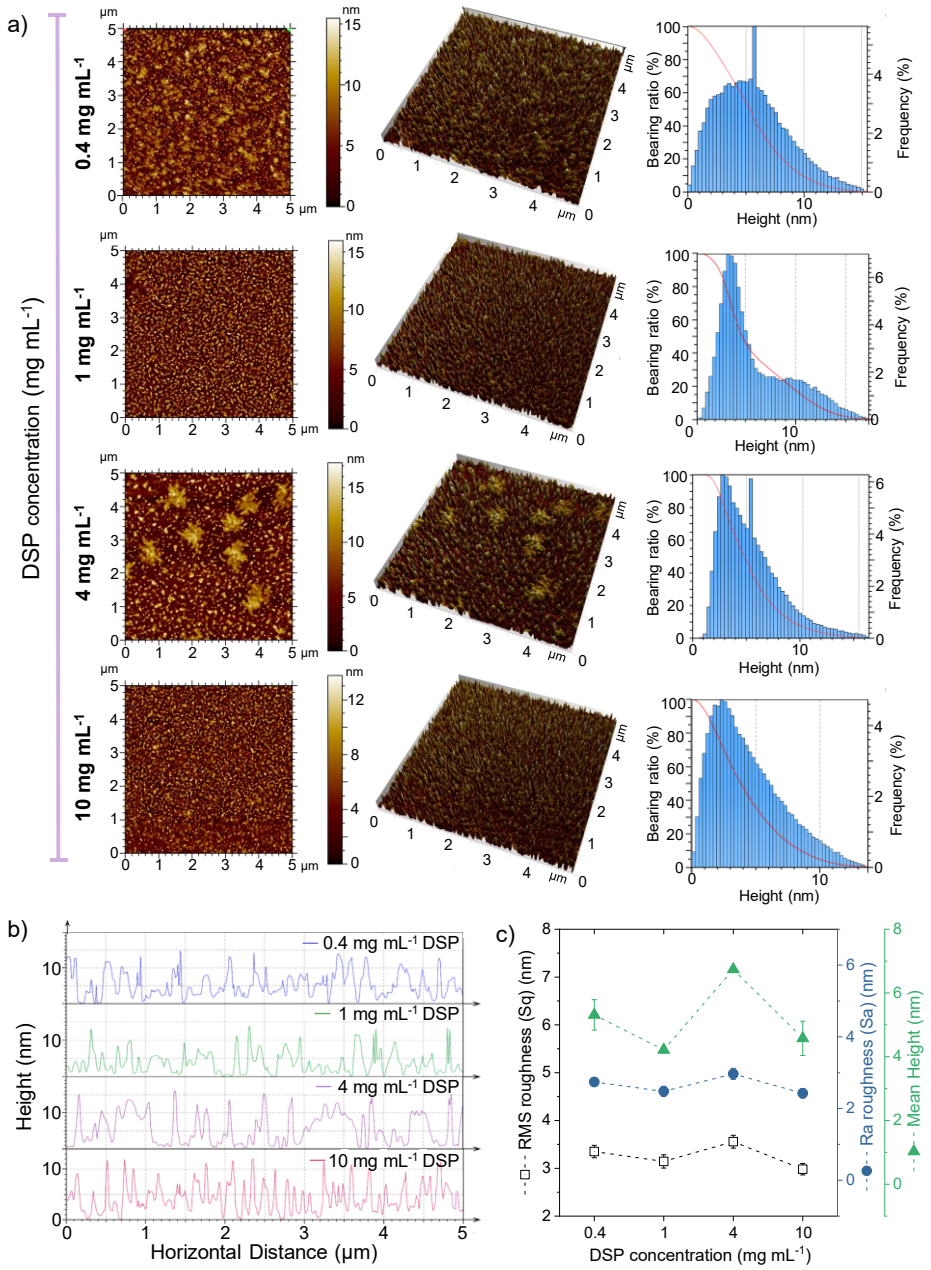


Figure S3.1. Influence of the DSP cross-linker concentration in the morphology of plasma-activated thin films (300 s). (a) Two-dimensional (2D), three-dimensional (3D) AFM height images and height distribution profiles, (b) topographic profile, and (c) morphological parameters (i.e., root mean square roughness (Sq), surface mean roughness (Sa), and mean height).

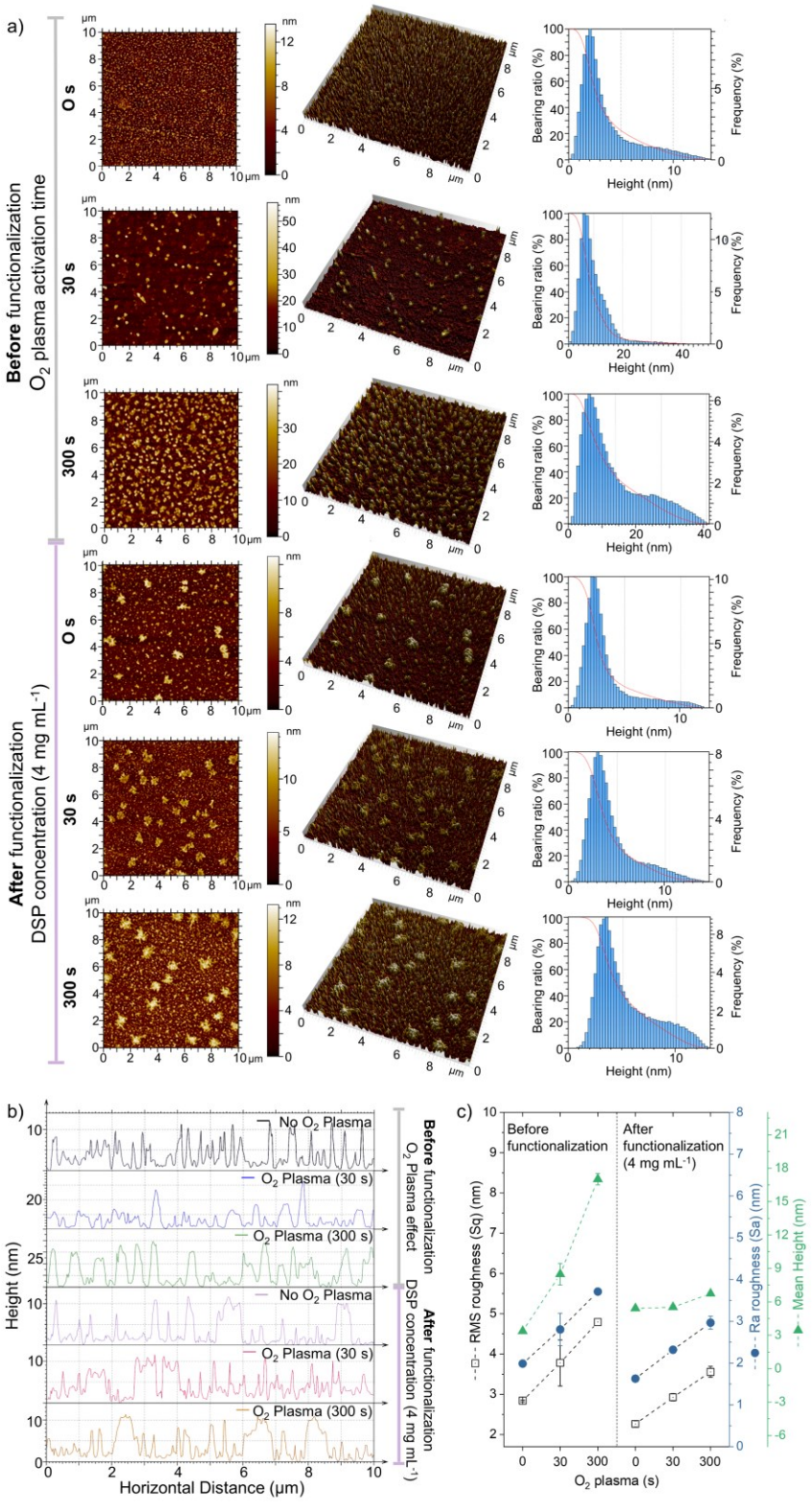


Figure S3.2.Influence of O_2 plasma treatment time in the morphology of plasma-activated (without DSP) and DSP-functionalized Au-TiO_2 thin films with the specific concentration of 4 mg mL^{-1}. (a) Two-dimensional (2D), three-dimensional (3D) AFM height images and height distribution profiles, (b) topographic profile, and (c) morphological parameters (i.e., root mean square roughness (Sq), surface mean roughness (Sa), and mean height).

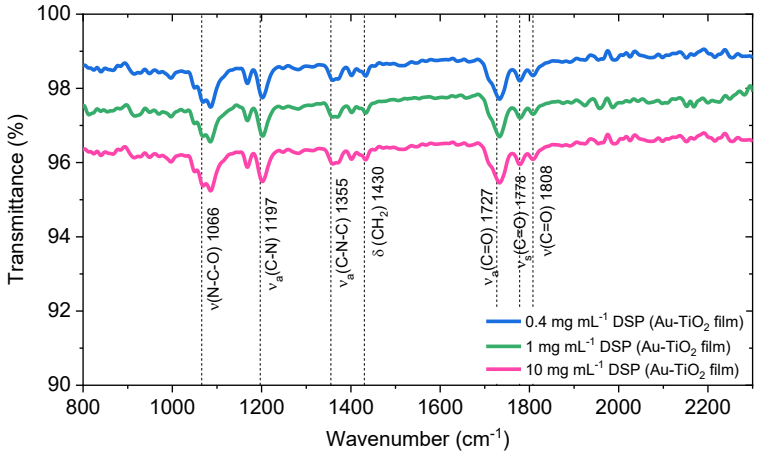


Figure S3.3. Infrared spectra of DSP-functionalized Au-TiO_2 thin films, with 0.4, 1 and 10 mg mL^{-1} concentrations.

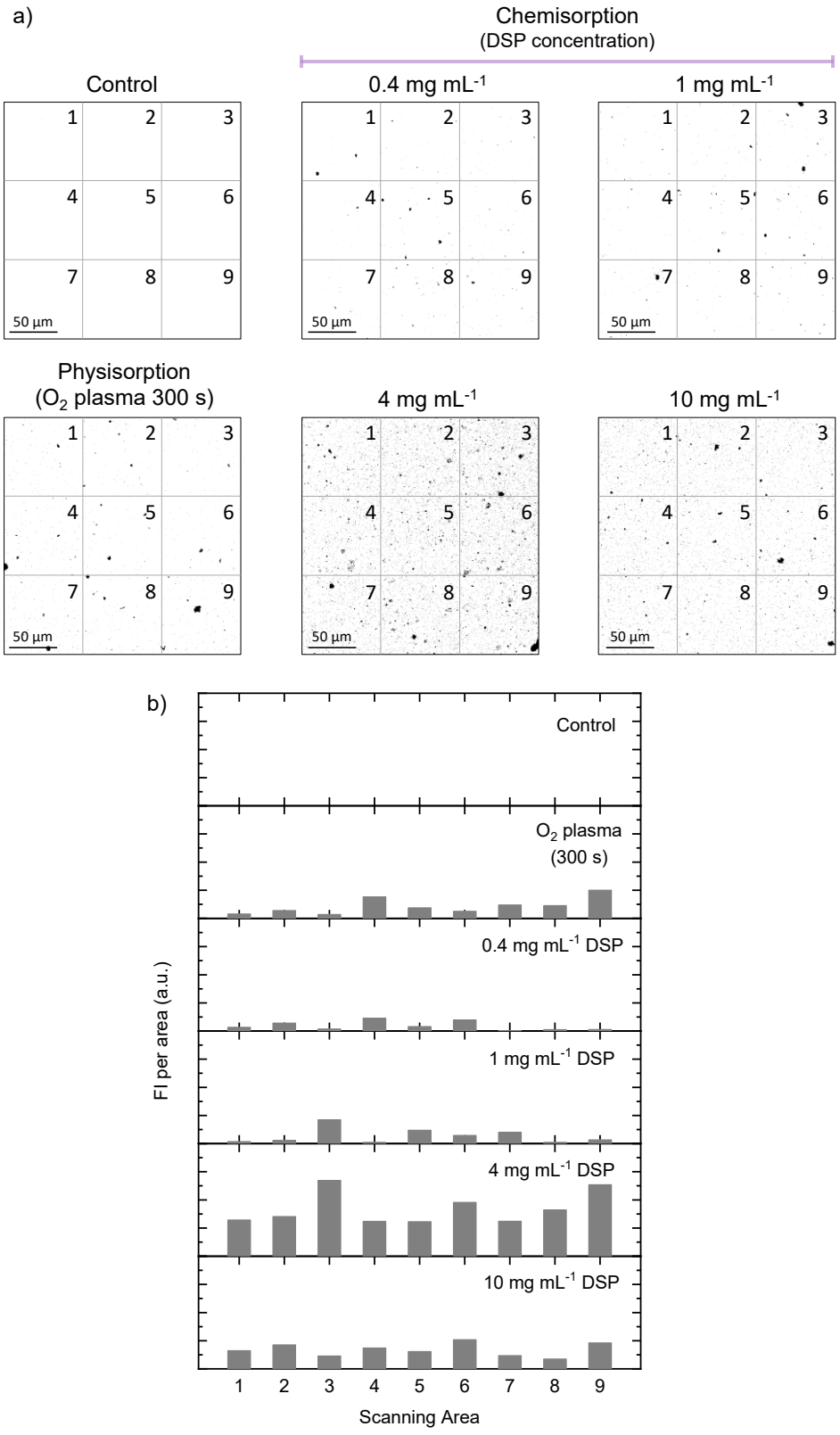


Figure S3.4. Uniformity of the antibody surface coverage on O_2 plasma-activated (without DSP) and DSP-functionalized Au-TiO_2 thin film. (a) Processed confocal microscopy images were divided into nine distinct areas (82 × 82 µm²) and (b) fluorescent intensity (a.u.) per thin film's area, considering the physisorption and chemisorption immobilization approaches, at different DSP concentrations.

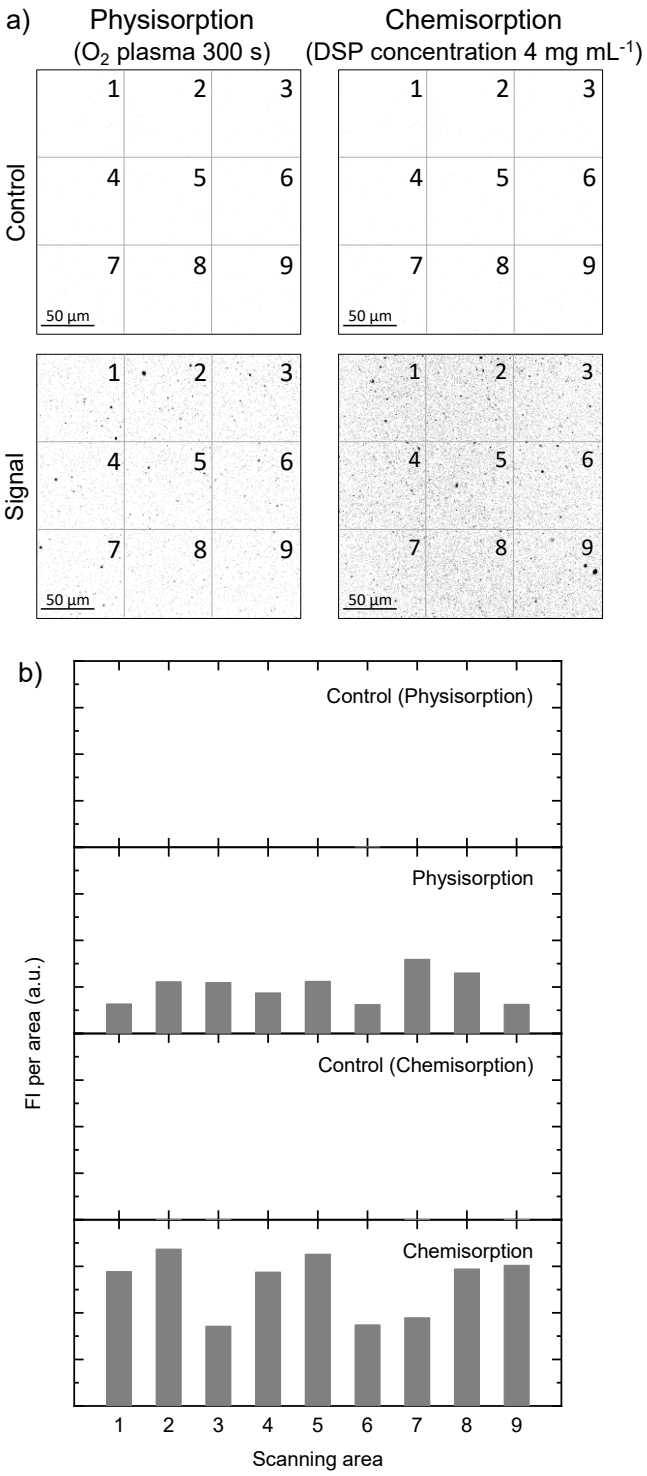


Figure S3.5. Uniformity of the fluorescent immunoassay on O_2 plasma-activated (without DSP) and DSP-functionalized Au-TiO_2 thin film. (a) Processed confocal microscopy images were divided into nine distinct areas (82 × 82 µm²) and (b) fluorescent intensity (a.u.) per thin film's area, considering the physisorption and chemisorption immobilization approaches.

Chapter 4

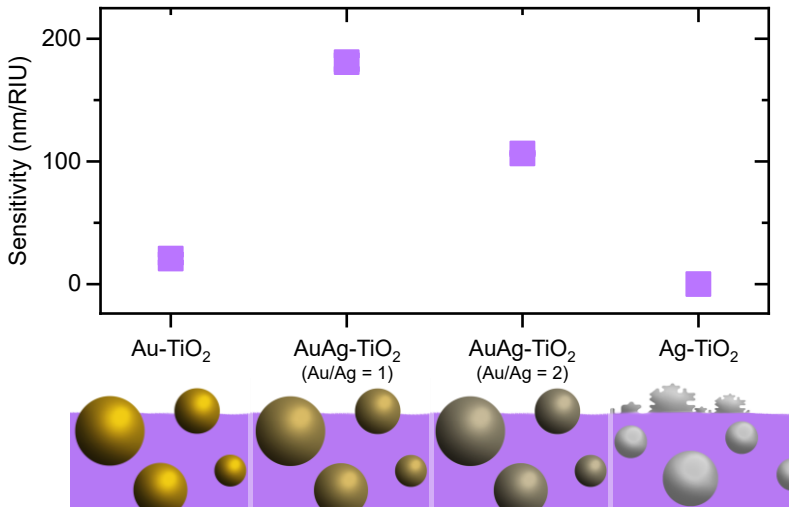
Enhancing the Extinction Efficiency and Plasmonic Response of Bimetallic Nanoparticles of Au-Ag in Robust Thin Film Sensing Platforms

D.I. Meira, M.S. Rodrigues, J. Borges, F. Vaz, Enhancing the Extinction Efficiency and Plasmonic Response of Bimetallic Nanoparticles of Au-Ag In Robust Thin Film Sensing Platforms, Sensors 23 (2023) 9618. https://doi.org/10.3390/s23239618.

4.1. Abstract

The extinction efficiency of noble metal nanoparticles (NPs), namely gold (Au) and silver (Ag), are dependent on their size and surrounding dielectric. Exploiting the Localized Surface Plasmon Resonance (LSPR) phenomenon, the composition and structure of the NPs might be tailored to achieve a configuration that optimizes their response (sensitivity) to environmental changes. This can be done by preparing a bimetallic system, benefiting from the chemical stability of Au NPs and the higher scattering efficiency of Ag NPs. To enhance the LSPR sensing robustness, incorporating solid supports in the form of nanocomposite thin films is a suitable alternative. In this context, the NPs composed of gold (Au), silver (Ag), and their mixture in bimetallic Au-Ag NPs, were grown in a titanium dioxide (TiO_2) matrix using reactive DC magnetron sputtering. Thermal treatment at different temperatures (up to 700 °C) tuned the LSPR response of the films and, consequently, their sensitivity. Notably, the bimetallic film with Au/Ag atomic ratio 1 exhibited the highest refractive index sensitivity (RIS), with a value of 181 nm/RIU, almost one order of magnitude higher than monometallic Au-TiO_2. The nanostructural analysis revealed a wide NP size distribution of bimetallic NPs with an average size of 31 nm, covering about 20% of the overall surface area. These findings underscore the significant potential of bimetallic film systems, namely AuAg-TiO_2, in LSPR sensing enhancement.

Keywords: Plasmonics; Localized Surface Plasmon Resonance (LSPR); AuAg-TiO_2 thin film; Au-Ag nanoparticle; Refractive Index Sensitivity (RIS)



4.2. Introduction

Several nanoscience areas (e.g., materials, physical, chemical, and biological) take advantage of the Localized Surface Plasmon Resonance (LSPR) phenomenon by exploring the optical properties of metallic nanostructures [298–300]. The LSPR phenomenon can be interpreted as an interaction between an incident electromagnetic field and the free electrons of metallic nanoparticles (NPs), resulting in a collective oscillation of the electron cloud with a certain resonance frequency [26,212,301,302]. These plasmon excitations are non-propagating, i.e., are highly confined to the metal nanostructure-dielectric interface. The resultant light–matter interaction gives rise to several distinct phenomena: (i) strong extinction (LSPR) bands, due to absorption and scattering, when the wavelength of the incident light is about one order of magnitude higher than the NP size, and (ii) enhancement of the electromagnetic field near the metallic surface [23,303,304]. The LSPR band position, intensity, and width can be tuned by metal composition, geometrical characteristics (size, shape, and interparticle distance) of the nanostructures, and surrounding conditions (e.g., temperature, pressure, and refractive index (RI)) [26,305–308].

The most commonly studied noble metal nanostructures are Au and Ag NPs since their resonance frequency falls into the visible region of the electromagnetic spectrum [309,310]. In plasmonics applications, the Au NPs present some pertinent features: inert nature and stability, relatively simple synthesis bioconjugation, as well as, bio-inertness, biocompatibility, and poor toxicity [311,312]. In turn, the Ag NPs reveal higher extinction cross-sections (i.e., higher absorption and scattering efficiencies), yet for higher energies (lower wavelengths) [313,314]. In addition, it also exhibits a higher inherent optical loss compared to the Au NPs [315]. To demonstrate these features, Figure 4.1 depicts the calculated spectra of extinction, scattering, and absorption efficiencies for the Au and Ag NPs with the same size and surrounding dielectric medium. The efficiency spectra were calculated using a software from Nanohub.org (v1.03UQ) [316], considering spherical shapes and three different diameters (10, 20, and 30 nm), embedded in a dielectric medium with a refractive index of 2.3 (close to the anatase phase of titanium dioxide (TiO_2), as previously calculated by the authors [205]).

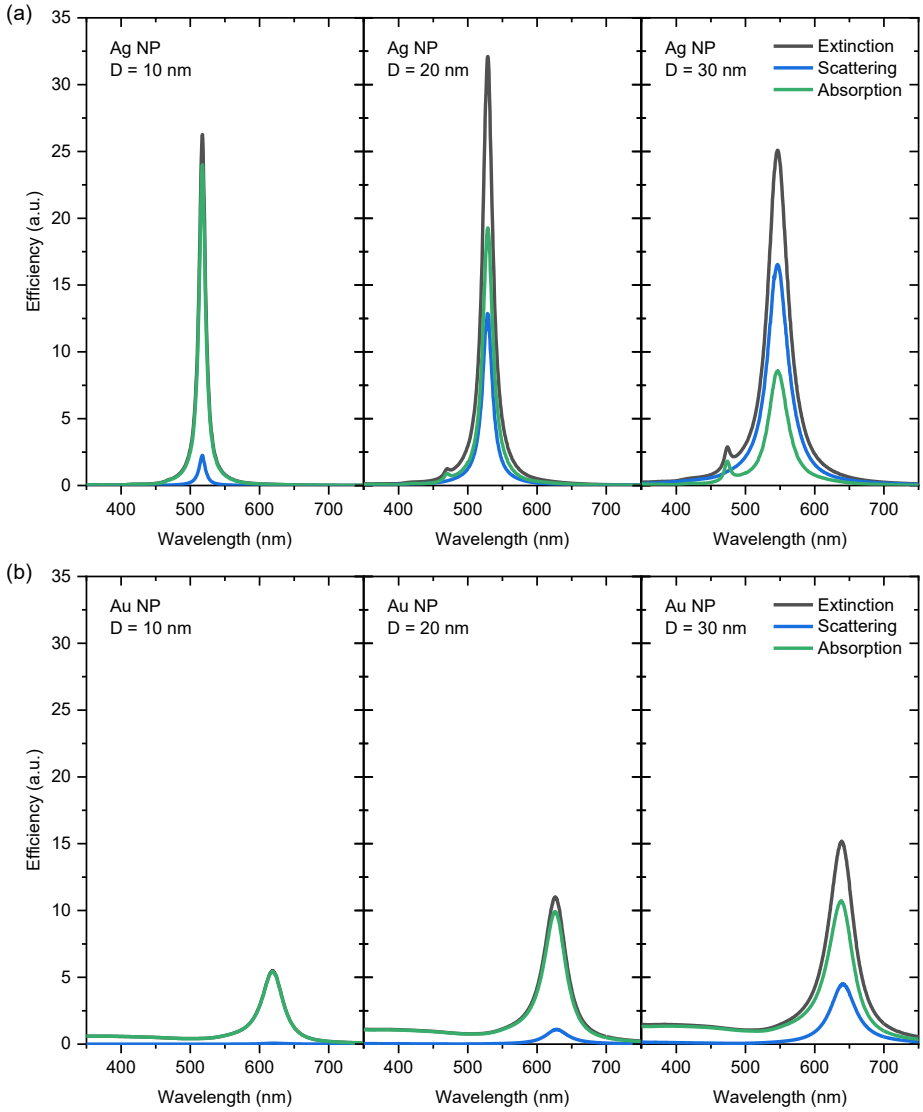


Figure 4.1. Calculated extinction, scattering, and absorption efficiencies of a spherical nanoparticle with variable size (D = 10, 20, 30 nm), composed of (a) Ag and (b) Au, surrounded by a dielectric medium with a constant refractive index of 2.3 (simulating a TiO_2 matrix). Calculations were performed using a software from Nanohub.org [316].

As depicted in Figure 4.1, the absorption and scattering efficiencies can be tuned by the NP size. For instance, if the NP is smaller than 20 nm, the predominant process is absorption. An increase in NP size leads to a scattering efficiency enhancement [206,207,301,317]. Comparing both monometallic counterparts at the same conditions, the Ag NPs are more efficient in scattering light at the resonance condition and, therefore, will exhibit enhanced sensitivity factors, i.e., higher responsiveness to environmental changes [318].

In Figure 4.2, the refractive index sensitivity (RIS) was simulated for both the Au and Ag NPs covered with a TiO_2 cap layer, considering different NPs sizes and layer thicknesses. Considering the same layer thicknesses, the sensing ability of both the metallic NPs is enhanced with the increasing NPs size. Moreover, Figure 4.2 also highlights the significant influence of the surrounding media on the NP's sensing ability. Variations in the refractive index of the NP surrounding medium will lead to a measurable resonance band shift. However, this shift only occurs if the refractive index variation takes place in the sensing volume contained within the plasmon's electric field decay length. The plasmon field decay decreases exponentially with the distance from the NP, limited between a length range of 10 to 30 nm, depending on the NP size and shape [30,31]. Hence, increasing the TiO_2 layer around the NP will lead to a decrease in the intensity of the LSPR extinction band and, consequently, in the sensing ability [29].

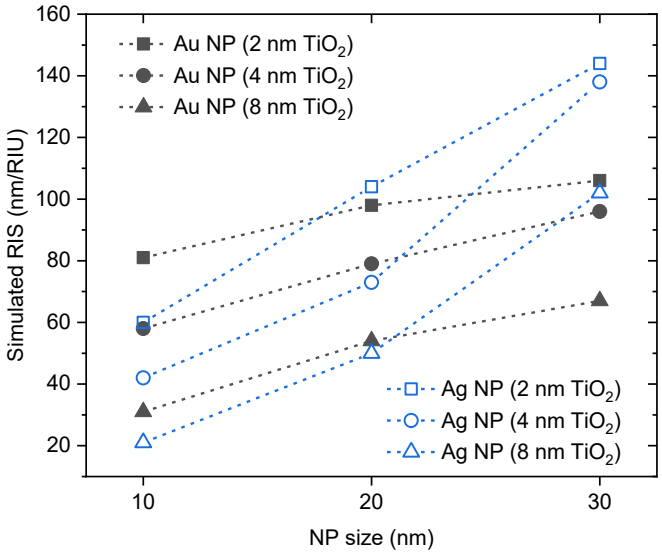


Figure 4.2. Simulated refractive index sensitivity (RIS) of a spherical nanoparticle (D = 10, 20, 30 nm) surrounded by a TiO_2 finite layer (d = 2, 4, 8 nm), immersed into two environments with different refractive index units, η_1 (RIU) = 1.333 and η_2 (RIU) = 1.381 ($\Delta\eta$ = 0.048) [316]. RIS was calculated by the difference in the wavelength of extinction maxima, divided by the difference in refractive index units, according to $RIS = (\lambda_2 - \lambda_1)/\Delta\eta$.

Typically, the noble metal monometallic NPs have been recognized for a broad range of sensing applications. These NPs are frequently commercialized as colloids, and an example of their use is the Lateral Flow Immunoassay (LFIA) platforms (e.g., the COVID test [319]). However, the synergistic combination of the Au and Ag NPs in bimetallic systems may offer several advantages in different dimensions (e.g., economic, and functional aspects in plasmonic sensing technology), compared to their monometallic counterparts [318,320,321]. Incorporating the Au NPs in bimetallic systems improves the

chemical and thermal stability of the Ag NPs, preventing oxidation and enabling biocompatibility [315,322,323]. In turn, the Ag NPs can enhance and tune the plasmonic properties, while being reasonably priced [324]. All of these characteristics and properties have enabled the development of more effective plasmonic (e.g., LSPR [309,325–329], SERS (surface-enhanced Raman spectroscopy) [330,331], and SPCE (surface plasmon-coupled emission) [332–334]) sensing applications. For instance, Alkhalayfeh et al. [335] reported a significant enhancement of broadband light absorption in polymer solar cells by up to 69.6% due to the LSPR effect of the incorporated combined Au-Ag NPs. Regarding a biosensing application example, Zheng et al. [336] reported a novel aptasensor for ochratoxin-A detection based on enhanced electromagnetic fields (near-field) caused by the plasmonic coupling behavior of the bimetallic Au-Ag Janus NPs. Furthermore, Costa et al. [219] prepared bimetallic Au-Ag NPs dispersed in a TiO_2 matrix. In that work, the thin films have been reported as potentially efficient LSPR-based sensing platforms since they were able to reproduce significant changes in the LSPR band's parameters (i.e., wavelength shift and LSPR band central moments) upon different surrounding media.

In the present work, the sensing ability of the Au-TiO_2, Ag-TiO_2, and bimetallic AuAg-TiO_2 nanocomposite thin films was analyzed to develop an LSPR-sensing platform with optimal sensitivity. For that, nanocomposite thin films were deposited by reactive DC magnetron sputtering, using a Ti target with varying amounts of the Au and/or Ag pellets to obtain different noble metal ratios (from Au and Ag to Au-Ag in different ratios) throughout the TiO_2 dielectric matrix. Following the deposition, the nanocomposite thin films were thermally annealed at different temperatures. This treatment favors the growth and coalescence of NPs and, consequently, develops an enhanced plasmonic response. To identify the LSPR response of the thin films and assess their sensitivity (refractive index sensitivity, RIS), optical (transmittance) spectra measurements were conducted. Further, the LSPR sensing experiments were performed using deionized water and a model solution of sucrose (30% *w/w*), exhibiting different RI. The surface morphology and nanostructure of the nanocomposite thin film that revealed the highest RIS were further investigated, correlating both Scanning Electron Microscopy (SEM) and Atomic Force Microscopy (AFM) analysis.

4.3. Materials and Methods

4.3.1. Reactive DC Magnetron Sputtering Deposition

Nanocomposite thin films composed of Au NPs, Ag NPs, and Au-Ag NPs dispersed throughout a TiO_2 dielectric matrix were deposited onto quartz substrates (SiO_2) (quality JS1from Neyco Vacuum and Materials, Vanves, France). The substrates were placed on a hexagonal sample holder centered on the

high-vacuum sputtering chamber, 70 mm far from the target. Before the deposition, the substrates were treated and activated, using an in situ etching process with the Ar plasma using a pulsed DC power supply (model TruPlasma DC 4005 from Hüttinger Elektronik, Nuremberg, Germany), while the sample holder rotated at 5.5 rpm speed. The sputtering target was composed of three-quarters of a noble metal disk (total area, 12 mm^2) symmetrically placed in the erosion track of a rectangular titanium (Ti) target (200 × 100 × 6 mm^3, 99.99% purity) from Testbourne Ltd, Hampshire, England. The noble metal pellet area varied between 12 mm^2 of Au, 12 mm^2 of Ag, and mixtures of Au and Ag (8 mm^2 of Au + 4 mm^2 of Ag and 4 mm^2 of Au + 8 mm^2 of Ag). In a plasma composed of Ar (working gas, 3.8 × 10^{-1} Pa) and O_2 (reactive gas, 3.6 × 10^{-2} Pa), the target was sputtered for 8 min, aiming to deposit a nanocomposite thin film with a thickness of approximately 50 nm. The deposition process was performed with base pressure below 6.0 × 10^{-4} Pa, while the DC current density was set to 75 A m^{-2}, and the (negative) target potential was (370 ± 4) V.

4.3.2. Post-Deposition Annealing Treatment

The films were subjected to a post-deposition thermal annealing treatment at atmospheric pressure to promote the formation and growth of the NPs throughout the TiO_2 matrix, consequently developing an enhanced plasmonic (LSPR) behavior. In a programmable in-air muffle furnace (model LE 6/11/R7 from Nabertherm, Lilienthal, Germany), the thin films were annealed at different temperatures, ranging from 400 to 700 °C [36]. The heating ramp used was 5 °C/min, from room temperature to reach the predetermined annealing temperature, and an isothermal period was maintained for 5 h. Subsequently, the thin films cooled freely inside the furnace until they reached room temperature.

4.3.3. Chemical Composition Analysis

Rutherford Backscattering Spectrometry (RBS) was utilized to determine in-depth chemical concentrations of the as-deposited thin films, using a Van Graaff accelerator (model AN-2500 Type-A from High Voltage Engineering Europe, Amersfoort, Netherlands) in a small chamber with three detectors. Inside the chamber, 2.2 MeV $^4He^+$ beam impinged on the surface (1 mm^2) of thin films at an incidence angle of 0° (normal incidence) and 25°. A standard detector was placed at 140°, and two pin-diode detectors were positioned symmetrically to each other at 165° of scattering angle respective to the beam direction. The RBS data were analyzed using the IBA DataFurnace NDF v10.0b software [233,234,337].

4.3.4. Optical Response Measurements

A custom-made optical system was utilized to investigate the optical response of the nanocomposite thin films. The system comprised a tungsten light source, an enclosed thin film holder, and an Ocean Optics spectrometer (model HR4000, Edinburgh, UK), all interconnected by optical fibers, which operated in transmittance mode. The optical measurements were conducted by observing the transmittance spectra within the wavelength range from 300 to 900 nm. The NANOPTICS software (v2022a) [238] was used to analyze the LSPR bands' parameters (i.e., wavelength and transmittance coordinate at the transmittance minimum, full height, and full width at half height (FWHH)).

4.3.5. Nanoparticles Distribution Analysis by SEM

The morphology of a selected nanocomposite thin film system was examined using Scanning Electron Microscopy (SEM), using an ultra-high resolution Field Emission Gun Scanning Electron Microscope (FEG-SEM) (NOVA 200 Nano SEM, FEI Company, Oregon, United States). The SEM micrographs were obtained at an acceleration voltage of 10 kV, using an ultra-high resolution detector (Through-lens detector (TLD)). The SEM micrographs were analyzed using a MATLAB algorithm to determine the NPs distributions (i.e., average Feret diameter, nearest neighbor (N.N.) distance, and aspect ratio (A.R.)).

4.3.6. Thin Film Surface Nano-Morphology by AFM

Atomic Force Microscopy (AFM) analysis was performed using a high-resolution Nano-Observer AFM microscope by CSI Instruments (Les Ulis, France). The AFM microscope was operated in resonant mode using an SPM probe model FORTA (n-type Si; resonance frequency 43–81 kHz; spring constant 0.6–3.7 N/m; tip radium < 10 nm). The AFM height images were scanned at 5 × 5 μm^2 and 10 × 10 μm^2, with a resolution of 1024 × 1024 pixels. After performing the AFM scans, the topography profiles were analyzed using the freely available Gwyddion software (v2.59).

4.3.7. Refractive Index Sensitivity Tests

Refractive Index Sensitivity (RIS) was assessed by measuring the optical response of nanocomposite thin films, annealed at 400 and 700 °C, at different surrounding media with various refractive indices (RIs). The surrounding media switched between deionized water (DI water) (η = 1.333 RIU) and a 30% (*w/w*) sucrose solution (η = 1.3811 RIU) at room temperature. During the immersion, the transmittance spectra were monitored in real-time for 1 min (per half-cycle) using an Ocean Optics

spectrometer (model HR4000, Edinburgh, UK) with an integration time of 4 ms and an average of 500 scans. The NANOPTICS software (v2022a) analyzed the average wavelength peak position of the LSPR band over time and estimated the RIS value. This RIS value was calculated by the ratio of the average wavelength shift to the RI difference of the surrounding medium, according to RIS = $(\lambda_2 - \lambda_1)/\Delta\eta$. Furthermore, the NANOPTICS software (v2022a) also considered the signal-to-noise ratio (SNR) of the measurements.

4.4. Results and Discussion

4.4.1. Chemical Composition Analysis

For this work, different sets of thin films were produced: monometallic Au-TiO_2 and Ag-TiO_2 and bimetallic AuAg-TiO_2 thin films. The atomic concentration of the noble metal elements (Au, Ag) dispersed in the TiO_2 matrix varied as a function of the number of Au and/or Ag pellets placed on the titanium target (Table 4.1).

Table 4.1. Atomic concentration of Au and Ag in nanocomposite Au-TiO_2, AuAg-TiO_2, and Ag-TiO_2 thin film systems.

Plasmonic System	Pellet dimension		Pellet area (mm^2)		Atomic percentage (at. %)		Atomic concentration ratio (Au/Ag)
	Au	Ag	Au	Ag	Au (±0.5)	Ag (±0.5)	
Au-TiO_2	¾	-	12	-	16.7	-	-
AuAg-TiO_2	½	¼	8	4	8.6	9.1	1
	¼	½	4	8	6.5	11.8	2
Ag-TiO_2	-	¾	-	12	-	18.2	-

In the case of the Au-TiO_2 thin film system, the noble metal content was found to be 16.7 ± 0.5 at.%. In one of the prepared AuAg-TiO_2 thin films, it was estimated a noble metal concentration of 8.6 (± 0.5) at.% for Au and 9.1 (±0.5) at.% for Ag. Despite the thin film being prepared with distinct metal pellet areas (8 mm^2 of Au and 4 mm^2 of Ag), the Au/Ag atomic ratio was very close to 1. Another bimetallic film, prepared with 4 mm^2 of Au and 8 mm^2 of Ag pellet areas, exhibited a metal composition of 6.5 (±0.5) at.% for Au and 11.8 (±0.5) at.% for Ag, resulting in an Au/Ag atomic ratio approaching 2. The distinct Au/Ag atomic ratio results from the difference in sputtering yield between Ag (2.20) and Au (1.65) during the deposition process [338], thus translating into a higher sputtered Ag content compared to the Au for the same pellet area. Finally, regarding the Ag-TiO_2, the Ag content was found to be 18.2 ± 0.5 at.%.

4.4.2. Optical Response Analysis

The optical transmittance spectra of the nanocomposite thin films were analyzed at various annealing temperatures (400, 600, and 700 °C) to evaluate their relevant plasmonic response, as depicted in Figure 4.3.

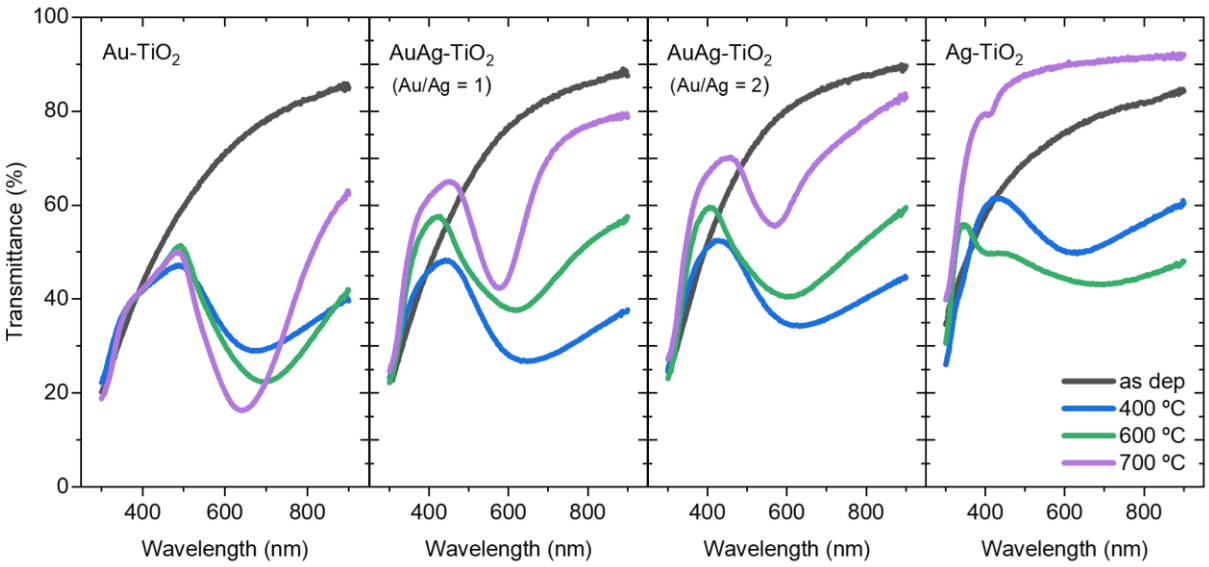


Figure 4.3. Optical transmittance spectra of the Au-TiO_2, AuAg-TiO_2, and Ag-TiO_2 films with different Au and/or Ag contents and subjected to different annealing temperatures.

Despite the possible presence of non-crystallized NPs formed during the sputtering process, the transmittance profiles of all thin films exhibited no LSPR response. As Koneti et al. [239] stated, this negligible plasmonic response can be attributed to the limited size of the metallic NPs within the matrix, most likely a few nanometers below the quantum size limit (around 10 nm). In contrast, the annealing treatment in the nanocomposite thin film favors the metallic atoms diffusion within the TiO_2 matrix and the progressive formation of the NPs. As the annealing temperature increases, the small-size group of the NPs acts as nucleation sites for the crystallization and "normal growth" of the monometallic and/or bimetallic NPs. The coalescence of adjacent NPs and Oswald ripening phenomena may also occur at higher temperatures [339]. As a result, the plasmonic response is enhanced, leading to changes in the LSPR bands' measurable parameters, as shown in Table 4.2.

Table 4.2. LSPR band parameters of Au-TiO_2, AuAg-TiO_2 (Au/Ag atomic ratio of 1 and 2), and Ag-TiO_2 films subjected to different annealing temperatures.

Plasmonic System	Annealing Temperature	LSPR band parameters			
		Wavelength (nm)	Transmittance (%)	Full height (p.p.)	FWHH (nm)
Au-TiO_2	400 °C	671.93	28.93	18.27	292.09
	600 °C	693.19	22.90	28.48	281.76
	700 °C	639.41	16.07	33.96	190.95
AuAg-TiO_2 Au/Ag=1	400 °C	641.66	26.69	21.56	367.39
	600 °C	613.98	37.97	19.64	257.22
	700 °C	574.89	42.98	22.04	124.66
AuAg-TiO_2 Au/Ag=2	400 °C	626.17	34.22	18.17	358.01
	600 °C	602.41	40.74	18.76	285.49
	700 °C	568.65	56.28	13.89	130.55
Ag-TiO_2	400 °C	627.46	49.86	11.63	272.24
	600 °C	-	-	-	-
	700 °C	-	-	-	-

According to the literature, higher annealing temperatures induce the NPs size increase, enhancing the scattering-to-absorption ratio, and consequently, the LSPR band tends to shift to higher wavelengths [239,301,340,341]. In fact, according to the simulations depicted in Figure 4.1, both the Ag and Au NPs display a reasonable redshift as their size increases. However, it is crucial to note that the calculations presented in Figure 4.1 are intended solely for qualitative correlation between the LSPR behavior and Ag and Au NP sizes. A quantitative correlation analysis, such as the exact position of extinction maxima (that corresponds to transmittance minima), cannot be performed since the thin film nanomaterial prepared experimentally comprises a wide distribution of NP sizes, revealing it as a more complex system.

Nevertheless, as perceivable from Figure 4.3 and taking into consideration the calculations in Figure 4.1, the observed trends are different from what would be expected. All the LSPR bands of Au-containing systems shifted to lower wavelengths (blueshift) when the temperature increased from 600 to 700 °C. The plasmonic behavior of NPs is influenced by the RI of their surrounding medium. Yet, the effective RI of the medium surrounding the NPs might be influenced not only by the host TiO_2 matrix. The smaller NPs would be fully embedded within the matrix, while the larger ones could be partially exposed. As observed in previous work [34], the TiO_2 matrix crystallization favors the presence of "grooves" resulting from grain boundary formation. These grooves serve as pathways that facilitate the growth of the NPs towards larger sizes, enabling them to "emerge" on the surface of the thin film. In turn, the TiO_2 matrix crystallizes into two phases: anatase and rutile, above 300 °C and 600 °C, respectively, with successively higher RIs [342,343]. TiO_2 not only tunes the LSPR band by modulating the surrounding refractive index, but also constrains the NPs size distribution [29]. Considering that the plasmon decay length of the NP is typically around 30 nm [30,31] and the estimated thickness of the film is approximately

50 nm, the effective RI of the dielectric medium (air plus matrix) will thereby significantly influence the LSPR band position.

In Ag-containing systems, the Ag concentration deeply influences the LSPR band position. As the Ag content in the nanocomposite thin film increases, the LSPR band shifts towards lower wavelengths, considering the same annealing temperature. This LSPR band blueshift can be primarily attributed to the increased contribution of Ag and bimetallic NPs to the overall extinction cross-section. In fact, LSPs in Ag NPs are excited at lower wavelengths than in Au NPs, and hence, the difference in excitation wavelengths between Ag and Au NPs would be predictable [344]. This distinct LSPR behavior between Ag and Au NPs can also be confirmed by the simulations presented in Figure 4.1. Nevertheless, as aforementioned, the annealing treatment may induce certain instability in the Ag NPs, leading to the formation of unique NP aggregation patterns and, beyond, making them more susceptible to oxidation and degradation. Particularly, in the case of the Ag-TiO_2 film annealed at 600 °C, the broad LSPR band may indicate the presence of Ag fractal structures on the film's surface, as already observed in previous works [342,345]. At higher annealing temperatures (700 °C), the Ag NPs may suffer from sublimation [346,347], leading to a vanishing of the plasmonic behavior. Yet, in the bimetallic systems, this behavior seems to be avoided due to the presence of gold, as the occurrence of the LSPR bands confirms (Figure 4.3). Therefore, as anticipated in the introductory section, incorporating Au in bimetallic systems seems to improve the stability and plasmonic behavior of Ag-containing films. Furthermore, the highly stable host TiO_2 matrix that is embedding the NPs, will also confer that long time stability to the plasmonic system.

Still focusing on the LSPR band minimum (extinction maximum), it is anticipated that the transmittance coordinate would decrease with increasing annealing temperature. This LSPR band transmittance decrease is indicative of enhanced plasmonic behavior, which arises from the formation of a greater number of NPs with increasing dimensions, resulting from the atoms dissolved within the host matrix and coalescence phenomena [339]. This phenomenon is particularly notable in the monometallic (Au) thin films. On the other hand, the transmittance coordinates of the LSPR bands of Ag-containing films have increased. Unlike the Au-TiO_2 film, the annealing process in bimetallic films may lead to some Ag sublimation, decreasing the overall noble metal content. Consequently, the transmittance spectra of such films deviate to higher transmittance values.

In addition, other LSPR band parameters evolved with the annealing temperature, namely the full height and the FWHH. Commonly, the LSPR bands tend to become sharper (i.e., the increase of full height) and narrower (i.e., the decrease of FWHH) with an enhanced plasmonic resonance behavior [36,205,212]. Once again, the Au-TiO_2 thin film system followed this trend [239]. However, the increment

of the Ag content in the bimetallic thin films caused a decrease in the full height of the LSPR band, suggesting again that only the bimetallic NPs remain, and the "excess" of Ag probably has sublimated. Consequently, the concentration of noble metal in the films decreases with the annealing treatment, affecting the full height.

In contrast, the FWHH of the LSPR band decreased in all the plasmonic nanocomposite thin film sets with the annealing treatment, indicating that the dispersion of the NPs size decreases, thus fine-tuning their distribution. For instance, the NP's sensing capability can be characterized through a figure of merit (FoM) determined by a ratio between the sensitivity and the FWHH of the LSPR band [212,348–350]. A high FoM (and sensitivity) is mainly caused by a narrow FWHM [351]. Hence, it can be claimed that the annealing treatment at higher temperatures may improve the sensing ability of the plasmonic nanocomposite thin film.

4.4.3. Refractive Index Sensitivity

The sensing performance of the plasmonic nanocomposite thin films was evaluated by monitoring the LSPR band, by exposing them to different surrounding media with varying refractive index, repeated for a total of five cycles. For the RIS assay, only the plasmonic nanocomposite thin films annealed at 400 °C and 700 °C were considered. The lowest annealing temperature was contemplated since it allows the application of plasmonic films on economically viable substrates such as glass, thereby enabling the development of cost-effective nanotechnology solutions. On the one hand, the highest temperature was used since it gave the narrower bands for all the Au-containing films. The plasmonic sensing ability was characterized based on three parameters: the average wavelength peak position of the LSPR band, SNR, and calculated RIS values, as depicted in Table 4.3.

Table 4.3. The optical response analysis of Au-TiO_2, AuAg-TiO_2 (Au/Ag atomic ratio of 1 and 2), and Ag-TiO_2 films, annealed at 400 °C and 700 °C, to the sensitivity assay, considering the LSPR band wavelength shift, SNR and RIS (nm/RIU) values.

Plasmonic system	Annealing temperature	Wavelength shift (nm)	SNR	RIS (nm/RIU)
Au-TiO_2	400 °C	-	-	-
	700 °C	1.06 ± 0.03	80	20.8 ± 0.6
AuAg-TiO_2 Au/Ag=1	400 °C	4.64 ± 0.09	59	96.3 ± 1.8
	700 °C	11.02 ± 0.43	126	180.9 ± 3.2
AuAg-TiO_2 Au/Ag=2	400 °C	2.76 ± 0.04	29	57.2 ± 0.9
	700 °C	5.13 ± 0.27	65	106.5 ± 5.6
Ag-TiO_2	400 °C	-	-	-
	700 °C	-	-	-

Considering the lowest annealing temperature, 400 °C, the sensitivity of the monometallic plasmonic nanocomposite thin films, both the Au-TiO_2 and Ag-TiO_2, could not be determined. The LSPR band position of the Au-TiO_2 thin film, annealed at 400 °C, is 671.41 nm (as mentioned above), which is very close to the wavelength range where the noise contribution of the optical system is significant. In this case, the high noise contribution lowered the SNR, leading to a non-reproducible sensing test. Furthermore, the Ag-TiO_2 thin film did not demonstrate a consistent plasmonic response during the sensitivity tests.

In turn, the RIS value was successfully determined in the bimetallic systems annealed at 400 °C, by measuring the LSPR band peak position shift in response to different RI, as presented in Figure 4.4. In the AuAg-TiO_2 plasmonic nanocomposite thin film, with an Au/Ag atomic ratio of 1, the wavelength peak shifted by approximately 4.64 ± 0.09 nm. However, the wavelength shifts of the AuAg-TiO_2 thin film, with the highest Au content, decreased to around 2.76 ± 0.04 nm. As a result, the RIS values were determined at 96.3 ± 1.8 nm/RIU and 57.2 ± 0.9 nm/RIU, with an SNR of 59 and 29, for the two bimetallic systems, respectively.

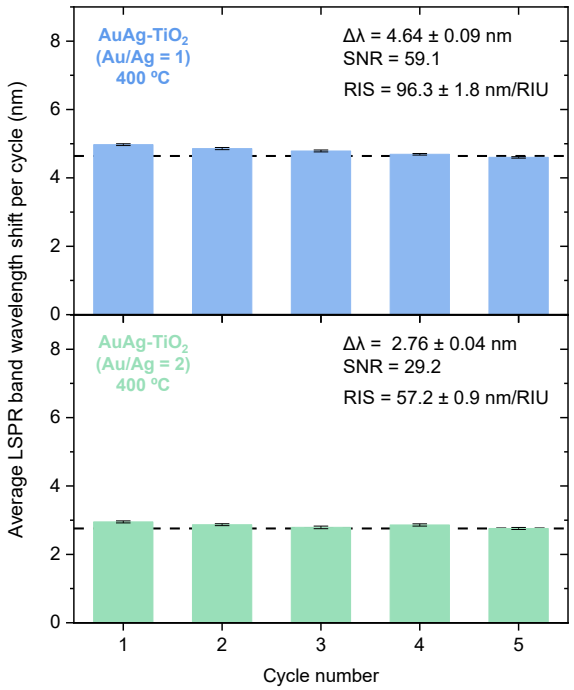


Figure 4.4. LSPR band minimum wavelength shift of AuAg-TiO_2 thin films (Au/Ag atomic ratio of 1 and 2), annealed at 400 °C, during the RIS assessment, concerning each cycle. The surrounding media of the plasmonic nanocomposite thin film changed between DI water and sucrose solution of 30% (w/w) of sucrose.

The effect of the thermal annealing treatment induces different nanostructural changes, namely the increase of the size of the NPs, leading to enhanced sensitivity of the nanocomposite thin films, as

anticipated by the simulations depicted in Figure 4.2. Therefore, the sensing response of the Au-TiO_2 and AuAg-TiO_2 thin films annealed at the highest annealing temperature is plotted in Figure 4.5.

Specifically, the Au-TiO_2 thin film annealed at 700 °C exhibited a sharper and more intense LSPR band positioned at lower wavelengths than 400 °C, enabling accurate RIS determination. In this specific case, the peak position of the LSPR band shifted approximately 1.06 ± 0.03 nm in response to media with different RI, corresponding to an RIS value of 20.8 ± 0.6 nm/RIU, with an SNR of 80. In turn, the AuAg-TiO_2 thin film, with a lower Ag content, exhibited a more significant shift in the LSPR band of 11.02 ± 0.43 nm, leading to a higher RIS estimation of 180.9 ± 3.2 nm/RIU and SNR of 126. Conversely, the bimetallic system, with an Au/Ag atomic ratio of 2, displayed a reduced wavelength peak shift of 5.13 ± 0.27 nm, resulting in an RIS value of 106.5 ± 5.6 nm/RIU and SNR of 65.

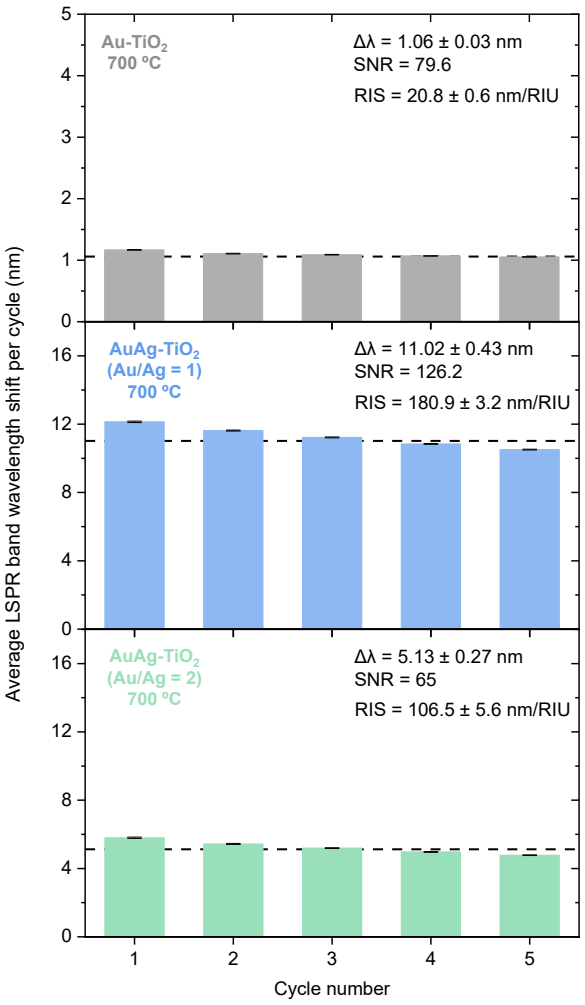


Figure 4.5. LSPR band minimum wavelength shift of Au-TiO_2, and AuAg-TiO_2 thin films (Au/Ag atomic ratio of 1 and 2), annealed at 700 °C, during the RIS assessment, concerning each cycle. The surrounding media of the plasmonic nanocomposite thin film changed between DI water and sucrose solution of 30% (w/w) of sucrose.

The combination of specific bimetallic compositions and annealing conditions plays a critical role in optimizing the plasmonic properties and sensitivity of the thin films for sensing applications. Particularly, the inclusion of the Ag content into the Au-TiO_2 resulted in higher LSPR band shifts, leading to an improved RIS performance. Notably, the bimetallic system with an Au/Ag atomic ratio close to 1 consistently demonstrated the highest RIS performance compared to the others, regardless of the annealing temperature. Reinforcing the previous assumptions, the sensing ability increased at higher annealing temperatures, reaching a notable value of 181 nm/RIU. Compared to other Au/Ag bimetallic nanocomposites, the sensing ability was considerably similar to numerical modeling using a unit approach [352], and higher than thermal embedded Au–Ag bimetallic thin films [353,354]. This specific bimetallic combination facilitated the formation of stable bimetallic NPs in nanocomposite thin films, where the Au NPs contribute to the stability of the Ag. In turn, the Ag seems to confer an enhanced plasmonic effect and, consequently, improves the sensitivity compared to the Au-TiO_2. However, when the Au/Ag atomic ratio further increases (Au/Ag = 2), the sensitivity of the plasmonic film drops again. This decline can be attributed to the lower amount of Au required to maintain the stability of bimetallic NPs in the film, diminishing the film's ability to respond to changes in the RI.

4.4.4. Morphological Analysis of High-Sensitive AuAg-TiO_2 Thin Film

The AuAg-TiO_2 thin film with an Au/Ag atomic ratio of 1, annealed at 700 °C, was specifically chosen for surface morphological analysis (Figures 4.6 and 4.7) based on the earlier optical characterization and its notable sensitivity.

The SEM top-view micrographs of the nanocomposite thin film show a characteristic pattern of roughly spherical NPs, characterized by bright semi-circular spots, surrounded by a darker background that corresponds to the TiO_2 matrix (Figure 4.6a). The NPs size distributions of the AuAg-TiO_2 thin film were analyzed using the SEM top-view micrograph at the highest amplification (at right), plotted in Figure 4.6b. The metallic NPs covered 19.4% of the total surface area, corresponding to a total countable NP number of 1770 and NP density of 241.5 particles.μm^{-2}. The NP size distribution analysis revealed an average NP size (<Feret diameter>) of 31 nm, with a broad distribution of sizes (σ = 14), dispersed with an average distance (<Nearest Neighbor>) of 18 nm (σ = 8). Noteworthy, the NPs with sizes smaller than 10 nm were intentionally disregarded in the analysis owing to their negligible extinction efficiency and plasmonic response, as previously explained in the discussion of Section 4.4.2. The SEM micrographs showed that most of the NPs are close to spherical, while about 30% are irregularly shaped, resulting in an average aspect ratio of 1.5 nm (σ = 0.4). These slightly elongated NPs (with an aspect ratio > 1) result

from the adjacent NPs merging, probably induced by the coalescence phenomena during the annealing treatment [339] and may be associated with enhanced sensitivity exhibited by the plasmonic nanocomposite thin film [212,340].

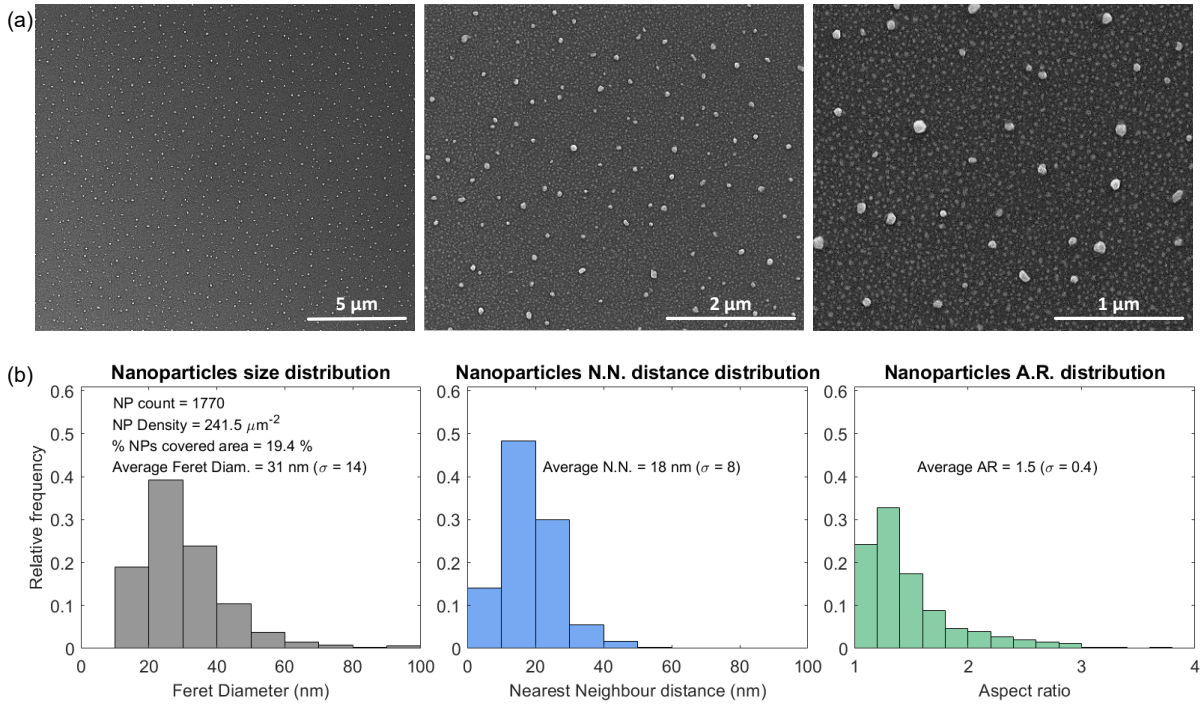


Figure 4.6. SEM micrographs of the AuAg-TiO_2 thin film annealed at 700 °C, at increasing amplifications in (a), and the bimetallic NPs size distributions analysis in (b), considering the Feret diameter, nearest neighbor distance, and aspect ratio parameters.

To complement the morphological analysis, the surface morphology of the AuAg-TiO_2 thin film was studied using two-dimensional (2D) height images scanned 10 × 10 μm^2 and 5 × 5 μm^2 obtained through the AFM analysis, shown in Figure 4.7. The scanning images enabled the estimation of morphological parameters, topographic profile, and height distribution.

The 2D AFM height images depict a heterogeneous morphology of the thin film's surface, characterized by numerous grain-like structures, most likely related to the presence of the NPs near or at the film's surface (Figure 4.7a), as predicted by the LSPR band position trends. Moreover, the topographic profile, identified by the black dashed line in Figure 4.7a, reveals the distinct presence of higher (hills) and lower (valleys) regions. The hills can be attributed to the presence of NPs surrounded by the TiO_2 matrix, or close to the surface, while the valleys correspond to the host matrix that separates the NPs. From the topography scans of the thin film, the surface mean roughness (Sa) and root mean square roughness (Sq) were estimated to be 3.77 ± 0.70 nm and 5.37 ± 1.02 nm, respectively. The height

distribution ranged from 0 to 50 nm; however, the average height was estimated to be 17.87 ± 0.02 nm, as a demarcated orange dotted line in Figure 4.7b and represented in Figure 4.7c. Once again, this analysis suggests that the NPs are partially exposed at the film's surface, highlighting the matrix's ability to confer robustness while preserving their optical activity for sensing purposes. Both characterization analyses offer complementary information about the surface morphology of the AuAg-TiO_2 thin film pertinent to forthcoming sensing applications.

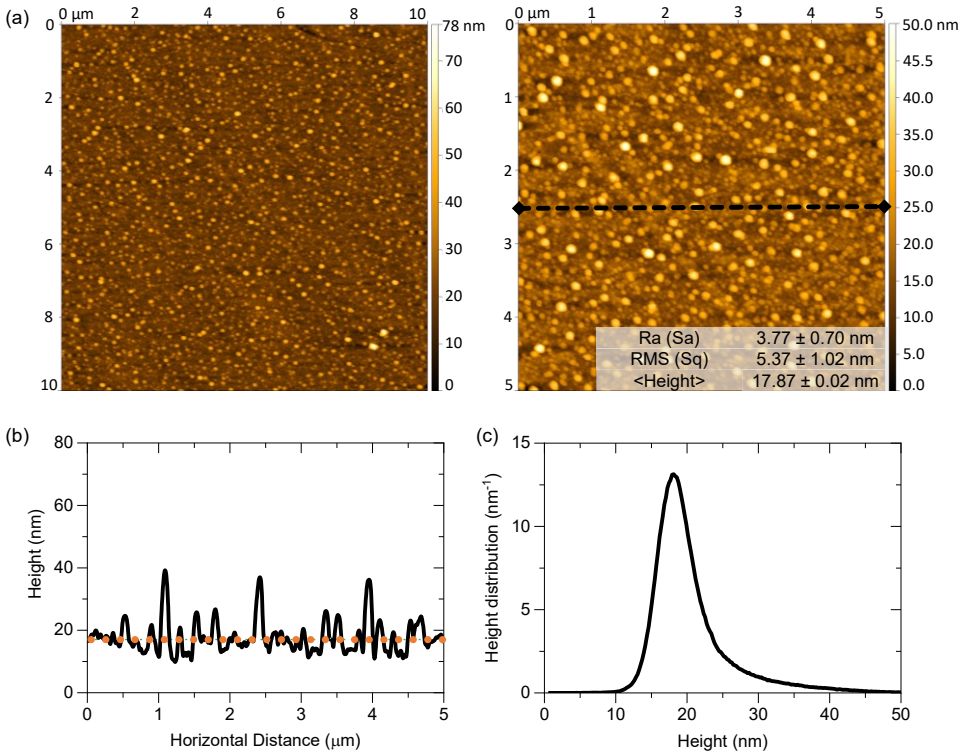


Figure 4.7. Morphological analysis of the AuAg-TiO_2 thin films annealed at 700 °C: (a) two-dimensional (2D) AFM height images of 10 × 10 µm² and 5 × 5 µm², with roughness and height parameters. Considering the 2D AFM height image 5 × 5 µm², the topographic profile (delimited in the black dashed line in (a)), average height estimation (delimited by orange dotted line), and height distribution profile are represented in (b), and (c), respectively.

4.5. Conclusion

This study aimed to investigate the influence of noble metal (Au, Ag) composition on the sensing capabilities of a plasmonic nanocomposite thin film. Monometallic and bimetallic thin films were produced, including the Au-TiO_2, AuAg-TiO_2, and Ag-TiO_2 thin films. The monometallic thin films exhibited a metal concentration of around 18 at.%. In turn, the bimetallic film system with an Au/Ag atomic ratio of 1 was achieved by adjusting the area covered by the Au twice the Ag pellets area on the target. Conversely, when the dimensions of the Au pellets were halved compared to the Ag pellets on the target, the Au/Ag atomic ratio approached 2.

Among these films, the AuAg-TiO_2 film with an Au/Ag atomic ratio of 1 exhibited a distinct optical response characterized by a well-defined LSPR band, specifically at the highest annealing temperature (700 °C). Furthermore, it demonstrated higher sensing capability, displaying a remarkable RIS value, exceeding other plasmonic film systems. The film's surface morphology characterization revealed a relevant metallic surface coverage area very close to 20%. Notably, the surface topography exhibited distinct features, where the NPs and their immediate surrounding matrix were observed as hills, while the TiO_2 matrix itself appeared as valleys. In conclusion, taking theoretical simulations as a starting point, the findings confirm that it is possible to optimize the extinction efficiency and plasmonic sensitivity of bimetallic systems composed of the Au-Ag NPs embedded in a host TiO_2 matrix. Notably, the film with an Au/Ag atomic ratio of 1 was revealed as a highly promising transducer platform for the LSPR-based sensors.

Chapter 5

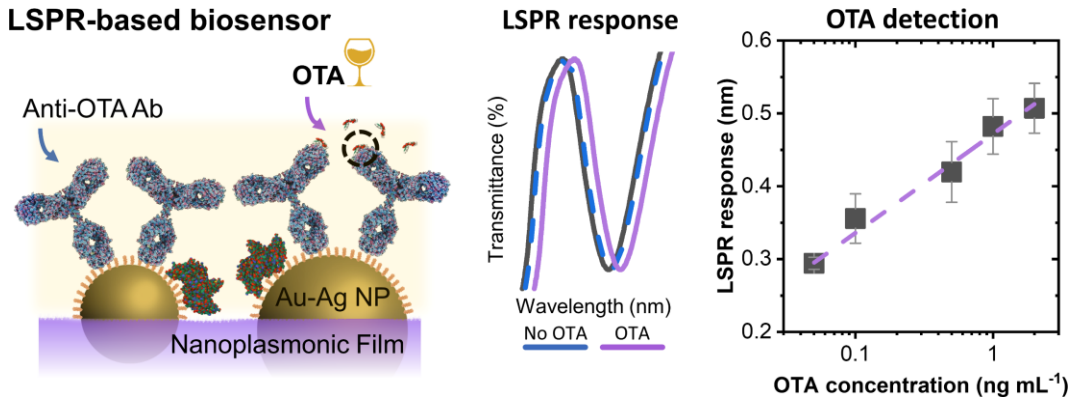
Novel Label-Free Localized Surface Plasmon Resonance (LSPR) Biosensor, based on Au-Ag NPs Embedded in TiO_2 Matrix, for On-site and Sensitive Detection of Ochratoxin-A (OTA) in Wine

D.I. Meira, A.I. Barbosa, J. Borges, R.L. Reis, V.M. Correlo, F. Vaz, Novel Label-Free Localized Surface Plasmon Resonance (LSPR) Biosensor, based on Au-Ag NPs Embedded in TiO_2 Matrix, for On-Site and Sensitive Detection of Ochratoxin-A (OTA) in Wine. *Submitted to Sensors and Actuators B: Chemical* (2024).

5.1. Abstract

Ochratoxin-A (OTA) is a widespread foodstuff contamination with potential carcinogenic effects. Innovative sensing technologies that allow on-site and sensitive food screening can have a significant impact on food safety. In this work, a novel and quantitative label-free LSPR-based biosensor was specifically designed for OTA detection, immobilizing monoclonal anti-OTA antibodies in a sensitive nanoplasmonic thin film. The thin film is deposited by magnetron sputtering, followed by thermal annealing, resulting in bimetallic plasmonic Au-Ag NPs embedded in a TiO_2 matrix. The thin film biosensor is placed into a holder connected to a LED source and a portable spectrophotometer (LSPR spectroscopy sensing system), allowing on-site and cost-effective OTA detection. Under optimized conditions, the LSPR-based biosensor demonstrated a linear dynamic response from 0.05 to 2 ng mL^{-1}, with a limit of detection estimated at 7 pg mL^{-1}, using 55 µL of sample, outperforming commercial ELISA technique in relevant bioanalytical parameters. Sensitivity in OTA detection is crucial because it ensures the accurate identification of low concentrations, which is essential for preventing health risks associated to cumulative ingestion of contaminated food products. The robustness and feasibility of the presented LSPR-based biosensing was tested using real wine samples spiked with OTA, exhibiting a satisfactory recovery of 93% to 113%, confirming its efficacy in complex sample matrices. LSPR-based biosensor strategy stands out with great potential for OTA detection, with robust and sensitive quantitation.

Keywords: Ochratoxin-A; Localized Surface Plasmon Resonance (LSPR); Biosensing; Au-Ag nanoparticles;TiO_2 matrix.



5.2. Introduction

Ochratoxin-A (OTA) contamination is a reported worldwide concern since its prevalence and levels in food can vary due to different environmental conditions, agricultural practices, and storage conditions that favor fungal growth [4,14,355]. Therefore, OTA can be found in different types of food products, such as grains [356], cereal-based products [357], dried fruits [358], wine [359], and certain meats [360]. Furthermore, OTA remains chemically stable during food processing, and typical thermal treatments are insufficient to remove it from contaminated products [19,21,357,361].

OTA has been categorized as a possible human carcinogen (Group 2B) by the International Agency for Research on Cancer (IARC) [6]. Over the past few decades, scientific research uncovered several toxicological effects (i.e., nephrotoxic, hepatotoxic, embryotoxic, teratogenic, neurotoxic, immunotoxic, genotoxic, and carcinogenic) correlating Balkan Endemic Nephropathy (BEN), Chronic Interstitial Nephropathy (CIN) and Alzheimer's diseases [2,76,362,363]. The extended half-life of OTA in the bloodstream – lasting up to 35 days after a single exposure in humans, results from extensive reabsorption along the nephron in kidneys, affinity to plasma proteins, as well the possibility of enterohepatic recirculation that additionally retains OTA in the circulation [74]. Given the slow OTA bio-metabolism, frequent consumption of even slightly contaminated foods can gradually enhance its harmful health impact. Thus, it is essential to develop and implement highly sensitive technologies capable of quantifying extremely low levels of OTA throughout the food production and processing chain to ensure food safety and identify possible mitigation strategies to minimize human exposure.

Several regulatory food safety institutions, including the European Union [17], established maximum levels (MLs) for OTA in potentially contaminated food products. Notably, in the case of wine, a product particularly scrutinized for OTA presence, the established limit is 2 ng mL^{-1} [17], underscoring the stringent measures taken to ensure consumer health and maintain product quality. The European Food Safety Authority (EFSA) considers 4.7 μg kg^{-1} [2] of OTA as the tolerable daily intake (TDI), while the Joint FAO/WHO Expert Committee on Food Additives (JECFA) establishes the value of 16 ng kg^{-1} bw/day [364]. Accordingly, for an individual weighing 60 kg, the maximum TDI would be 282 μg/day per EFSA guidelines, and 960 ng/day following JECFA's standards. These diverse thresholds highlight the critical need for vigilant OTA monitoring, to adhere to these safety limits and protect consumers.

Currently, food samples are sent to laboratories to measure OTA concentration during various stages of the food production to ensure consumer safety. Laboratories use High-Performance Liquid Chromatography with Fluorescence Detection (HPLC-FLD) and competitive Enzyme-Linked Immunosorbent Assay (ELISA), among others [117,365–367]. These techniques are sensitive and

accurate for quantitative analysis; however, they are also time-consuming, demanding expensive laboratory equipment and well-trained technicians. Novel cost-effective analytical techniques that allow quantitation, with small equipment easily installed alongside the food production process and with user-friendly operations, can bring a significant economic and safety advantage to the food industry. Optical biosensors have emerged as a distinct alternative to traditional analytical techniques, providing rapid, sensitive, and selective detection of target analytes by converting biological reactions into discernible optical signals [198,254,368].

Label-free detection methods, such as Localized Surface Plasmon Resonance (LSPR), eliminate the need for secondary labels on target molecules, simplifying the biosensing process and reducing the potential for interference [32]. This biosensing approach has been recognized as effective for the sensitive detection of OTA in extremely low concentrations [254]. The LSPR phenomenon arises when an electromagnetic field interacts with noble metal nanoparticles (NPs) (e.g., gold (Au) or silver (Ag)). During this interaction, the conduction electrons of the NPs resonate with the incident electromagnetic field, resulting in near-field enhancement (e.g., used in surface-enhance spectroscopies [369]) and in pronounced extinction (LSPR) bands due to highly efficient light absorption and scattering [26,306]. The LSPR phenomenon is sensitive to refractive index (RI) changes near the NPs, and this feature has been explored in several biosensing applications [370–374]. As a result, it can be employed to detect specific biomolecular interactions near the NP surface, effectively transducing binding events into an LSPR band shift.

This work presents a novel label-free LSPR-based biosensor suitable for sensitive, on-site OTA detection. A nanoplasmonic thin film composed of bimetallic Au-Ag NPs dispersed in the TiO_2 dielectric matrix serves as the optical-based (LSPR) transducer. To confer specificity to the LSPR-based biosensor, monoclonal anti-OTA antibodies were immobilized, creating a bioreceptor layer on the film's surface. In a detailed sensing principle description, OTA binds specifically to its corresponding immobilized Ab, leading to the formation of immunocomplexes on the surface of AuAg-TiO_2 thin film. This binding event induces a local RI change, and, consequently, an LSPR sensing response (Figure 5.1a, b). In contrast, in the absence of the target mycotoxin, the environmental RI remains unchanged, not generating any LSPR response (Figure 5.1c).

To achieve an enhanced sensing performance, two crucial immunoassay optimization parameters were considered: Ab immobilization design strategies (i.e., physisorption and chemisorption) and Ab concentration, where the sample volume was kept constant at 20 µL. Upon defining the optimal immobilization conditions, the LSPR-based biosensor demonstrated the ability to detect OTA in both

standard (PBS buffer) and spiked wine samples, using a volume of 55 µL. Additionally, when compared to a laboratory standard technique (i.e., ELISA), the LSPR-based biosensor revealed an improved LOD (lower detection limit). The optical design includes a compact and modular optical system that is connected to a computer, featuring portable components (i.e., LED light source, thin film holder, and a spectrophotometer). Hence, the proposed LSPR biosensing approach offers a sensitive and on-site approach for OTA detection.

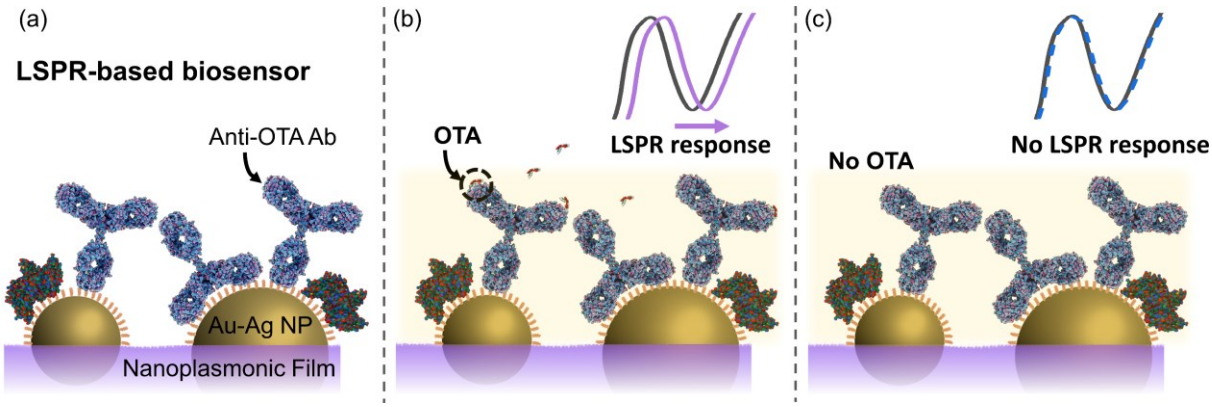


Figure 5.1. Schematic representation of OTA detection using the developed LSPR-based biosensor. (a) Anti-OTA antibody immobilized on the surface of AuAg-TiO_2 thin film; (b) In the presence of OTA, it binds to the immobilized anti-OTA Ab. This binding event alters the local refractive index near the NP surface, leading to a measurable LSPR sensing response, and (c) OTA is absent, the LSPR response remains unchanged.

5.3. Materials and Methods

5.3.1. Preparation and Characterization of Nanoplasmonic AuAg-TiO_2 Thin Film

5.3.1.1. AuAg-TiO_2 Thin Films Deposition and Annealing

The optical-based LSPR transducer consists of a thin film containing bimetallic Au-Ag NPs embedded in a TiO_2 matrix, deposited by one-step reactive DC magnetron sputtering and submitted to thermal treatment. Prior to sputter deposition, the substrates (several pieces of quartz and a TEM grid) were cleaned and activated via an in-situ plasma treatment with argon, generated by a pulsed DC power supply connected to the substrate holder. The sputtering target consisted of three-quarters of a noble metal disk (6 and 3 mm^2 of Au and Ag, respectively) symmetrically aligned in the preferential erosion zone of the Ti target (99.99% purity). Such arrangement leads to an almost equal amount of Au and Ag atomic concentrations (atomic ratio, Au/Ag= 1) in the thin film, as demonstrated in a previous study [375]. The deposition was carried out for 8 min in a plasma composed of argon (working gas, 3.8×10^{-1}

Pa) and O_2 (reactive gas, 3.6×10^{-2} Pa), to produce a 50 nm thin film. A direct current density of 75 A m^{-2} was applied, setting the target potential at a (negative) voltage of 370 V.

After the sputtering deposition, the nanocomposite thin films were thermal annealed at 700 °C (atmospheric pressure), to induce the formation of the Au-Ag NPs within the TiO_2 matrix.

5.3.1.2. Nanoparticles Distribution Analysis by STEM

Scanning Transmission Electron Microscopy (STEM) was used to evaluate the nano-morphology of the thin film, using an ultra-high resolution Field Emission Gun Scanning Electron Microscope. STEM micrographs were obtained at an acceleration voltage of 15 kV. The NPs distributions were determined using a MATLAB algorithm.

5.3.2. Preparation of LSPR-based Biosensor for OTA Detection

5.3.2.1. Plasma Activation and DSP Functionalization

The AuAg-TiO_2 nanoplasmonic thin films were subjected to O_2 activation plasma (15 W, 5 min, 80 Pa), which favors the functionalization of DSP (dithiobis(succinimidyl propionate)), as it increases the hydrophilicity of the surface by promoting the formation of hydroxyl groups. The crosslinker solution was dissolved in DMSO (dimethylsulfoxide, ≥ 99.9%) at a concentration of 4 mg mL^{-1}. After 30 min of static immersion, the films were double-cleaned with DMSO solvent and PBS (phosphate-buffered saline, pH 7.4, 10 mM) to remove residual unbound cross-linker molecules.

5.3.2.2. LSPR-based Biosensor Optimization

For the antibody immobilization process, 20 µL of anti-OTA Ab solution (from Petromyces albertensis, ≥ 98%) was loaded onto the nanoplasmonic film's surface. During the overnight incubation at a steady 4 ˚C, the films remained covered with a humidified paper tissue and hermetically sealed with aluminum foil in a well-plate. A solution of 5% (*w/v*) protease-free BSA (Bovine Serum Albumin) replaced the anti-OTA Ab solution, and it was incubated for 2 hours at room temperature, followed by a rigorous washing step including 0.05% (*v/v*) of Tween-20 diluted in PBS and just PBS. OTA solution (55 µL) was incubated on the nanoplasmonic films' surface for 30 min, also, followed by the cleaning rinse.

To optimize the LSPR-based biosensor performance, different Ab immobilization strategies and concentrations were considered. Both physisorption (i.e., direct adsorption) and chemisorption (i.e., DSP functionalization) strategies were studied. Furthermore, the concentrations of anti-OTA Ab solution were adjusted from 0 to 75 µg mL^{-1}, in increments of 25 µg mL^{-1}. For this optimization, the OTA solution was

maintained at 2 ng mL^{-1}, in accordance with the established threshold for foodstuffs set by regulatory authorities [17]. The control experiment was considered the blocked nanoplasmonic thin films with BSA.

5.3.3. OTA Detection: T-LSPR Spectroscopy *vs.* Microplate Standard ELISA

5.3.3.1. LSPR Testing with Increasing OTA Concentrations

Once the optimal conditions were identified, the aforementioned experimental procedure was repeated to evaluate biosensor analytical performance. The concentrations of the OTA solution were modified to include 0.05, 0.1, 0.5, 1, 4, 5, and 8 ng mL^{-1}. In this case, the blank was established as an OTA concentration of 0 ng mL^{-1}.

5.3.3.2. Standard Competitive ELISA

For validation purposes, a commercially available competitive ELISA kit was used following the manufacturer's guidelines. OTA calibrators of 0.5, 2, and 8 ng mL^{-1} were employed, and the absorbance was measured at 450 nm utilizing an ELISA reader. Absorbance values were expressed in cm^{-1} based on a light path length of 0.30 cm for a 96-well microtiter plate.

5.3.3.3. OTA Detection: Spiked White Wine

White wine was purchased from a local supermarket. The wine sample was centrifuged at 10,000 rpm for 10 min, to reduce the matrix influence. Followed by the pH adjustment of the resulting supernatant to 7.4 with NaOH (sodium hydroxide) 1M, and it was diluted 20 times with PBS buffer. OTA was added to these pre-treated samples at known concentrations of 0.5, 2, and 8 ng mL^{-1} [131]. Following the methodology outlined, the wine samples were then subjected to quantitative analysis using LSPR-based biosensing.

5.3.4. Experimental Setup and Data Analysis

5.3.4.1. Experimental Setup for T-LSPR Sensing

During the OTA detection experiment (Figure S5.1), the LSPR-based biosensors were optical monitored both before and after OTA incubation. The optical response (T-LSPR band) was monitored for 4 min, acquiring a total number of 48 transmittance spectra at 5-second intervals. Throughout this period, the samples remained submerged in a PBS buffer. The optical response was acquired using a modular and miniaturized optical system featuring a LED light source, a sealed LSPR thin film holder, with a high-resolution spectrometer (Sarspec, Lda) ranging from 420 to 720 nm wavelength, all connected by optical

fibers. Lightscan software allows the visualization of the spectra in real-time, while NANOPTICS software, [238], was used to process the data.

5.3.4.2. Data Analysis

NANOPTICS software [238] processes the optical response of the nanoplasmonic thin films and analyzes the T-LSPR bands minimum (wavelength of transmittance minimum) over time, facilitating its average estimation. LSPR sensing response is determined by the average shift of the T-LSPR band minimum between the pre- and post-OTA incubation periods. The experimental data, represented as LSPR sensing response, were corrected by subtracting the average of the T-LSPR band minimum of each OTA concentration from the established blank. The limit of detection (LOD) of the optical system was calculated by $LOD = Y_0 + 3\sigma_0$, where the Y_0 is the LSPR response of the blank and $3\sigma_0$ is three times the standard deviation. The average LSPR response of three replicates was plotted against their corresponding OTA concentration. The experimental data were fitted to a 4-parameter logistic (4PL) mathematical model [376], using the minimum square difference for each response curve, establishing the preliminary calibration curve:

$$Y = A2 + \frac{(A1 - A2)}{1 + \left(\frac{x}{x_0}\right)^p} \quad (1)$$

where *A1* is the LSPR response of the blank, *A2* the LSPR response for "infinite" OTA concentration, *x* is OTA concentration, x_0 is inflection point, *p* is sigmoidal curve slope (steepness of the curve), and *Y* is LSPR response.

Beyond, the precision (i.e., coefficient of variation (CV)) and the accuracy (i.e., recovery (R)) [141] were considered and calculated as:

$$CV\ (\%) = \left(\frac{\sigma}{\bar{x}}\right) \times 100 \quad (2),$$

and

$$R(\%) = \left(\frac{p_a}{p_c}\right) \times 100 \quad (3),$$

where σ is the standard deviation, and $\bar{x}$ is the LSPR response. In turn, p_a is the LSPR response of actual detected OTA concentration in real sample, and p_c is the LSPR response of predicted OTA concentration under buffer conditions.

In the conventional ELISA detection analysis, the percentage of inhibition was calculated using the following equation:

$$Inhibition\ (\%) = 100 - \left(\frac{OD}{OD_0}\right) \times 100 \quad (4)$$

where OD is the optical density (average absorbance) of each standard OTA concentration, and OD_0 is the optical density of the blank. Following this, inhibition (%) is plotted against their corresponding OTA concentration. The experimental data was also fitted to 4PL mathematical model (Eq. 1), and the CV was calculated.

5.4. Results and Discussion

5.4.1. Nanoplasmonic AuAg-TiO_2 Thin Films as LSPR-based Transducers

Nanocomposite thin films, composed by bimetallic Au-Ag NPs embedded in a TiO_2 thin film matrix, were prepared to be used as suitable optical transducers for (bio)sensing applications. The nanostructural analysis of the AuAg-TiO_2 thin film reveals a distinct pattern of metallic NPs, discernible as darker semi-circular spots against a bright background consistent with the TiO_2 matrix, as shown in the STEM top-view micrographs (Figure 5.2a). A detailed NPs distribution analysis, in Figure 5.2b, revealed that 20.4 % of the total surface area is occupied by metallic NPs, amounting to 1024 NPs and a particle density of 558.8 μm^{-2}. These NPs exhibit an average size of 19 nm (σ = 10), separated by an average distance of 13 nm (σ = 5). Moreover, the aspect ratio of the shaped nature of NPs was estimated in 1.4 nm (σ = 0.5).

Building on the nanostructural findings, the embedded bimetallic NPs within the TiO_2 matrix present notable optical properties, namely an enhanced plasmonic (LSPR) behavior. A sharply defined T-LSPR band is emphasized in Figure 5.2c, where its minimum is centered at the wavelength and transmittance coordinates of 575 nm and 43 %, respectively. The T-LSPR band exhibited a high transmittance amplitude of about 22 percentage points and a relatively narrow full width at half maximum (FWHM) of 125 nm. This nanoplasmonic thin film revealed also an outstanding sensitivity (bulk refractive index sensitivity of 181 ± 3 nm/RIU [375]), before functionalization, suggesting acute responsiveness to RI variations within the NPs surrounding and, hence, making it highly suitable for responsive and precise biosensing applications.

Moreover, these nanoplasmonic AuAg-TiO_2 thin films are prepared using a robust, cost-effective, and up-scalable reactive DC magnetron sputtering deposition method, which is capable of producing more than 200 samples in a single deposition run. The combination of enhanced sensitivity, along with

the scalable and reproducible production positions this method as a highly advantageous approach in the field of optical transducers.

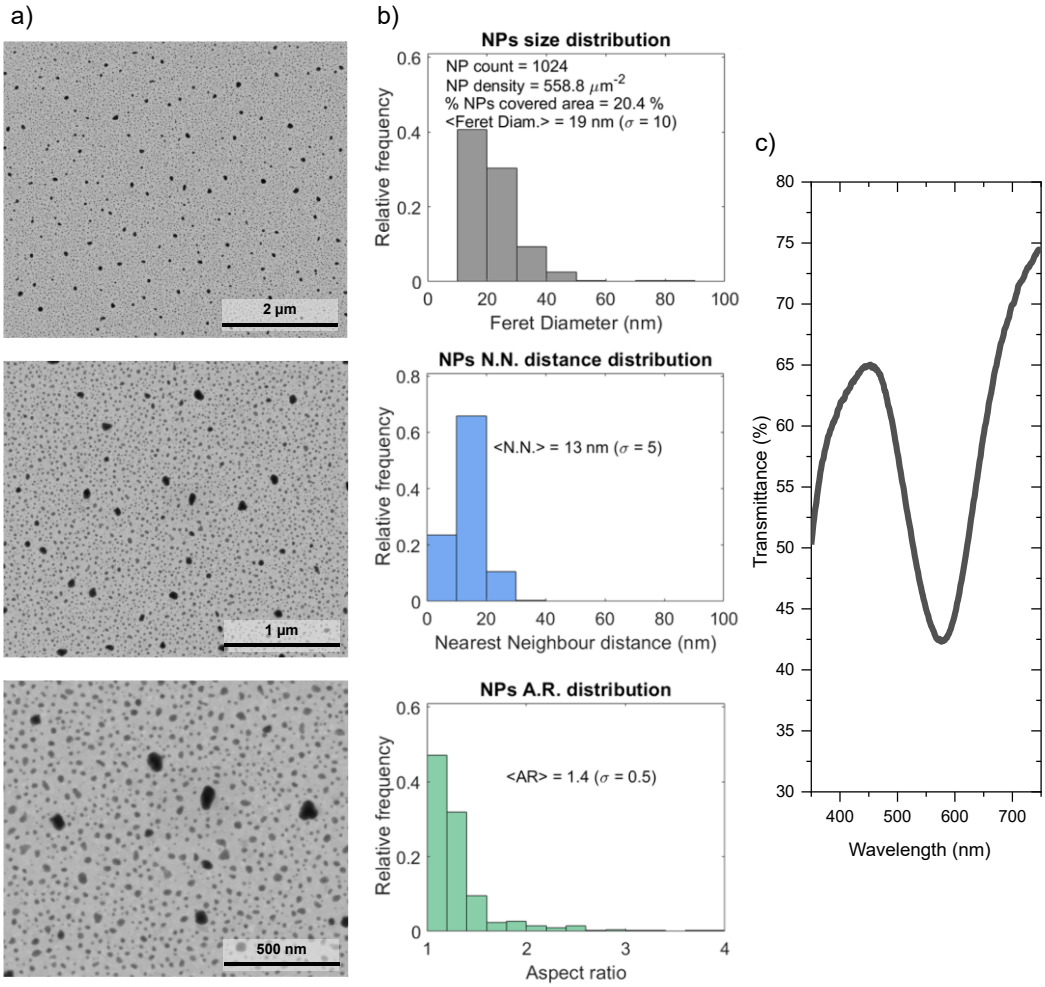


Figure 5.2. Nanostructural and optical characteristics of the AuAg-TiO_2 thin film: (a) STEM micrographs, (b) analysis of bimetallic NPs size distributions, and (c) T-LSPR band.

5.4.2. LSPR-based Biosensor Optimization

Immunoassays are the golden standard analytical tools for precisely quantifying specific analytes, relying on the natural stable bond between an antibody and an antigen. Biosensors that use immunoassays for analyte detection have their performance intrinsically related to the effectiveness of the bioreceptor layer, particularly its coverage, orientation, and functionality, since all these parameters will affect antibody-antigen binding and equilibrium [255,256,377]. Since LSPR detection using AuAg-TiO_2 thin films is label-free, without signal amplification method, the overall performance of the biosensor is even more dependent on the immunoassay optimized conditions and antibody types. Hence, two primary aspects were investigated: (i) the immobilization design strategy of the monoclonal anti-OTA Ab and (ii) antibody concentration (Figure 5.3). Note that monoclonal antibodies are capable of binding a

single epitope of the analyte, therefore they are more likely to become non-functional upon immobilization, compared to polyclonal antibodies [378].

Two distinct immobilization strategies were compared: direct adsorption (physisorption) and cross-linker functionalization (chemisorption), as illustrated in Figure 5.3a. Although direct adsorption is the most common and simplest biofunctionalization strategy compared to covalent immobilization, the orientation and stability of the immobilized Ab, along with bioreceptor layer reproducibility, are common challenges [255,259,379]. In contrast, chemisorption offers pertinent advantages, since it confers irreversible binding to the thin film's surface, ensuring the long-term stability of linked Ab and, moreover, promoting uniform surface orientation and coverage [256,259,266]. Still, functionalization of an adhesion layer using DSP cross-linker, will increase the distance between the AuAg-TiO_2 thin film's surface and the OTA binding site in the capture Ab. Given that the efficacy of plasmonic (LSPR) bio-detection depends on chemical interactions within the plasmon decay length, which is typically limited to 30 nm [30,31], adding an intermediate layer could lead to a discernible decline in the LSPR sensing response. Alongside, to ensure the maximum Ab surface capacity, increasing concentrations (0, 7.5, 25, 50, and 75 μg mL^{-1}) were immobilized on the nanoplasmonic film's surface for optimization purposes. The optimal Ab concentration influences the bioreceptor coverage across the thin film's surface and, consequently, the biosensor's sensitivity. This optimized bioreceptor coverage ensures a greater area for effective OTA binding, leading to a stronger LSPR response and improved bioanalytical performance, characterized by a lower detection limit and an expanded linear dynamic range.

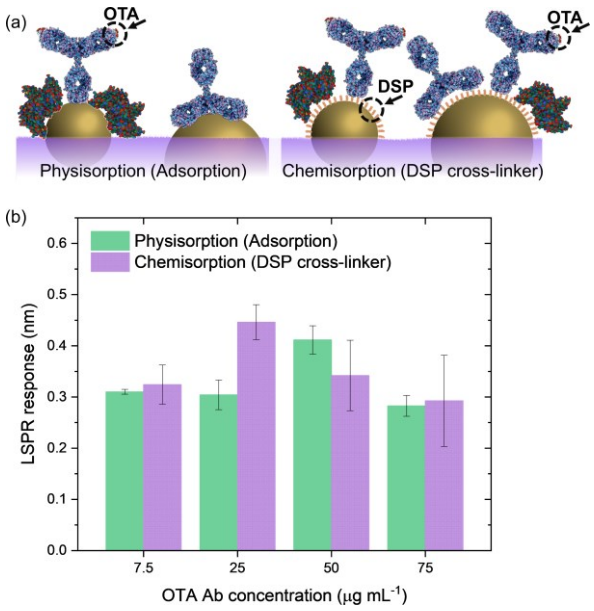


Figure 5.3. Immobilization strategies on AuAg-TiO_2 thin films for OTA detection (a) Illustration of immobilization strategies: physisorption and chemisorption. (b) LSPR response (nm) as a function of immobilization strategy and anti-OTA Ab concentration.

In this particular experiment, the OTA concentration (55 µL) is held constant at 2 ng mL^{-1}, allowing the optimal combination of immobilization parameters to be identified. As shown in Figure 5.3b, a consistent trend is observed: as the anti-OTA Ab concentration rises, both immobilization strategies displayed detectable changes in the LSPR sensing response, identified by a T-LSPR band shift.

Concerning the immobilization strategy, the chemisorption exceeded physisorption until the anti-OTA Ab concentrations increased up to 25 µg mL^{-1}, reaching a maximum LSPR response of 0.45 ± 0.03 nm. At Ab concentration of 50 µg mL^{-1}, the physisorption strategy exhibited a higher LSPR response, achieving a wavelength shift of $\Delta\lambda$ = 0.41 ± 0.03 nm. Nevertheless, upon reaching a maximum LSPR response in both immobilization approaches, the LSPR signal decreases at higher anti-OTA Ab concentrations.

At this stage, and based on the results displayed in Figure 5.3b, it is possible to ascertain that the chemisorption approach produces an overall higher LSPR response for lower Ab concentrations. This enhanced LSPR response can be attributed to the presence of the DSP cross-linker layer. The presence of such adhesion layer suggests that it not only strengthens the Ab attachment, but also favors their proper orientation, enhancing its recognition stability and efficiency. Additionally, the DSP layer may promote a higher bioreceptor coverage with lower concentrations, contributing to the cost-effectiveness of the overall biosensing technology.

For both immobilization methods, the LSPR response decreased after reaching a certain concentration of anti-OTA Ab, possibly due to steric hindrance in Fab region of capture Ab, hindering OTA binding. This suggests that a higher Ab density does not necessarily equate to a more functional and higher affinity bioreceptor layer [34]. This phenomenon is more evident when monoclonal antibodies are used to form the bioreceptors layer [378].

Moreover, in the absence of the capture Ab (commonly named noise, or background), no discernible LSPR response was detected, suggesting that the LSPR response was specific to the formation of anti-OTA-OTA immunocomplex.

To summarize, the optimal performance of the LSPR-based biosensor was accomplished by combining the chemisorption strategy with an Ab bulk concentration of 25 µg mL^{-1}.

5.4.3. OTA Detection: T-LSPR Spectroscopy *vs.* Microplate Standard ELISA

Under optimized immunoassay conditions, the bioanalytical performance of the LSPR-based biosensing approach was assessed using increasing OTA concentrations ranging from 0.05 to 8 ng mL^{-1} (Figure 5.4a). The LSPR response (T-LSPR band shift) increases until 2 ng mL^{-1} ($\Delta\lambda$ = 0.51 ± 0.03 nm),

where it reaches the saturation limit. At this stage, there is an equilibrium between unbound and bound OTA, as all available binding sites are occupied, reaching the maximum amount of immunocomplexes. A linear correlation between the LSPR response and OTA concentration covered was obtained between the range of 0.05 to 2 ng mL^{-1} (R^2=0.9919), with a coefficient variation up to 24.3%. Considering all OTA concentrations, the cross-correlation coefficient R^2 between the 4PL model (Eq. 1) and the experimental data was 0.9970, establishing the LOD value at 7 pg mL^{-1}.

OTA is routinely detected in laboratories for food safety reasons using competitive ELISA. In order to compare the performance of the LSPR-based biosensor, a commercially available kit was used (Figure 5.4b). This kit operates within a range from 0.5 to 8 ng mL^{-1} utilizing 25 µL volume samples, 45 minutes total assay time, and a standard laboratory microplate reader. This enzyme amplification-based assay indirectly measures target OTA by facilitating direct competition between the target analyte actually available in the sample and an OTA-HRP conjugate (from the kit), both competing to bind with the anti-OTA Ab immobilized on the plate surface. On the contrary, the label-free LSPR-based biosensor directly detects the binding of OTA to the monoclonal anti-OTA Ab immobilized on the film. The competitive inhibition curve was fitted in a 4PL model (Eq. 1) within this range, with an ideal regression coefficient (R^2=1), and established LOD value at 110 pg mL^{-1} with a variation below 16%.

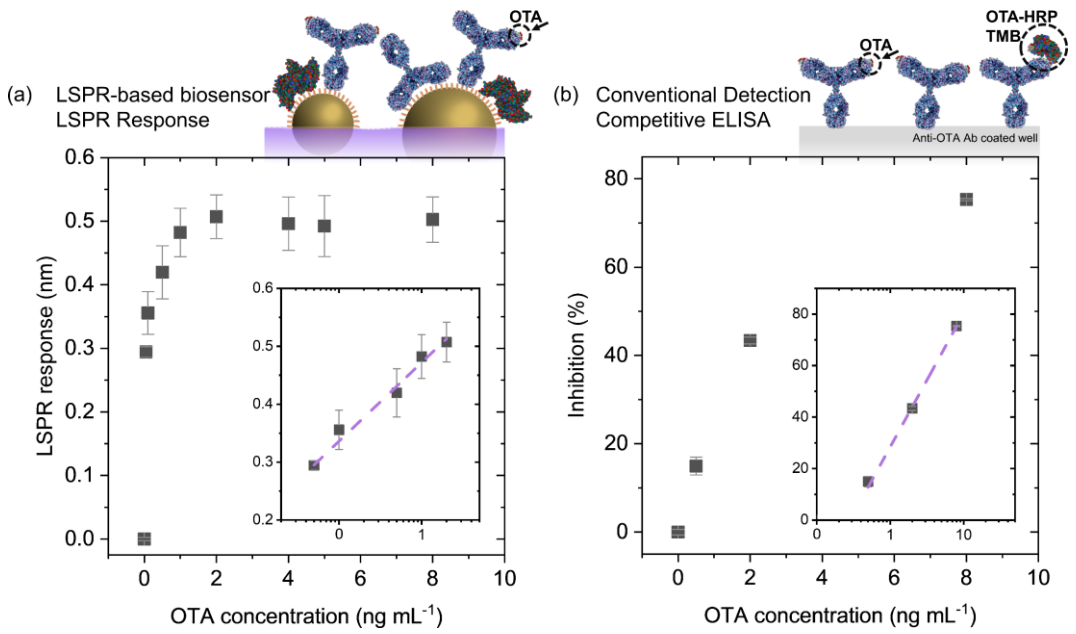


Figure 5.4. Comparison between LSPR-based biosensor and competitive ELISA for OTA detection. (a) LSPR response in wavelength shift (nm) caused by different OTA concentrations (insert shows the linear relationship between the LSPR response and OTA concentration (in log scale), resulting in a dynamic range from 0.05 to 2 ng mL^{-1}). (b) Inhibition (%) caused by different OTA concentrations (insert presented in log scale).

Comparing the performance of the two presented analytical methods (Table S5.1), the LSPR-based method (0.05 to 2 ng mL^{-1}) offered an OTA broader dynamic range, as opposed to the standard commercial technique (from 0.5 to 8 ng mL^{-1}). Furthermore, the LSPR biosensing method revealed a lower LOD value (7 pg mL^{-1} compared to 110 pg mL^{-1} from the standard technique), thus positioning itself as a more sensitive OTA detection approach. Regarding this comparison, it is important to mention that the dynamic range of the developed LSPR-based biosensor can be widened by proceeding with AuAg-TiO_2 thin films assay development adjusting the functionalization conditions, optimizing sample volume and assay time to meet the required needs. Since higher sensitivity was the aimed performance parameter to show assay feasibility, there was no limit on sample volume (55 µL) and total antibody-target interaction time (30 min), neither were these parameters optimized. LSPR-based biosensor effectively quantifies OTA concentrations at regulatory food safety thresholds. With a linear dynamic range extending up to 2 ng mL^{-1}, under these specific conditions, the bioanalytical performance of the proposed LSPR-based biosensor is well-suited for monitoring OTA in various food matrices (i.e., beverage (fruit juice, wine) and cereal-based products for infant feeding, where the established threshold is 2 and 0.5 ng mL^{-1} , respectively [17,75,380]).

Two main approaches are reported in the literature for LSPR transducers for OTA detection (Table 5.1): metallic nanostructures suspended in solution (colloidal approach) and surface immobilized nanostructures. Fully colloidal approaches, using Au NPs in solution, have been reported for OTA detection, focusing on changes in absorbance intensity [137,381]. These approaches achieved LOD of 32 pg mL^{-1} in 15 min and 0.001 pg mL^{-1} in 5 min, using sample volumes of 50 µL and 110 µL, respectively [137,381]. In turn, Park et al. [382] and Lee et al. [175] explored OTA detection through LSPR wavelength shifts in surface immobilized nanostructures. The first study [382] reported OTA detection through aptamers functionalized Au NRs immobilized onto a glass slide, achieving a LOD of 404 ng mL^{-1}. This result was obtained with a 20 min OTA incubation period and a 200 µL sample volume. The second mentioned study [175] developed an LSPR aptasensor composed of Au NRs immobilized onto a glass fiber requiring 30 min to achieve the LOD of 5 pg mL^{-1}, with a simple dip of the glass fiber into the OTA solution. However, a common challenge in these methods is metallic nanostructures aggregation, even if they are subsequently immobilized on a substrate, which can significantly affect the detection capability and overall feasibility of the biosensor [383–385]. In contrast, the novel detection approach presented in this work is based on a highly stable optical transducer consisting of Au-Ag NPs embedded within a solid TiO_2 matrix, avoiding NPs aggregation related issues. Also, the ability to control the parameters and produce more than 200 samples in one deposition step shows the potential for

reproducibility of the sputtering technique. Hence, this biosensing transducer design can be easily up scaled, with consistent reproducibility and potential for miniaturization within microfluidic systems. In terms of performance, the proposed LSPR-based biosensor exhibits an LOD in a similar range as the reported substrate immobilized nanostructures LSPR sensors. Despite these advantages, there is still scope for improvements to enhance the biosensor's performance further.

Table 5.1. Overview of LSPR strategies for OTA detection, highlighting their biosensing strategy (i.e., biorecognition element, transducer) and bioanalytical performance.

Biorecognition element	Transducer	LOD	Linear Dynamic Range	Ref., year
Aptamer	Au NPs - colloidal	$10^{-10.5}$ g mL^{-1} (32 pg mL^{-1})	0.0316 to 316 ng mL^{-1}	[381], 2018
Anti-OTA Ab	Au NPs – colloidal	0.001 pg mL^{-1}	10^{-9} µg mL^{-1} to 10^{-1} µg mL^{-1} (0.000001 to 100 ng mL^{-1})	[137], 2021
Aptamer	Au NRs immobilized onto glass slide	1 nM (404 ng mL^{-1})	0.1 nM to 10 µM (0.04 to 4038 ng mL^{-1})	[382], 2014
Aptamer	Au NRs immobilized onto glass fiber	12 pM (5 pg mL^{-1})	10 pM to 100 nM (0.004 to 40 ng mL^{-1})	[175], 2018
Anti-OTA Ab	**Au-Ag NPs embedded in TiO_2**	**7 pg mL^{-1}**	**0.05 to 2 ng mL^{-1}**	**This work**

5.4.4. OTA Detection: Spiked White Wine

The bioanalytical performance of a biosensor can be affected by the sample complex matrix (i.e., alcohol, phenolic compounds, sugars, proteins, volatile elements, and minerals). These matrix elements can induce non-specific binding (competition or blocking the active sites of Ab), denaturation, or conformational alterations, resulting in steric hindrance and compromising the OTA-Ab binding affinity. Therefore, the feasibility of a biosensor is highly dependent on the nature of the sample matrix used, or on the sample pre-treatment performed.

In this work, white wine was chosen as a real food sample for testing, due to the prevalent presence of OTA in this type of beverage. The European Union has set a regulatory limit of 2 ng mL^{-1} [17,75,380] for this mycotoxin. Hence, white wine samples were pre-treated by centrifugation, and their pH were adjusted to 7.4 to mitigate the matrix interference and maintain the physiological environment. Subsequently, the wine was diluted 20-fold in PBS and spiked with OTA [131] to achieve specific concentrations of 0.5, 2, and 8 ng mL^{-1}. Compared to the standard buffer concentrations, similar LSPR responses were obtained, as shown in Figure 5.5a. According to Table S5.2, the LSPR-based biosensing

reproduced OTA concentration values near the corresponding spiked concentrations with an average recovery of 93% to 113%, with a variance within 23% (Figure 5.5b). These findings confirmed that this nanoplasmonic biosensing approach was able to effectively detect OTA in real foodstuff samples, under a complex sample matrix environment. Moreover, the proposed LSPR-based biosensor designed for OTA detection closely aligns with the performance standards set by the European Commission regulations [16], which specify that average recoveries should range between 70% and 110%.

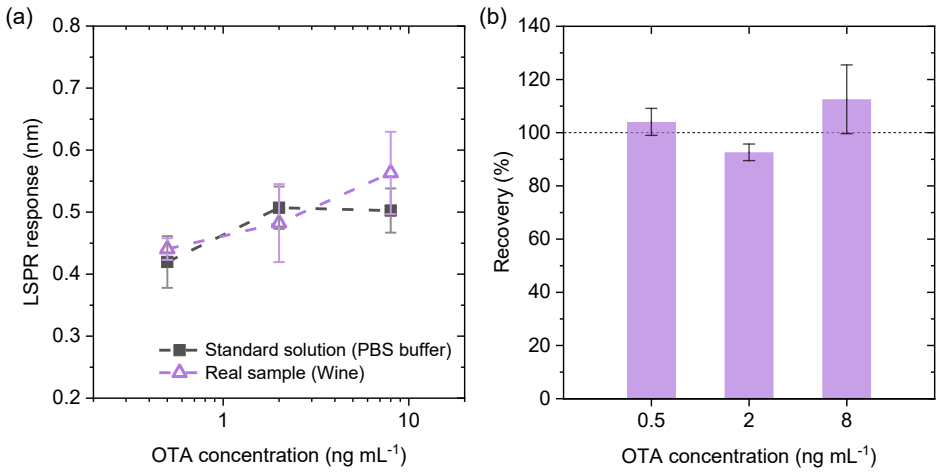


Figure 5.5. (a) LSPR response (nm) caused by different OTA concentrations, using standard solutions (PBS buffer) and real sample solution (wine). (b) Recovery (%) of spiked wine samples with 3 different OTA concentrations, 0.5, 2 and 8 ng mL^{-1}.

5.5. Conclusion

A novel label-free LSPR-based biosensing strategy has been developed for sensitive OTA detection. The LSPR-based biosensing principle relies on the enhanced plasmonic behavior manifested by bimetallic Au-Ag NPs embedded in a TiO_2 thin film matrix. The AuAg-TiO_2 thin films were prepared by cost-effective reactive DC magnetron sputtering, followed by a thermal annealing procedure. The ability to control the process parameters and produce more than 200 samples in one deposition shows the potential for reproducibility and scale-up of this LSPR sensor. Furthermore, the embedded nature of NPs ensures the absence of aggregation during OTA detection.

The LSPR-based biosensor achieves its high specificity through the strategic immobilization of tailored 20 µL anti-OTA Ab on the surface of the nanoplasmonic thin film. Upon binding to OTA, using sample volumes of 55 µL, these chemical interactions are transduced into a quantifiable optical response (i.e., T-LSPR band shift), measured on a compact and modular LSPR spectroscopy sensing system allowing on-site monitoring.

Under optimized bioanalytical conditions, the LSPR-based biosensor exhibited a dynamic range from 0.05 to 2 ng mL^{-1}, demonstrating its ability to detect OTA over a broad concentration range with a significantly low LOD, estimated to be 7 pg mL^{-1}. The biosensor's performance was further validated using spiked wine samples, achieving good OTA recovery values ranging from 93% to 113%. These findings confirm the accuracy of the biosensor's efficacy in detecting OTA in complex sample matrices.

Future work will focus on a comprehensive bioanalytical evaluation, assessing aspects such as volume sample and response time. Moreover, integrating this LSPR-based biosensor into microfluidic systems will allow the handling of even smaller volumes and the automation of the analytical process for a user-friendly, portable, and suitable real-world application.

5.6. Supporting Information

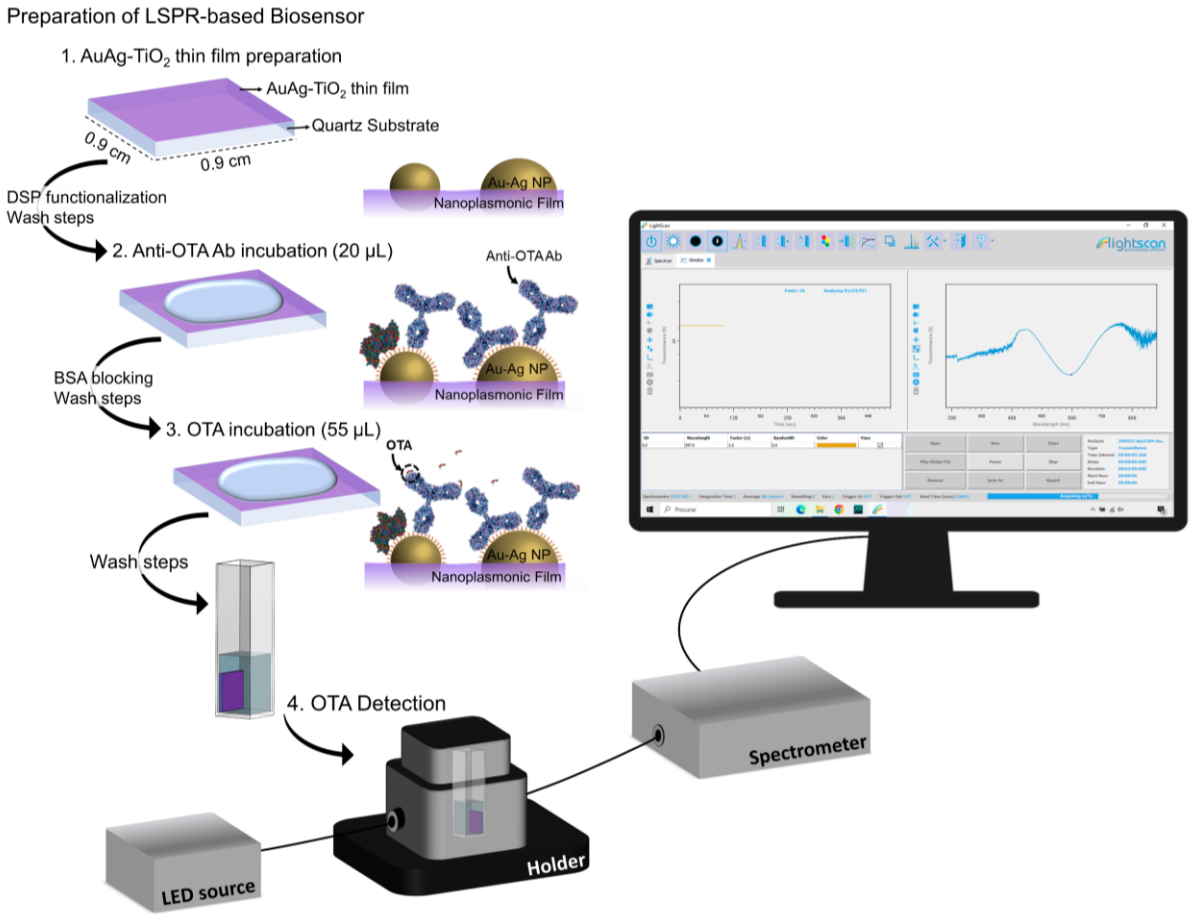


Figure S5.1. Schematic representation of experimental protocol and setup for T-LSPR spectroscopy.

Table S5.1. Comparative analysis of LSPR-based biosensor versus commercially ELISA for OTA detection.

	Proposed biosensing approach (AuAg-TiO_2 thin film)	**Commercially available microwell**
Assay type	Direct	Indirect Competitive
Detection Method	LSPR	Colorimetric (ELISA)
Amplification	Absence (label-free)	Enzymatic
Dynamic range	0.05 to 2 ng mL^{-1}	0.5 to 8 ng mL^{-1}
Precision	24%	16%
LOD	7 pg mL^{-1}	110 pg mL^{-1}
Coefficient of correlation (R^2)	0.997	1

Table S5.2. OTA detection in wine samples using LSPR-based biosensor.

Known OTA concentration (ng mL^{-1})	**LSPR sensing**		
	Found (ng mL^{-1})	**CV (%)**	**Recovery (%)**
0.5	0.52±0.03	9.76	104.1
2	1.9±0.06	6.70	92.6
8	9±1	22.96	112.6

Chapter 6

Final Remarks, Conclusions and Future Perspectives

.

6.1. Final Remarks and Conclusions

The rapid global population growth intensifies food safety challenges, particularly concerning mycotoxin contamination. Ochratoxin-A (OTA) brings serious health risks, including carcinogenic and neurological effects [6–12]. Addressing this, international regulations have set stringent OTA limits in food products [2,17]. Innovative methods for detection are currently in development, designed to overcome the limitations of traditional techniques. These advanced approaches aim to effectively monitor OTA contamination, thereby ensuring food safety and mitigating economic impacts.

This PhD project aimed to develop and tailor nano-designed Localized Surface Plasmon Resonance (LSPR) thin films with an enhanced sensitivity for OTA detection, using a combination of optical properties of plasmonic materials. Nanoplasmonic thin films were employed as LSPR-based transducers, where their sensing principle relied on an enhanced optical (plasmonic) response in transmittance (T-LSPR). Thin films composed of noble metallic nanoparticles (Au and/or Ag NPs) embedded in a host titanium dioxide (TiO_2) matrix were prepared by reactive magnetron sputtering, an environmentally friendly physical vapor deposition technique, and subjected to post-deposition (thermal and plasma, e.g.) treatments.

As a starting point, nanoplasmonic Au-TiO_2 thin films were selected to ascertain their suitability as LSPR transducers. In this initial biosensing assessment, a widely recognized bioreceptor-analyte model system, namely streptavidin-biotin pair, was employed. The bioreceptor layer, streptavidin, was effectively immobilized (by adsorption) on the surface of nanoplasmonic thin films, previously activated by an O_2 plasma treatment. This LSPR-based biosensing approach is based on measurable LSPR responses, notably observed as a T-LSPR band shift induced by refractive index (RI) variations within the LSP decay length of the Au NPs. In fact, the biochemical interaction between biotin and the streptavidin-immobilized films resulted in an expected distinctive optical change, evident through a T-LSPR band shift (0.8 ± 0.1 nm). This interaction was further corroborated through a secondary labeled sensing method, namely Enzyme-Linked Immunosorbent Assay (ELISA), confirming the anticipated results. This outcome underscored the significant potential of nanoplasmonic thin films as effective LSPR-based transducers. However, the sensing ability of Au-TiO_2 thin film was considered significantly low (refractive index sensitivity in the order of 33 ± 5 nm/RIU), negatively affecting its biosensing performance. These findings prompted further optimization efforts, focusing on both the biorecognition interface's effectiveness and improving the plasmonic sensing ability. Effectively, the size of the biomolecules (bioreceptors immobilized and target analyte) and the sensing ability of the nanoplasmonic thin film are crucial factors to tune the final LSPR-based biosensor's sensitivity.

In pursuit of maximizing the LSPR-based sensor's capabilities and achieving maximum biosensing performance, the biorecognition layer stands out as a pivotal component. This biorecognition layer's efficacy directly influences the biosensor's sensitivity, specificity, and overall reliability. Firstly, the determination of the most appropriate biorecognition element for the OTA detection was evaluated, considering the LSPR sensing context. The bioreceptor layer was composed of antibodies (Ab), due to their high specificity, strong affinity for target molecules, and robustness against environmental variations, which are key advantages over other biorecognition elements. Beyond the choice of an appropriate biorecognition element for OTA detection, the immobilization strategy is a fundamental parameter in the development of a biosensor. In fact, each immobilization method has its advantages, but the primary goal was to develop an exceptionally sensitive LSPR-based biosensor. For that, it is paramount to ensure optimal orientation, uniform coverage, and preserved activity of the biorecognition elements for effective OTA detection, while their maintained biological activity ensures accurate and consistent results. Hence, both physisorption (adsorption) and chemisorption (cross-linking) strategies were evaluated in this optimization. Considering the surface nature of the nanoplasmonic thin film, a thiol-based dithiobis(succinimidyl propionate) (DSP) cross-linker was chosen for its well-known strong interaction with the Au NPs, while its amine group facilitates interaction with the bioreceptor, creating an intermediate adhesion layer. In identically deposited nanoplasmonic Au-TiO_2 thin films, DSP functionalization caused both morphological and chemical changes. The influence of various parameters, such as O_2 plasma treatment and cross-linker concentration, was studied. O_2 plasma activation not only enhanced DSP functionalization but also, at a specific concentration (4 mg mL^{-1}), promoted the formation of distinct islands with increasing dimensions. Indeed, a uniformly coated adhesion layer was formed over the entire surface of the thin film, in which the DSP is functionalized on Au NPs and extends to the surrounding areas, through thiol (-SH) and hydroxyl (-OH) interactions, respectively. Considering the functional groups of DSP, the bioreceptor can chemically interact with both -NH_2 (amine) and -SH groups, facilitating the creation of an oriented Ab layer. Both immobilization approaches achieved uniform bioreceptor coverage with preserved activity. For these studies, well-known anti-IgG-FITC and mouse IgG Ab pair was used in fluorescent experiments. The chemisorption strategy was able to immobilize a larger quantity of functional Ab, thereby forming a larger sensitive area across the nanoplasmonic thin film available to chemically interact with a greater amount of analytes and, therefore, the bioanalytical performance is improved. Therefore, chemisorption emerges as the most viable approach for future immobilizations, offering an enhanced platform for effective analyte detection and signal amplification in biosensing applications.

Simultaneously, the sensing response of the LSPR-based biosensor was a critical aspect studied. As described above, the plasmonic response observed in the proof-of-concept experiment was noticeably reduced, leading to a low signal transduction efficiency and affecting the biosensor's ability to detect the presence of the analyte (biotin) accurately. Although the thin films were produced under certain deposition conditions, these conditions were optimized prior to this research and proved unsuitable for this study. Hence, specific parameters in the preparation and development of the thin films were considered in this sensing optimization, such as the NPs' nature and size embedded in the thin film. The combination of specific bimetallic compositions and annealing conditions would enhance the plasmonic properties and sensitivity of the thin films. In this context, monometallic (Au; Ag) and bimetallic (Au-Ag) thin films were deposited and annealed at increasing temperatures. Au NPs are renowned for their inert nature, stability, and relatively straightforward synthesis and bioconjugation processes, while Ag NPs are more efficient to scatter light at the resonance condition and, therefore, typically exhibit enhanced sensitivity factors. Along with this, annealing temperature will influence the NPs sizes, providing the energy necessary for the growth of NPs with increasing dimensions, as a result of the coalescence and Ostwald ripening phenomena. This NPs size increase enhances the scattering-to-absorption ratio and, consequently, its sensitivity. In the pursuit of optimizing the optical and sensing capabilities of the new thin films, the metallic concentration was meticulously maintained within a range similar to previous films (approximately 18 to 20%). Notably, the increasing annealing temperature led to the development of a sharper T-LSPR band in Au-containing systems, accompanied by a notable increase in sensitivity. In fact, the inclusion of Ag atoms into Au-TiO_2, accompanied by an increase in the annealing temperature, led to a significant enhancement in the sensing ability of nanoplasmonic thin films, which was most evident when the metallic atomic ratio in the AuAg-TiO_2 films was close to 1. Notably, this nanoplasmonic film annealed at 700 °C showed a 5.5-fold sensitivity improvement compared to the Au-TiO_2 used in previous work, from 33 ± 5 to 181 ± 3 nm/RIU. Upon conducting a detailed morphological analysis of the AuAg-TiO_2 films by Scanning Electron Microscopy (SEM), it was observed that metallic NPs covered 20% of the nanoplasmonic film's surface, with an average size of 31 nm (σ=14). A topographic profile reveals the presence of higher (hills) and lower (valleys) regions correlated by the semi-exposed NPs dispersed by the host TiO_2 matrix, respectively.

Both optimization efforts, namely the biorecognition’s effectiveness and sensing ability enhancement, revealed an essential contribution to developing a suitable LSPR-based biosensor for OTA detection. A further nanostructure characterization of the thin film using Scanning Transmission Electron Microscopy (STEM) confirmed the metallic coverage of about 20% with an average NPs size of 19 nm

(σ=10), yet this technique accounts also for small sized nanoparticles (< 10 nm), that do not contribute to LSPR band, and were not observed by SEM in previous analysis due to a difference in the resolution between techniques (STEM and SEM). In order to develop of an LSPR-based biosensor for OTA detection, a biorecognition layer, composed of anti-OTA Ab, was immobilized into optimized nanoplasmonic AuAg-TiO_2 thin films. An initial immunoassay optimization was required, focusing on the Ab immobilization design strategy and its concentration. Despite the improved performance of the chemisorption strategy in previous optimization efforts, the introduction of an intermediate DSP layer might reduce the effectiveness of the LSPR response. This is because the distance between the Ab antigen-binding site (paratope) and the NP's surface may be greater than the sensing volume contained within the LSPs decay length, hindering the LSPR sensor response. However, the chemisorption strategy provided an enhanced LSPR response to the OTA presence, as it apparently facilitated an optimal Ab orientation and strength, thus favoring the biorecognition stability and efficiency. In addition, the DSP layer seems to allow higher bioreceptor functionality, even at lower concentrations, contributing to the cost-effectiveness of the overall biosensing technology. The LSPR-based biosensor, when exposed to increasing OTA concentrations, demonstrated a dynamic detection range from 0.05 to 2 ng mL^{-1}, with a good correlation value (0.997), and a significantly low LOD value (7 pg mL^{-1}). This biosensing performance aligns with the requirements for monitoring OTA in various food matrices, including wine. The sensing ability of the proposed LSPR-based biosensor was compared against a standard commercially detection technique used for OTA detection, namely the competitive ELISA. The commercial ELISA kit provided only three OTA concentration levels; therefore, its dynamic range was established between the higher and lower concentrations tested, namely between 0.5 and 8 ng mL^{-1}. However, its LOD was determined to be 0.11 ng mL^{-1}, which is higher than that achieved by the LSPR-based biosensor, underlining the enhanced LSPR sensitivity of the AuAg-TiO_2 thin film for OTA detection. Beyond that, the LSPR-based biosensor's practicality and reliability were confirmed through testing with spiked wine samples, achieving suitable recovery rates of 93% to 113%. These findings demonstrate the LSPR-based biosensor's accuracy in detecting OTA in complex matrices, highlighting its feasibility and robustness in real-world applications.

In summary, the development of a novel label-free LSPR-based biosensor, using nanoplasmonic thin film, is a significant advancement in biosensing applications, specifically in OTA detection. These nanoplasmonic AuAg-TiO_2 thin films, produced through a cost-effective and up-scalable one-step reactive DC magnetron sputtering process and annealed at higher annealing temperatures, revealed an enhanced LSPR response. After the proper biorecognition interface preparation, the LSPR-based biosensor is included into a portable, modular and compact optical system, composed by holder connected to an LED

source, a spectrophotometer and a computer, facilitating (future) on-site testing in the food production and processing chain. The combination of optimized conditions (i.e., biorecognition interface and sensitivity) enable to detect the aimed target with a suitable LOD value, making it a promising tool for ensuring food safety and quality control.

6.2. Future Perspectives

After achieving the primary objective of this doctoral thesis, detect OTA using enhanced LSPR response of optimized nanoplasmonic AuAg-TiO_2 thin films, additional considerations are needed, namely in terms of theoretical studies, biosensing optimization and applications in real-world scenarios, which are crucial for future implementation and commercialization.

Firstly, some future work may be focused on a theoretical study of the physical principles underlying plasmonic responses in biosensing applications. This theoretical study may understand plasmonic behavior, emphasizing the interaction mechanisms between biomolecules, specifically OTA, and the NPs present in the nanocomposite thin films. This study aims to understand how these interactions lead to observable alterations in the optical properties of the films, primarily caused by changes in their refractive index (RI), and how various compositions of nanoparticles (NPs), including their size, shape, and distribution, along with the surrounding dielectric medium, influence these interactions.

Focusing in the LSPR-based biosensor development, a comprehensive bioanalytical evaluation should be performed, assessing aspects such as volume sample, response time, and selectivity. Beyond these, the stability of the LSPR-based biosensor composed by antibodies, as a chosen bioreceptor, should be considered through the drying procedures with minimal loss of antibody activity, to evaluate its commercial suitability. Although the LSPR-based biosensor was able to detect OTA in spiked wine samples, other application tests using various real feed and foodstuff may demonstrate the biosensor's applicability in further practical settings.

LSPR-based biosensors offer a label-free monitoring with real-time analysis with a high sensing performance. The synergistic combination of enhanced nanoplasmonic thin films with microfluidic technologies may enable highly sensitive OTA quantification, benefiting from miniaturization, low sample, reagent consumption, and precise fluid control for suitable biosensing performance. Thus, the use of microfluidic technologies (in particular, an LSPR chip) seems to be a natural and important area for future research. The microfluidic LSPR chip might be composed of two main components: nanoplasmonic thin film chemically bonded to a microfluidic module, usually a polymer like poly(dimethylsiloxane) (PDMS), using plasma treatment. Alternatively, and as already reported by the PhD candidate, nanoplasmonic thin

films could be deposited directly on the transparent polymer substrates, such as PDMS, which is typically the base material to develop microfluidic channels to be incorporated in LSPR sensing systems [339]. However, in this last context, the preparation LSPR-based biosensors should be optimized towards a high-sensing performance, considering several limitations (e.g., annealing temperature). Leveraging label-free and real-time detection capabilities, this LSPR-based biosensor arranged to a microfluidic system paves the way for user-friendly 'lab-on-chip' applications suited for the food industry, by offering convenience and practicality in food safety monitoring.

For effective commercialization, an innovative optical scanning device configuration will benefit from inclusion in a compact and portable device, allowing on-site biosensing. This all-in-one device would integrate an LSPR chip holder with an LED source and a miniaturized spectrophotometer, providing a simple and quick-to-interpret result displayed on a screen. The acquisition software must be adapted to real-time monitoring and analysis of LSPR data. In addition to its usefulness, features such as wireless data transmission and cloud integration would be advantageous for remote accessibility and convenient data management. A practical and user-friendly format that opens up new possibilities for biosensing in various environments.

Ultimately, the proposed LSPR-based sensor has the potential to significantly expand its biosensing target (within the specified sensing parameters). This versatility is attributed to its customizable biorecognition interface, which can be adapted using other specific antibodies or aptamers on the nanoplasmonic AuAg-TiO_2 thin film. In fact, aptamers can be a suitable bioreceptor element for further studies, since they can be denatured and refolded multiple times without losing their activity or, even, affecting the biosensor's performance, allowing for cost-effective and reusable LSPR-based biosensors. As a result, this LSPR sensing technology based on nanoplasmonic films have the potential to be applied in a wide range of fields, including food safety, environmental monitoring, and medical diagnostics.

BIBLIOGRAPHY

1. Food and Agricultural Organization of the United Nations *Global Agriculture towards 2050*; Rome, 2009;
2. Schrenk, D.; Bodin, L.; Chipman, J.K.; del Mazo, J.; Grasl-Kraupp, B.; Hogstrand, C.; Hoogenboom, L.; Leblanc, J.C.; Nebbia, C.S.; Nielsen, E.; et al. *Risk Assessment of Ochratoxin A in Food*; 2020; Vol. 18;.
3. Liu, W.C.; Pushparaj, K.; Meyyazhagan, A.; Arumugam, V.A.; Pappuswamy, M.; Bhotla, H.K.; Baskaran, R.; Issara, U.; Balasubramanian, B.; Mousavi Khaneghah, A. Ochratoxin A as an Alarming Health Threat for Livestock and Human: A Review on Molecular Interactions, Mechanism of Toxicity, Detection, Detoxification, and Dietary Prophylaxis. *Toxicon* **2022**, *213*, 59–75, doi:10.1016/j.toxicon.2022.04.012.
4. Kumar, P.; Mahato, D.K.; Sharma, B.; Borah, R.; Haque, S.; Mahmud, M.M.C.; Shah, A.K.; Rawal, D.; Bora, H.; Bui, S. Ochratoxins in Food and Feed: Occurrence and Its Impact on Human Health and Management Strategies. *Toxicon* **2020**, *187*, 151–162, doi:10.1016/j.toxicon.2020.08.031.
5. Gruber-Dorninger, C.; Jenkins, T.; Schatzmayr, G. Global Mycotoxin Occurrence in Feed: A Ten-Year Survey. *Toxins (Basel).* **2019**, *11*, 375, doi:10.3390/toxins11070375.
6. IARC *Some Naturally Occurring Substances: Food Items and Constituents, Heterocyclic Aromatic Amines and Mycotoxins*; 1993; Vol. 56; ISBN 9283212568.
7. Ringot, D.; Chango, A.; Schneider, Y.J.; Larondelle, Y. Toxicokinetics and Toxicodynamics of Ochratoxin A, an Update. *Chem. Biol. Interact.* **2006**, *159*, 18–46, doi:10.1016/j.cbi.2005.10.106.
8. Kőszegi, T.; Poór, M. Ochratoxin A: Molecular Interactions, Mechanisms of Toxicity and Prevention at the Molecular Level. *Toxins (Basel).* **2016**, *8*, 111, doi:10.3390/toxins8040111.
9. Sorrenti, V.; Di Giacomo, C.; Acquaviva, R.; Barbagallo, I.; Bognanno, M.; Galvano, F. Toxicity of Ochratoxin A and Its Modulation by Antioxidants: A Review. *Toxins (Basel).* **2013**, *5*, 1742–1766, doi:10.3390/toxins5101742.
10. Niaz, K.; Shah, S.Z.A.; Khan, F.; Bule, M. Ochratoxin A–Induced Genotoxic and Epigenetic Mechanisms Lead to Alzheimer Disease: Its Modulation with Strategies. *Environ. Sci. Pollut. Res.* **2020**, *27*, 44673–44700, doi:10.1007/s11356-020-08991-y.
11. Stoev, S.D. New Evidences about the Carcinogenic Effects of Ochratoxin A and Possible Prevention by Target Feed Additives. *Toxins (Basel).* **2022**, *14*, 380, doi:10.3390/toxins14060380.

12. Obafemi, B.A.; Adedara, I.A.; Rocha, J.B.T. Neurotoxicity of Ochratoxin A: Molecular Mechanisms and Neurotherapeutic Strategies. *Toxicology* **2023**, *497–498*, 153630, doi:10.1016/j.tox.2023.153630.
13. Kochman, J.; Jakubczyk, K.; Janda, K. Mycotoxins in Red Wine: Occurrence and Risk Assessment. *Food Control* **2021**, *129*, 108229, doi:10.1016/j.foodcont.2021.108229.
14. Li, X.; Ma, W.; Ma, Z.; Zhang, Q.; Li, H. The Occurrence and Contamination Level of Ochratoxin a in Plant and Animal-Derived Food Commodities. *Molecules* **2021**, *26*, 6928, doi:10.3390/molecules26226928.
15. International Organisation of Vine and Wine *State of the World Vitivinicultural Sector in 2022*; Paris, France, 2023;
16. European Commission *Commission Regulation (EC) No. 401/2006 Laying down the Methods of Sampling and Analysis for the Official Control of the Levels of Mycotoxins in Foodstuffs*; 2006; Vol. L70;.
17. European Commission *Commission Regulation (EU) 2023/915 of 25 April 2023 on Maximum Levels for Certain Contaminants in Food and Repealing Regulation (EC) No 1881/2006*; 2023;
18. Hassan, R.A.; Abu Hanifah, S.; Heng, L.Y.; Al-badaii, F.; Ulianas, A. Systematic Review on Biosensors for the Early Detection of Mycotoxins as Endocrine Disruptors. *Food Control* **2024**, *157*, 110195, doi:10.1016/j.foodcont.2023.110195.
19. Wang, L.; Hua, X.; Shi, J.; Jing, N.; Ji, T.; Lv, B.; Liu, L.; Chen, Y. Ochratoxin A: Occurrence and Recent Advances in Detoxification. *Toxicon* **2022**, *210*, 11–18, doi:10.1016/j.toxicon.2022.02.010.
20. Wang, L.; Wang, Q.; Wang, S.; Cai, R.; Yuan, Y.; Yue, T.; Wang, Z. Bio-Control on the Contamination of Ochratoxin A in Food: Current Research and Future Prospects. *Curr. Res. Food Sci.* **2022**, *5*, 1539–1549, doi:10.1016/j.crfs.2022.09.007.
21. Yang, Q.; Dhanasekaran, S.; Ngea, G.L.N.; Tian, S.; Li, B.; Zhang, H. Unveiling Ochratoxin a Controlling and Biodetoxification Molecular Mechanisms: Opportunities to Secure Foodstuffs from OTA Contamination. *Food Chem. Toxicol.* **2022**, *169*, 113437, doi:10.1016/j.fct.2022.113437.
22. Kim, D.M.; Park, J.S.; Jung, S.W.; Yeom, J.; Yoo, S.M. Biosensing Applications Using Nanostructure-Based Localized Surface Plasmon Resonance Sensors. *Sensors* **2021**, *21*, 3191, doi:10.3390/s21093191.
23. Pitarke, J.M.; Silkin, V.M.; Chulkov, E. V.; Echenique, P.M. Theory of Surface Plasmons and Surface-Plasmon Polaritons. *Reports Prog. Phys.* **2007**, *70*, 1–87, doi:10.1088/0034-

4885/70/1/R01.

24. Kahl, P.; Podbiel, D.; Schneider, C.; Makris, A.; Sindermann, S.; Witt, C.; Kilbane, D.; Hoegen, M.H. von; Aeschlimann, M.; zu Heringdorf, F.M. Direct Observation of Surface Plasmon Polariton Propagation and Interference by Time-Resolved Imaging in Normal-Incidence Two Photon Photoemission Microscopy. *Plasmonics* **2018**, *13*, 239–246, doi:10.1007/s11468-017-0504-6.
25. Maier, S.A. *Plasmonics: Fundamentals and Applications*; Springer US: New York, NY, 2007; ISBN 0387331506.
26. Willets, K.A.; Van Duyne, R.P. Localized Surface Plasmon Resonance Spectroscopy and Sensing. *Annu. Rev. Phys. Chem.* **2007**, *58*, 267–297, doi:10.1146/annurev.physchem.58.032806.104607.
27. Kedem, O.; Vaskevich, A.; Rubinstein, I. Critical Issues in Localized Plasmon Sensing. *J. Phys. Chem. C* **2014**, *118*, 8227–8244, doi:10.1021/jp409954s.
28. Li, D.B.; Sun, X.J.; Jia, Y.P.; Stockman, M.I.; Paudel, H.P.; Song, H.; Jiang, H.; Li, Z.M. Direct Observation of Localized Surface Plasmon Field Enhancement by Kelvin Probe Force Microscopy. *Light Sci. Appl.* **2017**, *6*, e17038–e17038, doi:10.1038/lsa.2017.38.
29. Rodrigues, M.S.; Borges, J.; Lopes, C.; Pereira, R.M.S.; Vasilevskiy, M.I.; Vaz, F. Gas Sensors Based on Localized Surface Plasmon Resonances: Synthesis of Oxide Films with Embedded Metal Nanoparticles, Theory and Simulation, and Sensitivity Enhancement Strategies. *Appl. Sci.* **2021**, *11*, doi:10.3390/app11125388.
30. Zalyubovskiy, S.J.; Bogdanova, M.; Deinega, A.; Lozovik, Y.; Pris, A.D.; An, K.H.; Hall, W.P.; Potyrailo, R.A. Theoretical Limit of Localized Surface Plasmon Resonance Sensitivity to Local Refractive Index Change and Its Comparison to Conventional Surface Plasmon Resonance Sensor. *J. Opt. Soc. Am. A* **2012**, *29*, 994, doi:10.1364/josaa.29.000994.
31. Ozhikandathil, J.; Packirisamy, M. Simulation and Implementation of a Morphology-Tuned Gold Nano-Islands Integrated Plasmonic Sensor. *Sensors (Switzerland)* **2014**, *14*, 10497–10513, doi:10.3390/s140610497.
32. Unser, S.; Bruzas, I.; He, J.; Sagle, L. Localized Surface Plasmon Resonance Biosensing: Current Challenges and Approaches. *Sensors (Switzerland)* **2015**, *15*, 15684–15716, doi:10.3390/s150715684.
33. Jung, L.S.; Campbell, C.T.; Chinowsky, T.M.; Mar, M.N.; Yee, S.S. Quantitative Interpretation of the Response of Surface Plasmon Resonance Sensors to Adsorbed Films. *Langmuir* **1998**, *14*,

5636–5648, doi:10.1021/la971228b.

34. Barbosa, A.I.; Borges, J.; Meira, D.I.; Costa, D.; Rodrigues, M.S.; Rebelo, R.; Correlo, V.M.; Vaz, F.; Reis, R.L. Development of Label-Free Plasmonic Au-TiO_2 Thin Film Immunosensor Devices. *Mater. Sci. Eng. C* **2019**, *100*, 424–432, doi:10.1016/j.msec.2019.03.029.
35. Borges, J.; Rodrigues, M.S.; Kubart, T.; Kumar, S.; Leifer, K.; Evaristo, M.; Cavaleiro, A.; Apreutesei, M.; Pereira, R.M.S.; Vasilevskiy, M.I.; et al. Thin Films Composed of Gold Nanoparticles Dispersed in a Dielectric Matrix: The Influence of the Host Matrix on the Optical and Mechanical Responses. *Thin Solid Films* **2015**, *596*, 8–17, doi:10.1016/j.tsf.2015.08.058.
36. Rodrigues, M.S.; Costa, D.; Domingues, R.P.; Apreutesei, M.; Pedrosa, P.; Martin, N.; Correlo, V.M.; Reis, R.L.; Alves, E.; Barradas, N.P.; et al. Optimization of Nanocomposite Au/TiO_2 Thin Films towards LSPR Optical-Sensing. *Appl. Surf. Sci.* **2018**, *438*, 74–83, doi:10.1016/j.apsusc.2017.09.162.
37. Ben Taheur, F.; Kouidhi, B.; Al Qurashi, Y.M.A.; Ben Salah-Abbès, J.; Chaieb, K. Review: Biotechnology of Mycotoxins Detoxification Using Microorganisms and Enzymes. *Toxicon* **2019**, *160*, 12–22, doi:10.1016/j.toxicon.2019.02.001.
38. Eskola, M.; Kos, G.; Elliott, C.T.; Hajšlová, J.; Mayar, S.; Krska, R. Worldwide Contamination of Food-Crops with Mycotoxins: Validity of the Widely Cited 'FAO Estimate' of 25%. *Crit. Rev. Food Sci. Nutr.* **2020**, *60*, 2773–2789, doi:10.1080/10408398.2019.1658570.
39. Hussein, H.S.; Brasel, J.M. Toxicity, Metabolism, and Impact of Mycotoxins on Humans and Animals. *Toxicology* **2001**, *167*, 101–134, doi:10.1016/S0300-483X(01)00471-1.
40. Prieto-Simón, B.; Campàs, M.; Marty, J.L.; Noguer, T. Novel Highly-Performing Immunosensor-Based Strategy for Ochratoxin A Detection in Wine Samples. *Biosens. Bioelectron.* **2008**, *23*, 995–1002, doi:10.1016/j.bios.2007.10.002.
41. Haschek, W.M.; Voss, K.A. Mycotoxins. In *Haschek and Rousseaux's Handbook of Toxicologic Pathology*; Elsevier, 2013; pp. 1187–1258 ISBN 9780124157590.
42. Agriopoulou, S.; Stamatelopoulou, E.; Varzakas, T. Advances in Occurrence, Importance, and Mycotoxin Control Strategies: Prevention and Detoxification in Foods. *Foods* **2020**, *9*, 137, doi:10.3390/foods9020137.
43. Mitchell, N.J.; Bowers, E.; Hurburgh, C.; Wu, F. Potential Economic Losses to the US Corn Industry from Aflatoxin Contamination. *Food Addit. Contam. - Part A Chem. Anal. Control. Expo. Risk Assess.* **2016**, *33*, 540–550, doi:10.1080/19440049.2016.1138545.
44. Pitt, J.I.; David Miller, J. A Concise History of Mycotoxin Research. *J. Agric. Food Chem.* **2017**,

65, 7021–7033, doi:10.1021/acs.jafc.6b04494.

45. Kumar, P.; Mahato, D.K.; Kamle, M.; Mohanta, T.K.; Kang, S.G. Aflatoxins: A Global Concern for Food Safety, Human Health and Their Management. *Front. Microbiol.* **2017**, *7*, doi:10.3389/fmicb.2016.02170.
46. Bennett, J.W.; Klich, M. Mycotoxins. *Clin. Microbiol. Rev.* **2003**, *16*, 497–516, doi:10.1128/CMR.16.3.497-516.2003.
47. Battilani, P.; Palumbo, R.; Giorni, P.; Dall'Asta, C.; Dellafiora, L.; Gkrillas, A.; Toscano, P.; Crisci, A.; Brera, C.; De Santis, B.; et al. Mycotoxin Mixtures in Food and Feed: Holistic, Innovative, Flexible Risk Assessment Modelling Approach: *EFSA Support. Publ.* **2020**, *17*, doi:10.2903/sp.efsa.2020.en-1757.
48. International Organisation of Vine and Wine *State of the World Vitivinicultural Sector in 2020*; Paris, France, 2021;
49. Vitali Čepo, D.; Pelajić, M.; Vinković Vrček, I.; Krivohlavek, A.; Žuntar, I.; Karoglan, M. Differences in the Levels of Pesticides, Metals, Sulphites and Ochratoxin A between Organically and Conventionally Produced Wines. *Food Chem.* **2018**, *246*, 394–403, doi:10.1016/j.foodchem.2017.10.133.
50. Mousavi Khaneghah, A.; Fakhri, Y.; Raeisi, S.; Armoon, B.; Sant'Ana, A.S. Prevalence and Concentration of Ochratoxin A, Zearalenone, Deoxynivalenol and Total Aflatoxin in Cereal-Based Products: A Systematic Review and Meta-Analysis. *Food Chem. Toxicol.* **2018**, *118*, 830–848, doi:10.1016/j.fct.2018.06.037.
51. Khaneghah, A.M.; Fakhri, Y.; Abdi, L.; Coppa, C.F.S.C.; Franco, L.T.; de Oliveira, C.A.F. The Concentration and Prevalence of Ochratoxin A in Coffee and Coffee-Based Products: A Global Systematic Review, Meta-Analysis and Meta-Regression. *Fungal Biol.* **2019**, *123*, 611–617, doi:10.1016/j.funbio.2019.05.012.
52. El Khoury, A.; Atoui, A. Ochratoxin A: General Overview and Actual Molecular Status. *Toxins (Basel).* **2010**, *2*, 461–493, doi:10.3390/toxins2040461.
53. Pohland, A.E.; Schuller, P.L.; Steyn, P.S.; Van Egmond, H.P. Physicochemical Data for Some Selected Mycotoxins. *Pure Appl. Chem.* **1982**, *54*, 2219–2284, doi:10.1351/pac198254112219.
54. Pohland, A.E.; Nesheim, S.; Friedman, L. Ochratoxin A: A Review (Technical Report). *Pure Appl. Chem.* **1992**, *64*, 1029–1046, doi:10.1351/pac199264071029.
55. Ha, T.H. Recent Advances for the Detection of Ochratoxin A. *Toxins (Basel).* **2015**, *7*, 5276–

5300, doi:10.3390/toxins7124882.

56. Pires, P.N.; Vargas, E.A.; Gomes, M.B.; Vieira, C.B.M.; Santos, E.A. dos; Bicalho, A.A.C.; Silva, S. de C.; Rezende, R.P.; Oliveira, I.S. De; Luz, E.D.M.N.; et al. Aflatoxins and Ochratoxin A: Occurrence and Contamination Levels in Cocoa Beans from Brazil. *Food Addit. Contam. - Part A Chem. Anal. Control. Expo. Risk Assess.* **2019**, *36*, 815–824, doi:10.1080/19440049.2019.1600749.

57. Mehri, F.; Esfahani, M.; Heshmati, A.; Jenabi, E.; Khazaei, S. The Prevalence of Ochratoxin A in Dried Grapes and Grape-Derived Products: A Systematic Review and Meta-Analysis. *Toxin Rev.* **2020**, 1–10, doi:10.1080/15569543.2020.1845739.

58. Iqbal, S.Z.; Mehmood, Z.; Asi, M.R.; Shahid, M.; Sehar, M.; Malik, N. Co-Occurrence of Aflatoxins and Ochratoxin A in Nuts, Dry Fruits, and Nuty Products. *J. Food Saf.* **2018**, *38*, e12462, doi:10.1111/jfs.12462.

59. Zareshahrabadi, Z.; Bahmyari, R.; Nouraei, H.; Khodadadi, H.; Mehryar, P.; Asadian, F.; Zomorodian, K. Detection of Aflatoxin and Ochratoxin A in Spices by High-Performance Liquid Chromatography. *J. Food Qual.* **2020**, *2020*, 1–8, doi:10.1155/2020/8858889.

60. Altafini, A.; Fedrizzi, G.; Roncada, P. Occurrence of Ochratoxin A in Typical Salami Produced in Different Regions of Italy. *Mycotoxin Res.* **2019**, *35*, 141–148, doi:10.1007/s12550-018-0338-x.

61. Freire, L.; Braga, P.A.C.; Furtado, M.M.; Delafiori, J.; Dias-Audibert, F.L.; Pereira, G.E.; Reyes, F.G.; Catharino, R.R.; Sant'Ana, A.S. From Grape to Wine: Fate of Ochratoxin A during Red, Rose, and White Winemaking Process and the Presence of Ochratoxin Derivatives in the Final Products. *Food Control* **2020**, *113*, 107167, doi:10.1016/j.foodcont.2020.107167.

62. Mateo, R.; Medina, Á.; Mateo, E.M.; Mateo, F.; Jiménez, M. An Overview of Ochratoxin A in Beer and Wine. *Int. J. Food Microbiol.* **2007**, *119*, 79–83, doi:10.1016/j.ijfoodmicro.2007.07.029.

63. Dachery, B.; Veras, F.F.; Dal Magro, L.; Manfroi, V.; Welke, J.E. Exposure Risk Assessment to Ochratoxin A through Consumption of Juice and Wine Considering the Effect of Steam Extraction Time and Vinification Stages. *Food Chem. Toxicol.* **2017**, *109*, 237–244, doi:10.1016/j.fct.2017.09.013.

64. Bennett, J.W. Mycotoxins, Mycotoxicoses, Mycotoxicology and Mycopathologia. *Mycopathologia* **1987**, *100*, 3–5, doi:10.1007/BF00769561.

65. Fink-Gremmels, J. Mycotoxins: Their Implications for Human and Animal Health. *Vet. Q.* **1999**, *21*, 115–120, doi:10.1080/01652176.1999.9695005.

66. Studer-Rohr, I.; Schlatter, J.; Dietrich, D.R. Kinetic Parameters and Intraindividual Fluctuations of Ochratoxin A Plasma Levels in Humans. *Arch. Toxicol.* **2000**, *74*, 499–510, doi:10.1007/s002040000157.

67. Ratola, N.; Abade, E.; Simões, T.; Venâncio, A.; Alves, A. Evolution of Ochratoxin A Content from Must to Wine in Port Wine Microvinification. *Anal. Bioanal. Chem.* **2005**, *382*, 405–411, doi:10.1007/s00216-005-3176-6.

68. Popescu, R.G.; Bulgaru, C.; Untea, A.; Vlassa, M.; Filip, M.; Hermenean, A.; Marin, D.; Ţăranu, I.; Georgescu, S.E.; Dinischiotu, A. The Effectiveness of Dietary Byproduct Antioxidants on Induced CYP Genes Expression and Histological Alteration in Piglets Liver and Kidney Fed with Aflatoxin B1 and Ochratoxin A. *Toxins (Basel).* **2021**, *13*, 148, doi:10.3390/toxins13020148.

69. Duarte, S.C.; Pena, A.; Lino, C.M. Ochratoxin A Non-Conventional Exposure Sources - A Review. *Microchem. J.* **2009**, *93*, 115–120, doi:10.1016/j.microc.2009.06.002.

70. Pfohl-Leszkowicz, A. Ochratoxin A and Aristolochic Acid Involvement in Nephropathies and Associated Urothelial Tract Tumours. *Arch. Ind. Hyg. Toxicol.* **2009**, *60*, 465–483, doi:10.2478/10004-1254-60-2009-2000.

71. Schwerdt, G.; Freudinger, R.; Silbernagl, S.; Gekle, M. Ochratoxin A-Binding Proteins in Rat Organs and Plasma and in Different Cell Lines of the Kidney. *Toxicology* **1999**, *135*, 1–10, doi:10.1016/S0300-483X(99)00028-1.

72. Fuchs, R.; Radić, B.; Peraica, M.; Hult, K.; Pleština, R. Enterohepatic Circulation of Ochratoxin A in Rats. *Period. Biol.* **1988**, *90*, 39–42.

73. Belmadani, A.; Tramu, G.; Betbeder, A.M.; Steyn, P.S.; Creppy, E.E. Regional Selectivity to Ochratoxin A, Distribution and Cytotoxicity in Rat Brain. *Arch. Toxicol.* **1998**, *72*, 656–662, doi:10.1007/s002040050557.

74. Bui-Klimke, T.R.; Wu, F. Ochratoxin A and Human Health Risk: A Review of the Evidence. *Crit. Rev. Food Sci. Nutr.* **2015**, *55*, 1860–1869, doi:10.1080/10408398.2012.724480.

75. European Commission *Commission Regulation (EC) No 1881/2006 of 19 December 2006 Setting Maximum Levels for Certain Contaminants in Foodstuffs*; 2006; Vol. 364;.

76. European Food Safety Authority (EFSA) Opinion of the Scientific Panel on Contaminants in the Food Chain [CONTAM] Related to Ochratoxin A in Food. *EFSA J.* **2006**, *4*, 365, doi:10.2903/j.efsa.2006.365.

77. Joint FAO/WHO Expert Committee on Food Additives Evaluation of Certain Food Additives and Contaminants. *World Health Organ. Tech. Rep. Ser.* **2007**, 1–92, 1 p following 94.

78. Agriopoulou, S.; Stamatelopoulou, E.; Varzakas, T. Advances in Analysis and Detection of Major Mycotoxins in Foods. *Foods* **2020**, *9*, 518, doi:10.3390/foods9040518.

79. Bueno, D.; Muñoz, R.; Marty, J. Common Methods to Detect Mycotoxins: A Review with Particular Emphasis on Electrochemical Detection. *Sens. Electroanal.* **2014**, *8*, 85–114.

80. Janik, E.; Niemcewicz, M.; Podogrocki, M.; Ceremuga, M.; Gorniak, L.; Stela, M.; Bijak, M. The Existing Methods and Novel Approaches in Mycotoxins' Detection. *Molecules* **2021**, *26*, 3981, doi:10.3390/molecules26133981.

81. Zimmerli, B.; Dick, R. Ochratoxin A in Table Wine and Grape-Juice: Occurrence and Risk Assessment. *Food Addit. Contam.* **1996**, *13*, 655–668, doi:10.1080/02652039609374451.

82. Blesa, J.; Soriano, J.M.; Moltó, J.C.; Mañes, J. Factors Affecting the Presence of Ochratoxin A in Wines. *Crit. Rev. Food Sci. Nutr.* **2006**, *46*, 473–478, doi:10.1080/10408390500215803.

83. Mishra, G.K.; Barfidokht, A.; Tehrani, F.; Mishra, R.K. Food Safety Analysis Using Electrochemical Biosensors. *Foods* **2018**, *7*, 141, doi:10.3390/foods7090141.

84. Visconti, A.; Pascale, M.; Centonze, G. Determination of Ochratoxin A in Wine and Beer by Immunoaffinity Column Cleanup and Liquid Chromatographic Analysis with Fluorometric Detection: Collaborative Study. *J. AOAC Int.* **2001**, *84*, 1818–1827, doi:10.1093/jaoac/84.6.1818.

85. Var, I.; Kabak, B. Occurrence of Ochratoxin A in Turkish Wines. *Microchem. J.* **2007**, *86*, 241–247, doi:10.1016/j.microc.2007.04.002.

86. Mukherjee, M.; Nandhini, C.; Bhatt, P. Colorimetric and Chemiluminescence Based Enzyme Linked Apta-Sorbent Assay (ELASA) for Ochratoxin A Detection. *Spectrochim. Acta - Part A Mol. Biomol. Spectrosc.* **2021**, *244*, 118875, doi:10.1016/j.saa.2020.118875.

87. Teixeira, T.R.; Hoeltz, M.; Einloft, T.C.; Dottori, H.A.; Manfroi, V.; Noll, I.B. Determination of Ochratoxin A in Wine from the Southern Region of Brazil by Thin Layer Chromatography with a Charge-Coupled Detector. *Food Addit. Contam. Part B Surveill.* **2011**, *4*, 289–293, doi:10.1080/19393210.2011.638088.

88. Soleas, G.J.; Yan, J.; Goldberg, D.M. Assay of Ochratoxin A in Wine and Beer by High-Pressure Liquid Chromatography Photodiode Array and Gas Chromatography Mass Selective Detection. *J. Agric. Food Chem.* **2001**, *49*, 2733–2740, doi:10.1021/jf0100651.

89. Andrade, M.A.; Lanças, F.M. Determination of Ochratoxin A in Wine by Packed In-Tube Solid Phase Microextraction Followed by High Performance Liquid Chromatography Coupled to Tandem Mass Spectrometry. *J. Chromatogr. A* **2017**, *1493*, 41–48, doi:10.1016/j.chroma.2017.02.053.

90. Nolan, P.; Auer, S.; Spehar, A.; Elliott, C.T.; Campbell, K. Current Trends in Rapid Tests for Mycotoxins. *Food Addit. Contam. - Part A Chem. Anal. Control. Expo. Risk Assess.* **2019**, *36*, 800–814, doi:10.1080/19440049.2019.1595171.

91. Karami-Osboo, R. Nanofluid Extraction of Ochratoxin A in Food. *J. Food Compos. Anal.* **2020**, *87*, 103425, doi:10.1016/j.jfca.2020.103425.

92. López-Puertollano, D.; Agulló, C.; Mercader, J. V.; Abad-Somovilla, A.; Abad-Fuentes, A. Immunoanalytical Methods for Ochratoxin A Monitoring in Wine and Must Based on Innovative Immunoreagents. *Food Chem.* **2021**, *345*, 128828, doi:10.1016/j.foodchem.2020.128828.

93. Streit, E.; Schatzmayr, G.; Tassis, P.; Tzika, E.; Marin, D.; Taranu, I.; Tabuc, C.; Nicolau, A.; Aprodu, I.; Puel, O.; et al. Current Situation of Mycotoxin Contamination and Co-Occurrence in Animal Feed—Focus on Europe. *Toxins (Basel).* **2012**, *4*, 788–809, doi:10.3390/toxins4100788.

94. Błajet-Kosicka, A.; Twaruzek, M.; Kosicki, R.; Sibiorowska, E.; Grajewski, J. Co-Occurrence and Evaluation of Mycotoxins in Organic and Conventional Rye Grain and Products. *Food Control* **2014**, *38*, 61–66, doi:10.1016/j.foodcont.2013.10.003.

95. Hosnedlova, B.; Sochor, J.; Baron, M.; Bjørklund, G.; Kizek, R. Application of Nanotechnology Based-Biosensors in Analysis of Wine Compounds and Control of Wine Quality and Safety: A Critical Review. *Crit. Rev. Food Sci. Nutr.* **2020**, *60*, 3271–3289, doi:10.1080/10408398.2019.1682965.

96. Cong, H.; Zhang, N. Perspectives in Translating Microfluidic Devices from Laboratory Prototyping into Scale-up Production. *Biomicrofluidics* **2022**, *16*, 021301, doi:10.1063/5.0079045.

97. Thakur, M.S.; Ragavan, K. V. Biosensors in Food Processing. *J. Food Sci. Technol.* **2013**, *50*, 625–641, doi:10.1007/s13197-012-0783-z.

98. Bunney, J.; Williamson, S.; Atkin, D.; Jeanneret, M.; Cozzolino, D.; Chapman, J.; Power, A.; Chandra, S. The Use of Electrochemical Biosensors in Food Analysis. *Curr. Res. Nutr. Food Sci.* **2017**, *5*, 183–195, doi:10.12944/CRNFSJ.5.3.02.

99. Rotariu, L.; Lagarde, F.; Jaffrezic-Renault, N.; Bala, C. Electrochemical Biosensors for Fast Detection of Food Contaminants - Trends and Perspective. *TrAC - Trends Anal. Chem.* **2016**, *79*, 80–87, doi:10.1016/j.trac.2015.12.017.

100. Krishna, V.D.; Wu, K.; Su, D.; Cheeran, M.C.J.; Wang, J.P.; Perez, A. Nanotechnology: Review of Concepts and Potential Application of Sensing Platforms in Food Safety. *Food Microbiol.* **2018**, *75*, 47–54, doi:10.1016/j.fm.2018.01.025.

101. Nayl, A.A.; Abd-Elhamid, A.I.; El-Moghazy, A.Y.; Hussin, M.; Abu-Saied, M.A.; El-Shanshory, A.A.; Soliman, H.M.A. The Nanomaterials and Recent Progress in Biosensing Systems: A Review. *Trends Environ. Anal. Chem.* **2020**, *26*, e00087, doi:10.1016/j.teac.2020.e00087.

102. Holzinger, M.; Goff, A. Le; Cosnier, S. Nanomaterials for Biosensing Applications: A Review. *Front. Chem.* **2014**, *2*, doi:10.3389/fchem.2014.00063.

103. Shan, H.; Li, X.; Liu, L.; Song, D.; Wang, Z. Recent Advances in Nanocomposite-Based Electrochemical Aptasensors for the Detection of Toxins. *J. Mater. Chem. B* **2020**, *8*, 5808–5825, doi:10.1039/d0tb00705f.

104. Byrne, B.; Stack, E.; Gilmartin, N.; O'Kennedy, R. Antibody-Based Sensors: Principles, Problems and Potential for Detection of Pathogens and Associated Toxins. *Sensors (Switzerland)* **2009**, *9*, 4407–4445, doi:10.3390/s90604407.

105. Krska, R.; Schubert-Ullrich, P.; Molinelli, A.; Sulyok, M.; MacDonald, S.; Crews, C. Mycotoxin Analysis: An Update. *Food Addit. Contam. - Part A Chem. Anal. Control. Expo. Risk Assess.* **2008**, *25*, 152–163, doi:10.1080/02652030701765723.

106. Zhang, L.; Dou, X.W.; Zhang, C.; Logrieco, A.F.; Yang, M.H. A Review of Current Methods for Analysis of Mycotoxins in Herbal Medicines. *Toxins (Basel).* **2018**, *10*, 65, doi:10.3390/toxins10020065.

107. Vashist, S.K.; Luong, J.H.T. Bioanalytical Requirements and Regulatory Guidelines for Immunoassays. In *Handbook of Immunoassay Technologies: Approaches, Performances, and Applications*; Elsevier, 2018; pp. 81–95 ISBN 9780128117620.

108. Santos, A.; Vaz, A.; Rodrigues, P.; Veloso, A.; Venâncio, A.; Peres, A. Thin Films Sensor Devices for Mycotoxins Detection in Foods: Applications and Challenges. *Chemosensors* **2019**, *7*, 3, doi:10.3390/chemosensors7010003.

109. Naresh, V.; Lee, N. A Review on Biosensors and Recent Development of Nanostructured Materials-Enabled Biosensors. *Sensors (Switzerland)* **2021**, *21*, 1–35, doi:10.3390/s21041109.

110. Artigues, M.; Abellà, J.; Colominas, S. Analytical Parameters of an Amperometric Glucose Biosensor for Fast Analysis in Food Samples. *Sensors (Switzerland)* **2017**, *17*, 2620, doi:10.3390/s17112620.

111. Sawant, S.N. Development of Biosensors from Biopolymer Composites. In *Biopolymer Composites in Electronics*; Elsevier, 2017; pp. 353–383 ISBN 9780081009741.

112. Van Dorst, B.; Mehta, J.; Bekaert, K.; Rouah-Martin, E.; De Coen, W.; Dubruel, P.; Blust, R.; Robbens, J. Recent Advances in Recognition Elements of Food and Environmental Biosensors: A

Review. *Biosens. Bioelectron.* **2010**, *26*, 1178–1194, doi:10.1016/j.bios.2010.07.033.

113. Alahi, M.E.E.; Mukhopadhyay, S.C. Detection Methodologies for Pathogen and Toxins: A Review. *Sensors (Switzerland)* **2017**, *17*, 1885, doi:10.3390/s17081885.

114. Yasmin, J.; Ahmed, M.R.; Cho, B.-K. Biosensors and Their Applications in Food Safety: A Review. *J. Biosyst. Eng.* **2016**, *41*, 240–254, doi:10.5307/jbe.2016.41.3.240.

115. MarketDataForecast Mycotoxin Testing Market Analysis - Segmented By Type (Aflatoxins, Ochratoxin A, Patulin, Fusarium Toxins), By Technology (HPLC-Based, LC-MS/MS-Based, Immunoassay-Based), By Food And Feed, Tested & Region - Global Forecast To 2027 Available online: https://www.marketdataforecast.com/market-reports/mycotoxin-testing-market.

116. Li, R.; Wen, Y.; Wang, F.; He, P. Recent Advances in Immunoassays and Biosensors for Mycotoxins Detection in Feedstuffs and Foods. *J. Anim. Sci. Biotechnol.* **2021**, *12*, 108, doi:10.1186/s40104-021-00629-4.

117. Fadlalla, M.H.; Ling, S.; Wang, R.; Li, X.; Yuan, J.; Xiao, S.; Wang, K.; Tang, S.; Elsir, H.; Wang, S. Development of ELISA and Lateral Flow Immunoassays for Ochratoxins (OTA and OTB) Detection Based on Monoclonal Antibody. *Front. Cell. Infect. Microbiol.* **2020**, *10*, doi:10.3389/fcimb.2020.00080.

118. Anfossi, L.; Giovannoli, C.; Giraudi, G.; Biagioli, F.; Passini, C.; Baggiani, C. A Lateral Flow Immunoassay for the Rapid Detection of Ochratoxin a in Wine and Grape Must. *J. Agric. Food Chem.* **2012**, *60*, 11491–11497, doi:10.1021/jf3031666.

119. Huang, L.; Tian, S.; Zhao, W.; Liu, K.; Ma, X.; Guo, J. Multiplexed Detection of Biomarkers in Lateral-Flow Immunoassays. *Analyst* **2020**, *145*, 2828–2840, doi:10.1039/c9an02485a.

120. Gordon, J.; Michel, G. Analytical Sensitivity Limits for Lateral Flow Immunoassays. *Clin. Chem.* **2008**, *54*, 1250–1251, doi:10.1373/clinchem.2007.102491.

121. Posthuma-Trumpie, G.A.; Korf, J.; van Amerongen, A. Lateral Flow (Immuno)Assay: Its Strengths, Weaknesses, Opportunities and Threats. A Literature Survey. *Anal. Bioanal. Chem.* **2009**, *393*, 569–582, doi:10.1007/s00216-008-2287-2.

122. Andryukov, B.G. Six Decades of Lateral Flow Immunoassay: From Determining Metabolic Markers to Diagnosing Covid-19. *AIMS Microbiol.* **2020**, *6*, 280–304, doi:10.3934/microbiol.2020018.

123. Neethirajan, S.; Ragavan, V.; Weng, X.; Chand, R. Biosensors for Sustainable Food Engineering: Challenges and Perspectives. *Biosensors* **2018**, *8*, 23, doi:10.3390/bios8010023.

124. Akgönüllü, S.; Denizli, A. Recent Advances in Optical Biosensing Approaches for Biomarkers Detection. *Biosens. Bioelectron. X* **2022**, *12*, 100269, doi:10.1016/j.biosx.2022.100269.

125. Hitabatuma, A.; Pang, Y. hong; Yu, L. hong; Shen, X. fang A Competitive Fluorescence Assay Based on Free-Complementary DNA for Ochratoxin A Detection. *Food Chem.* **2021**, *342*, 128303, doi:10.1016/j.foodchem.2020.128303.

126. Guo, Z.; Tian, J.; Cui, C.; Wang, Y.; Yang, H.; Yuan, M.; Yu, H. A Label-Free Aptasensor for Turn-on Fluorescent Detection of Ochratoxin a Based on SYBR Gold and Single Walled Carbon Nanohorns. *Food Control* **2021**, *123*, 107741, doi:10.1016/j.foodcont.2020.107741.

127. Becheva, Z.R.; Atanasova, M.K.; Ivanov, Y.L.; Godjevargova, T.I. Magnetic Nanoparticle-Based Fluorescence Immunoassay for Determination of Ochratoxin A in Milk. *Food Anal. Methods* **2020**, *13*, 2238–2248, doi:10.1007/s12161-020-01848-7.

128. Chen, R.; Sun, Y.; Huo, B.; Zhao, X.; Huang, H.; Li, S.; Bai, J.; Liang, J.; Gao, Z. A Copper Monosulfide-Nanoparticle-Based Fluorescent Probe for the Sensitive and Specific Detection of Ochratoxin A. *Talanta* **2021**, *222*, 121678, doi:10.1016/j.talanta.2020.121678.

129. Liu, L.; Huang, Q.; Tanveer, Z.I.; Jiang, K.; Zhang, J.; Pan, H.; Luan, L.; Liu, X.; Han, Z.; Wu, Y. "Turn off-on" Fluorescent Sensor Based on Quantum Dots and Self-Assembled Porphyrin for Rapid Detection of Ochratoxin A. *Sensors Actuators, B Chem.* **2020**, *302*, 127212, doi:10.1016/j.snb.2019.127212.

130. Xiong, Z.; Wang, Q.; Xie, Y.; Li, N.; Yun, W.; Yang, L. Simultaneous Detection of Aflatoxin B1 and Ochratoxin A in Food Samples by Dual DNA Tweezers Nanomachine. *Food Chem.* **2021**, *338*, 128122, doi:10.1016/j.foodchem.2020.128122.

131. Wang, Q.; Yang, Q.; Wu, W. Graphene-Based Steganographic Aptasensor for Information Computing and Monitoring Toxins of Biofilm in Food. *Front. Microbiol.* **2020**, *10*, doi:10.3389/fmicb.2019.03139.

132. Bi, X.; Luo, L.; Li, L.; Liu, X.; Chen, B.; You, T. A FRET-Based Aptasensor for Ochratoxin A Detection Using Graphitic Carbon Nitride Quantum Dots and CoOOH Nanosheets as Donor-Acceptor Pair. *Talanta* **2020**, *218*, 121159, doi:10.1016/j.talanta.2020.121159.

133. Tang, Z.; Liu, X.; Su, B.; Chen, Q.; Cao, H.; Yun, Y.; Xu, Y.; Hammock, B.D. Ultrasensitive and Rapid Detection of Ochratoxin A in Agro-Products by a Nanobody-Mediated FRET-Based Immunosensor. *J. Hazard. Mater.* **2020**, *387*, 121678, doi:10.1016/j.jhazmat.2019.121678.

134. Qian, J.; Cui, H.; Lu, X.; Wang, C.; An, K.; Hao, N.; Wang, K. Bi-Color FRET from Two Nano-Donors to a Single Nano-Acceptor: A Universal Aptasensing Platform for Simultaneous Determination of Dual Targets. *Chem. Eng. J.* **2020**, *401*, 126017, doi:10.1016/j.cej.2020.126017.

135. Jiang, Y.Y.; Zhao, X.; Chen, L.J.; Yang, C.; Yin, X.B.; Yan, X.P. Persistent Luminescence Nanorod

Based Luminescence Resonance Energy Transfer Aptasensor for Autofluorescence-Free Detection of Mycotoxin. *Talanta* **2020**, *218*, 121101, doi:10.1016/j.talanta.2020.121101.

136. Akgönüllü, S.; Armutcu, C.; Denizli, A. Molecularly Imprinted Polymer Film Based Plasmonic Sensors for Detection of Ochratoxin A in Dried Fig. *Polym. Bull.* **2021**, doi:10.1007/s00289-021-03699-6.
137. Pereira, R.H.A.; Keijok, W.J.; Prado, A.R.; de Oliveira, J.P.; Guimarães, M.C.C. Rapid and Sensitive Detection of Ochratoxin A Using Antibody-Conjugated Gold Nanoparticles Based on Localized Surface Plasmon Resonance. *Toxicon* **2021**, *199*, 139–144, doi:10.1016/j.toxicon.2021.06.012.
138. Jing, X.; Chang, L.; Shi, L.; Liu, X.; Zhao, Y.; Zhang, W. Au Film-Au@Ag Core-Shell Nanoparticle Structured Surface-Enhanced Raman Spectroscopy Aptasensor for Accurate Ochratoxin A Detection. *ACS Appl. Bio Mater.* **2020**, *3*, 2385–2391, doi:10.1021/acsabm.0c00120.
139. Ding, Y.; Shang, H.; Wang, X.; Chen, L. A SERS-Based Competitive Immunoassay for Highly Sensitive and Specific Detection of Ochratoxin A. *Analyst* **2020**, *145*, 6079–6084, doi:10.1039/d0an01220c.
140. Zhang, W.; Tang, S.; Jin, Y.; Yang, C.; He, L.; Wang, J.; Chen, Y. Multiplex SERS-Based Lateral Flow Immunosensor for the Detection of Major Mycotoxins in Maize Utilizing Dual Raman Labels and Triple Test Lines. *J. Hazard. Mater.* **2020**, *393*, 122348, doi:10.1016/j.jhazmat.2020.122348.
141. Kutsanedzie, F.Y.H.; Agyekum, A.A.; Annavaram, V.; Chen, Q. Signal-Enhanced SERS-Sensors of CAR-PLS and GA-PLS Coupled AgNPs for Ochratoxin A and Aflatoxin B1 Detection. *Food Chem.* **2020**, *315*, 126231, doi:10.1016/j.foodchem.2020.126231.
142. Tian, F.; Zhou, J.; Fu, R.; Cui, Y.; Zhao, Q.; Jiao, B.; He, Y. Multicolor Colorimetric Detection of Ochratoxin A via Structure-Switching Aptamer and Enzyme-Induced Metallization of Gold Nanorods. *Food Chem.* **2020**, *320*, 126607, doi:10.1016/j.foodchem.2020.126607.
143. Zhu, H.; Liu, C.; Liu, X.; Quan, Z.; Liu, W.; Liu, Y. A Multi-Colorimetric Immunosensor for Visual Detection of Ochratoxin A by Mimetic Enzyme Etching of Gold Nanobipyramids. *Microchim. Acta* **2021**, *188*, 62, doi:10.1007/s00604-020-04699-5.
144. Zhang, L.; Zhang, Z.; Tian, Y.; Cui, M.; Huang, B.; Luo, T.; Zhang, S.; Wang, H. Rapid, Simultaneous Detection of Mycotoxins with Smartphone Recognition-Based Immune Microspheres. *Anal. Bioanal. Chem.* **2021**, *413*, 3683–3693, doi:10.1007/s00216-021-03316-5.

145. Suea-Ngam, A.; Deck, L.T.; Howes, P.D.; deMello, A.J. An Ultrasensitive Non-Noble Metal Colorimetric Assay Using Starch-Iodide Complexation for Ochratoxin A Detection. *Anal. Chim. Acta* **2020**, *1135*, 29–37, doi:10.1016/j.aca.2020.08.028.

146. Wu, Y.; Zhou, Y.; Huang, H.; Chen, X.; Leng, Y.; Lai, W.; Huang, X.; Xiong, Y. Engineered Gold Nanoparticles as Multicolor Labels for Simultaneous Multi-Mycotoxin Detection on the Immunochromatographic Test Strip Nanosensor. *Sensors Actuators B Chem.* **2020**, *316*, 128107, doi:10.1016/j.snb.2020.128107.

147. Hao, L.; Chen, J.; Chen, X.; Ma, T.; Cai, X.; Duan, H.; Leng, Y.; Huang, X.; Xiong, Y. A Novel Magneto-Gold Nanohybrid-Enhanced Lateral Flow Immunoassay for Ultrasensitive and Rapid Detection of Ochratoxin A in Grape Juice. *Food Chem.* **2021**, *336*, 127710, doi:10.1016/j.foodchem.2020.127710.

148. Alizadeh, N.; Hashemi, J.; Shahdost-Fard, F. Spectrofluorimetric Study of the Complexation of Ochratoxin A and Cu2+: Towards the Hybrid Fluorimetric Sensor and Visual Detection of Ochratoxin A in Wheat Flour Samples from Farm to Fork. *Food Chem.* **2021**, *350*, 129204, doi:10.1016/j.foodchem.2021.129204.

149. Cheng, Y.; Liu, L.; Liu, H.; Xu, L.; Kuang, H. Rapid and Sensitive Detection of Ochratoxin A in Rice Flour Using a Fluorescent Microsphere Immunochromatographic Test Strip Assay. *Food Agric. Immunol.* **2020**, *31*, 563–574, doi:10.1080/09540105.2020.1745157.

150. Zhou, J.; Yang, Q.; Liang, C.; Chen, Y.; Zhang, X.; Liu, Z.; Wang, A. Detection of Ochratoxin A by Quantum Dots–Based Fluorescent Immunochromatographic Assay. *Anal. Bioanal. Chem.* **2021**, *413*, 183–192, doi:10.1007/s00216-020-02990-1.

151. Zhu, H.; Cai, Y.; Qileng, A.; Quan, Z.; Zeng, W.; He, K.; Liu, Y. Template-Assisted Cu2O@Fe(OH)3 Yolk-Shell Nanocages as Biomimetic Peroxidase: A Multi-Colorimetry and Ratiometric Fluorescence Separated-Type Immunosensor for the Detection of Ochratoxin A. *J. Hazard. Mater.* **2021**, *411*, 125090, doi:10.1016/j.jhazmat.2021.125090.

152. Zangheri, M.; Di Nardo, F.; Calabria, D.; Marchegiani, E.; Anfossi, L.; Guardigli, M.; Mirasoli, M.; Baggiani, C.; Roda, A. Smartphone Biosensor for Point-of-Need Chemiluminescence Detection of Ochratoxin A in Wine and Coffee. *Anal. Chim. Acta* **2021**, *1163*, 338515, doi:10.1016/j.aca.2021.338515.

153. Lu, L.; Yuan, W.; Xiong, Q.; Wang, M.; Liu, Y.; Cao, M.; Xiong, X. One-Step Grain Pretreatment for Ochratoxin A Detection Based on Bipolar Electrode-Electrochemiluminescence Biosensor. *Anal. Chim. Acta* **2021**, *1141*, 83–90, doi:10.1016/j.aca.2020.10.035.

154. Zhang, X.; Zhi, H.; Zhu, M.; Wang, F.; Meng, H.; Feng, L. Electrochemical/Visual Dual-Readout Aptasensor for Ochratoxin A Detection Integrated into a Miniaturized Paper-Based Analytical Device. *Biosens. Bioelectron.* **2021**, *180*, 113146, doi:10.1016/j.bios.2021.113146.

155. Hao, N.; Dai, Z.; Meng, X.; Hua, R.; Lu, J.; Wang, K. A Portable Solar-Driven Ratiometric Photo-Electrochromic Visualization Biosensor for Detection of Ochratoxin A. *Sensors Actuators B Chem.* **2020**, *306*, 127594, doi:10.1016/j.snb.2019.127594.

156. Tsia, K.K. *Understanding Biophotonics - Fundamentals, Advances, and Applications*; Tsia, K., Ed.; 1st Editio.; Jenny Stanford Publishing: New York, NY, 2016; ISBN 9780429168314.

157. Almendral Parra, M.J.; Paradinas, S.S. Spectroscopic Techniques Basedon the Use of Gold Nanoparticles. In *Comprehensive Analytical Chemistry*; 2014; Vol. 66, pp. 477–527.

158. Bhattacharya, K.; Bernasconi, L.; Picard, D. Luminescence Resonance Energy Transfer between Genetically Encoded Donor and Acceptor for Protein-Protein Interaction Studies in the Molecular Chaperone HSP70/HSP90 Complexes. *Sci. Rep.* **2018**, *8*, 2801, doi:10.1038/s41598-018-21210-6.

159. Zalevsky, Z.; Abdulhalim, I. Plasmonics. In *Integrated Nanophotonic Devices*; Elsevier, 2014; pp. 179–245.

160. Peixoto de Almeida, M.; Pereira, E.; Baptista, P.; Gomes, I.; Figueiredo, S.; Soares, L.; Franco, R. Gold Nanoparticles as (Bio)Chemical Sensors. In *Comprehensive Analytical Chemistry*; 2014; Vol. 66, pp. 529–567.

161. Ravindran, N.; Kumar, S.; M, Y.; S, R.; C A, M.; Thirunavookarasu S, N.; C K, S. Recent Advances in Surface Plasmon Resonance (SPR) Biosensors for Food Analysis: A Review. *Crit. Rev. Food Sci. Nutr.* **2021**, 1–23, doi:10.1080/10408398.2021.1958745.

162. Langer, J.; de Aberasturi, D.J.; Aizpurua, J.; Alvarez-Puebla, R.A.; Auguié, B.; Baumberg, J.J.; Bazan, G.C.; Bell, S.E.J.; Boisen, A.; Brolo, A.G.; et al. Present and Future of Surface-Enhanced Raman Scattering. *ACS Nano* **2020**, *14*, 28–117, doi:10.1021/acsnano.9b04224.

163. Rycenga, M.; Camargo, P.H.C.; Li, W.; Moran, C.H.; Xia, Y. Understanding the SERS Effects of Single Silver Nanoparticles and Their Dimers, One at a Time. *J. Phys. Chem. Lett.* **2010**, *1*, 696–703, doi:10.1021/jz900286a.

164. Uskoković-Marković, S.; Kuntić, V.; Bajuk-Bogdanović, D.; Holclajtner-Antunović, I. Surface-Enhanced Raman Scattering (SERS) Biochemical Applications. In *Encyclopedia of Spectroscopy and Spectrometry*; Elsevier, 2017; pp. 383–388 ISBN 9780128032244.

165. Rodriguez, R.S.; Szlag, V.M.; Reineke, T.M.; Haynes, C.L. Multiplex Surface-Enhanced Raman

Scattering Detection of Deoxynivalenol and Ochratoxin A with a Linear Polymer Affinity Agent. *Mater. Adv.* **2020**, *1*, 3256–3266, doi:10.1039/d0ma00608d.

166. Huang, D.; Chen, J.; Ding, L.; Guo, L.; Kannan, P.; Luo, F.; Qiu, B.; Lin, Z. Core-Satellite Assemblies and Exonuclease Assisted Double Amplification Strategy for Ultrasensitive SERS Detection of Biotoxin. *Anal. Chim. Acta* **2020**, *1110*, 56–63, doi:10.1016/j.aca.2020.02.058.
167. Huang, X. Bin; Wu, S.H.; Hu, H.C.; Sun, J.J. AuNanostar@4-MBA@Au Core-Shell Nanostructure Coupled with Exonuclease III-Assisted Cycling Amplification for Ultrasensitive SERS Detection of Ochratoxin A. *ACS Sensors* **2020**, *5*, 2636–2643, doi:10.1021/acssensors.0c01162.
168. Wang, H.; Rao, H.; Luo, M.; Xue, X.; Xue, Z.; Lu, X. Noble Metal Nanoparticles Growth-Based Colorimetric Strategies: From Monocolorimetric to Multicolorimetric Sensors. *Coord. Chem. Rev.* **2019**, *398*, 113003, doi:10.1016/j.ccr.2019.06.020.
169. Alberti, G.; Zanoni, C.; Magnaghi, L.R.; Biesuz, R. Disposable and Low-Cost Colorimetric Sensors for Environmental Analysis. *Int. J. Environ. Res. Public Health* **2020**, *17*, 8331, doi:10.3390/ijerph17228331.
170. Mauriz, E. Clinical Applications of Visual Plasmonic Colorimetric Sensing. *Sensors (Switzerland)* **2020**, *20*, 1–31, doi:10.3390/s20216214.
171. Li, G. Biosensing Technologies for Protein Assay. In *Nano-inspired Biosensors for Protein Assay with Clinical Applications*; Elsevier, 2018; pp. 313–330 ISBN 9780128150535.
172. Martínez-Periñán, E.; Gutiérrez-Sánchez, C.; García-Mendiola, T.; Lorenzo, E. Electrochemiluminescence Biosensors Using Screen-Printed Electrodes. *Biosensors* **2020**, *10*, 118, doi:10.3390/bios10090118.
173. Kim, M.-G.; Park, J.-H.; Byun, J.Y. LSPR-Based High Sensitivity Aptamer Sensor Using Intercalation Agent 2018.
174. Kim, M.G.; Lee, B.B.; Park, J.H.; Byun, J.Y. A Reusable Optical Fiber Aptasensor Based on Photo-Thermal Effect 2018.
175. Lee, B.; Park, J.H.; Byun, J.Y.; Kim, J.H.; Kim, M.G. An Optical Fiber-Based LSPR Aptasensor for Simple and Rapid in-Situ Detection of Ochratoxin A. *Biosens. Bioelectron.* **2018**, *102*, 504–509, doi:10.1016/j.bios.2017.11.062.
176. Yingju, L.; Ying, L.; Jie, W.; Haoran, S.; Huaming, C. Dual-Mode Separation Type Immunosensor Based on Enzyme-Induced Biological Etching and Preparation Method Thereof 2021.
177. Wei, J.; Chen, H.; Chen, H.; Cui, Y.; Qileng, A.; Qin, W.; Liu, W.; Liu, Y. Multifunctional Peroxidase-Encapsulated Nanoliposomes: Bioetching-Induced Photoelectrometric and Colorimetric

Immunoassay for Broad-Spectrum Detection of Ochratoxins. *ACS Appl. Mater. Interfaces* **2019**, *11*, 23832–23839, doi:10.1021/acsami.9b04136.

178. Righetti, L.; Paglia, G.; Galaverna, G.; Dall'Asta, C. Recent Advances and Future Challenges in Modified Mycotoxin Analysis: Why HRMS Has Become a Key Instrument in Food Contaminant Research. *Toxins (Basel).* **2016**, *8*, 361, doi:10.3390/toxins8120361.
179. Freire, L.; Sant'Ana, A.S. Modified Mycotoxins: An Updated Review on Their Formation, Detection, Occurrence, and Toxic Effects. *Food Chem. Toxicol.* **2018**, *111*, 189–205, doi:10.1016/j.fct.2017.11.021.
180. Morales, M.A.; Halpern, J.M. Guide to Selecting a Biorecognition Element for Biosensors. *Bioconjug. Chem.* **2018**, *29*, 3231–3239, doi:10.1021/acs.bioconjchem.8b00592.
181. Turner, N.W.; Subrahmanyam, S.; Piletsky, S.A. Analytical Methods for Determination of Mycotoxins: A Review. *Anal. Chim. Acta* **2009**, *632*, 168–180, doi:10.1016/j.aca.2008.11.010.
182. Xu, L.; Zhang, Z.; Zhang, Q.; Li, P. Mycotoxin Determination in Foods Using Advanced Sensors Based on Antibodies or Aptamers. *Toxins (Basel).* **2016**, *8*, 239, doi:10.3390/toxins8080239.
183. Rhouati, A.; Bulbul, G.; Latif, U.; Hayat, A.; Li, Z.H.; Marty, J.L. Nano-Aptasensing in Mycotoxin Analysis: Recent Updates and Progress. *Toxins (Basel).* **2017**, *9*, 349, doi:10.3390/toxins9110349.
184. Zhang, C.; Jiang, C.; Lan, L.; Ping, J.; Ye, Z.; Ying, Y. Nanomaterial-Based Biosensors for Agro-Product Safety. *TrAC - Trends Anal. Chem.* **2021**, *143*, 116369, doi:10.1016/j.trac.2021.116369.
185. Mahmoudpour, M.; Ezzati Nazhad Dolatabadi, J.; Torbati, M.; Pirpour Tazehkand, A.; Homayouni-Rad, A.; de la Guardia, M. Nanomaterials and New Biorecognition Molecules Based Surface Plasmon Resonance Biosensors for Mycotoxin Detection. *Biosens. Bioelectron.* **2019**, *143*, 111603, doi:10.1016/j.bios.2019.111603.
186. Xiong, Y.; Li, W.; Wen, Q.; Xu, D.; Ren, J.; Lin, Q. Aptamer-Engineered Nanomaterials to Aid in Mycotoxin Determination. *Food Control* **2022**, *135*, 108661, doi:10.1016/j.foodcont.2021.108661.
187. Barbosa, A.I.; Reis, N.M. A Critical Insight into the Development Pipeline of Microfluidic Immunoassay Devices for the Sensitive Quantitation of Protein Biomarkers at the Point of Care. *Analyst* **2017**, *142*, 858–882, doi:10.1039/c6an02445a.
188. Barbosa, A.I.; Castanheira, A.P.; Reis, N.M. Sensitive Optical Detection of Clinically Relevant Biomarkers in Affordable Microfluidic Devices: Overcoming Substrate Diffusion Limitations.

Sensors Actuators, B Chem. **2018**, *258*, 313–320, doi:10.1016/j.snb.2017.11.086.

189. Barbosa, A.I.; Edwards, A.D.; Reis, N.M. Antibody Surface Coverage Drives Matrix Interference in Microfluidic Capillary Immunoassays. *ACS Sensors* **2021**, acssensors.1c00704, doi:10.1021/acssensors.1c00704.
190. Castanheira, A.P.; Barbosa, A.I.; Edwards, A.D.; Reis, N.M. Multiplexed Femtomolar Quantitation of Human Cytokines in a Fluoropolymer Microcapillary Film. *Analyst* **2015**, *140*, 5609–5618, doi:10.1039/c5an00238a.
191. Kim, Y.; Gonzales, J.; Zheng, Y. Sensitivity-Enhancing Strategies in Optical Biosensing. *Small* **2021**, *17*, 2004988, doi:10.1002/smll.202004988.
192. Sang, S.; Wang, Y.; Feng, Q.; Wei, Y.; Ji, J.; Zhang, W. Progress of New Label-Free Techniques for Biosensors: A Review. *Crit. Rev. Biotechnol.* **2016**, *36*, 465–481, doi:10.3109/07388551.2014.991270.
193. Guo, L.; Jackman, J.A.; Yang, H.H.; Chen, P.; Cho, N.J.; Kim, D.H. Strategies for Enhancing the Sensitivity of Plasmonic Nanosensors. *Nano Today* **2015**, *10*, 213–239, doi:10.1016/j.nantod.2015.02.007.
194. Justino, C.I.L.; Duarte, A.C.; Rocha-Santos, T.A.P. Recent Progress in Biosensors for Environmental Monitoring: A Review. *Sensors (Basel).* **2017**, *17*, doi:10.3390/S17122918.
195. Kim, J.; Campbell, A.S.; de Ávila, B.E.F.; Wang, J. Wearable Biosensors for Healthcare Monitoring. *Nat. Biotechnol. 2019 374* **2019**, *37*, 389–406, doi:10.1038/s41587-019-0045-y.
196. Kawamura, A.; Miyata, T. Biosensors. *Biomater. Nanoarchitectonics* **2016**, 157–176, doi:10.1016/B978-0-323-37127-8.00010-8.
197. Bhalla, N.; Jolly, P.; Formisano, N.; Estrela, P. Introduction to Biosensors. *Essays Biochem.* **2016**, *60*, 1–8, doi:10.1042/EBC20150001.
198. Damborský, P.; Švitel, J.; Katrlík, J. Optical Biosensors. *Essays Biochem.* **2016**, *60*, 91–100, doi:10.1042/EBC20150010.
199. Hutter, E.; Fendler, J.H. Exploitation of Localized Surface Plasmon Resonance. *Adv. Mater.* **2004**, *16*, 1685–1706, doi:10.1002/adma.200400271.
200. Xiao, L.; Youji, L.; Feitai, C.; Peng, X.; Ming, L. Facile Synthesis of Mesoporous Titanium Dioxide Doped by Ag-Coated Graphene with Enhanced Visible-Light Photocatalytic Performance for Methylene Blue Degradation. *RSC Adv.* **2017**, *7*, 25314–25324, doi:10.1039/c7ra02198d.
201. Toudert, J.; Simonot, L.; Camelio, S.; Babonneau, D. Advanced Optical Effective Medium Modeling for a Single Layer of Polydisperse Ellipsoidal Nanoparticles Embedded in a Homogeneous

Dielectric Medium: Surface Plasmon Resonances. *Phys. Rev. B - Condens. Matter Mater. Phys.* **2012**, *86*, doi:10.1103/PhysRevB.86.045415.

202. Deng, Y.; Cao, G.; Wu, Y.; Zhou, X.; Liao, W. Theoretical Description of Dynamic Transmission Characteristics in MDM Waveguide Aperture-Side-Coupled with Ring Cavity. *Plasmonics* **2015**, *10*, 1537–1543, doi:10.1007/s11468-015-9971-9.
203. Chen, F.; Yang, W. Plasmonic Induced Reflection Based on Al2O3 Nanoslit Side Coupled with Silicon Nanodisk Resonator. *Results Opt.* **2021**, *5*, 100126, doi:10.1016/j.rio.2021.100126.
204. Pereira, R.M.S.; Borges, J.; Peres, F.C.R.; Pereira, P.A.S.; Smirnov, G. V.; Vaz, F.; Cavaleiro, A.; Vasilevskiy, M.I. Effect of Clustering on the Surface Plasmon Band in Thin Films of Metallic Nanoparticles. *J. Nanophotonics* **2014**, *9*, 093796, doi:10.1117/1.jnp.9.093796.
205. Borges, J.; Pereira, R.M.S.; Rodrigues, M.S.; Kubart, T.; Kumar, S.; Leifer, K.; Cavaleiro, A.; Polcar, T.; Vasilevskiy, M.I.; Vaz, F. Broadband Optical Absorption Caused by the Plasmonic Response of Coalesced Au Nanoparticles Embedded in a TiO_2 Matrix. *J. Phys. Chem. C* **2016**, *120*, 16931–16945, doi:10.1021/acs.jpcc.6b03684.
206. Petryayeva, E.; Krull, U.J. Localized Surface Plasmon Resonance: Nanostructures, Bioassays and Biosensing-A Review. *Anal. Chim. Acta* **2011**, *706*, 8–24, doi:10.1016/j.aca.2011.08.020.
207. Chen, H.; Kou, X.; Yang, Z.; Ni, W.; Wang, J. Shape- and Size-Dependent Refractive Index Sensitivity of Gold Nanoparticles. *Langmuir* **2008**, *24*, 5233–5237, doi:10.1021/la800305j.
208. Chen, H.; Chen, Z.; Yang, H.; Wen, L.; Yi, Z.; Zhou, Z.; Dai, B.; Zhang, J.; Wu, X.; Wu, P. Multi-Mode Surface Plasmon Resonance Absorber Based on Dart-Type Single-Layer Grapheme. *RSC Adv.* **2022**, *12*, 7821–7829, doi:10.1039/d2ra00611a.
209. Wu, X.; Zheng, Y.; Luo, Y.; Zhang, J.; Yi, Z.; Wu, X.; Cheng, S.; Yang, W.; Yu, Y.; Wu, P. A Four-Band and Polarization-Independent BDS-Based Tunable Absorber with High Refractive Index Sensitivity. *Phys. Chem. Chem. Phys.* **2021**, *23*, 26864–26873, doi:10.1039/d1cp04568g.
210. Jain, S.; Paliwal, A.; Gupta, V.; Tomar, M. Refractive Index Tuning of SiO2 for Long Range Surface Plasmon Resonance Based Biosensor. *Biosens. Bioelectron.* **2020**, *168*, 112508, doi:10.1016/j.bios.2020.112508.
211. Jia, S.; Bian, C.; Sun, J.; Tong, J.; Xia, S. A Wavelength-Modulated Localized Surface Plasmon Resonance (LSPR) Optical Fiber Sensor for Sensitive Detection of Mercury(II) Ion by Gold Nanoparticles-DNA Conjugates. *Biosens. Bioelectron.* **2018**, *114*, 15–21, doi:10.1016/j.bios.2018.05.004.
212. Mayer, K.M.; Hafner, J.H. Localized Surface Plasmon Resonance Sensors. *Chem. Rev.* **2011**,

111, 3828–3857, doi:10.1021/CR100313V.

213. Haes, A.J.; Van Duyne, R.P. Preliminary Studies and Potential Applications of Localized Surface Plasmon Resonance Spectroscopy in Medical Diagnostics. *Expert Rev. Mol. Diagn.* **2004**, *4*, 527–537, doi:10.1586/14737159.4.4.527.

214. Proença, M.; Borges, J.; Rodrigues, M.S.; Domingues, R.P.; Dias, J.P.; Trigueiro, J.; Bundaleski, N.; Teodoro, O.M.N.D.; Vaz, F. Development of Au/CuO Nanoplasmonic Thin Films for Sensing Applications. *Surf. Coatings Technol.* **2018**, *343*, 178–185, doi:10.1016/j.surfcoat.2017.08.033.

215. Lopez, G.A.; Estevez, M.C.; Soler, M.; Lechuga, L.M. Recent Advances in Nanoplasmonic Biosensors: Applications and Lab-on-a-Chip Integration. *Nanophotonics* **2017**, *6*, 123–136, doi:10.1515/nanoph-2016-0101.

216. Aćimović, S.S.; Ortega, M.A.; Sanz, V.; Berthelot, J.; Garcia-Cordero, J.L.; Renger, J.; Maerkl, S.J.; Kreuzer, M.P.; Quidant, R. LSPR Chip for Parallel, Rapid, and Sensitive Detection of Cancer Markers in Serum. *Nano Lett.* **2014**, *14*, 2636–2641, doi:10.1021/nl500574n.

217. Lee, W.; Shaban, S.M.; Pyun, D.G.; Kim, D.H. Solid-Phase Colorimetric Apta-Biosensor for Thrombin Detection. *Thin Solid Films* **2019**, *686*, 137428, doi:10.1016/j.tsf.2019.137428.

218. Kim, J.; Moon, B.S.; Hwang, E.; Shaban, S.; Lee, W.; Pyun, D.G.; Lee, D.H.; Kim, D.H. Solid-State Colorimetric Polydiacetylene Liposome Biosensor Sensitized by Gold Nanoparticles. *Analyst* **2021**, *146*, 1682–1688, doi:10.1039/d0an02375b.

219. Costa, D.; Rodrigues, M.S.; Roiban, L.; Aouine, M.; Epicier, T.; Steyer, P.; Alves, E.; Barradas, N.P.; Borges, J.; Vaz, F. In-Situ Annealing Transmission Electron Microscopy of Plasmonic Thin Films Composed of Bimetallic Au–Ag Nanoparticles Dispersed in a TiO_2 Matrix. *Vacuum* **2021**, *193*, 110511, doi:10.1016/j.vacuum.2021.110511.

220. Pereira-Silva, P.; Borges, J.; Rodrigues, M.S.M.S.; Oliveira, J.C.J.C.; Alves, E.; Barradas, N.P.N.P.; Dias, J.P.J.P.; Cavaleiro, A.; Vaz, F. Nanocomposite Au-ZnO Thin Films: Influence of Gold Concentration and Thermal Annealing on the Microstructure and Plasmonic Response. *Surf. Coatings Technol.* **2020**, *385*, 125379, doi:10.1016/j.surfcoat.2020.125379.

221. Meira, D.I.; Domingues, R.P.; Rodrigues, M.S.; Alves, E.; Barradas, N.P.; Borges, J.; Vaz, F. Thin Films of Au-Al2O3 for Plasmonic Sensing. *Appl. Surf. Sci.* **2020**, *500*, 144035, doi:10.1016/j.apsusc.2019.144035.

222. Howarth, M.; Chinnapen, D.J.F.; Gerrow, K.; Dorrestein, P.C.; Grandy, M.R.; Kelleher, N.L.; El-Husseini, A.; Ting, A.Y. A Monovalent Streptavidin with a Single Femtomolar Biotin Binding Site.

Nat. Methods **2006**, *3*, 267–273, doi:10.1038/nmeth861.

223. Dundas, C.M.; Demonte, D.; Park, S. Streptavidin-Biotin Technology: Improvements and Innovations in Chemical and Biological Applications. *Appl. Microbiol. Biotechnol.* **2013**, *97*, 9343–9353, doi:10.1007/s00253-013-5232-z.
224. Wilchek, M.; Bayer, E.A.; Livnah, O. Essentials of Biorecognition: The (Strept)Avidin-Biotin System as a Model for Protein-Protein and Protein-Ligand Interaction. *Immunol. Lett.* **2006**, *103*, 27–32, doi:10.1016/j.imlet.2005.10.022.
225. Kim, H.M.; Jin, S.M.; Lee, S.K.; Kim, M.G.; Shin, Y.B. Detection of Biomolecular Binding Through Enhancement of Localized Surface Plasmon Resonance (LSPR) by Gold Nanoparticles. *Sensors (Basel).* **2009**, *9*, 2334–2344, doi:10.3390/S90402334.
226. Pol, L.; Eckstein, C.; Acosta, L.K.; Xifré-Pérez, E.; Ferré-Borrull, J.; Marsal, L.F. Real-Time Monitoring of Biotinylated Molecules Detection Dynamics in Nanoporous Anodic Alumina for Bio-Sensing. *Nanomaterials* **2019**, *9*, doi:10.3390/nano9030478.
227. Heidari, A.; Yoon, Y.J.; Park, W.T.; Su, P.C.; Miao, J.; Ming Lin, J.T.; Park, M.K. Biotin-Streptavidin Binding Interactions of Dielectric Filled Silicon Bulk Acoustic Resonators for Smart Label-Free Biochemical Sensor Applications. *Sensors (Switzerland)* **2014**, *14*, 4585–4598, doi:10.3390/s140304585.
228. Hermanson, G.T. Enzyme Modification and Conjugation. In *Bioconjugate Techniques*; Elsevier, 2013; pp. 951–957.
229. Mouse TNF Alpha Uncoated ELISA - Invitrogen by Thermo Fischer Scientific Available online: https://bit.ly/3MGt0Zu (accessed on 3 May 2021).
230. Borges, J.; Rodrigues, M.S.; Lopes, C.; Costa, D.; Couto, F.M.; Kubart, T.; Martins, B.; Duarte, N.; Dias, J.P.; Cavaleiro, A.; et al. Thin Films Composed of Ag Nanoclusters Dispersed in TiO_2: Influence of Composition and Thermal Annealing on the Microstructure and Physical Responses. *Appl. Surf. Sci.* **2015**, *358*, 595–604, doi:10.1016/j.apsusc.2015.08.148.
231. Domingues, R.P.; Rodrigues, M.S.; Proença, M.; Costa, D.; Alves, E.; Barradas, N.P.; Oliveira, F.J.; Silva, R.F.; Borges, J.; Vaz, F. Thin Films Composed of Au Nanoparticles Embedded in AlN: Influence of Metal Concentration and Thermal Annealing on the LSPR Band. *Vacuum* **2018**, *157*, 414–421, doi:10.1016/j.vacuum.2018.09.013.
232. Barradas, N.P.; Marriott, P.K.; Jeynes, C.; Webb, R.P. The RBS Data Furnace: Simulated Annealing. *Nucl. Instruments Methods Phys. Res. Sect. B Beam Interact. with Mater. Atoms* **1998**, *136–138*, 1157–1162, doi:10.1016/S0168-583X(97)00808-2.

233. Barradas, N.P.; Pascual-Izarra, C. Double Scattering in RBS Analysis of PtSi Thin Films on Si. *Nucl. Instruments Methods Phys. Res. Sect. B Beam Interact. with Mater. Atoms* **2005**, *228*, 378–382, doi:10.1016/j.nimb.2004.10.074.

234. Barradas, N.P.; Reis, M.A. Accurate Calculation of Pileup Effects in PIXE Spectra from First Principles. *X-Ray Spectrom.* **2006**, *35*, 232–237, doi:10.1002/xrs.903.

235. Kim, W.J.; Kim, S.; Lee, B.S.; Kim, A.; Ah, C.S.; Huh, C.; Sung, G.Y.; Yun, W.S. Enhanced Protein Immobilization Efficiency on a TiO_2 Surface Modified with a Hydroxyl Functional Group. *Langmuir* **2009**, *25*, 11692–11697, doi:10.1021/la901615e.

236. Krishnan, A.; Liu, Y.H.; Cha, P.; Woodward, R.; Allara, D.; Vogler, E.A. An Evaluation of Methods for Contact Angle Measurement. *Colloids Surfaces B Biointerfaces* **2005**, *43*, 95–98, doi:10.1016/j.colsurfb.2005.04.003.

237. Rodrigues, M.S.; Borges, J.; Proença, M.; Pedrosa, P.; Martin, N.; Romanyuk, K.; Kholkin, A.L.; Vaz, F. Nanoplasmonic Response of Porous Au-TiO_2 Thin Films Prepared by Oblique Angle Deposition. *Nanotechnology* **2019**, *30*, 225701, doi:10.1088/1361-6528/ab068e.

238. Rodrigues, M.S.; Pereira, R.M.S.; Vasilevskiy, M.I.; Borges, J.; Vaz, F. NANOPTICS: In-Depth Analysis of NANomaterials for OPTICal Localized Surface Plasmon Resonance Sensing. *SoftwareX* **2020**, *12*, 100522, doi:10.1016/j.softx.2020.100522.

239. Koneti, S.; Borges, J.; Roiban, L.; Rodrigues, M.S.; Martin, N.; Epicier, T.; Vaz, F.; Steyer, P. Electron Tomography of Plasmonic Au Nanoparticles Dispersed in a TiO_2 Dielectric Matrix. *ACS Appl. Mater. Interfaces* **2018**, *10*, 42882–42890, doi:10.1021/acsami.8b16436.

240. Costa, D.; Oliveira, J.; Rodrigues, M.S.; Borges, J.; Moura, C.; Sampaio, P.; Vaz, F. Development of Biocompatible Plasmonic Thin Films Composed of Noble Metal Nanoparticles Embedded in a Dielectric Matrix to Enhance Raman Signals. *Appl. Surf. Sci.* **2019**, *496*, 143701, doi:10.1016/j.apsusc.2019.143701.

241. Borges, J.; Costa, D.; Antunes, E.; Lopes, C.; Rodrigues, M.S.; Apreutesei, M.; Alves, E.; Barradas, N.P.; Pedrosa, P.; Moura, C.; et al. Biological Behaviour of Thin Films Consisting of Au Nanoparticles Dispersed in a TiO_2 Dielectric Matrix. *Vacuum* **2015**, *122*, 360–368, doi:10.1016/j.vacuum.2015.03.036.

242. Sotnikov, D. V.; Berlina, A.N.; Ivanov, V.S.; Zherdev, A. V.; Dzantiev, B.B. Adsorption of Proteins on Gold Nanoparticles: One or More Layers? *Colloids Surfaces B Biointerfaces* **2019**, *173*, 557–563, doi:10.1016/j.colsurfb.2018.10.025.

243. Vesel, A.; Mozetic, M. New Developments in Surface Functionalization of Polymers Using

Controlled Plasma Treatments. *J. Phys. D. Appl. Phys.* **2017**, *50*, 293001, doi:10.1088/1361-6463/aa748a.

244. Huhtamäki, T.; Tian, X.; Korhonen, J.T.; Ras, R.H.A. Surface-Wetting Characterization Using Contact-Angle Measurements. *Nat. Protoc.* **2018**, *13*, 1521–1538, doi:10.1038/s41596-018-0003-z.
245. Vogler, E.A. Structure and Reactivity of Water at Biomaterial Surfaces. *Adv. Colloid Interface Sci.* **1998**, *74*, 69–117, doi:10.1016/S0001-8686(97)00040-7.
246. Lakshmipriya, T.; Gopinath, S.C.B.; Tang, T.H. Biotin-Streptavidin Competition Mediates Sensitive Detection of Biomolecules in Enzyme Linked Immunosorbent Assay. *PLoS One* **2016**, *11*, doi:10.1371/journal.pone.0151153.
247. Haes, A.J.; Van Duyne, R.P. A Unified View of Propagating and Localized Surface Plasmon Resonance Biosensors. *Anal. Bioanal. Chem.* **2004**, *379*, 920–930, doi:10.1007/s00216-004-2708-9.
248. Hegde, H.R.; Chidangil, S.; Sinha, R.K. Refractive Index Sensitivity of Au Nanostructures in Solution and on the Substrate. *J. Mater. Sci. Mater. Electron. 2021* **2021**, 1–14, doi:10.1007/S10854-021-07593-9.
249. Martinsson, E.; Sepulveda, B.; Chen, P.; Elfwing, A.; Liedberg, B.; Aili, D. Optimizing the Refractive Index Sensitivity of Plasmonically Coupled Gold Nanoparticles. *Plasmonics* **2014**, *9*, 773–780, doi:10.1007/s11468-013-9659-y.
250. Focsan, M.; Campu, A.; Craciun, A.M.; Potara, M.; Leordean, C.; Maniu, D.; Astilean, S. A Simple and Efficient Design to Improve the Detection of Biotin-Streptavidin Interaction with Plasmonic Nanobiosensors. *Biosens. Bioelectron.* **2016**, *86*, 728–735, doi:10.1016/j.bios.2016.07.054.
251. Moyo, M.; Okonkwo, J.O.; Agyei, N.M. Recent Advances in Immobilization Strategies in Biomaterial Nanotechnology for Biosensors. *Bioeng. Nanomater.* **2013**, 33–64, doi:10.1201/b15403-7.
252. Yamaguchi, H.; Miyazaki, M. Enzyme-Immobilized Microfluidic Devices for Biomolecule Detection. *TrAC - Trends Anal. Chem.* **2023**, *159*, 116908, doi:10.1016/j.trac.2022.116908.
253. Vashist, S.K. Effect of Antibody Modifications on Its Biomolecular Binding as Determined by Surface Plasmon Resonance. *Anal. Biochem.* **2012**, *421*, 336–338, doi:10.1016/j.ab.2011.10.036.
254. Meira, D.I.; Barbosa, A.I.; Borges, J.; Reis, R.L.; Correlo, V.M.; Vaz, F. Recent Advances in Nanomaterial-Based Optical Biosensors for Food Safety Applications: Ochratoxin-A Detection, as Case Study. *Crit. Rev. Food Sci. Nutr.* **2023**, 1–43, doi:10.1080/10408398.2023.2168248.

255. Soler, M.; Lechuga, L.M. Principles, Technologies, and Applications of Plasmonic Biosensors. *J. Appl. Phys.* **2021**, *129*, 111102, doi:10.1063/5.0042811.

256. Soler, M.; Lechuga, L.M. Biochemistry Strategies for Label-Free Optical Sensor Biofunctionalization: Advances towards Real Applicability. *Anal. Bioanal. Chem.* **2022**, *414*, 5071–5085, doi:10.1007/s00216-021-03751-4.

257. Rusmini, F.; Zhong, Z.; Feijen, J. Protein Immobilization Strategies for Protein Biochips. *Biomacromolecules* **2007**, *8*, 1775–1789, doi:10.1021/bm061197b.

258. Kausaite-Minkstimiene, A.; Ramanaviciene, A.; Kirlyte, J.; Ramanavicius, A. Comparative Study of Random and Oriented Antibody Immobilization Techniques on the Binding Capacity of Immunosensor. *Anal. Chem.* **2010**, *82*, 6401–6408, doi:10.1021/ac100468k.

259. Gao, S.; Guisán, J.M.; Rocha-Martin, J. Oriented Immobilization of Antibodies onto Sensing Platforms - A Critical Review. *Anal. Chim. Acta* **2022**, *1189*, 338907, doi:10.1016/j.aca.2021.338907.

260. Spahn, C.; Minteer, S. Enzyme Immobilization in Biotechnology. *Recent Patents Eng.* **2008**, *2*, 195–200, doi:10.2174/187221208786306333.

261. Taheri, R.A.; Rezayan, A.H.; Rahimi, F.; Mohammadnejad, J.; Kamali, M. Comparison of Antibody Immobilization Strategies in Detection of Vibrio Cholerae by Surface Plasmon Resonance . *Biointerphases* **2016**, *11*, doi:10.1116/1.4971270.

262. Poghossian, A.; Weil, M.; Cherstvy, A.G.; Schöning, M.J. Electrical Monitoring of Polyelectrolyte Multilayer Formation by Means of Capacitive Field-Effect Devices. *Anal. Bioanal. Chem.* **2013**, *405*, 6425–6436, doi:10.1007/s00216-013-6951-9.

263. Cherstvy, A.G. Electrostatics and Charge Regulation in Polyelectrolyte Multilayered Assembly. *J. Phys. Chem. B* **2014**, *118*, 4552–4560, doi:10.1021/jp502460v.

264. Hussan, K.P.S.; Moidu, H.H.; Thayyil, M.S.; Jinitha, T. V.; Antony, A.; Govindaraj, G. Physisorption Mechanism in a Novel Ionogel Membrane Based CO_2 Gas Sensor. *J. Mater. Sci. Mater. Electron.* **2021**, *32*, 25164–25174, doi:10.1007/s10854-021-06973-5.

265. Weng, Q.; Zeng, L.; Chen, Z.; Han, Y.; Jiang, K.; Bando, Y.; Golberg, D. Hydrogen Storage in Carbon and Oxygen Co-Doped Porous Boron Nitrides. *Adv. Funct. Mater.* **2021**, *31*, doi:10.1002/adfm.202007381.

266. Peterson, A.W.; Heaton, R.J.; Georgiadis, R.M. The Effect of Surface Probe Density on DNA Hybridization. *Nucleic Acids Res.* **2001**, *29*, 5163–5168, doi:10.1093/nar/29.24.5163.

267. Prieto-Simon, B.; Campas, M.; Marty, J.-L. Biomolecule Immobilization in Biosensor Development:

Tailored Strategies Based on Affinity Interactions. *Protein Pept. Lett.* **2008**, *15*, 757–763, doi:10.2174/092986608785203791.

268. Liu, Y.; Yu, J. Oriented Immobilization of Proteins on Solid Supports for Use in Biosensors and Biochips: A Review. *Microchim. Acta* **2016**, *183*, 1–19, doi:10.1007/s00604-015-1623-4.
269. Oliverio, M.; Perotto, S.; Messina, G.C.; Lovato, L.; De Angelis, F. Chemical Functionalization of Plasmonic Surface Biosensors: A Tutorial Review on Issues, Strategies, and Costs. *ACS Appl. Mater. Interfaces* **2017**, *9*, 29394–29411, doi:10.1021/acsami.7b01583.
270. Steen Redeker, E.; Ta, D.T.; Cortens, D.; Billen, B.; Guedens, W.; Adriaensens, P. Protein Engineering for Directed Immobilization. *Bioconjug. Chem.* **2013**, *24*, 1761–1777, doi:10.1021/bc4002823.
271. Camarero, J.A. Recent Developments in the Site-Specific Immobilization of Proteins onto Solid Supports. *Biopolym. - Pept. Sci. Sect.* **2008**, *90*, 450–458, doi:10.1002/bip.20803.
272. Yoshimura, S.H.; Khan, S.; Ohno, S.; Yokogawa, T.; Nishikawa, K.; Hosoya, T.; Maruyama, H.; Nakayama, Y.; Takeyasu, K. Site-Specific Attachment of a Protein to a Carbon Nanotube End without Loss of Protein Function. *Bioconjug. Chem.* **2012**, *23*, 1488–1493, doi:10.1021/bc300131w.
273. Králik, M. Adsorption, Chemisorption, and Catalysis. *Chem. Pap.* **2014**, *68*, 1625–1638, doi:10.2478/s11696-014-0624-9.
274. Pereira-Silva, P.; Meira, D.I.; Costa-Barbosa, A.; Costa, D.; Rodrigues, M.S.; Borges, J.; Machado, A. V.; Cavaleiro, A.; Sampaio, P.; Vaz, F. Immobilization of Streptavidin on a Plasmonic Au-TiO_2 Thin Film towards an LSPR Biosensing Platform. *Nanomaterials* **2022**, *12*, 1526, doi:10.3390/nano12091526.
275. Achour, A.; Islam, M.; Solaymani, S.; Vizireanu, S.; Saeed, K.; Dinescu, G. Influence of Plasma Functionalization Treatment and Gold Nanoparticles on Surface Chemistry and Wettability of Reactive-Sputtered TiO_2 Thin Films. *Appl. Surf. Sci.* **2018**, *458*, 678–685, doi:10.1016/j.apsusc.2018.07.145.
276. Deng, X.; Ding, Y.; Wang, X.; Jia, X.; Zhang, S.; Li, X. Insight into the Properties of Plasmonic Au/TiO_2 Activated by O_2/Ar Plasma. *Nanomaterials* **2021**, *12*, 106, doi:10.3390/nano12010106.
277. Zhu, B.; Zhang, L.Y.; Liu, J.L.; Zhang, X.M.; Li, X.S.; Zhu, A.M. TiO2-Supported Au-Ag Plasmonic Nanocatalysts Achieved by Plasma Restructuring and Activation. *J. Hazard. Mater.* **2021**, *402*, doi:10.1016/j.jhazmat.2020.123508.

278. Anbumani, S.; da Silva, A.M.; Roggero, U.F.S.; Silva, A.M.P.A.; Hernández-Figueroa, H.E.; Cotta, M.A. Oxygen Plasma-Enhanced Covalent Biomolecule Immobilization on SU-8 Thin Films: A Stable and Homogenous Surface Biofunctionalization Strategy. *Appl. Surf. Sci.* **2021**, *553*, 149502, doi:10.1016/j.apsusc.2021.149502.

279. Junkar, I.; Kulkarni, M.; Drašler, B.; Rugelj, N.; Recek, N.; Drobne, D.; Kovač, J.; Humpolicek, P.; Iglič, A.; Mozetič, M. Enhanced Biocompatibility of TiO_2 Surfaces by Highly Reactive Plasma. *J. Phys. D. Appl. Phys.* **2016**, *49*, doi:10.1088/0022-3727/49/24/244002.

280. Lomant, A.J.; Fairbanks, G. Chemical Probes of Extended Biological Structures: Synthesis and Properties of the Cleavable Protein Cross-Linking Reagent [35S]Dithiobis(Succinimidyl Propionate). *J. Mol. Biol.* **1976**, *104*, 243–261, doi:10.1016/0022-2836(76)90011-5.

281. Arya, S.K.; Chornokur, G.; Venugopal, M.; Bhansali, S. Dithiobis(Succinimidyl Propionate) Modified Gold Microarray Electrode Based Electrochemical Immunosensor for Ultrasensitive Detection of Cortisol. *Biosens. Bioelectron.* **2010**, *25*, 2296–2301, doi:10.1016/j.bios.2010.03.016.

282. Schmid, A.H.; Stanca, S.E.; Thakur, M.S.; Thampi, K.R.; Suri, C.R. Site-Directed Antibody Immobilization on Gold Substrate for Surface Plasmon Resonance Sensors. *Sensors Actuators, B Chem.* **2006**, *113*, 297–303, doi:10.1016/j.snb.2005.03.018.

283. Toma, K.; Oishi, K.; Yoshimura, N.; Arakawa, T.; Yatsuda, H.; Mitsubayashi, K. Repeated Immunosensing by a Dithiobis(Succinimidyl Propionate)-Modified SAW Device. *Talanta* **2019**, *203*, 274–279, doi:10.1016/j.talanta.2019.05.080.

284. Dhamu, V.N.; Poudyal, D.C.; Muthukumar, S.; Prasad, S. A Highly Sensitive Electrochemical Sensor System to Detect and Distinguish Between Glyphosate and Glufosinate. *J. Electrochem. Soc.* **2021**, *168*, 057531, doi:10.1149/1945-7111/ac00f7.

285. Frasconi, M.; Mazzei, F.; Ferri, T. Protein Immobilization at Gold-Thiol Surfaces and Potential for Biosensing. *Anal. Bioanal. Chem.* **2010**, *398*, 1545–1564, doi:10.1007/s00216-010-3708-6.

286. Durocher, S.; Rezaee, A.; Hamm, C.; Rangan, C.; Mittler, S.; Mutus, B. Disulfide-Linked, Gold Nanoparticle Based Reagent for Detecting Small Molecular Weight Thiols. *J. Am. Chem. Soc.* **2009**, *131*, 2475–2477, doi:10.1021/ja808548x.

287. Lim, C.Y.; Owens, N.A.; Wampler, R.D.; Ying, Y.; Granger, J.H.; Porter, M.D.; Takahashi, M.; Shimazu, K. Succinimidyl Ester Surface Chemistry: Implications of the Competition between Aminolysis and Hydrolysis on Covalent Protein Immobilization. *Langmuir* **2014**, *30*, 12868–12878, doi:10.1021/la503439g.

288. Vericat, C.; Vela, M.E.; Benitez, G.; Carro, P.; Salvarezza, R.C. Self-Assembled Monolayers of Thiols

and Dithiols on Gold: New Challenges for a Well-Known System. *Chem. Soc. Rev.* **2010**, *39*, 1805–1834, doi:10.1039/b907301a.

289. Koslowski, B.; Boyen, H.G.; Wilderotter, C.; Kästle, G.; Ziemann, P.; Wahrenberg, R.; Oelhafen, P. Oxidation of Preferentially (1 1 1)-Oriented Au Films in an Oxygen Plasma Investigated by Scanning Tunneling Microscopy and Photoelectron Spectroscopy. *Surf. Sci.* **2001**, *475*, 1–10, doi:10.1016/S0039-6028(00)00986-9.
290. Raiber, K.; Terfort, A.; Benndorf, C.; Krings, N.; Strehblow, H.H. Removal of Self-Assembled Monolayers of Alkanethiolates on Gold by Plasma Cleaning. *Surf. Sci.* **2005**, *595*, 56–63, doi:10.1016/j.susc.2005.07.038.
291. Stevenson, H.S.; Shetty, S.S.; Thomas, N.J.; Dhamu, V.N.; Bhide, A.; Prasad, S. Ultrasensitive and Rapid-Response Sensor for the Electrochemical Detection of Antibiotic Residues within Meat Samples. *ACS Omega* **2019**, *4*, 6324–6330, doi:10.1021/acsomega.8b03534.
292. Owens, N.A.; Pinter, A.; Porter, M.D. Surface-Enhanced Resonance Raman Scattering for the Sensitive Detection of a Tuberculosis Biomarker in Human Serum. *J. Raman Spectrosc.* **2019**, *50*, 15–25, doi:10.1002/jrs.5500.
293. Munje, R.D.; Muthukumar, S.; Jagannath, B.; Prasad, S. A New Paradigm in Sweat Based Wearable Diagnostics Biosensors Using Room Temperature Ionic Liquids (RTILs). *Sci. Rep.* **2017**, *7*, doi:10.1038/s41598-017-02133-0.
294. Stevenson, H.; Bacon, A.; Joseph, K.M.; Gwandaru, W.R.W.; Bhide, A.; Sankhala, D.; Dhamu, V.N.; Prasad, S. A Rapid Response Electrochemical Biosensor for Detecting Thc In Saliva. *Sci. Rep.* **2019**, *9*, 1–12, doi:10.1038/s41598-019-49185-y.
295. Mintah Churcher, N.K.; Upasham, S.; Rice, P.; Bhadsavle, S.; Prasad, S. Development of a Flexible, Sweat-Based Neuropeptide Y Detection Platform. *RSC Adv.* **2020**, *10*, 23173–23186, doi:10.1039/d0ra03729j.
296. Bhadra, P.; Siu, S.W.I. Effect of Concentration, Chain Length, Hydrophobicity, and an External Electric Field on the Growth of Mixed Alkanethiol Self-Assembled Monolayers: A Molecular Dynamics Study. *Langmuir* **2021**, *37*, 1913–1924, doi:10.1021/acs.langmuir.0c03414.
297. Christopoulos, T.K.; Diamandis, E.P. Theory of Immunoassays. In *Immunoassay*; Diamandis, E., Christopoulos, T., Eds.; Elsevier, 1996; Vol. 4, pp. 25–50 ISBN 0-12-214730-8.
298. Stockman, M.I. Nanoplasmonics: The Physics behind the Applications. *Phys. Today* **2011**, *64*, 39–44, doi:10.1063/1.3554315.
299. Divya, J.; Selvendran, S.; Raja, A.S.; Sivasubramanian, A. Surface Plasmon Based Plasmonic

Sensors: A Review on Their Past, Present and Future. *Biosens. Bioelectron. X* **2022**, *11*, 100175, doi:10.1016/j.biosx.2022.100175.

300. Stockman, M.I.; Kneipp, K.; Bozhevolnyi, S.I.; Saha, S.; Dutta, A.; Ndukaife, J.; Kinsey, N.; Reddy, H.; Guler, U.; Shalaev, V.M.; et al. Roadmap on Plasmonics. *J. Opt.* **2018**, *20*, 043001, doi:10.1088/2040-8986/aaa114.
301. Coronado, E.A.; Encina, E.R.; Stefani, F.D. Optical Properties of Metallic Nanoparticles: Manipulating Light, Heat and Forces at the Nanoscale. *Nanoscale* **2011**, *3*, 4042–4059, doi:10.1039/c1nr10788g.
302. Lu, X.; Rycenga, M.; Skrabalak, S.E.; Wiley, B.; Xia, Y. Chemical Synthesis of Novel Plasmonic Nanoparticles. *Annu. Rev. Phys. Chem.* **2009**, *60*, 167–192, doi:10.1146/annurev.physchem.040808.090434.
303. Scholl, J.A.; Koh, A.L.; Dionne, J.A. Quantum Plasmon Resonances of Individual Metallic Nanoparticles. *Nature* **2012**, *483*, 421–427, doi:10.1038/nature10904.
304. Zheng, J.; Cheng, X.; Zhang, H.; Bai, X.; Ai, R.; Shao, L.; Wang, J. Gold Nanorods: The Most Versatile Plasmonic Nanoparticles. *Chem. Rev.* **2021**, *121*, 13342–13453, doi:10.1021/acs.chemrev.1c00422.
305. Sovizi, M.; Aliannezhadi, M. Localized Surface Plasmon Resonance (LSPR) of Coupled Metal Nanospheres in Longitudinal, Transverse and Three-Dimensional Coupling Configurations. *Optik (Stuttg).* **2022**, *252*, 168518, doi:10.1016/j.ijleo.2021.168518.
306. Yu, H.; Peng, Y.; Yang, Y.; Li, Z.Y. Plasmon-Enhanced Light–Matter Interactions and Applications. *npj Comput. Mater.* **2019**, *5*, 45, doi:10.1038/s41524-019-0184-1.
307. Liz-Marzán, L.M. Tailoring Surface Plasmons through the Morphology and Assembly of Metal Nanoparticles. *Langmuir* **2006**, *22*, 32–41, doi:10.1021/la0513353.
308. Truong, P.L.; Ma, X.; Sim, S.J. Resonant Rayleigh Light Scattering of Single Au Nanoparticles with Different Sizes and Shapes. *Nanoscale* **2014**, *6*, 2307–2315, doi:10.1039/c3nr05211g.
309. Khurana, K.; Jaggi, N. Localized Surface Plasmonic Properties of Au and Ag Nanoparticles for Sensors: A Review. *Plasmonics* **2021**, *16*, 981–999, doi:10.1007/s11468-021-01381-1.
310. Qiu, G.; Ng, S.P.; Wu, C.M.L. Bimetallic Au-Ag Alloy Nanoislands for Highly Sensitive Localized Surface Plasmon Resonance Biosensing. *Sensors Actuators, B Chem.* **2018**, *265*, 459–467, doi:10.1016/j.snb.2018.03.066.
311. Zeng, S.; Yong, K.T.; Roy, I.; Dinh, X.Q.; Yu, X.; Luan, F. A Review on Functionalized Gold Nanoparticles for Biosensing Applications. *Plasmonics* **2011**, *6*, 491–506,

doi:10.1007/s11468-011-9228-1.

312. Amendola, V.; Pilot, R.; Frasconi, M.; Maragò, O.M.; Iatì, M.A. Surface Plasmon Resonance in Gold Nanoparticles: A Review. *J. Phys. Condens. Matter* **2017**, *29*, 203002, doi:10.1088/1361-648X/aa60f3.
313. Amendola, V.; Bakr, O.M.; Stellacci, F. A Study of the Surface Plasmon Resonance of Silver Nanoparticles by the Discrete Dipole Approximation Method: Effect of Shape, Size, Structure, and Assembly. *Plasmonics* **2010**, *5*, 85–97, doi:10.1007/s11468-009-9120-4.
314. Rycenga, M.; Cobley, C.M.; Zeng, J.; Li, W.; Moran, C.H.; Zhang, Q.; Qin, D.; Xia, Y. Controlling the Synthesis and Assembly of Silver Nanostructures for Plasmonic Applications. *Chem. Rev.* **2011**, *111*, 3669–3712, doi:10.1021/cr100275d.
315. Gao, C.; Hu, Y.; Wang, M.; Chi, M.; Yin, Y. Fully Alloyed Ag/Au Nanospheres: Combining the Plasmonic Property of Ag with the Stability of Au. *J. Am. Chem. Soc.* **2014**, *136*, 7474–7479, doi:10.1021/ja502890c.
316. Juluri, B.K.; Huang, J.; Jensen, L. Extinction, Scattering and Absorption Efficiencies of Single and Multilayer Nanoparticles 2016.
317. Kelly, K.L.; Coronado, E.; Zhao, L.L.; Schatz, G.C. The Optical Properties of Metal Nanoparticles: The Influence of Size, Shape, and Dielectric Environment. *ChemInform* **2003**, *34*, doi:10.1002/chin.200316243.
318. Borah, R.; Verbruggen, S.W. Silver-Gold Bimetallic Alloy versus Core-Shell Nanoparticles: Implications for Plasmonic Enhancement and Photothermal Applications. *J. Phys. Chem. C* **2020**, *124*, 12081–12094, doi:10.1021/acs.jpcc.0c02630.
319. Rabiee, N.; Bagherzadeh, M.; Ghasemi, A.; Zare, H.; Ahmadi, S.; Fatahi, Y.; Dinarvand, R.; Rabiee, M.; Ramakrishna, S.; Shokouhimehr, M.; et al. Point-of-Use Rapid Detection of Sars-Cov-2: Nanotechnology-Enabled Solutions for the Covid-19 Pandemic. *Int. J. Mol. Sci.* **2020**, *21*, 1–23, doi:10.3390/ijms21145126.
320. Lindquist, N.C.; Nagpal, P.; McPeak, K.M.; Norris, D.J.; Oh, S.H. Engineering Metallic Nanostructures for Plasmonics and Nanophotonics. *Reports Prog. Phys.* **2012**, *75*, 036501, doi:10.1088/0034-4885/75/3/036501.
321. Loza, K.; Heggen, M.; Epple, M. Synthesis, Structure, Properties, and Applications of Bimetallic Nanoparticles of Noble Metals. *Adv. Funct. Mater.* **2020**, *30*, doi:10.1002/adfm.201909260.
322. Mott, D.M.; Anh, D.T.N.; Singh, P.; Shankar, C.; Maenosono, S. Electronic Transfer as a Route to Increase the Chemical Stability in Gold and Silver Core-Shell Nanoparticles. *Adv. Colloid Interface*

Sci. **2012**, *185–186*, 14–33, doi:10.1016/j.cis.2012.08.007.

323. Park, M.; Hwang, C.S.H.; Jeong, K.H. Nanoplasmonic Alloy of Au/Ag Nanocomposites on Paper Substrate for Biosensing Applications. *ACS Appl. Mater. Interfaces* **2018**, *10*, 290–295, doi:10.1021/acsami.7b16182.
324. Liu, H.; Zeng, J.; Song, L.; Zhang, L.; Chen, Z.; Li, J.; Xiao, Z.; Su, F.; Huang, Y. Etched-Spiky Au@Ag Plasmonic-Superstructure Monolayer Films for Triple Amplification of Surface-Enhanced Raman Scattering Signals. *Nanoscale Horizons* **2022**, *7*, 554–561, doi:10.1039/d2nh00023g.
325. Stephanie, R.; Kim, M.W.; Kim, S.H.; Kim, J.K.; Park, C.Y.; Park, T.J. Recent Advances of Bimetallic Nanomaterials and Its Nanocomposites for Biosensing Applications. *TrAC - Trends Anal. Chem.* **2021**, *135*, 116159, doi:10.1016/j.trac.2020.116159.
326. Homola, J.; Yee, S.S.; Gauglitz, G. Surface Plasmon Resonance Sensors: Review. *Sensors Actuators, B Chem.* **1999**, *54*, 3–15, doi:10.1016/S0925-4005(98)00321-9.
327. Stewart, M.E.; Anderton, C.R.; Thompson, L.B.; Maria, J.; Gray, S.K.; Rogers, J.A.; Nuzzo, R.G. Nanostructured Plasmonic Sensors. *Chem. Rev.* **2008**, *108*, 494–521, doi:10.1021/cr068126n.
328. Navas, M.P.; Soni, R.K. Laser Generated Ag and Ag-Au Composite Nanoparticles for Refractive Index Sensor. *Appl. Phys. A Mater. Sci. Process.* **2014**, *116*, 879–886, doi:10.1007/s00339-014-8460-x.
329. Li, J.J.; Qin, Q.X.; Weng, G.J.; Zhu, J.; Zhao, J.W. Improve the Hole Size–Dependent Refractive Index Sensitivity of Au–Ag Nanocages by Tuning the Alloy Composition. *Plasmonics* **2022**, *17*, 597–612, doi:10.1007/s11468-021-01536-0.
330. Sultangaziyev, A.; Ilyas, A.; Dyussupova, A.; Bukasov, R. Trends in Application of SERS Substrates beyond Ag and Au, and Their Role in Bioanalysis. *Biosensors* **2022**, *12*, 967, doi:10.3390/bios12110967.
331. Barbillon, G. Latest Novelties on Plasmonic and Non-Plasmonic Nanomaterials for SERS Sensing. *Nanomaterials* **2020**, *10*, 1–17, doi:10.3390/nano10061200.
332. Rai, A.; Bhaskar, S.; Ramamurthy, S.S. Plasmon-Coupled Directional Emission from Soluplus-Mediated AgAu Nanoparticles for Attomolar Sensing Using a Smartphone. *ACS Appl. Nano Mater.* **2021**, *4*, 5940–5953, doi:10.1021/acsanm.1c00841.
333. Rai, A.; Bhaskar, S.; Ganesh, K.M.; Ramamurthy, S.S. Hottest Hotspots from the Coldest Cold: Welcome to Nano 4.0. *ACS Appl. Nano Mater.* **2022**, *5*, 12245–12264, doi:10.1021/acsanm.2c02556.

334. Bhaskar, S. Biosensing Technologies: A Focus Review on Recent Advancements in Surface Plasmon Coupled Emission. *Micromachines* **2023**, *14*, 574, doi:10.3390/mi14030574.

335. Alkhalayfeh, M.A.; Aziz, A.A.; Pakhuruddin, M.Z.; Katubi, K.M.M. Plasmonic Effects of Au@Ag Nanoparticles in Buffer and Active Layers of Polymer Solar Cells for Efficiency Enhancement. *Materials (Basel).* **2022**, *15*, 5472, doi:10.3390/ma15165472.

336. Zheng, F.; Ke, W.; Shi, L.; Liu, H.; Zhao, Y. Plasmonic Au-Ag Janus Nanoparticle Engineered Ratiometric Surface-Enhanced Raman Scattering Aptasensor for Ochratoxin A Detection. *Anal. Chem.* **2019**, *91*, 11812–11820, doi:10.1021/acs.analchem.9b02469.

337. Barradas, N.P.; Jeynes, C.; Webb, R.P.; Kreissig, U.; Grötzschel, R. Unambiguous Automatic Evaluation of Multiple Ion Beam Analysis Data with Simulated Annealing. *Nucl. Instruments Methods Phys. Res. Sect. B Beam Interact. with Mater. Atoms* **1999**, *149*, 233–237, doi:10.1016/S0168-583X(98)00731-9.

338. Laegreid, N.; Wehner, G.K. Sputtering Yields of Metals for Ar^+ and Ne^+ Ions with Energies from 50 to 600 ev. *J. Appl. Phys.* **1961**, *32*, 365–369, doi:10.1063/1.1736012.

339. Rodrigues, M.S.; Meira, D.I.; Lopes, C.; Borges, J.; Vaz, F. Preparation of Plasmonic Au-TiO_2 Thin Films on a Transparent Polymer Substrate. *Coatings* **2020**, *10*, 227, doi:10.3390/coatings10030227.

340. Sekhon, J.S.; Verma, S.S. Refractive Index Sensitivity Analysis of Ag, Au, and Cu Nanoparticles. *Plasmonics* **2011**, *6*, 311–317, doi:10.1007/s11468-011-9206-7.

341. Saleh, N.M.; Aziz, A.A. Simulation of Surface Plasmon Resonance on Different Size of a Single Gold Nanoparticle. *J. Phys. Conf. Ser.* **2018**, *1083*, 012041, doi:10.1088/1742-6596/1083/1/012041.

342. Borges, J.; Ferreira, C.G.; Fernandes, J.P.C.; Rodrigues, M.S.; Proença, M.; Apreutesei, M.; Alves, E.; Barradas, N.P.; Moura, C.; Vaz, F. Thin Films of Ag-Au Nanoparticles Dispersed in TiO_2: Influence of Composition and Microstructure on the LSPR and SERS Responses. *J. Phys. D. Appl. Phys.* **2018**, *51*, 205102, doi:10.1088/1361-6463/aabc49.

343. Bendavid, A.; Martin, P.J. Review of Thin Film Materials Deposition by the Filtered Cathodic Vacuum Arc Process at CSIRO. *J. Aust. Ceram. Soc.* **2014**, *50*, 86–101.

344. Tan, M.I.S.M.H.; Omar, A.F.; Rashid, M.; Hashim, U. VIS-NIR Spectral and Particles Distribution of Au, Ag, Cu, Al and Ni Nanoparticles Synthesized in Distilled Water Using Laser Ablation. *Results Phys.* **2019**, *14*, 102497, doi:10.1016/j.rinp.2019.102497.

345. Borges, J.; Rodrigues, M.S.; Lopes, C.; Costa, D.; Ferreira, A.; Pereira, R.M.S.; Costa, M.F.;

Vasilevskiy, M.I.; Vaz, F. Ag Fractals Formed on Top of a Porous TiO_2 Thin Film. *Phys. Status Solidi - Rapid Res. Lett.* **2016**, *10*, 530–534, doi:10.1002/pssr.201600131.

346. Asoro, M.A.; Kovar, D.; Ferreira, P.J. In Situ Transmission Electron Microscopy Observations of Sublimation in Silver Nanoparticles. *ACS Nano* **2013**, *7*, 7844–7852, doi:10.1021/nn402771j.
347. Pandey, P.; Kunwar, S.; Sui, M.; Zhang, Q.; Li, M.Y.; Lee, J. Morphological and Optical Evolution of Silver Nanoparticles on Sapphire (0001) Along with the Concurrent Influence of Diffusion, Ostwald's Ripening, and Sublimation. *IEEE Trans. Nanotechnol.* **2017**, *16*, 321–332, doi:10.1109/TNANO.2017.2664102.
348. Offermans, P.; Schaafsma, M.C.; Rodriguez, S.R.K.; Zhang, Y.; Crego-Calama, M.; Brongersma, S.H.; Gómez Rivas, J. Universal Scaling of the Figure of Merit of Plasmonic Sensors. *ACS Nano* **2011**, *5*, 5151–5157, doi:10.1021/nn201227b.
349. Doiron, B.; Mota, M.; Wells, M.P.; Bower, R.; Mihai, A.; Li, Y.; Cohen, L.F.; Alford, N.M.N.; Petrov, P.K.; Oulton, R.F.; et al. Quantifying Figures of Merit for Localized Surface Plasmon Resonance Applications: A Materials Survey. *ACS Photonics* **2019**, *6*, 240–259, doi:10.1021/acsphotonics.8b01369.
350. Baqir, M.A.; Choudhury, P.K. Hyperbolic Metamaterial-Based Optical Biosensor for Detecting Cancer Cells. *IEEE Photonics Technol. Lett.* **2022**, *35*, 183–186, doi:10.1109/LPT.2022.3228943.
351. Shen, Y.; Zhou, J.; Liu, T.; Tao, Y.; Jiang, R.; Liu, M.; Xiao, G.; Zhu, J.; Zhou, Z.K.; Wang, X.; et al. Plasmonic Gold Mushroom Arrays with Refractive Index Sensing Figures of Merit Approaching the Theoretical Limit. *Nat. Commun.* **2013**, *4*, 2381, doi:10.1038/ncomms3381.
352. Chung, T.; Hwang, C.S.H.; Ahn, M.S.; Jeong, K.H. Au/Ag Bimetallic Nanocomposites as a Highly Sensitive Plasmonic Material. *Plasmonics* **2019**, *14*, 407–413, doi:10.1007/s11468-018-0818-z.
353. Cao Van, P.; Surabhi, S.; Quoc, V.D.; Lee, J.W.; Tae, C.C.; Kuchi, R.; Jeong, J.R. Broadband Tunable Plasmonic Substrate Using Self-Assembled Gold–Silver Alloy Nanoparticles. *Curr. Appl. Phys.* **2019**, *19*, 1245–1251, doi:10.1016/j.cap.2019.08.009.
354. Kyaw, H.H.; Myint, M.T.Z.; Al-Harthi, S.H.; Maekawa, T.; Yanagisawa, K.; Sellai, A.; Dutta, J. Observation of Exchanging Role of Gold and Silver Nanoparticles in Bimetallic Thin Film upon Annealing above the Glass Transition Temperature. *Mater. Res. Express* **2017**, *4*, 086409, doi:10.1088/2053-1591/aa84e6.
355. Klingelhöfer, D.; Braun, M.; Schöffel, N.; Oremek, G.M.; Brüggmann, D.; Groneberg, D.A.

Ochratoxin – Characteristics, Influences and Challenges of Global Research. *Food Control* **2020**, *114*, 107230, doi:10.1016/j.foodcont.2020.107230.

356. Mahmudiono, T.; Fakhri, Y.; Sarafraz, M.; Mehri, F.; Hoseinvandtabar, S.; Mousavi Khaneghah, A. The Prevalence and Concentration of Ochratoxin A in Green Coffee-Based Products: A Worldwide Systematic Review, Meta-Analysis, and Health Risk Assessment. *J. Food Compos. Anal.* **2023**, *122*, 105423, doi:10.1016/j.jfca.2023.105423.
357. Lee, H.J.; Ryu, D. Worldwide Occurrence of Mycotoxins in Cereals and Cereal-Derived Food Products: Public Health Perspectives of Their Co-Occurrence. *J. Agric. Food Chem.* **2017**, *65*, 7034–7051, doi:10.1021/acs.jafc.6b04847.
358. Celik, D.; Kabak, B. Assessment to Propose a Maximum Permitted Level for Ochratoxin A in Dried Figs. *J. Food Compos. Anal.* **2022**, *112*, 104705, doi:10.1016/j.jfca.2022.104705.
359. Welke, J.E. Fungal and Mycotoxin Problems in Grape Juice and Wine Industries. *Curr. Opin. Food Sci.* **2019**, *29*, 7–13, doi:10.1016/j.cofs.2019.06.009.
360. Sharafi, H.; Alizadeh, N.; Moradi, M.; Sharafi, K.; Mousavi Khaneghah, A. The Prevalence and Concentration of Ochratoxin A in Meat and Edible Offal: A Global Systematic Review and Meta-Analysis. *Food Chem. Toxicol.* **2023**, *178*, 113921, doi:10.1016/j.fct.2023.113921.
361. Mir, S.A.; Dar, B.N.; Shah, M.A.; Sofi, S.A.; Hamdani, A.M.; Oliveira, C.A.F.; Hashemi Moosavi, M.; Mousavi Khaneghah, A.; Sant'Ana, A.S. Application of New Technologies in Decontamination of Mycotoxins in Cereal Grains: Challenges, and Perspectives. *Food Chem. Toxicol.* **2021**, *148*, 111976, doi:10.1016/j.fct.2021.111976.
362. Pfohl-Leszkowicz, A.; Manderville, R.A. Ochratoxin A: An Overview on Toxicity and Carcinogenicity in Animals and Humans. *Mol. Nutr. Food Res.* **2007**, *51*, 61–99, doi:10.1002/mnfr.200600137.
363. Krogh, P.; Hald, B.; Pedersen, E.J. Occurrence of Ochratoxin a and Citrinin in Cereals Associated With Mycotoxic Porcine Nephropathy. *Acta Pathol. Microbiol. Scand. Sect. B Microbiol. Immunol.* **1973**, *81 B*, 689–695, doi:10.1111/j.1699-0463.1973.tb02261.x.
364. World Health Organization *Evaluation of Certain Food Additives and Contaminants: Sixty-Eighth Report of the Joint FAO/WHO Expert Committee on Food Additives*; Geneva, Switzerland, 2007;
365. Pena, A.; Cerejo, F.; Lino, C.; Silveira, I. Determination of Ochratoxin A in Portuguese Rice Samples by High Performance Liquid Chromatography with Fluorescence Detection. *Anal. Bioanal. Chem.* **2005**, *382*, 1288–1293, doi:10.1007/s00216-005-3254-9.
366. Skarkova, J.; Ostry, V.; Malir, F.; Roubal, T. Determination of Ochratoxin A in Food by High

Performance Liquid Chromatography. *Anal. Lett.* **2013**, *46*, 1495–1504, doi:10.1080/00032719.2013.771266.

367. Flajs, D.; Domijan, A.M.; Ivić, D.; Cvjetković, B.; Peraica, M. ELISA and HPLC Analysis of Ochratoxin A in Red Wines of Croatia. *Food Control* **2009**, *20*, 590–592, doi:10.1016/j.foodcont.2008.08.021.
368. Altug, H.; Oh, S.H.; Maier, S.A.; Homola, J. Advances and Applications of Nanophotonic Biosensors. *Nat. Nanotechnol.* **2022**, *17*, 5–16, doi:10.1038/s41565-021-01045-5.
369. Díaz-Núñez, P.; García-Martín, J.M.; González, M.U.; González-Arrabal, R.; Rivera, A.; Alonso-González, P.; Martín-Sánchez, J.; Taboada-Gutiérrez, J.; González-Rubio, G.; Guerrero-Martínez, A.; et al. On the Large Near-Field Enhancement on Nanocolumnar Gold Substrates. *Sci. Rep.* **2019**, *9*, doi:10.1038/s41598-019-50392-w.
370. Anker, J.N.; Hall, W.P.; Lyandres, O.; Shah, N.C.; Zhao, J.; Van Duyne, R.P. Biosensing with Plasmonic Nanosensors. *Nat. Mater.* **2008**, *7*, 442–453, doi:10.1038/nmat2162.
371. Hamza, M.E.; Othman, M.A.; Swillam, M.A. Plasmonic Biosensors: Review. *Biology (Basel).* **2022**, *11*, 621, doi:10.3390/biology11050621.
372. Mejía-Salazar, J.R.; Oliveira, O.N. Plasmonic Biosensing. *Chem. Rev.* **2018**, *118*, 10617–10625, doi:10.1021/acs.chemrev.8b00359.
373. Xu, T.; Geng, Z. Strategies to Improve Performances of LSPR Biosensing: Structure, Materials, and Interface Modification. *Biosens. Bioelectron.* **2021**, *174*, 112850, doi:10.1016/j.bios.2020.112850.
374. Csáki, A.; Stranik, O.; Fritzsche, W. Localized Surface Plasmon Resonance Based Biosensing. *Expert Rev. Mol. Diagn.* **2018**, *18*, 279–296, doi:10.1080/14737159.2018.1440208.
375. Meira, D.I.; Rodrigues, M.S.; Borges, J.; Vaz, F. Enhancing the Extinction Efficiency and Plasmonic Response of Bimetallic Nanoparticles of Au-Ag in Robust Thin Film Sensing Platforms. *Sensors* **2023**, *23*, 9618, doi:10.3390/s23239618.
376. Rehmat, Z.; Mohammed, W.S.; Sadiq, M.B.; Somarapalli, M.; Kumar Anal, A. Ochratoxin A Detection in Coffee by Competitive Inhibition Assay Using Chitosan-Based Surface Plasmon Resonance Compact System. *Colloids Surfaces B Biointerfaces* **2019**, *174*, 569–574, doi:10.1016/j.colsurfb.2018.11.060.
377. Shen, M.; Rusling, J.F.; Dixit, C.K. Site-Selective Orientated Immobilization of Antibodies and Conjugates for Immunodiagnostics Development. *Methods* **2017**, *116*, 95–111, doi:10.1016/j.ymeth.2016.11.010.

378. Lipman, N.S.; Jackson, L.R.; Trudel, L.J.; Weis-Garcia, F. Monoclonal versus Polyclonal Antibodies: Distinguishing Characteristics, Applications, and Information Resources. *ILAR J.* **2005**, *46*, 258–267, doi:10.1093/ilar.46.3.258.

379. Wiseman, M.E.; Frank, C.W. Antibody Adsorption and Orientation on Hydrophobic Surfaces. *Langmuir* **2012**, *28*, 1765–1774, doi:10.1021/la203095p.

380. European Commission *Commision Regulation (EC) No. 123/2005 of 26 January 2005 Amending Regulation (EC) 466/2001 as Regard Ochratoxin A*; 2005; Vol. 25;.

381. Liu, B.; Huang, R.; Yu, Y.; Su, R.; Qi, W.; He, Z. Gold Nanoparticle-Aptamer-Based LSPR Sensing of Ochratoxin A at a Widened Detection Range by Double Calibration Curve Method. *Front. Chem.* **2018**, *6*, doi:10.3389/fchem.2018.00094.

382. Park, J.H.; Byun, J.Y.; Mun, H.; Shim, W.B.; Shin, Y.B.; Li, T.; Kim, M.G. A Regeneratable, Label-Free, Localized Surface Plasmon Resonance (LSPR) Aptasensor for the Detection of Ochratoxin A. *Biosens. Bioelectron.* **2014**, *59*, 321–327, doi:10.1016/j.bios.2014.03.059.

383. Shrestha, S.; Wang, B.; Dutta, P. Nanoparticle Processing: Understanding and Controlling Aggregation. *Adv. Colloid Interface Sci.* **2020**, *279*, 102162, doi:10.1016/j.cis.2020.102162.

384. Tim, B.; Błaszkiewicz, P.; Kotkowiak, M. Recent Advances in Metallic Nanoparticle Assemblies for Surface-Enhanced Spectroscopy. *Int. J. Mol. Sci.* **2022**, *23*, 291, doi:10.3390/ijms23010291.

385. Zhang, L.; Mazouzi, Y.; Salmain, M.; Liedberg, B.; Boujday, S. Antibody-Gold Nanoparticle Bioconjugates for Biosensors: Synthesis, Characterization and Selected Applications. *Biosens. Bioelectron.* **2020**, *165*, 112370, doi:10.1016/j.bios.2020.112370.